The Effect of Chemical and Isotopic Exchange on Mica Rb-Sr Closure Temperatures in the Lepontine Alps.

Hannah Townley

Geology Department

University of Leicester

November 2001

Submitted in accordance with the requirements for

the degree of Doctor of Philosophy

The candidate confirms that the work submitted is her own and that the appropriate credit has been given where reference has been made to the work of others.

ProQuest LLC
789 East Eisenhower Parkway
P.O. Box 1346
Ann Arbor, MI 48106-1346

Hannah Townley: The Effect of Chemical and Isotopic Exchange on Mica Rb-Sr Closure Temperatures in the Lepontine Alps.

Abstract

The aim of this study is to provide a greater understanding of the resetting processes, which produce the Rb-Sr closure temperature, allowing the production of more relevant models of closure temperature. This study provides information on the scale, mechanism and pathways of transport of species within rocks to understand how chemical exchange during cooling affects the closure temperatures of isotopic systems.

To complete these objectives three areas are addressed: a literature review of the processes thought to be involved in defining a closure temperature, microanalytical work, and modelling of results. The samples studied are closed system marbles, implying that any exchange effects can be quantified, as any species lost from one mineral must be balanced by gain in another mineral or minerals.

TIMS Rb-Sr suggests the phlogopite closure temperature is higher than that of biotite. This study and previous modelling work of chemical exchange suggest that closure temperatures are partly controlled by the mineral mode and the elemental concentration of species within each mineral. LA-ICP-MS studies of calcite reveal gradients of $^{87}Sr/^{86}Sr$, which decrease away from the mica bands present in the samples over a few centimetres. Ion and electron microprobe work suggest that the movement of elements may be in the opposite sense to that of isotopic exchange, but the results from this part of the study are inconclusive.

During cooling from peak metamorphism, isotopic and chemical gradients are "frozen" in different minerals. Modelling suggests that exchange occurs by a combination of volume and grain boundary diffusion. $^{87}Sr/^{86}Sr$ gradients in calcite are used to produce a new method of producing the age of peak metamorphism and the profile shape describes the cooling history. The results of this study imply that exchange within the Rb-Sr system is very complex and the closure temperature process is more complicated than previously thought.

Acknowledgements

First and foremost thank you to Gawen Jenkin and Randy Parrish for choosing me to mess around with isotopes and various ideas for the last three years. It has been a pleasure (well, mostly).

Thank you to all the staff who have offered help and advice over the past three years, especially to Rob Wilson of the electron microprobe and to Colin Cunningham for making all my thin sections (University of Leicester); John Craven and Richard Hinton at the Ion Microprobe Facility at Edinburgh University; and to Matt Horstwood, Jane Evans and Geoff Nowell (formerly) from NIGL. Thank you to Martin Engi (University of Bern) for advice on sampling locations and to Sarah Gabbott for assisting in the field.

A big thank you goes to all those who have tried to keep me sane (and often failed) over the past days, weeks and months; Matt Hooper (for taking me to the pub); James Tomlinson and Dave Gladwell (for making sure I get home); Pat Thompson (for advice about jaffa cakes); and Dave Gelsthorpe (for cups of tea). Thanks must also go to Lorna Marsh, Duncan Ross, Richard Thomas, Kathryn Hoyle, Rob Corker, Jo Chouler, Keith Ellison, Tamsin Russell, Catherine Neal and Matt Insell for reminding me there is life outside the geology department. Thanks also to Mum and Dad, you've been great.

I also acknowledge NERC grant GT04/1998/ES/0134 and funding support from NIGL as the CASE partner for the grant award.

He Tells Her

He tells her that the world is flat –
He knows the facts and that is that.
In altercations fierce and long
She tries her best to prove him wrong.
But he has learnt to argue well.
He calls her arguments unsound
And often asks her not to yell.
She cannot win. He stands his ground.

The planet goes on being round.

By Wendy Cope

Contents

List of Figures

List of Figures

List of Tables

Chapter 1

Introduction

1.1 Background to the Study

Geochronological systems together with those geothermetric systems based upon exchange equilibria frequently record ages and temperatures different from those at the peak of metamorphism. This effect is related to a resetting process, which may be used in determining cooling rates if a "closure temperature" can be defined for the radiometric system in question.

Currently, the precise mechanism of exchange is poorly understood and models of resetting processes are necessarily simplistic. For example, the Dodson (1973) closure temperature model indicates that mineral grain size should be important in controlling closure temperatures. Reddy *et al.* (1994) and Hess & Lippolt (1994) have demonstrated this for Ar in biotite and, more recently by Jenkin *et al.* (2001) and in this work, for biotite Rb-Sr. Other factors in the Dodson (1973) closure temperature equation that could be considered are the effects of the cooling rate and the rate of the diffusion coefficient. Another factor, not considered by Dodson (1973), is the mineral mode and the distribution of elements and isotopes of those elements among these minerals. This has previously been evaluated by Jenkin (1997) and will be considered further in this work.

1.1.2 *The Importance of Rb-Sr Ages*

Deciphering how mountain belts have uplifted relies on measuring ages for different geochronological systems that relate to certain closure temperatures. The measured ages record the time at which that mineral became cool enough to effectively retain the fission tracks or daughter products from radioactive decay. Each radioactive parent-daughter pair corresponds to a different temperature in each mineral. This allows the determination of a series of times when the rock cooled below various closure temperatures. Assuming a thermal profile for that region, the rate of uplift can be determined from these measurements (England & Molnar, 1990), as

$$\textit{uplift rate} = \frac{\textit{cooling rate}}{\textit{geothermal gradient}}$$

In mathematical terms:

$$\textit{uplift rate} = \frac{dT/dt}{dT/dh} = \frac{dh}{dt} \qquad (1.1)$$

Where:

dT/dt is the cooling rate in °C/Ma

dT/dh is the geothermal gradient in °C/km

dh/dt is the uplift rate in km/Ma

Different minerals have different closure temperatures for the same radiometric system, so mineral Rb-Sr ages alone can begin to produce a cooling curve for a metamorphic terrane giving the age of metamorphism and the rate of uplift.

1.2 Aims of the Study

The aim of this study is to provide a greater understanding of the resetting processes, which produce a particular closure temperature. This will allow; a better understanding of the application of the closure temperature concept to igneous and metamorphic rocks; the production of more relevant models of closure temperature; and provide information on the scale, mechanism and pathways of transport of isotopic and chemical species within rocks.

A principal objective of this project is to understand how chemical exchange during cooling affects the closure temperatures of isotopic systems. The ultimate aim is to provide better estimates of closure temperature in micas and, therefore, to better constrain the uplift histories of mountain belts. The results of the literature review and the microanalytical work will be combined to refine existing models of closure temperature.

The results from this project will have wider implications for all those working with closure temperature ages (in other systems as well as Rb-Sr) such as workers in palaeo-thermometry and -barometry. A more thorough understanding of the methods and likelihood of chemical and isotopic transport within rocks will have implications for radioactive and other chemical waste disposal.

1.3 Approaches to the Study

To complete these objectives three areas will be addressed: a literature review of the processes thought to be involved in defining a closure temperature (including partition coefficients, diffusion coefficients, grain size, mineral mode and cooling rate), microanalytical work, and modelling of results.

In trying to understand closure temperatures, it is important to assess closed system rock samples (criteria for sample selection are discussed in Section 1.4.1). Within a closed system, any down temperature exchange that occurs will be among the minerals present in the sample. This implies that any exchange effects (such as the change in concentration of species across grains or from one area to another within a rock sample) can be quantified, as any species lost from one mineral must be balanced by gain of that species in another mineral or minerals.

All the microanalytical work will be undertaken on closed system rocks, to look for the effects of chemical and isotopic exchange among minerals. Modelling of this exchange will encompass the results from the literature review, utilising data about partition coefficients (to establish which minerals are likely to gain and which are likely to lose certain species), diffusion coefficients (to assess to rate of exchange; species can only exchange at the rate of the slowest

moving atom or ion) and previously calculated cooling rates (to establish the thermal histories of the samples).

1.4 Sampling

The samples required for this study must have risen above their mineral closure temperatures at some stage in their history. Ideally samples would come from a metamorphic terrane or an area that has undergone regional metamorphism and meets the criteria outlined in Section 1.4.1.

1.4.1 *Sampling Criteria*

Samples should ideally meet the following criteria:

- A well-defined and simple cooling history. Any existing geochronological data should provide a good indication of the cooling rate. Rocks with a single peak of metamorphism, followed by slow cooling are preferred over those with more complex metamorphic histories. A simple cooling history from a single peak of metamorphism would imply that the minerals would have only been cooled through their closure temperatures once since metamorphism.
- Slow cooling. Small variations in the effective closure temperature (see Section 2.4) for the same mineral, in different rocks (i.e. different rock types have different mineral modes) cooled at the same rate will result in measurable differences in apparent age.
- A high metamorphic grade. Rocks that have reached a high grade of metamorphism, should have reached isotopic and chemical equilibrium before they started to cool.
- Samples with a simple mineralogy and texture. For example, a planar source for ^{87}Sr, such as a mica band, with one other phase (such as calcite) would be easier to understand than a rock with many different mineral types and grain sizes.
- Large modal variations on a fairly small scale. Samples from the same outcrop should have experienced the same cooling history, so any differences in age between them must be due other factors such as, grain size and mineral mode (Sections 2.4.4 and 2.4.6).
- Closed system rocks (see Section 1.3 and Table 1.1).

Table 1.1 Characteristics of open and closed system rock samples.

Criteria	Open System Characteristics	Closed System Characteristics
Retrograde alteration	Formation of fine grained hydrous retrograde alteration minerals replacing peak metamorphic assemblage, e.g. chloritisation of biotite and sericitisation of plagioclase	Absent
Fractures.	Fractures are filled with new material that cross cut the metamorphic texture. These may be associated with areas of retrograde alteration.	Absent
Aqueous fluid inclusion trails	Secondary two-phase (liquid-vapour) inclusions form trails (as healed microcracks) through primary minerals. These may be associated with areas of retrograde alteration	Absent
Exsolution in calcite	The presence of fluid appears to mediate the exsolution of dolomite from calcite down to low temperatures (Jenkin *et al.*, 2001).	Exsolution is less prone to occur, especially at low temperatures and calcite retains high temperature equilibrium with dolomite, especially in grain cores.
Oxygen isotope ratios	$\delta^{18}O$ values of the precursors of carbonates can be estimated (see section 4.1). Deviations from these values generally reflect oxygen isotope exchange at some time with fluids from another rock unit. This could be pre-, syn- or post-metamorphic in age. Only the latter is of importance here because pre- and early syn-metamorphic open-system effects will have been homogenised by the metamorphism. Late syn- and post-metamorphic fluid infiltration will be indicated by oxygen isotope disequilibrium among different minerals that differ from closed-system effects (Jenkin *et al.*, 1994) and disequilibrium within the same mineral in monomineralic rocks on small length scales.	Oxygen isotope fractionation among phases reflects peak metamorphic temperatures or, more likely, a closed-system cooling exchange model (Jenkin *et al.*, 1994). Monomineralic rocks will have homogeneous oxygen isotope values on small length scales (outcrop, hand-specimen, grain, sub-grain).
Mass balance of trace elements and their distributions	Mass balance will be violated and trace element profiles may be smooth diffusion profiles or step profiles that are spatially related to fractures and other late textural features.	Mass balance should be preserved and trace element profiles will be smooth diffusion profiles.

Previous Rb-Sr mineral separate studies show that deformation processes can also promote isotopic equilibration in highly deformed rocks (for example, Freeman *et al.*, 1997). At a grain-scale, deformation tends to be accommodated by a number of processes, which may also enhance

the rate of isotopic and chemical equilibration. Grains can deform via a wide variety of processes including; grain boundary diffusion creep, pressure solution and recrystallisation. A detailed review of grain-scale deformation processes can be found in Twiss & Moores (1992) and Hatcher (1995).

Deformation processes may enhance chemical and isotopic exchange, for example Freeman *et al.*, (1997). However, volume diffusion may be the rate-determining step for intracrystalline exchange in most geological situations. Deformation not only reduces the grain size (and therefore shortens the distance required for volume diffusion) and provides energy for mineral transitions, it also provides migrating dislocations, which may produce fast diffusion pathways for chemical and isotopic exchange.

1.4.2 *Sampling Methodology – Why the Central Alps?*

The closure temperature theory was first developed from fieldwork in the Lepontine Alps (Jäger *et al.* 1967), and the area's suitability to test the concept is discussed below. The Lepontine area (Figure 1.1) attained amphibolite facies metamorphism during the Alpine orogeny, allowing minerals within the Rb-Sr system to open to chemical and isotopic exchange (biotite T_c = 250-350 °C, Armstrong *et al.*, 1966; muscovite T_c = 450-550 °C, Jäger *et al.*, 1967) before cooling through their closure temperatures (T_c). However, some minerals and systems will remain closed to exchange, for example, the U-Pb closure temperature of zircon is significantly higher than the maximum temperature achieved by the Alpine metamorphism in the central Alps (U-Pb zircon T_c > 900 °C; Cherniak & Watson, 2000).

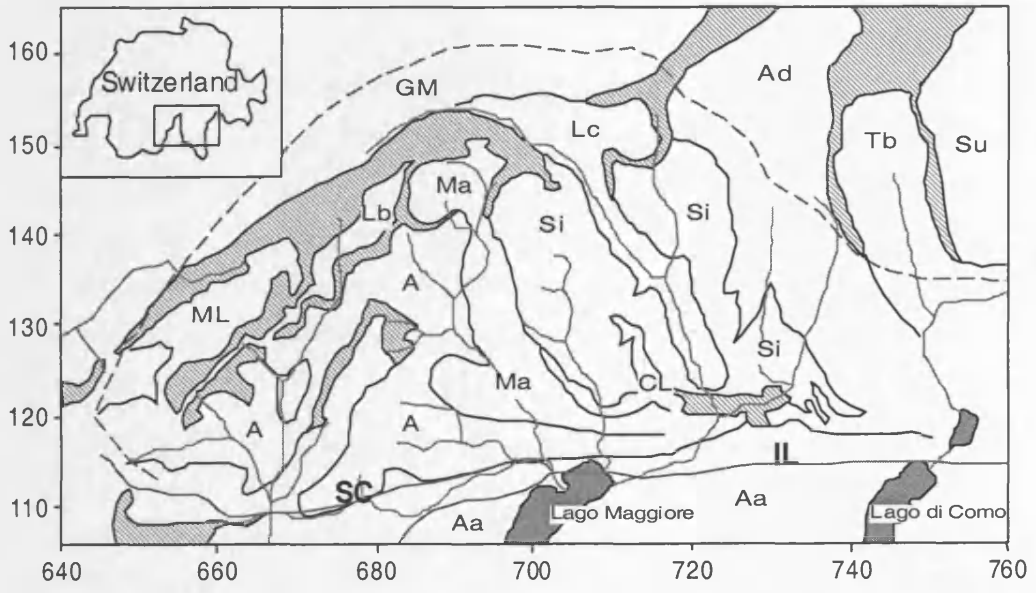

Figure 1.1 Map of the central Alps to show the main nappe boundaries for the Lepontine Alps. The grid around the outside of the diagram is in kilometres (Swiss National Grid), the black lines and shaded areas represent Mesozoic metasediments or nappe boundaries; the Insubric line (IL), the Simplon-Centovalli Line (SC) and the dashed line (the staurolite isograd) represent the limit of amphibolite grade metamorphism. The nappes marked are GM – Gotthard Massif, Ad – Adula, Tb - Tambo, Su – Suretta, Ma – Maggia, Lc – Lucomagno Gneiss, Si – Simano, Lb – Lebendun, A – Antigorio, ML – Monte Leone, CL – Cima Lunga and Aa - Austroalpine. Redrawn from Todd & Engi (1997) and Grujic & Mancktelow (1996).

The Lepontine Alps are found in the Ticino and Simplon areas of Switzerland and the Toce and Mera river valleys of northern Italy. The term Lepontine was coined by E. Wenk to describe the structural style, which more or less corresponds with upper boundary of amphibolite grade metamorphism (dashed line on Figure 1.1) in the Central Alps (Trümpy, 1980). The Pennine nappes dominate the Lepontine Alps, but small areas of the Ultrahelvetic Gotthard Massif (in the north) and some Austroalpine rocks (to the south) may also be included. The Insubric Line (a 1 km thick, steeply dipping mylonite zone), to the south, separates the Lepontine Alps from the Southern Alps.

The Alpine orogeny has been comprehensively studied, giving information on sampling localities, sample petrography, mineral reactions, stable isotope data, geo-thermo-barometry and geochronology (to estimate cooling rates). Previous dating work has usually only been completed on the basement gneisses, so it would be expected that previous geochronology would differ from this study due to the mineral mode effect (see Section 2.4). For those rocks involved in the Alpine orogeny, there is no overprinting by later geological events.

The metacarbonate samples generally have simple mineralogies that allow simple modelling of analysed chemical and isotopic profiles. Cooling histories in the Lepontine area are relatively simple, with peak amphibolite metamorphism at 20-30 Ma.

Chapter 2

The Closure Temperature Concept

2.1 Introduction

This chapter discusses the theory behind Rb-Sr geochronology, the concept of closure temperature and why closure temperatures are important when examining measured ages. The aim of this chapter is to introduce the unfamiliar reader to the processes controlling isotopic and chemical equilibrium during metamorphism.

2.2 Rb-Sr Geochronology

^{87}Rb decays to ^{87}Sr *via* β-decay (the emission of one electron) and has a half-life of 4.88×10^{10} years. This corresponds with a decay constant of 1.42×10^{-11} yr^{-1} (Steiger & Jäger, 1977). Measuring how much ^{87}Sr has formed from this decay allows calculation of the time elapsed since the closure of the system (Section 2.2.1). Rb-Sr geochronology is a very useful radiometric technique as both Rb and Sr reside in major rock-forming minerals (for example feldspars and micas). As micas often define the fabric of metamorphic rocks, the time of deformation may be determined (if the temperature of deformation is lower than the temperature corresponding to the cessation of isotopic exchange) using Rb-Sr geochronology.

2.2.1 *Defining a System*

In thermodynamics, a system can be described as "a portion of matter separated from the rest of the observable universe by well defined boundaries" (Nordstrom & Munoz, 1986). The observer defines these boundaries so a system may have any dimensions convenient to the observer. Spear (1993) defined a system as the collection of phases under investigation. Strictly, a closed system operates when matter cannot be transferred across the boundaries of the system, but energy can be transferred and work can be done on or by the system. Similarly, an open system arises when both energy and matter can be transferred across the system boundaries and work can be done either on or by the system (Figure 2.1).

Previous models of closure temperature (Dodson, 1973) imply open-system behaviour as all minerals in the rock are assumed to be equilibrating with an infinite reservoir. Jenkin *et al.* (1995) describe Sr isotope equilibration in a bi-mineralic pelitic rock (biotite and plagioclase), which would be surrounded by similar rock over distances greater than the effective length-scale of diffusion. After the plagioclase has ceased to exchange Sr isotopes, the biotite has no other reservoir with which to exchange isotopes, except for more biotite of a similar isotopic composition. The pelite described must, therefore, effectively act as a closed system throughout its cooling history. The two minerals in this sample could only exchange with an infinite reservoir *via* a fluid phase flowing through the rock. Joesten (1991) suggests that the combined effects of

volume and grain boundary diffusion in metamorphic rocks will operate over a length–scale of millimetres to centimetres in 1 Ma. Therefore, a closed system model can be applied to most hand specimens, provided that the specimen was extracted from a compositionally homogeneous outcrop.

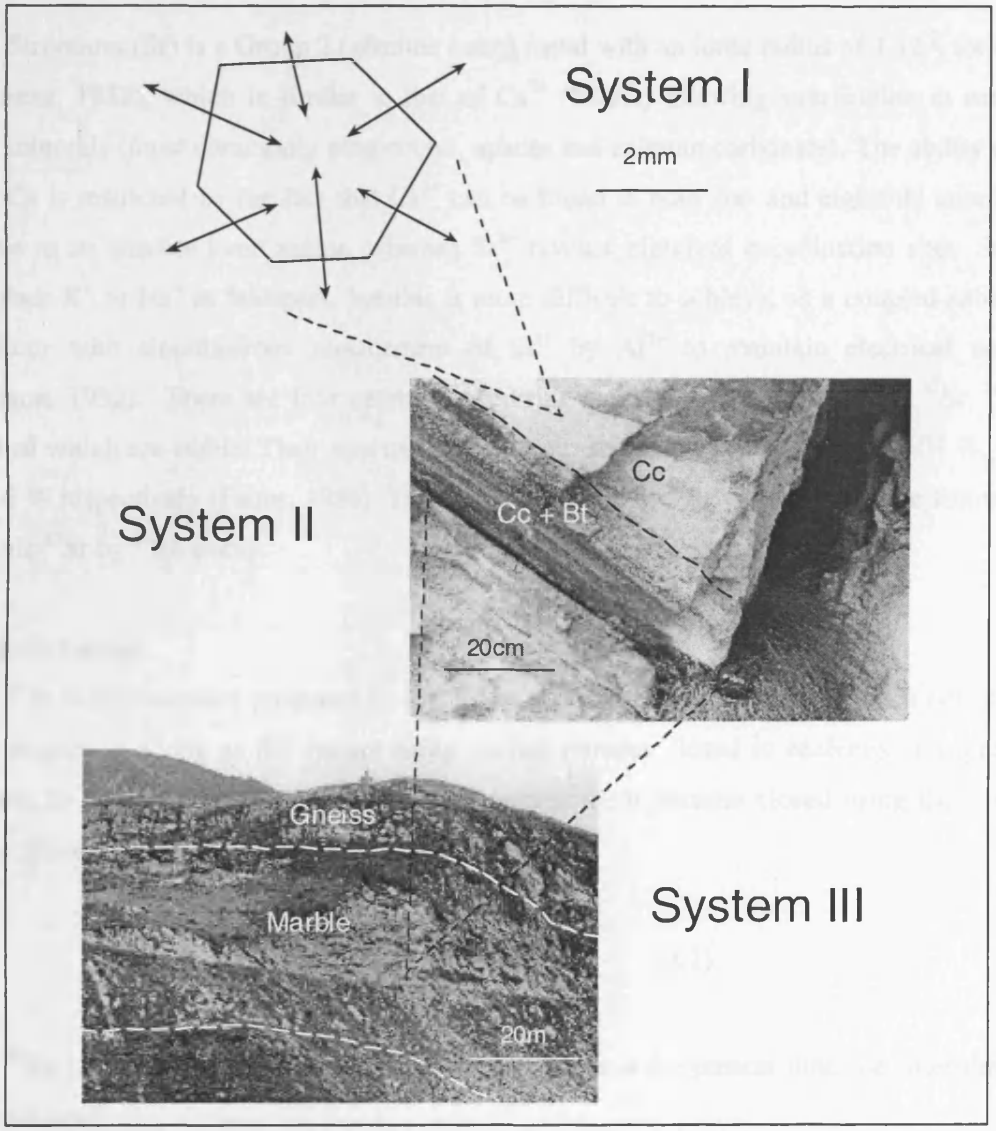

Figure 2.1 The different dimensions of a definable system. A system can be defined as; **System I**, a single mineral grain, **System II**, a hand specimen or **System III**, an outcrop. System I must be an open system at high temperature (the boundaries of the grain marking the limit of the system) as for exchange to take place, interaction must take place between the grain and its surroundings. System II can be either an open or closed system. If a closed system operates, exchange occurs among the grains within the hand specimen and mass balance must be achieved. If it operates as an open system, exchange can take place among the grains in the hand specimen and with grains outside the boundary of the hand specimen. System III operates as a closed system, as long as there is no evidence for fluid flow (and exchange with that fluid) through the system (Section 1.4.1). The photographs shown are of the sample location of HT15 (System II) and the marble outcrop at Lago del Narèt (System III).

2.2.2 *Rb and Sr Geochemistry*

Rubidium (Rb) is a relatively rare element, which does not form any common minerals of its own but occurs in many K-bearing minerals. Rb is a Group 1 (alkali) metal with an ionic radius

of 1.47 Å for the Rb^+ ion (Ahrens, 1952). This radius is small enough for Rb ions to fit comfortably in K^+ (1.33 Å) sites allowing Rb to substitute for K (e.g. in K-feldspar and mica). Rb has two naturally occurring isotopes, ^{87}Rb and ^{85}Rb, with isotopic abundances of 27.83 % and 72.17 % respectively (Faure, 1986). ^{85}Rb is a stable isotope, whereas ^{87}Rb is radioactive and decays to form ^{87}Sr.

Strontium (Sr) is a Group 2 (alkaline earth) metal with an ionic radius of 1.12Å for the Sr^{2+} ion (Ahrens, 1952), which is similar to that of Ca^{2+} (0.99Å) allowing substitution in many Ca-bearing minerals (most commonly plagioclase, apatite and calcium carbonate). The ability of Sr to replace Ca is restricted by the fact that Ca^{2+} can be found in both six- and eightfold coordination sites, due to its smaller ionic radius, whereas Sr^{2+} favours eightfold coordination sites. Sr^{2+} may also replace K^+ or Na^+ in feldspars, but this is more difficult to achieve, as a coupled substitution must occur with simultaneous replacement of Si^{4+} by Al^{3+} to maintain electrical neutrality (Henderson, 1982). There are four naturally occurring isotopes of strontium; ^{88}Sr, ^{87}Sr, ^{86}Sr and ^{84}Sr, all of which are stable. Their approximate isotopic abundances are 82.53 %, 7.04 %, 9.87 % and 0.56 % respectively (Faure, 1986). The relative amount of ^{87}Sr varies due to the formation of radiogenic ^{87}Sr by ^{87}Rb decay.

2.2.3 *Rb-Sr Dating*

^{87}Sr is continuously produced by the decay of ^{87}Rb and it accumulates in Rb rich minerals as time elapses. As long as the system being studied remains closed to exchange, the growth of radiogenic Sr can be used to calculate time elapsed since it became closed using the following equation (Faure, 1986):

$$^{87}Sr_t = {}^{87}Rb_t\left(e^{\lambda t} - 1\right) + {}^{87}Sr_i \qquad (2.1)$$

Where:

$^{87}\mathbf{Sr_t}$ is the total number of Sr atoms of this isotope at the present time (i.e. after time **t** has elapsed)

$^{87}\mathbf{Sr_i}$ is the initial number of Sr atom of this isotope

$^{87}\mathbf{Rb_t}$ is the total number of Rb atoms of this isotope at the present time.

$\boldsymbol{\lambda}$ is the decay constant of ^{87}Rb ($1.42 \times 10^{-11}\ yr^{-1}$)

t is the time elapsed in years since the system became closed to exchange

However, in mass spectrometry, it is more convenient to measure isotopic ratios rather than individual isotopic abundances and $^{87}Sr_i$ is an unknown quantity and therefore, Equation 2.1 cannot be solved. In the case of ^{87}Rb decay, the ^{87}Rb and ^{87}Sr are measured against ^{86}Sr, a stable isotope of strontium, giving Equation 2.2 :

$$\left(\frac{^{87}Sr}{^{86}Sr}\right)_t = \left(\frac{^{87}Sr}{^{86}Sr}\right)_i + \left(\frac{^{87}Rb}{^{86}Sr}\right)_t \left(e^{\lambda t} - 1\right) \qquad (2.2)$$

Equation 2.2 defines a straight-line relationship of the form $y = mx + c$ and may be solved simultaneously for the age of the system (t) and the initial ratio of strontium (at time = t years ago) by the analysis of two or more systems that closed at the same time, from the same region but with differing Rb contents. This relationship is useful because $^{87}Sr/^{86}Sr_i$ is not always known, so the age can be calculated from the gradient of the straight line.

Isochron diagrams (Nicolaysen, 1961) allow several Sr and Rb isotopic ratios to be plotted for several minerals or whole rock systems (Figure 2.2). Ideally, these ratios define the isochron; a line that connects isotopic ratios that represent the same measured age. Present-day $^{87}Rb/^{86}Sr$ and $^{87}Sr/^{86}Sr$ ratios are measured and plotted with $^{87}Rb/^{86}Sr$ defining the *x*-axis and $^{87}Sr/^{86}Sr$ defining the *y*-axis. The use of isotopic ratios means that a plot of several co-existing minerals will produce a line with gradient $m = (e^{\lambda t} - 1)$ and the *y*-intercept = $^{87}Sr/^{86}Sr_i$ (the initial $^{87}Sr/^{86}Sr$ ratio). Assuming an ideal system, (where all the minerals cease isotopic exchange at the same time) the age produced indicates the time elapsed since all the minerals in the system had the same $^{87}Sr/^{86}Sr$ ratio (i.e. the initial $^{87}Sr/^{86}Sr$ ratio). The calculation of precise radiometric ages requires a wide spread of $^{87}Rb/^{86}Sr$ ratios (Figure 2.2). Minerals enriched in Rb (such as biotite and white mica) have high $^{87}Rb/^{86}Sr$ ratios, whereas minerals with low Rb contents (such as calcite and plagioclase) have low $^{87}Rb/^{86}Sr$ ratios and therefore, $^{87}Sr/^{86}Sr$ ratios close to that of the initial ratio (and may be used to estimate it).

Any co-existing minerals that produce a straight line on an isochron diagram define the time elapsed since the last chemical and isotopic equilibration event.

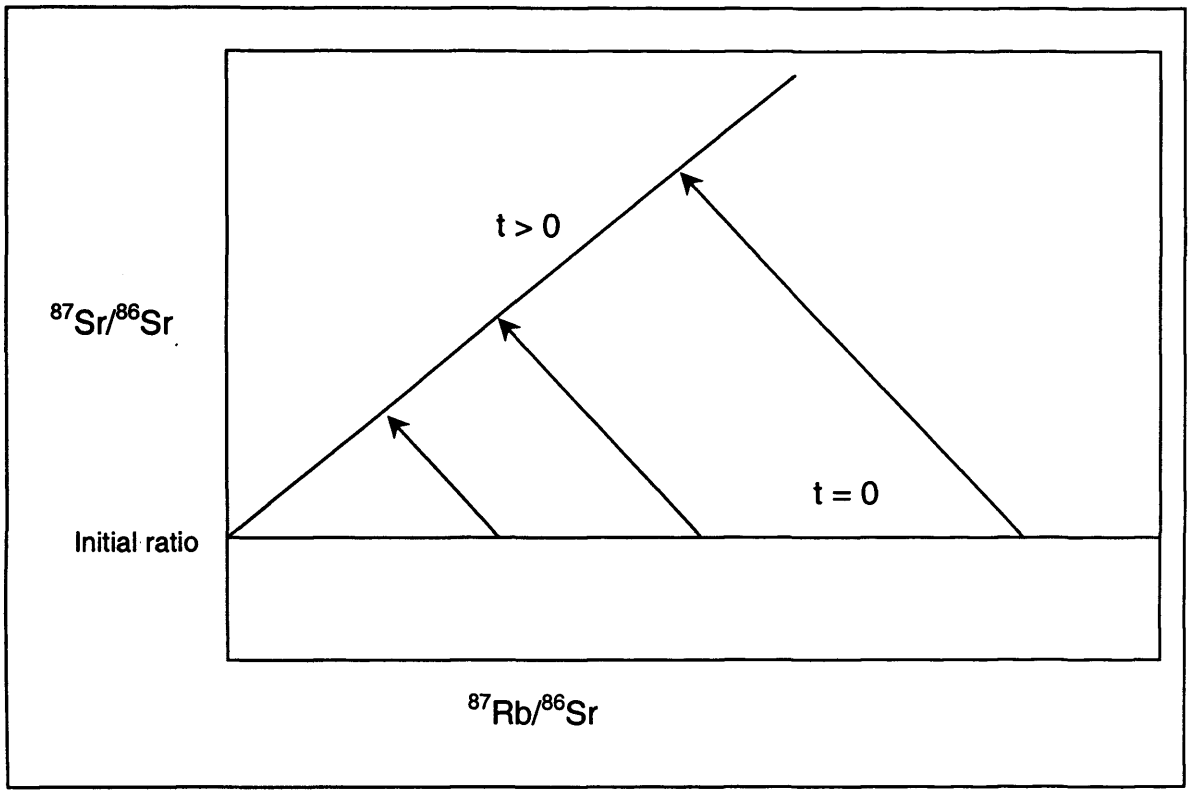

Figure 2.2 Rb-Sr isochron diagram, showing the evolution of a system over time since magmatic or metamorphic cooling (after Faure, 1986).

2.2.4 *Dating Metamorphism*

Rb-Sr geochronology is very useful for dating metamorphic events, as Rb and Sr are present in many metamorphic minerals. Dating metamorphic events is possible as exchange processes (after a mineral has formed) are primarily temperature controlled (Section 2.3). Different minerals become open and closed to exchange under different metamorphic conditions, which allows the construction of temperature-time paths. Under certain conditions, it is also possible to date metamorphic mineral growth (Section 2.2.6).

Once closed to exchange, Rb enriched minerals, such as biotite and white mica, produce and retain radiogenic Sr over time to define a line with slope $m > 0$ at $t > 0$ on an isochron diagram (Figure 2.2). However, a later metamorphic event could re-homogenise Rb and Sr among the minerals in the rock and a horizontal line with slope $m = 0$ will be created for t = time of metamorphism (Figure 2.4). The time elapsed since metamorphism can be calculated using isotopic ratios from mineral separates and Equation 2.2.

2.2.5 *Mineral separate ages*

In the simplest case, the peak temperature achieved during metamorphism is sufficiently high to re-equilibrate all the Rb and Sr bearing minerals within the rock. This case is illustrated in Figure 2.3 where the Rb/Sr of each mineral evolves independently until metamorphism (at t_3) when the Sr isotopes are re-equilibrated (in this case, chemical re-equilibration is not considered).

Assuming closed system behaviour, no Rb or Sr is lost from the sample, so the whole rock isotopic evolution remains unaltered after metamorphism.

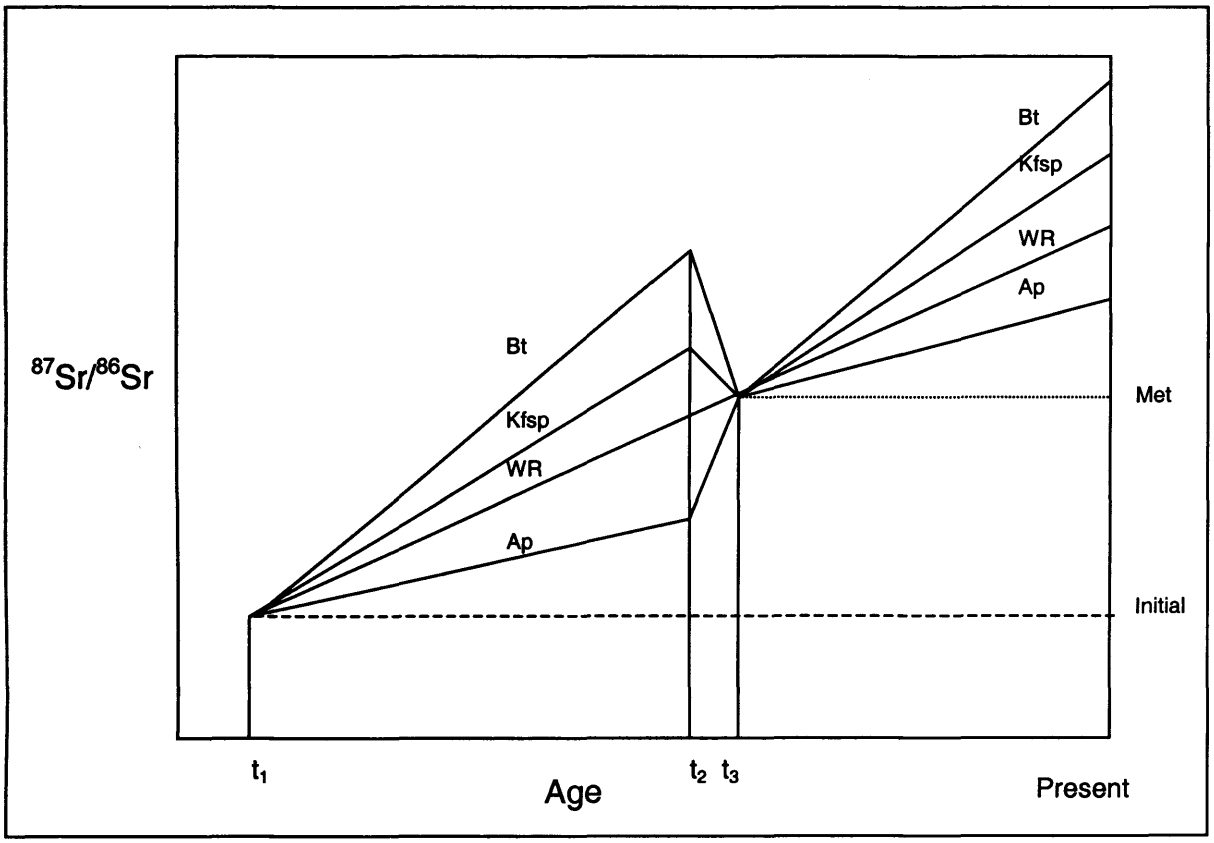

Figure 2.3 Strontium evolution diagram, assuming Sr isotopic exchange only, showing the isotopic homogenisation of the minerals in a rock as a result of thermal metamorphism. t_1 is the time elapsed since formation; t_2 shows the onset of metamorphism and t_3 is the time elapsed since isotopic and chemical re-homogenisation during metamorphism. At t_1, just after crystallisation, all the minerals have the initial $^{87}Sr/^{86}Sr$ ratio; immediately after thermal metamorphism (t_3) all the minerals have an isotopic signature $^{87}Sr/^{86}Sr_{met}$ (after Faure, 1986).

An isochron (Figure 2.4) constructed from the whole rock and minerals illustrated on Figure 2.3 would yield the age of the metamorphic event at t_3. The *y*-intercept of this isochron would be equivalent to the $^{87}Sr/^{86}Sr_{met}$ ratio. Using Rb-Sr geochronology, the only way to extract t_1 is by using several whole rock isotopic ratios from the same region, assuming exchange does not occur on a scale larger than that of a typical hand specimen.

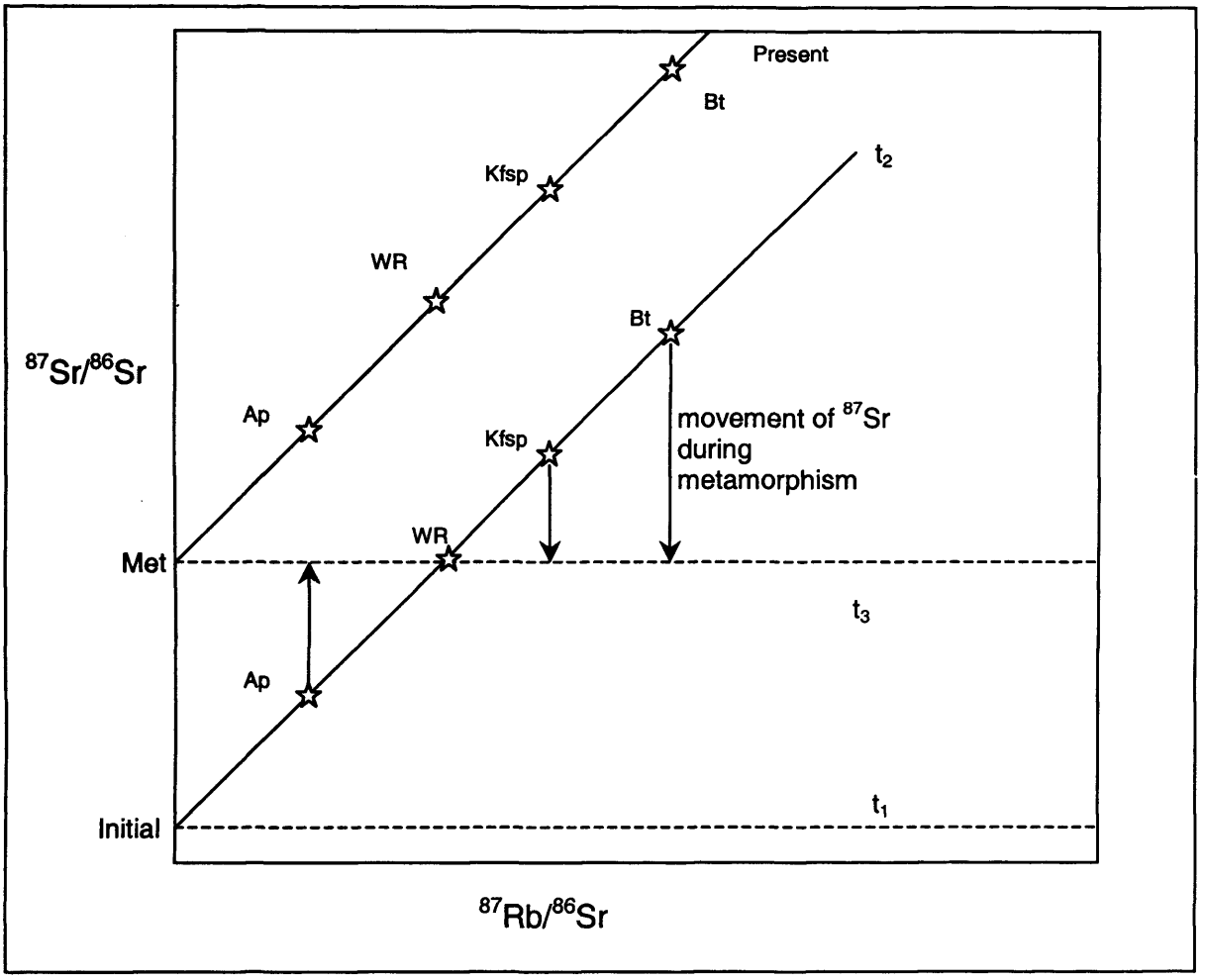

Figure 2.4 Isochron diagram, showing apatite, whole rock, K-feldspar and biotite $^{87}Rb/^{86}Sr$ and $^{87}Sr/^{86}Sr$ ratios as depicted in Figure 2.3. t_1 is the time elapsed since formation; t_2 shows the onset of metamorphism and t_3 is the time elapsed since isotopic and chemical re-homogenisation during metamorphism.

Mineral separate analysis employs the mechanical separation of mineral fractions from a single rock specimen to produce average isotopic compositions. Conventionally, minerals are separated from a crushed hand specimen (~5 to 10 kg) by density and magnetic susceptibility. Analysis of a combination of low and high Rb/Sr ratio minerals to form an isochron will give the time elapsed since metamorphism. Used in combination with closure temperatures (see Sections 2.2.6 & 2.4), mineral separate ages can be used to construct cooling curves.

Mineral separate analysis assumes closed system behaviour (i.e. no exchange) with respect to both Rb and Sr after the metamorphic event that caused the isotopic re-homogenisation within the hand specimen the minerals have been extracted from. This assumption is valid if the hand specimen in question comes from a large homogeneous outcrop with no evidence of large-scale fluid flow. Mineral separate ages may have large errors associated with them as the separates only yield average isotopic signatures (Section 2.4.4), i.e. in a bulk mineral crushed sample, the grain cores are preferentially selected (Jenkin *et al.* 2001). Problems also occur when more than one generation of a sampled mineral is present or isotopic equilibration during metamorphism has been

incomplete. The presence of large mineral grains or the occurrence of short thermal pulses result in restricted diffusion between grains and the grains may not re-equilibrate fully. However, ages produced from very high Rb/Sr phases, such as biotite, are not affected by minor variations in the estimated initial ratio, although the apparent age differences resulting from low Rb/Sr minerals can be significant in age calculations.

Figure 2.3 shows instantaneous cooling after the metamorphic event has caused isotopic re-homogenisation. However, in reality, there may be a long period of slow cooling from the metamorphic peak temperature, allowing the minerals to remain above their closure temperatures and leaving them open to chemical and isotopic exchange. In this case, any measured age produced will not date the metamorphic event itself, but the time at which the minerals reached their respective closure temperatures.

2.2.6 *A Definition of Closure Temperature*

Closure temperatures for geochronological systems were defined by Dodson (1979) as the "temperature of the system at the time given by its apparent age". Above its closure temperature, a mineral is effectively "open" to exchange, conversely below its closure temperature it is effectively "closed". By dating the closure of different mineral systems, Rb-Sr ages give information about the cooling and uplift history of mountain belts and metamorphic terranes. Closure temperatures have conventionally been assumed to relate to the effective cessation of isotopic exchange (for example, Sr isotopes in the Rb-Sr system) during cooling. However, one of the possibilities being examined in this thesis is that the down-temperature chemical exchange of elements involved in dating schemes (for example, Rb with K, or Sr with Ca) may be equally important in controlling closure temperatures of radiometric systems.

2.2.7 *Sub-Closure Temperature Mineral Growth*

Minerals that grow during metamorphism and deformation are potentially very useful to the geochronologist. Some minerals (such as feldspars and white mica, but most notably garnet) have the ability to grow below their closure temperature to Rb-Sr exchange. This means that their isotopic compositions will be "frozen" into the mineral lattice. Such behaviour allows dating of mineral crystallisation; if these minerals form the metamorphic fabric, links can be made between metamorphism, geochronology and structural geology. The white mica closure temperature is thought to be 500 ± 50 °C, Jäger *et al.*, 1967 (Section 2.4.1), however, it may crystallise at temperatures much lower than this (e.g. Cliff, 1985) and may be a powerful tool for dating deformation events in greenschist to lower amphibolite facies rocks (Freeman *et al.*, 1997).

2.3 Isotopic and Chemical Exchange Processes

Exchange can occur by one or more of three mechanisms: diffusion, recrystallisation (solution-reprecipitation) and *via* a chemical reaction which forms a new mineral phase. Giletti

(1974) discusses transport through vacancies in crystal structures, which can be independent of temperature. Vacancies can be introduced in two ways; an increase in energy allowing the atoms to jump out of their lattice positions or vacancies caused by maintaining electrical neutrality when impurity ions are introduced to the crystal lattice. The first type of vacancy is temperature dependent as the total energy of the system is also dependent on temperature. The second type of vacancy is entirely dependent upon the existence of impurities and as these are temperature independent, the vacancies can remain at low temperature. Villa (1998) suggests that exchange is caused by recrystallisation induced by fluid circulation and deformation, which are appreciably faster than diffusion. Giletti (1985) discusses the exchange of oxygen isotopes between minerals and hydrothermal fluids (for the cases of solution-reprecipitation and chemical reactions). For solution-reprecipitation to occur, only a small amount of fluid is required, however, the mineral must be in contact with a large reservoir of fluid in order to alter the isotopic composition of the mineral. For the reaction mechanism to be responsible for the exchange of isotopes the fluid reacting with the crystal locally must remain in direct communication with the main fluid reservoir. During diffusion, the crystal will remain unaltered and this process will continue to allow chemical or isotopic exchange as long as another mineral phase is open to exchange.

The specimens in this study have been carefully selected to avoid the effects of recrystallisation and the formation of new mineral phases, allowing the study of the effects of diffusion alone (Section 1.3.1). During metamorphism, temperatures can exceed the closure temperature of the mineral allowing chemical and isotopic exchange. I have assumed that this thermal effect on exchange processes is largely controlled by diffusion, which will be discussed in the subsequent sections.

2.3.1 *Diffusion Mechanisms*

Diffusion in solids occurs both by volume diffusion through regions of good crystal structure and *via* a variety of rapid diffusion pathways. Rapid diffusion pathways involve surface or line defects in the crystal, such as grain boundaries, twin or cleavage planes and free surfaces and may also be formed by deformation. Similarly, volume diffusion mechanisms also depend upon point defects in the crystal, such as vacancies or the presence of interstitial atoms.

2.3.2 *Volume Diffusion*

In any crystal, there is a regular array of lattice sites that are energetically favourable positions for atoms. During diffusion, these atoms perform a series of jumps from one lattice site to another. These jumps are generally in random directions and allow the atoms to migrate through the lattice. Manning (1974) describes four mechanisms for volume diffusion.

The *exchange mechanism* (2.5a) is simply the interchange of positions between two neighbouring atoms and, as such, requires no lattice defect. However, such a process would cause a large distortion of the lattice during the exchange and consequently requires a large activation

energy. A variation on this mechanism is the *ring mechanism* (2.5a) where three or more adjacent atoms move simultaneously to the next site around the ring. Although this process involves more atoms, there is less distortion of the lattice during the jump and consequently requires a lower activation energy.

Manning (1974) also describes diffusion mechanisms involving the use of vacancies and interstitial sites. During the *interstitial mechanism* (2.5b), small interstitial atoms can jump from one interstitial site to another without permanently disturbing the crystal lattice. When interstitial atoms are similar in size to the lattice atoms, the *interstitialcy mechanism* may operate. In this case, the original interstitial atom moves into a lattice site, displacing the lattice atom into a neighbouring interstitial site (2.5c). This motion moves the interstitialcy (site containing the additional atom) from one interstitial site to another. Two jumps of the interstitialcy are required to move an atom from one lattice site to another.

The *vacancy mechanism* (2.5d) depends on the presence of vacancy point defects within the crystal. At thermodynamic equilibrium, a certain number of vacancies will be present in the crystal. Atoms next to a vacancy can diffuse by jumping from their lattice site into the vacancy. This mechanism is much more likely than the exchange mechanism as it causes much less distortion of the crystal lattice and therefore, requires lower activation energy.

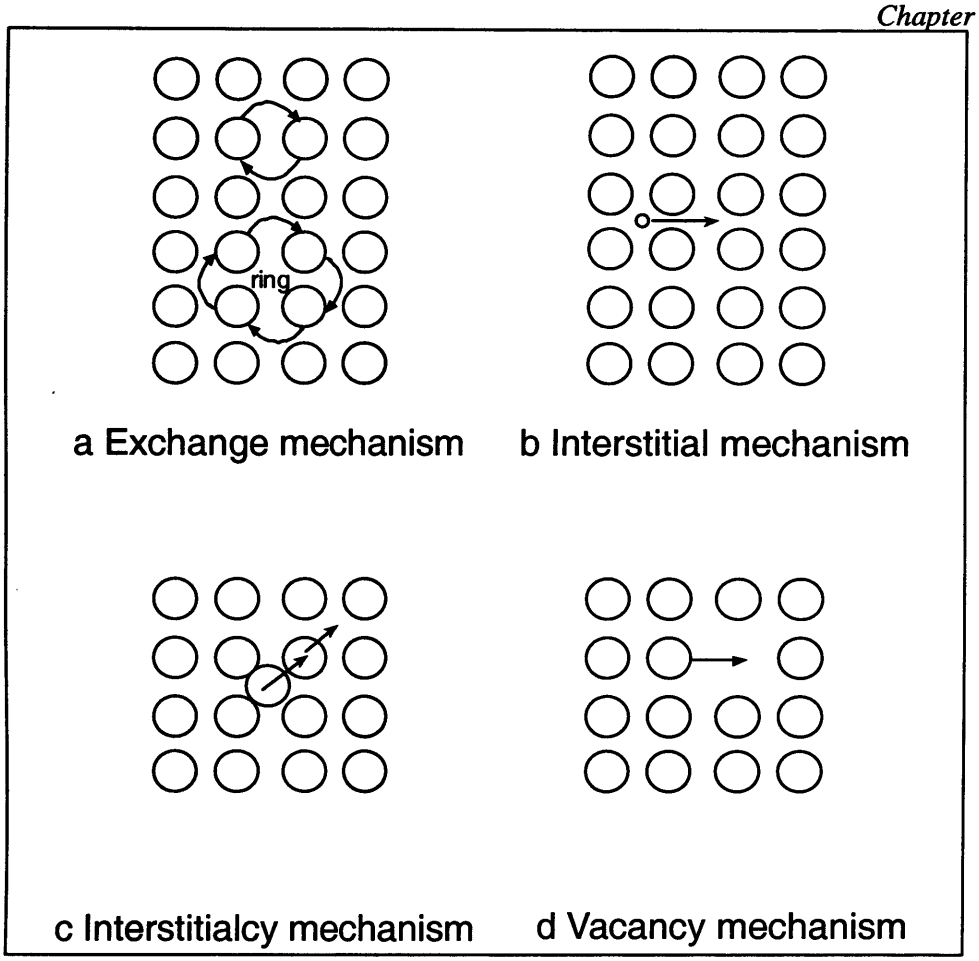

Figure 2.5 Mechanisms of volume diffusion (after Manning, 1974). **2.5a)** shows the exchange and the ring mechanisms, **2.5b)** shows the interstitial mechanism, **2.5c)** shows the interstitialcy mechanism and **2.5d)** shows the vacancy mechanism.

The process of diffusion tends to eliminate chemical and isotopic gradients (see Fick's Laws; Crank, 1975 and Section 2.3.3). In terms of isotopic equilibrium, this means that with time all minerals within a rock should tend towards the same isotopic signature. The rate of volume diffusion depends upon the number of crystal lattice defects, which increases with increasing temperature.

2.3.3 *Fick's Laws*

The transfer of atoms *via* diffusion occurs by random molecular motions, similar to the transfer of heat by conduction. Fick recognised this and derived a mathematical basis for diffusion using the previously formulated equation of heat conduction. The mathematical theory of diffusion in isotropic substances is based on the hypothesis that the rate of diffusion through a unit area of section is proportional to the concentration gradient measured normal to this section and is known as Fick's first law (Crank, 1975):

$$F = -D\frac{\partial C}{\partial x} \qquad (2.4)$$

Where:

F is the rate of transfer (or flux) per unit area of section ($gm^{-2}s^{-1}$)

D is the proportionality constant

C is the concentration of the diffusing substance (gm^{-3})

x is the space coordinate measured normal to the section (m)

The negative sign in Equation 2.4 arises because diffusion occurs in the opposite direction to increasing concentration (i.e. diffusion operates from areas of high to low concentration). Equation 2.4 is only correct for an isotropic medium, whose structural and diffusion properties are the same in all directions from any given point. Due to this symmetry, the flow of diffusing substance is along the normal to the surface of constant concentration. This is not true for anisotropic media, in which the diffusion properties are entirely dependent on the direction in which they are measured. Equation 2.4 is for steady-state flow, where the concentration gradient and therefore, the flux remain the same with time. However, in reality both of these change with time and differentiating 2.4 with respect to time gives Fick's second law:

$$\frac{\partial C}{\partial t} = D\frac{\partial^2 C}{\partial x^2} \qquad (2.5)$$

Where:

t is time (s)

D is the diffusion coefficient (m^2s^{-1})

C and ***x*** are as in Equation (2.4)

Equation 2.5 is the differential equation of diffusion in an isotropic medium, relating the diffusion coefficient to concentration, distance and time.

2.3.4 *The Rate of Diffusion*

The rate of diffusion increases with increasing temperature, this relationship being described by the Arrhenius relation:

$$D = D_o \exp(-Q/RT) \quad (2.3)$$

Where

D is the diffusion coefficient (m^2s^{-1})

$\mathbf{D_o}$ is the experimentally determined pre-exponential factor of diffusion (m^2s^{-1})

Q is the experimentally determined activation energy ($kJmol^{-1}$)

R is the gas constant ($kJK^{-1}mol^{-1}$) and

T is the absolute temperature (K)

The temperature dependence is readily shown on an Arrhenius plot of log D versus 1/T, the *y*-intercept being equal to D_o.

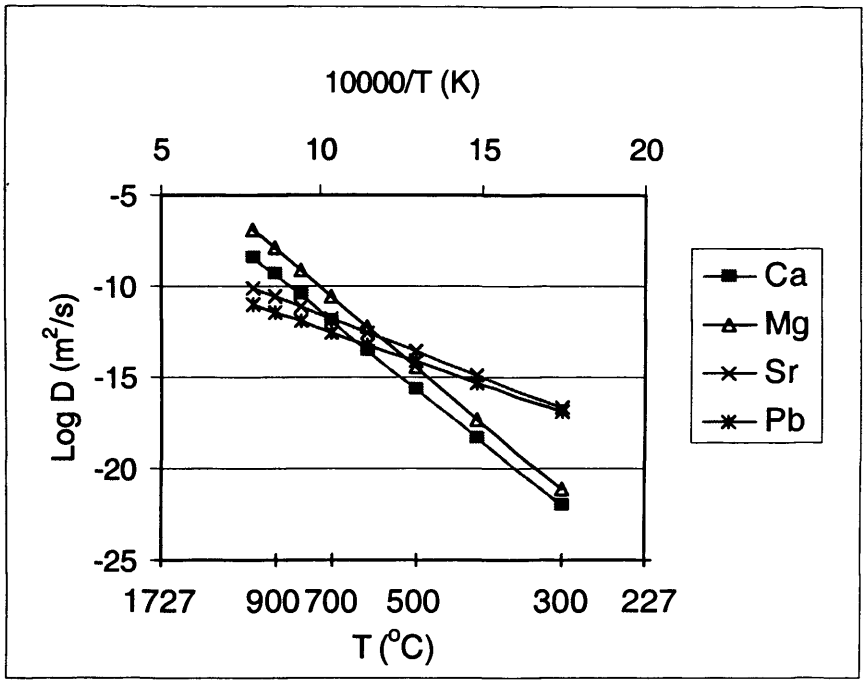

Figure 2.6 Arrhenius plot of diffusion in calcite. The data for Ca and Mg are from Fisler & Cygan (1999) and the data for Sr and Pb are from Cherniak (1997).

The exponential dependence of diffusion on temperature means that below a certain temperature (the closure temperature) diffusion will slow to such an extent that it becomes insignificant and exchange effectively ceases. Closure temperatures can be calculated using the temperature dependence of volume diffusion (Section 2.4.2).

2.3.5 *Rapid Diffusion Pathways*

Rapid diffusion pathways through a rock include grain boundaries, dislocation pipes, twin or cleavage planes and free surfaces. All of these are basically line or surface discontinuities within the crystals. The number of these discontinuities present is more or less independent of temperature and so diffusion processes by these mechanisms have a smaller temperature dependence than mechanisms involving point defects, whose concentration increases with temperature (Manning, 1968). This makes line and surface mechanisms relatively important at low temperatures, but less so at higher temperatures compared with volume diffusion mechanisms. Farver & Yund (1996), from calculations on experimental work to determine the bulk diffusion of calcium in a calcite aggregate at 700 °C, suggest the bulk diffusive transport will be dominated by grain boundary diffusion when grain sizes are less than 1 cm, and dominated by volume diffusion at grain sizes greater than 1 cm. In the absence of a grain boundary fluid, bulk diffusional mass transport will be dominated by grain boundary diffusion in most calcite rocks at temperatures below 600 °C due to the difference in activation energies between volume and grain boundary diffusion (Farver &

Yund, 1996). The bulk diffusion coefficient can be approximated using the following equation (after Brady, 1983):

$$D_{BULK} = D_{GB}(\delta/d) + D_{VOL}(1-\delta/d) \qquad (2.6)$$

Where:

D_{BULK} is the bulk diffusion coefficient

D_{GB} is the grain boundary diffusion coefficient

D_{VOL} is the volume diffusion coefficient

δ/d is an approximation of the fractional cross-sectional area occupied by the grain boundaries

This is a simple model for D_{BULK}, which assumes parallel grain boundaries and equal concentration of the diffusing species in grains and grain boundaries. The model weights the diffusion coefficients by the relative fractional cross-sectional area of the grains and grain boundaries.

Figure 2.7 shows an Arrhenius plot to compare volume and grain boundary diffusion of oxygen and calcium through calcite. This plot clearly shows that grain boundary diffusion is several orders of magnitude faster than volume diffusion. If grain boundaries dominate the sample, the bulk diffusion coefficient will be faster than if there is a larger grain size and therefore, fewer grain boundaries.

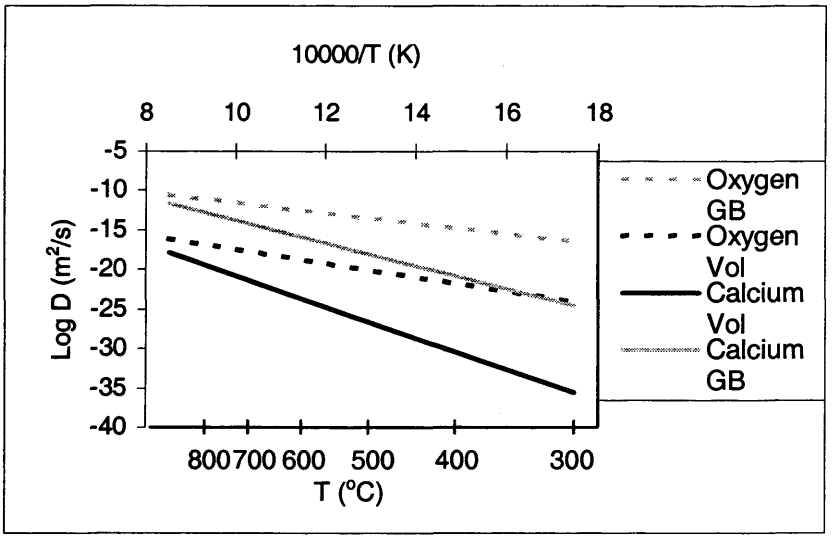

Figure 2.7 Arrhenius plot of grain boundary (GB) and volume diffusion (Vol) for oxygen (Farver & Yund, 1998) and calcium (Farver & Yund, 1996) in calcite. Grain boundary diffusion is often several orders of magnitude faster than volume diffusion.

2.4 Closure Temperatures

The concept of closure temperature, first suggested over thirty years ago, has been used to characterise the cessation of isotopic exchange between dated minerals and their neighbours. Above the closure temperature isotopic exchange can occur within the mineral and between it and its local environment. Below the closure temperature, losses decrease and the daughter product

starts to accumulate (Dodson, 1973). There is a short transitional interval within which the mineral is neither fully open nor fully closed, Figure 2.8.

2.4.1 *Empirical Closure Temperatures*

Jäger *et al.* (1967) first established the concept of closure temperature in the central Alps. They discovered that rocks of low metamorphic grade around the Central Alps gave Hercynian biotite and muscovite Rb-Sr ages (~300 Ma). However, rocks of higher metamorphic grade gave Tertiary biotite Rb-Sr ages (the zone of higher metamorphic grade was placed within the stilpnomelane isograd, which they believed to correspond with a temperature of 300 ± 50 °C). The younger ages for Rb-Sr in biotite were attributed to the peak of Lepontine metamorphism when the mineral systems opened due to high temperatures.

Jäger *et al.* (1967) then followed this argument by suggesting that if a metamorphic event of greater than 300°C opened the minerals to Rb-Sr loss it would also correspond to the temperature at which the system would close again upon cooling, which may be several million years after the high temperature peak of metamorphism. Jäger *et al.* (1967) also deduced a closure temperature for muscovite Rb-Sr at 500 °C using the staurolite isograd (the staurolite zone corresponds with a range of 500-575 °C; Todd & Engi, 1997).

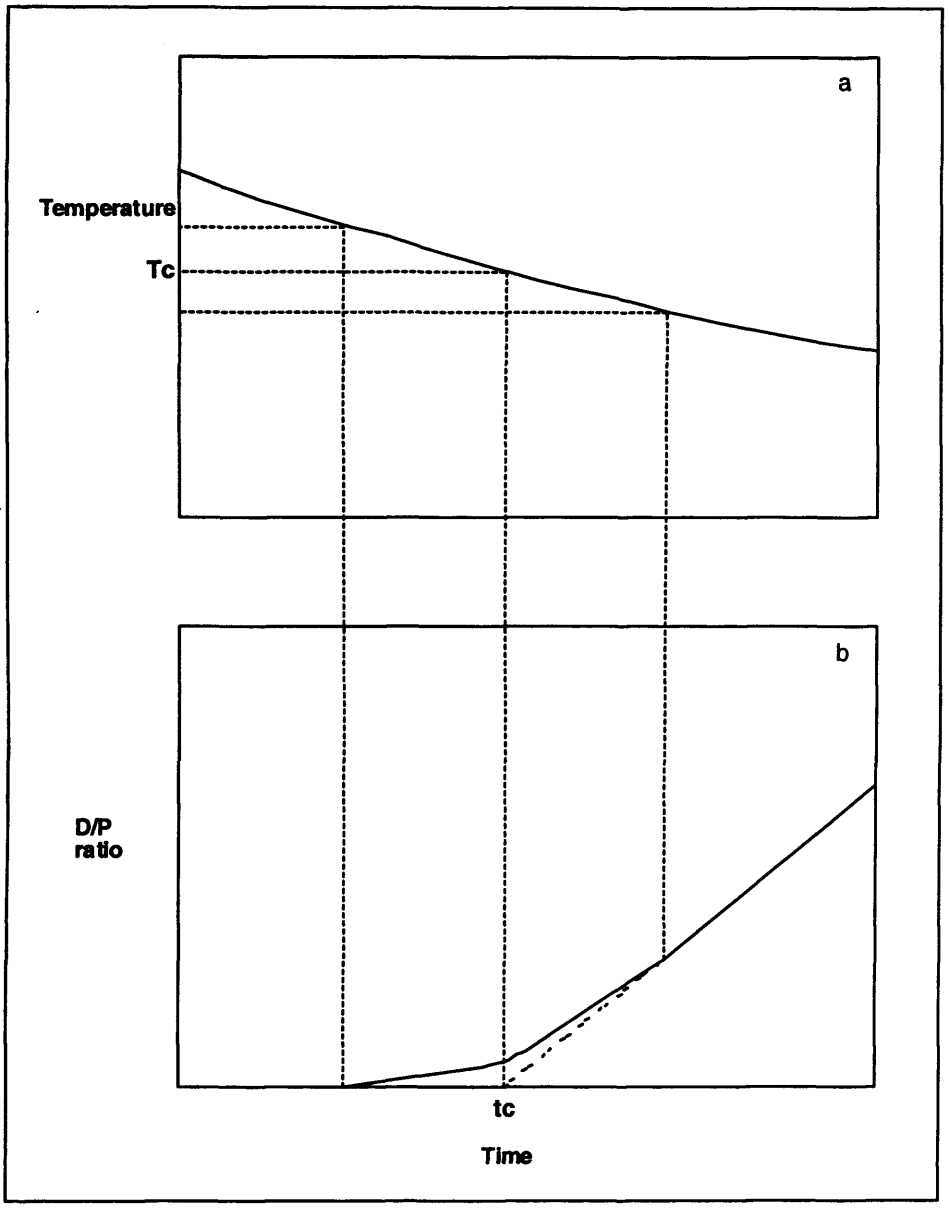

Figure 2.8 A diagrammatic definition of closure temperature (after Dodson, 1973). **a** Shows a cooling curve, **b** shows the accumulation of daughter product. D/P is the daughter/parent ratio, dashed lines indicate the approximate limits of the transitional time-temperature range. Dodson (1973) assumed that at high temperatures, the daughter product diffuses out of the crystal as fast as it is produced. Upon entering the transitional temperature range some of the daughter product accumulates and some is lost. At low temperatures, losses are reduced and the daughter product accumulates. In calculating an age for a system, the last portion of the daughter/parent curve is extrapolated back to the time axis to produce a measured age (i.e. the time when the daughter nuclide first appears to accumulate).

Closure temperatures have also been measured directly by measuring mineral ages down deep boreholes (Del Moro *et al.*, 1982). They determined biotite-whole rock Rb-Sr ages at depths of up to 3.8 km in the Sasso 22 hole, Larderello, Italy, where all the biotite grains show retention of radiogenic ^{87}Sr at directly measured temperatures of 380 °C, supporting biotite closure of around 400 °C. However, Cliff (1985) argued that the convective heat transport of geothermal systems would create localised thermal pulses whose duration is too short to cause significant Sr loss

through diffusion. The elevated temperature of a short-lived thermal pulse would imply a higher measured closure temperature for that area.

2.4.2 *Dodson's Formulation of Closure Temperature*

Dodson (1973 and 1979) produced a quantitative equation for deriving closure temperatures. He bases his calculations on the temperature dependence of volume diffusion. For thermally activated diffusion (Equation 2.3) Dodson (1973) generated the following equation, which relates closure temperature and cooling rate, assuming exchange with a well-mixed external infinite reservoir:

$$T_c = \frac{Q/R}{\ln\left[\frac{AR(T_c)^2 D_o/a^2}{Q(dT/dt)}\right]} \qquad (2.7)$$

Where

$\mathbf{T_c}$ is the closure temperature (K)

A is a geometric factor (see below)

a is the length scale of diffusion (m)

dT/dt is the cooling rate (°C/Ma)

R, **Q** and $\mathbf{D_o}$ are as in Equation (2.4)

Dodson (1973) calculated **A** (a constant which depends on the geometry of the grain and the decay constant of the parent) for three ideal models, a sphere (A=55), a plane sheet (A=8.7) and a cylinder (A=27). These models may be used to approximate the shapes of mineral grains; for example, the mica structure is strongly anisotropic, causing diffusion to be faster perpendicular to the c-axis and therefore, micas are modelled as cylinders. Diffusion in both feldspar and calcite is approximately isotropic and these minerals are modelled as spheres. For a sphere and a cylinder, the term **a** is the radius. For a plane sheet, **a** is half the width.

Equation 2.7 shows that $\mathbf{T_c}$ is approximately a linear function of **Q** and is dependent on the logarithm of the cooling rate. **Q** and $\mathbf{D_o}$ is a function of mineral structure and the composition of the mineral, so each different mineral will have a different closure temperature. Therefore, in a slowly cooled terrane, different minerals should yield different ages. Also closure temperature is clearly not a single value for a diffusing species in any given mineral as it depends upon the grain size (Section 2.4.3) and the cooling rate.

If two equally sized mineral grains crystallise at the same time, all other factors being equal, their measured age will depend upon their respective cooling rates. In mineral bodies that cool quickly, the moment of crystallisation represents Rb-Sr closure, as there is no time for equilibration (*via* diffusion) between minerals. Rapidly cooled mineral bodies reach low temperatures rapidly, at these temperatures diffusion is slow and daughter products are retained as

they are formed. In slowly cooled mineral bodies, such as those in a metamorphic terrane, equilibration can occur between minerals due to the small falls in temperature over a long time period. The mineral body remains at high temperatures, diffusion is rapid and the daughter products may be lost, *via* diffusion, as quickly as they are formed. In both cases, the daughter product is produced at the same rate but the daughter/parent ratios (and their measured ages) will be different due to the effects of diffusion.

Dodson (1973) calculated the Rb closure temperature for Alpine biotite of 280 to 300 °C (from measured diffusion parameters, assuming a grain size of 0.5 mm). Dodson (1973) assumes that the rock surrounding the mineral grain being studied acts as an infinite reservoir for the loss or gain of isotopes. This assumption is more likely to be valid when the daughter product of the radioactive decay is a gas, for example in the K-Ar system, as the diffusion along grain boundaries and fractures is much faster compared to loss from the mineral grains. This results in a constant low equilibrium concentration in the rock, which acts as an infinite reservoir for gases, as it behaves as an open system (Jenkin *et al.*, 1995).

2.4.3 *Published Closure Temperatures*

Table 2.1 shows the published closure temperatures for commonly used isotopic dating systems in selected minerals.

Table 2.1 Published closure temperatures.

System	Mineral	Closure Temperature	Author
K-Ar	Hornblende	450-550 °C	Hunziker *et al.* (1992)
K-Ar	White mica	300-400 °C	Purdy & Jäger (1976)
K-Ar	Biotite	250-350 °C	Armstrong *et al.* (1966)
Rb-Sr	White mica	450-550 °C	Jäger *et al.* (1967)
Rb-Sr	Biotite	250-350 °C	Armstrong *et al.* (1966)
U-Pb	Zircon	> 800 °C	[a]Cherniak & Watson (2000)
U-Pb	Monazite	≥ 650 °C	Mezger (1991)
Fission Track	Zircon	200-250 °C	Hurford (1986)
Fission Track	Apatite	60-120 °C	Hurford (1986)

[a] Calculated from their diffusion data, using Dodson's (1973) closure temperature formulation, for grains of less than 1 cm radius.

In addition to the data presented in Table 2.1, it is possible to calculate closure temperatures, dependent upon grain size (Figure 2.9 illustrates this relationship for species in calcite) for feldspar, apatite and calcite using the Dodson (1973) equation (Equation 2.7) based upon published diffusion data (for example, Giletti 1991b and Giletti & Casserly 1994; Cherniak & Ryerson, 1993; and Cherniak 1997 respectively).

2.4.4 *Expected Age Change with Grain Size*

If different grain sizes have different closure temperatures they should, therefore, have different ages. Closure temperatures are dependent on grain size, as shown in the Dodson (1973)

closure temperature model (Equation 2.7), as the length scale of diffusion may be shorter than the radius of the grain. This means that in large crystals, exchange may only occur at the edge, whereas in small crystals, exchange may occur throughout the entire grain. Figure 2.9 shows that larger grains have higher closure temperatures, so it would be expected that these grains also exhibit an older measured age.

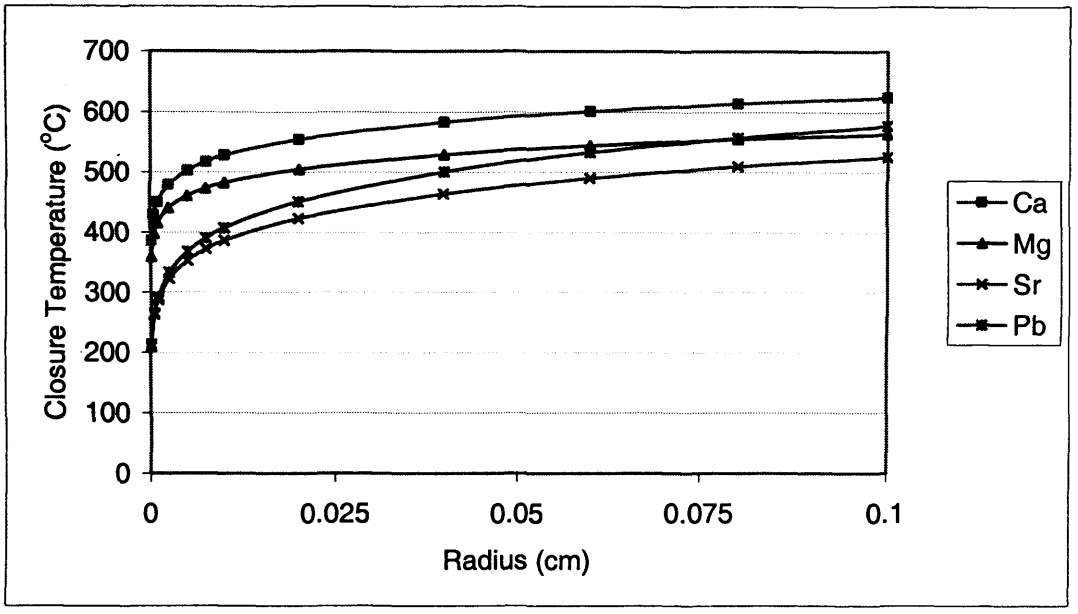

Figure 2.9 Graph of grain size versus closure temperature. The curves show the closure temperature / grain size relationship for calcium, strontium, lead and magnesium in calcite. All these curves use the Dodson (1979) closure temperature equation with a cooling rate of 32 °C/Ma and assuming a spherical model. The diffusion data were taken from Fisler & Cygan (1999) for Ca and Mg and Cherniak (1997) for Sr and Pb.

2.4.5 *Zonation within Grains*

The formation of growth zoning is related to the rate of volume diffusion of the zoned element and the growth rate of the crystal (Watson & Liang, 1995). Sector zoning develops in crystals when specific growth faces exhibit selective enrichment of the element. Paquette & Reeder (1995) report sector and concentric zoning of Mn, Mg and Sr^{2+} in laboratory grown calcites. Cherniak (1997) suggests that zoning of Sr may be retained under certain conditions, depending upon the size of the zones, the temperature attained and the length of time that temperature in maintained.

In cooling rocks, exchange *via* diffusion between minerals will occur above the closure temperature and over the transitional temperature range (Figure 2.8). Depending upon the rate of volume diffusion, zoning may be created. If volume diffusion is comparatively slow, elements (or isotopes) may only exchange at the edge of the mineral grains creating a rim to core zonation. However, if volume diffusion were rapid (or the grain size particularly small) equilibration throughout the grain would be expected, giving a less pronounced rim to core variation.

2.4.6 *Effect of Mode on Closure Temperature*

Current closure temperature models applied to mica Rb-Sr ages assume radiogenic Sr (from the decay of Rb in mica) has isotopically equilibrated with Sr in the whole rock at high temperature and then is retained in the mica at lower temperatures. The radiogenic Sr lost from the mica at high temperature is assumed to be absorbed into an "infinite reservoir" which assimilates it without change in its isotopic composition (Dodson, 1973).

Jenkin *et al.* (1995) and Jenkin (1997) suggest that exchange *via* diffusion of Sr isotopes among different minerals in a closed system rock may be more realistic than the Dodson (1973) model. For example, loss of radiogenic ^{87}Sr from mica may be balanced by gain of radiogenic ^{87}Sr in plagioclase (or another Sr rich phase), so in effect exchange is occurring with a finite reservoir. The magnitude of this finite reservoir depends on which minerals are "open" to exchange. Jenkin *et al.* (1995), present a closed-system model for diffusion in the Rb-Sr system within cooling rocks. It describes Sr isotope exchange by diffusion between two minerals, which is accompanied by the production of ^{87}Sr from the decay of Rb during slow cooling.

Jenkin (1997) and Jenkin *et al.* (1995) present results from a closed-system model for Sr isotope exchange, with equilibration occurring within grains (*via* volume diffusion) and amongst grains (*via* grain boundary diffusion). The Jenkin (1997) model predicts Rb-Sr mica ages in slowly cooled biotite-muscovite-K-feldspar rocks.

Results from the Jenkin *et al.* (1995) closed-system model show that the apparent age, or the corresponding apparent temperature, of a mineral pair in a bi-mineralic rock, will vary with modal composition (or more strictly the proportion of Sr in each mineral) between the Dodson closure temperatures of the two minerals involved. When the proportion of one mineral tends towards 100 %, the apparent closure temperature will tend towards the Dodson closure temperature of the other mineral. Thus, the diffusion properties of both the minerals involved and their modes are important in governing the age of the mineral pair. For example, a biotite-plagioclase pair cooling at 1°C/Ma, in rocks of different modal compositions could give ages differing by up to 100 Ma. This implies that the use of a fixed value for biotite closure temperature might be erroneous.

This mode effect could, however, provide an independent means of calculating the cooling rate by using two rocks of similar grain size, but different composition which have experienced the same cooling history. In this case, the difference between their measured ages will be a function of the mode and the cooling rate.

2.4.7 *Chemical Exchange*

In slowly cooled rocks as well as isotopic exchange, there is the additional potential for down temperature exchange of elements. For example, the chemical exchange of Mg and Fe between biotite and garnet to produce a geo-thermometer (Ferry & Spear, 1978). In geochronological systems there is, therefore, potential for both isotopic (^{87}Sr with ^{86}Sr) and

chemical (Rb with K and Ca with Sr) exchange as the rock cools that could cause variations in measured ages (Figure 2.10).

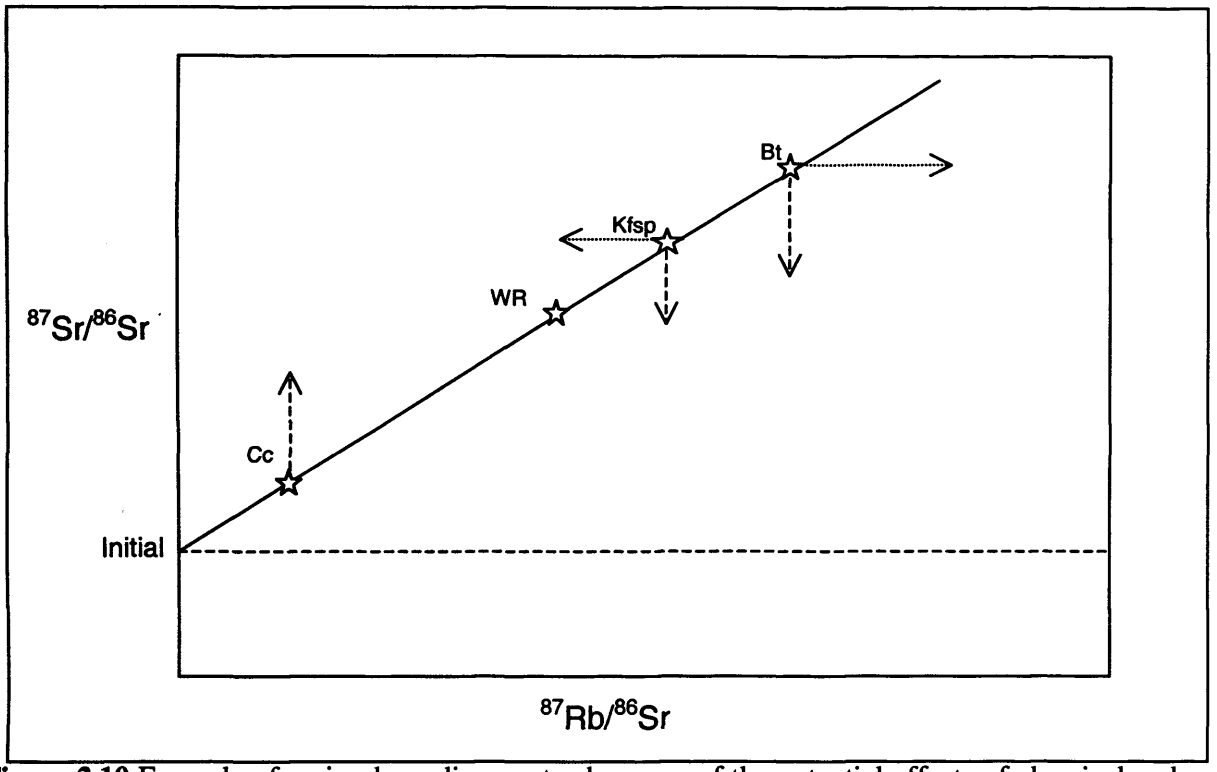

Figure 2.10 Example of an isochron diagram to show one of the potential effects of chemical and isotopic exchange. In this case, the short-dashed arrows represent chemical exchange, and the long-dashed arrows represent isotopic exchange. Jenkin *et al.* (1995) predict that biotite would lose ^{87}Sr and calcite would gain ^{87}Sr. Chemical exchange takes place at the same time and it is predicted (see Chapter 6) that Rb will exchange with K between biotite and K-feldspar.

The total amount of down-temperature exchange (for both elements and their isotopes) is limited by the inter-diffusion coefficient of the two species between the minerals in question. Increasing the amount of parent element in a mineral with a high parent/daughter ratio will decrease the age measured and lower the closure temperature compared to that calculated assuming exchange of daughter isotopes only.

2.5 Discussion: Problems with the Current Closure Temperature Formulations

At present, models for closure temperature are simplistic and give large error bars on their estimates. For example, the Dodson (1973), Jenkin *et al.* (1995) and Jenkin (1997) models do not take into account the influence of changing partitioning behaviour with temperature. Current models of closure temperature only deal with the equilibration of daughter isotopes among minerals as the rock cools, whereas other isotopes and chemical species may also exchange during slow cooling. Recent models (Giletti, 1991a, Jenkin *et al.*, 1995 and Jenkin 1997) suggest the closure temperature concept is not as simple as often assumed as infinite reservoirs for isotopic exchange may not be present in many cooling rocks (Section 2.4.2).

Factors that should be considered are changes in the partitioning behaviour of elements among minerals and the diffusion rate with temperature. Conventionally, closure temperatures have

been assumed to relate to the effective cessation of isotopic exchange (for example, Sr isotopes in the Rb-Sr system), however, chemical (Rb with K, and Sr with Ca) exchange may also occur as the rock cools. This chemical exchange may cause variations in measured ages in addition to those caused by isotopic exchange (as found by Jenkin *et al.* 1995).

At present, variations in measured age are found but we do not understand the processes causing these variations. Failing to recognise the effects of down-temperature exchange could lead to incorrect cooling histories being deciphered if only the Rb-Sr system is used. A more thorough understanding of the closure temperature–measured age relationship is required before it can be used with confidence to construct cooling curves.

2.6 Conclusion

Rb-Sr dating is a powerful technique for dating metamorphism and deformation in orogenic belts as Rb and Sr are contained in many minerals that crystallise or recrystallise during metamorphism and deformation. Sub-closure temperature growth of, for example, white micas or feldspars mean that it should be possible to date metamorphism (or deformation, if the mineral in question forms the fabric of the rock) directly. However, there are problems when dealing with traditional mineral separate analysis (Section 2.2.5). Although isotopic exchange occurs throughout the rock during metamorphism, isotopic re-equilibration may only occur on a grain scale, causing disequilibrium and variations in measured age within the same specimen. These variations are highly dependent on grain size, mineral mode, peak temperature and diffusion rate.

Understanding the processes which control chemical and isotopic exchange during metamorphism will give a clearer insight into the true meaning of measured ages from metamorphic rocks. In turn, this will allow higher confidence when constructing cooling curves giving a better understanding of the rate of uplift.

Chapter 3

A Short Geological Review of the Alp

The European Alps represent an excellent natural laboratory and are probably the most intensively studied orogenic belt in the world. This chapter defines the structural, metamorphic and chronological setting of the Lepontine Alps, the field-sampling area for this project. It is not intended to be a full review of Alpine geology, which can be found elsewhere, for example, Coward *et al.* (1989).

3.1 General Tectonic Development

Today the Alps form an arcuate mountain belt, which extends from northern Italy, through eastern France, Switzerland and Austria. The formation of the Alps can be treated in several stages:

- Permo-Carboniferous basement formation. The major geological evolution of the Central Alps started with the Variscan orogeny in the late Palaeozoic. This created the crystalline basement upon which the Mesozoic sediments were deposited. Work by Schaltegger & Corfu (1992) on U-Pb and Lu-Hf found that igneous rocks in the Aar massif were emplaced into a pre-existing Precambrian basement during the mid to late Carboniferous. Then followed a time of cooling, exhumation and erosion creating an unconformable surface upon which the Permo-Triassic deposits were laid down.
- Mesozoic extension, which culminated in the opening of the Tethys Ocean during the Jurassic-Cretaceous. Carbonate platforms formed in the late Triassic (often on top of evaporite sequences), which subsequently collapsed in the Jurassic. This collapse was followed by the deposition of deeper water pelagic sediments. Oceanic crust was created at one or more spreading ridges (Coward *et al.*, 1989; Hsü, 1989) and this later formed ophiolites.
- In the Mid-Cretaceous, the extensional regime changed to convergence due to the opening of the Northern Atlantic, which ultimately resulted in continental collision between the African and Eurasian plates. At this time, sedimentation continued on the European carbonate platform and the rising range to the southeast lead to the deposition of Cretaceous flysch. The presence of flysch and ophiolite-bearing melanges found throughout the Alpine range indicate the consumption of oceanic crust. In the Eastern Alps, rocks deposited during the Cretaceous contain blueschist and eclogite fragments, demonstrating that subduction and obduction were underway (Frank, 1987). Coward *et al.* (1989) suggested that early ophiolite obduction was followed by diachronous continent-continent collision, which occurred later in the Central and Western Alps than in the eastern Alps.

- Continent-continent collision between the African and European margins and the subsequent high temperature metamorphism in the foreland occurred during the Tertiary. Evidence from the molasse basins (Oligocene and Miocene in age) and radiometric ages suggest the collision and metamorphism occurred in the Eocene in the west, but may have been earlier in the east. Tectonic activity continued into the Pliocene in the external areas of the orogen, such as the Jura.

3.2 Alpine Lithologies

Alpine rock units can be broadly divided into:

- **Molasse** – Syn- to post-tectonic sediments (often cut by thrusts), associated with the erosion of the rising Alpine chain in the late Tertiary.
- **Flysch** – Cretaceous and Eocene marine shale, characterised by the presence of regular intercalations of sandstone and/or impure limestone beds (Hsü, 1989), probably originating as turbidites.
- **Helvetic** – Pre-Triassic granitic basement and Mesozoic sediments, deposited on the northern margin of Tethys.
- **Penninic** – The Penninic realm represents the remnants of the Tethys Ocean, which separated the Helvetic and Austroalpine units. This, essentially European, pre-Triassic basement is composed of polymetamorphic sedimentary and volcanic rocks, intruded by Variscan granites and overlain by a Mesozoic oceanic sediment and platform sequence.
- **Bündnerschiefer** – Incorporates all the dominantly schistose rocks of Mesozoic age in the Penninic units. The present usage, *senso stricto*, is limited to the slightly metamorphosed, pelitic rocks of the Penninic units (Hsü, 1995). This term originated in the area around Chur, to the north of the Lepontine Alps, and has a French Alps equivalent of "schistes lustrés", which contain more highly metamorphosed sediments.
- **Austroalpine** – Pre-Alpine metamorphic basement complex with associated Mesozoic cover, which formed part of the southern margin of Tethys and was part of the African plate and/or Adriatic microplate.

3.3 Geological History of the Central (Lepontine) Alps

3.3.1 *General Points*

The Lepontine Alps are found in the Ticino and Simplon areas of Switzerland and the Toce and Mera river valleys of northern Italy. The term Lepontine was coined by E. Wenk to describe the structural style (characterised by the triclinic geometry of rock bodies, complex planar and linear features and the mono-axial deformation of basement gneisses and Mesozoic sediments), which more or less corresponds with upper boundary of amphibolite grade metamorphism in the Central Alps (Trümpy, 1980). The Pennine nappes dominate the Lepontine Alps, but small areas of

the Ultrahelvetic Gotthard Massif (in the north) and some Austroalpine rocks (to the south) may also be included. The Insubric Line (a 1 km thick, steeply dipping mylonite zone), to the south, separates the Lepontine Alps from the Southern Alps.

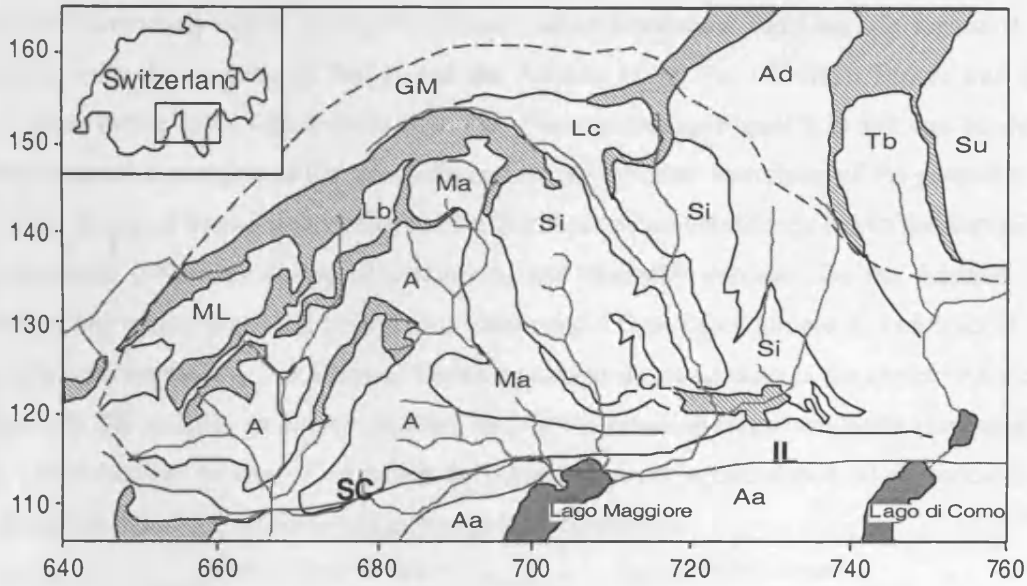

Figure 3.1 Map of the Central Alps to show the main nappe boundaries for the Lepontine Alps. The grid around the outside of the diagram is in kilometres (Swiss National Grid), the black lines and shaded areas represent Mesozoic metasediments or nappe boundaries; the Insubric line (IL), the Simplon-Centovalli Line (SC) and the dashed line (the staurolite isograd) represent the limit of amphibolite grade metamorphism. The nappes marked are Ad – Adula, CL – Cima Lunga, Tb - Tambo, Su – Suretta, Ma – Maggia, Lc – Lucomagno Gneiss, Si – Simano, Lb – Lebendun, A – Antigorio, ML – Monte Leone, GM – Gotthard Massif and Aa – Austroalpine units. Redrawn from Todd & Engi (1997) and Grujic & Manckeltow (1996).

Mesozoic rocks are mainly exposed in the north (Figure 3.1) and further south only thin bands of sediment are present (mainly marbles, dolomite, calcsilicates and quartzites) between the large basement gneiss units.

3.3.2 *Geological History*

Pre-Triassic Events

Pre-Alpine basement rocks are most abundant in the Central Alps and consist of high-grade crystalline rocks (a mixture of pre-Variscan basement, late-Variscan granitoids associated with clastic and volcaniclastic rocks and post-Variscan volcaniclastics). Within the Lepontine area, the nappes contain pre-Triassic basement blocks formed in three E-W trending granite belts, separated by volcaniclastic sediments. The volcaniclastics were, in part intruded by the granites then intensively folded, to leave an angular unconformity at the base of the Triassic (Pfiffner, 1992). For example, the Maggia Nappe contains Archaean to Lower Palaeozoic arkosic gneisses and the Variscan metagranitoid Matorello Gneiss (Günthert *et al.*, 1996).

Mesozoic Rifting

During the Mesozoic, the lithosphere underwent a phase of stretching and thinning associated with sinistral strike-slip between the European and the Adriatic/African plates. This rifting was particularly active during the Jurassic, when Gondwana and Laurasia separated and in association with the opening of Tethys and the Atlantic Ocean (c. 180 Ma). Tethys was only of truly oceanic nature in its westernmost part (the Piemont Ocean, Figure 3.2) and was bordered by the thinned passive margins of the European and Adriatic plates. Stretching of the passive margins produced a series of basins and swells; on the European plate subsidence led to the deposition of thick carbonate sequences on top of continental and evaporite deposits. On the Adriatic margin subsidence and rifting produced basaltic volcanism and a fault-block structure, which accumulated thick carbonate sequences. The Piemont Ocean opened at the same time as the central Atlantic as a result of NW-SE sinistral shear motion aided by NW-SE trending transform faults (Lemoine *et al.*, 1989). Mid Jurassic to early Cretaceous deep-sea sediments accumulated on the oceanic crust, such as radiolarian chert, siliceous shales and pelagic limestones.

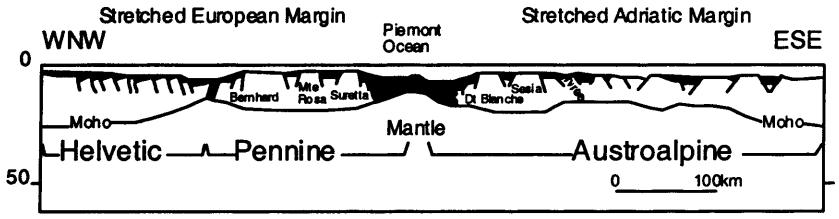

Figure 3.2 Cross-section of the rifted and thinned continental margins of the Piemont Ocean at the end of the Jurassic (150 Ma); black shading indicates oceanic crust and stippled shading indicates Jurassic sediments (after Pfiffner, 1992).

Convergence and Collision

The orogenic episode in the Cretaceous corresponds to NE-SW directed convergence between the European and the African plates (Dewey *et al.* 1989). The Adriatic microplate was separated from the African plate between 130-60 Ma and rotated 30° anticlockwise during that period (Dercourt *et al.*, 1986; Heller *et al.*, 1989). Many authors suggested this corresponded to a dextral transpressive movement relative to the European plate and lead to the southward subduction of oceanic crust, a mid-Cretaceous high-pressure metamorphism and west or northwest thrusting in the Alps. However, there are problems with reliability of the some of the geochronological data.

Numerous authors for example, Arnaud & Kelley, 1995; Inger *et al.*, 1996; and Reddy *et al.*, 1996 (in the Western Alps) have pointed out that excess argon presents a problem for measured ages in Alpine basement rocks. More recently, high-pressure metamorphism has been dated using Sm-Nd and Rb-Sr. For example, Amato *et al.* (1999) report a five point Rb-Sr isochron with an age of 40 ± 3.9 Ma for the Cigana eclogite (approximately 25 km to the southwest of the Simplon fault), which is in agreement with an Sm-Nd age of 40.6 ± 2.6 Ma for the same location. Duchêne *et al.* (1997) also give Tertiary ages for the peak of the high-pressure metamorphic event using garnet Lu-Hf in the Western Alps. From bottom to top of the nappe stack, the measured ages are 32.8 ± 1.2, 49.1 ± 1.2 and 69.2 ± 2.7 Ma, indicating that burial and exhumation was a continuous

process (Duchêne *et al.*, 1997). Vance & O'Nions (1992) also report Tertiary U-Pb, Sm-Nd and Rb-Sr ages for garnet analyses from the Central Alps, implying a Tertiary age for Alpine metamorphism. The high-pressure metamorphism affected the Eastern and Western Alps and the ophiolite sequence now located between the Penninic and Austroalpine nappes (Hunziker *et al.*, 1989).

Major deformation occurred between the upper Cretaceous and the Eocene-Oligocene with formation of the Pennine nappes from pre-Triassic crystalline basement and Tethyan Mesozoic sediments. Continent-continent collision resulted in the overthrusting of the Austroalpine nappes from the southern margin of Tethys and further northwards thrusting of the Pennine nappes and the underlying Helvetic nappes. Similarly, the Adriatic plate was imbricated in a series of southwards thrusts (Figure 3.3). The main updoming of the Lepontine area began at 32-30 Ma with the intrusion of the Bergell tonalities and granodiorites and southwards verging backthrusts and backfolds (Steck & Hunziker, 1994). The downloading and flexure of the lithosphere by the nappes caused the formation of foreland basins on both sides of the mountain chain, allowing the accumulation of molasse.

During the early Miocene, the Pennine nappes were uplifted by >9 km (Pfiffner, 1992) and the late stages of collision produced large-scale southward back-folds and back-thrusts. Mancktelow (1992) describes the orogen parallel extension caused by this rapid uplift, which is manifest in the Simplon fault zone, to the west for the Lepontine Alps. This normal faulting allowed lateral escape of the upper most nappes in the Lepontine area. Vance & O'Nions (1992) suggest the rapid cooling rates found in the Central Alps are due to tectonic exhumation and the back-thrusting of hot rocks over cold. Today, the central Swiss Alps are still uplifting at a rate of up to 2 mm yr^{-1} (Pfiffner, 1992).

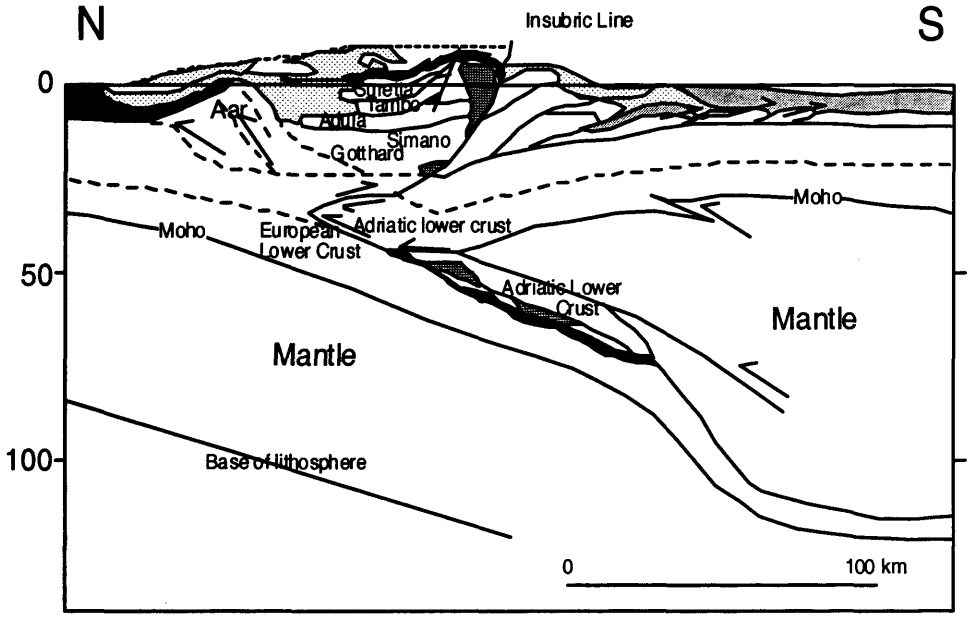

Figure 3.3 Present day cross-section along the European Geotraverse (redrawn from Pfiffner, 1992). A wedge of the Adriatic plate is forced into the thickened European plate, splitting the upper and lower crust. At the same time, the Pennine nappes are uplifted and eroded with back-folding near the Insubric Line.

3.3.3 *Peak Metamorphism*

In the Lepontine area, metamorphism reached amphibolite facies (Todd & Engi, 1997). Temperature increases from 500 to 550 °C in the north and west and attains 675 °C towards the south, at the Insubric Line (Figure 3.4). Maximum pressures, of around 7 kb, are in the central region (20 km to the north of the Insubric Line) and decrease to the north (5.5 kb) and south (4.5 kb), see Figure 3.5.

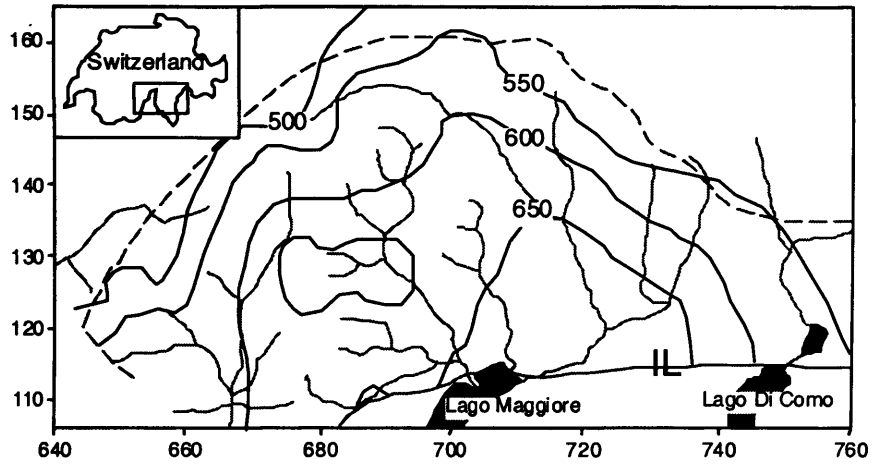

Figure 3.4 Map showing the locations of peak metamorphic temperatures (°C), redrawn from Todd & Engi (1997). See Figure 3.1 for details of the figure.

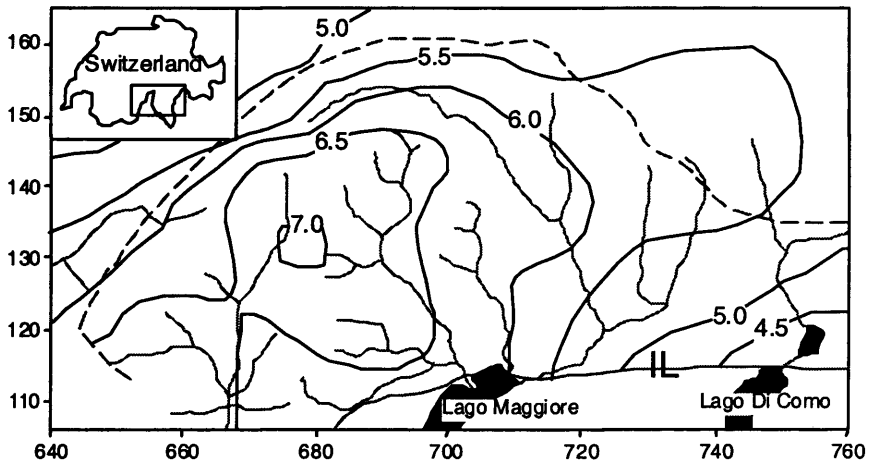

Figure 3.5 Map showing the locations of peak metamorphic pressures (kb), redrawn from Todd & Engi (1997). See Figure 3.1 for details of the figure.

Todd & Engi (1997) show that the rocks recording the youngest metamorphic peak ages are not from the region of hottest peak temperature. They suggest there were two stages of metamorphism; the first stage created the metamorphic field gradients present in the northern area and the second stage was a thermal pulse, which only affected the south-eastern part. They suggest this second stage occurred much later and under lower pressure conditions, possibly due to movement along the Insubric Line.

Outside the Lepontine area, structurally higher nappes have reached blueschist or eclogite grade, some of which are coesite-bearing. For example, Amato *et al.* (1999) describe coesite at the Zermatt-Sass ophiolite complex; and Duchêne *et al.* (1997) describe coesite at Dora Maira (both in the Western Alps). This implies that the nappes of the Central Alps may also have reached high T-P metamorphic levels.

In the Central Alps, garnet lherzolites outcrop within the Cima Lunga Nappe at Alpe Arami (approximately 10 km to the east of the Verzasca locality) and Cima di Gagnone (approximately 15 km to the northeast of Verzasca). These give P-T data of 32 kb and 840°C (Alpe Arami) and 30 kb and 740°C (Cima di Gagnone), Nimis & Trommsdorff (2001), implying a maximum subduction depth of approximately 100 km. These data imply that, at some point in their evolution, parts of the nappes of the Central Alps attained much higher temperatures and pressures than Todd & Engi (1997) suggest.

Today, the Cima Lunga and Adula Nappes represent amphibolite grade metamorphic rocks. Two alternative hypotheses have been proposed for the formation of amphibolite grade rock, either an early high-pressure event, which has subsequently been over-printed by an amphibolite event; or a single continuous retrograde event from high-pressure conditions to amphibolite or high greenschist grade (Meyre *et al.*, 1999). Meyre *et al.* (1999) present a two-phase model for the evolution of the Adula Nappe; firstly the formation an garnet peridotite complex, followed by retrogression, then a second metamorphic event causing the amphibolite grade overprint present today.

3.3.4 *Timing of Metamorphism*

The timing of peak metamorphism is controversial in the central Swiss Alps. Jäger (1973) proposed an age for peak metamorphism of 38-35 Ma on the basis of Rb-Sr analyses of phengite from outside the staurolite isograd (T < 500°C; Todd & Engi, 1997) implying they grew below the Rb-Sr closure temperature. In the Lago del Narèt region, cooling starts at approximately 25 Ma (extrapolation to peak temperature of 575°C, Rb-Sr age measurements by Steiner (1984a) of 22.7 ± 2.0 Ma for muscovite and 16.5 ± 1.2 Ma for biotite in Jenkin *et al.*, 2001). Around Someo, Köppel & Grünenfelder (1975) and Köppel *et al.* (1980) give concordant U-Pb monazite and xenotime ages of 22-23, which they believe date the end of amphibolite grade metamorphism. Further concordant U-Pb ages for Alpine monazite give 20-30 Ma and date the end of prograde metamorphism (20 Ma at Verampio in the west, to 30 Ma east of the Bergell granite), Köppel *et al.* (1980). Vance & O'Nions (1992) report Sm-Nd, U-Pb and Rb-Sr ages from garnet growth at the climax of metamorphism on the staurolite isograd at 32–28 Ma, 40 km to the west of Lago del Narèt; a sample from ~ 5 km north of Bellinzona gives a Sm-Nd age of 26.7 ± 1.7 Ma, which in conjunction with U-Pb data give very high cooling rates (> 100 °C/Ma).

3.3.5 *Cooling History*

Cooling rates for the central Lepontine (Valle Maggia) can be derived from Hurford (1986 & 1991) and Steiner (1984a) using the cooling ages for different systems and their respective closure temperatures (see Table 2.1 for a summary of closure temperature data). The ages given by fission tracks in apatite and zircon and Rb-Sr and K-Ar on micas in the Lepontine area are interpreted as cooling ages (Jäger *et al.*, 1967; Purdy & Jäger, 1976 and Hurford, 1986).

Generally the cooling rate increases from the south to the north of the Lepontine area (Figures 3.6 and 3.7). Steiner (1984a) gives cooling ages for muscovite Rb-Sr and biotite Rb-Sr and K-Ar of 22.0 ± 2.0 Ma and 16.5 ± 1.2 Ma respectively from Lago del Narèt gneiss samples, which give an overall cooling rate of ~32 °C/Ma (assuming closure temperatures of 500 and 300 °C respectively). Extrapolating this cooling curve back to the peak temperature (575 °C, Todd & Engi, 1997) suggests the onset of cooling at Narèt commenced at ~25 Ma.

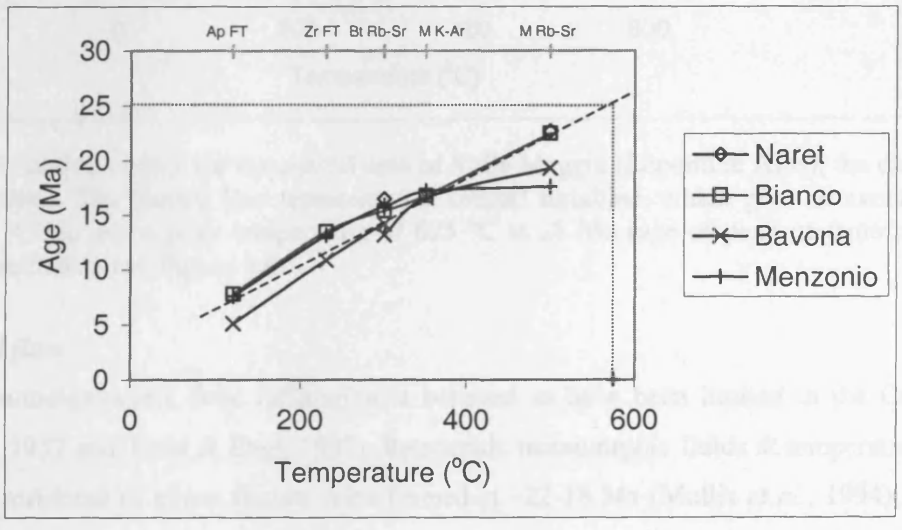

Figure 3.6 Cooling curves for the northern area of Valle Maggia (Lepontine Alps); the data are from Hurford (1986). The dashed line represents the overall trendline, which give an average cooling rate of 32 °C/Ma and a peak temperature of 575 °C at 25 Ma (solid lines). The mineral systems are marked; Ap FT – apatite fission track, Zr FT – zircon fission track, Bt Rb-Sr – biotite Rb-Sr, M K-Ar – muscovite K-Ar and M Rb-Sr – muscovite Rb-Sr.

Hurford (1986) gives muscovite K-Ar and biotite Rb-Sr and K-Ar ages of 18.5 ± 0.2 Ma, 16.2 ± 0.3 Ma and 16.3 ± 0.2 Ma respectively for Someo gneiss samples. These give an overall cooling rate of ~22 °C/Ma, assuming closure temperatures of 350 and 300 °C respectively. Cooling rates between individual closure temperatures indicate a period of rapid cooling between 23 and 16 Ma (and display greater variation than the samples from northern Valle Maggia; 50 to 80 °C/Ma), which decreases to 10-20 °C/Ma between 16 Ma and the present day (Hurford, 1986). Figure 3.7 shows all the cooling curves from Valle Maggia (data are from Hurford, 1986). Other cooling curves from the northern and central parts of the Maggia Valley, Hurford (1986 and 1991), show a sharp increase in cooling rate above 350 °C, suggesting an age of 23 Ma for the onset of cooling around Someo, which is consistent with the southward decrease in age of peak metamorphism of

other studies. However, extrapolating the average of these cooling curves (Figure 3.7) suggests an age of ~28 Ma for the peak of metamorphism at ~625°C (after Todd & Engi, 1997). The very high cooling rates towards the south of the Lepontine Alps are thought to be associated with late backthrusting over the Insubric Line (Vance & O'Nions, 1992).

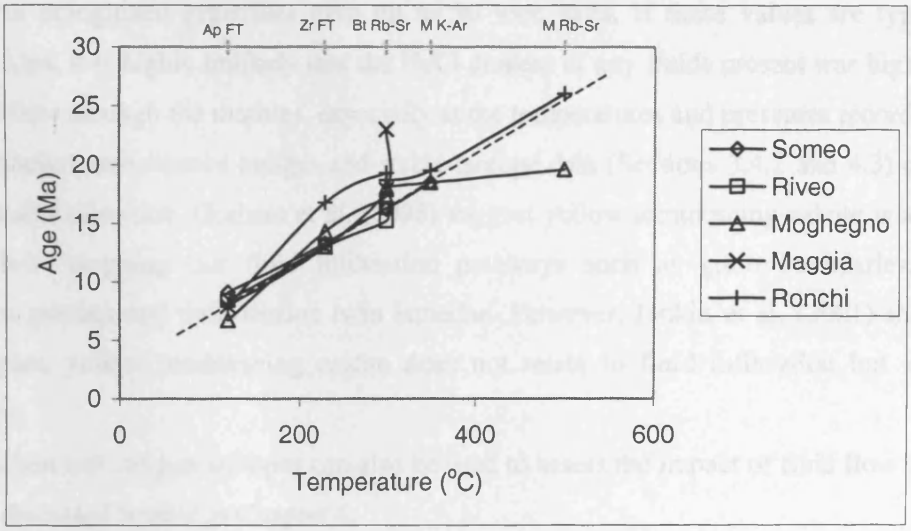

Figure 3.7 Cooling curves for the central area of Valle Maggia (Lepontine Alps); the data are from Hurford (1986). The dashed line represents the overall trendline, which give an average cooling rate of 22 °C/Ma and a peak temperature of 625 °C at 28 Ma (age of peak metamorphism). For mineral system data see Figure 3.6.

3.3.6 *Fluid flow*

Syn-metamorphic fluid infiltration is believed to have been limited in the Central Alps (Baertschi, 1957 and Todd & Engi, 1997). Retrograde metamorphic fluids at temperatures of 400-450°C are restricted to minor fissure veins formed at ~22-18 Ma (Mullis *et al.*, 1994) which may have been open as late as 13 Ma, 5 km to the west of Lago del Narèt (Purdy & Stalder, 1973).

Holness & Graham (1991) discuss fluid infiltration; for a fluid to penetrate a rock without hydrofracturing, the dihedral angle of the fluid against the rock must be less than 60°. For the system H_2O-CO_2-NaCl-calcite, the dihedral angle decreases from 80° (for pure water) to 44° (for 60 wt% NaCl). For the critical value of 60°, the NaCl content of the fluid is 35 wt%. Within the Central Alps, there is potential for NaCl-rich fluids due to the presence of Triassic evaporite sequences. Holness & Graham (1991) note that there is little difference between calcite-fluid dihedral angles over the temperature range 550 to 750 °C. Holness & Graham (1995) conclude that Ca-carbonates are only permeable to pervasive fluid flow under highly restricted conditions; at 650 °C, the pressure must be low (0.5-2 kb) combined with fluid compositions near $X_{CO2} = 0.5$ or very strong brines. They also suggest that all Mg-carbonates are impermeable to NaCl-CO_2-H_2O fluids at pressures below 7 kb. Figures 3.4 and 3.5 show the peak temperatures and pressures for the Lepontine Alps and indicate that peak pressures were between 5 and 7 kb with temperatures between 500 and 650 °C, suggesting marble from this area would be impermeable to fluid flow.

The fluid inclusions found in Lepontine fissure veins vary between 1-5 wt% NaCl in the Lucomagno Gneiss and the surrounding Permian to Tertiary cover sequence (calculated from Mullis *et al.*, 1994). In the Western Alps, work on the schistes lustrés on greenschist to blueschist facies veins indicates fluids of 0-15 wt% NaCl (Agard *et al.*, 2000). The highest wt% chloride fluid inclusions come from Mt. Emilius in the Western Alps (Scambelluri *et al.*, 1998) where fluid inclusions in eclogitized granulites give up to 50 wt% salts. If these values are typical of the Lepontine Alps, it is highly unlikely that the NaCl content of any fluids present was high enough to allow fluid flow through the marbles, especially at the temperatures and pressures recorded.

Cathodoluminescence images and stable isotope data (Sections 3.4.2 and 4.3) can be used to assess fluid infiltration. Graham et al. (1998) suggest yellow luminescing calcite is an indicator of fluid flow, mapping out fluid infiltration pathways such as grain boundaries, fractures, replacement patches and deformation twin lamellae. However, Jenkin et al. (2001) show that, in some samples, yellow luminescing calcite does not relate to fluid infiltration but isochemical replacement.

Carbon and oxygen isotopes can also be used to assess the impact of fluid flow on analyses and this is discussed further in Chapter 4.

3.4 Alpine Samples

3.4.1 *Samples Investigated*

The samples investigated in this study are amphibolite-grade calcite marbles containing one or more phlogopite layers. Other subsidiary phases may include muscovite, dolomite, quartz, K-feldspar, plagioclase, titanite and apatite. The sample locations are marked on Figure 3.8 and further details of the samples can be found below. Details of the mineralogy, grain sizes and sample co-ordinates can be found in Appendix 1 and in relevant subsections.

Dalpe

The sample is from a 20 m-thick outcrop in a disused marble quarry, which exposes a large antiform of mica-rich dolomitic marble. The dolomite is part of the metamorphosed Triassic deposits, which separate the Lucomagno Gneiss from the Simano Nappe.

Lago del Narèt

The samples come from a 40m-thick infold of Triassic marble on the northern margin of the Maggia nappe (Steiner, 1984; Günthert *et al.* 1996). Bündnerschiefer conformably underlies the marble and there is a thrust contact with alkali feldspar gneiss at the top of the outcrop.

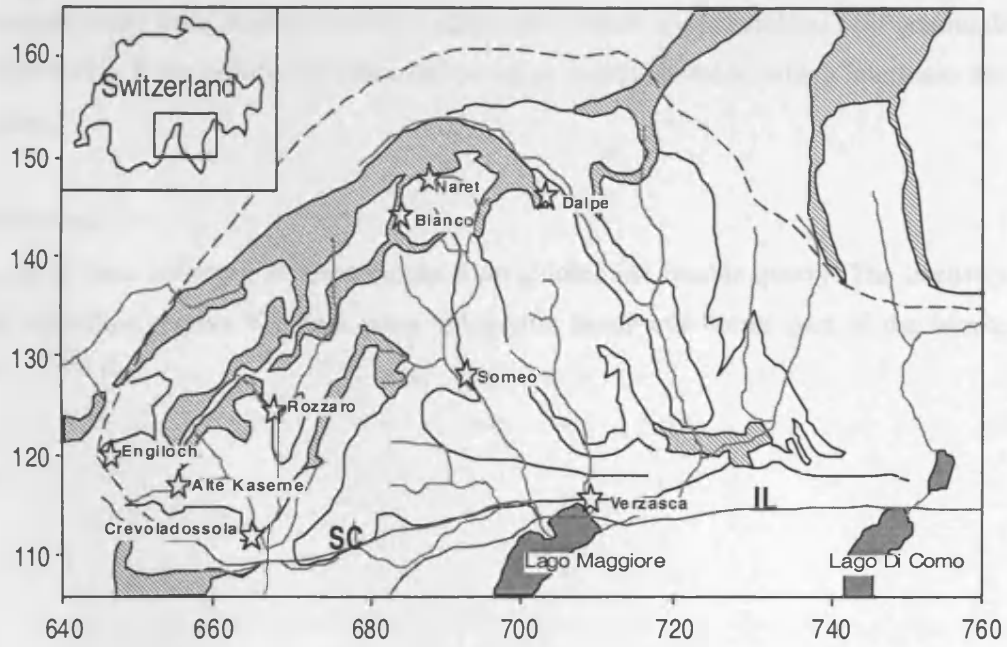

Figure 3.8 Map of sample locations. The samples collected are mainly calcite marbles, although there are some examples of quartzites, gneisses and Bündnerschiefer. Samples from Lago del Narèt and Someo were used in an Rb-Sr laser ablation ICP-MS study and along with other samples were used in the chemical equilibration study.

Lago Bianco

The samples are from steeply inclined interfolded marbles and quartzites between the Lebendun and Maggia nappes. The outcrop at Lago Bianco is part of the large-scale Basòdino fold (Grujic & Mancktelow, 1996)

Someo

The sample comes from a thin marble band (~ 2m-thick), which grades into more silicic material.

Rozzaro

Triassic marbles outcrop in cliffs (~30m-thick) above a thick deposit of Bündnerschiefer.

Engiloch

The sample comes from a marble lens, surrounded by gneiss within the Monte Leone nappe.

Alte Kaserne

The samples come from marble lenses within the calc-silicate schists and quartzites of the Lebendun nappe.

Valle Verzasca Dam

The samples come from marble outcrops (~2m-wide), which are interfolded acid granitoids gneiss and amphibolite. Kobe (1966) describes narrow large amplitude folds, which interleave the marble and gneiss.

Crevoladossola

The samples were collected as loose blocks from a dolomitic marble quarry. The intensely folded Triassic dolomitic marble contains many phlogopite bands and forms part of the Monte Leone nappe.

Chapter 4

Isotopic Data

Chapter 4 compiles the conventional bulk isotopic data used in this work and compares them with previously published work. Carbon and oxygen isotope data are used to assess the impact of fluid infiltration. The sections on Rb-Sr compare the results of this work with previously published data on biotite gneisses to examine the mineral mode effect proposed by Jenkin *et al.*, 1995. Whole phlogopite grains separated from the marble in a dissolution experiment are used to examine the grain size / age relationship proposed by Dodson (1973).

4.1 Carbon and Oxygen Data

Carbon and oxygen data are used to assess whether the samples have undergone exchange *via* fluid infiltration. The measured values of $\delta^{18}O$ and $\delta^{13}C$ are compared with known values for unmetamorphosed carbonate of the same age; if the values are similar, it can be argued that no stable isotope exchange has taken place and the measured metamorphic carbonate is said to be unaffected by fluids (Section 4.1.2).

Figure 4.1 shows a plot of $\delta^{18}O_{SMOW}$ (measured against Standard Mean Oceanic Water) and $\delta^{13}C_{PDB}$ (measured against the Pee Dee Belemnite) for the Alpine carbonate samples collected in this study and Table 4.1 tabulates the data from this study. The $\delta^{18}O_{SMOW}$ and $\delta^{13}C_{PDB}$ data were produced using calcite or dolomite mineral separates; see Appendix 2 for a brief description of the analytical technique

Table 4.1 Stable isotope data (in ‰).

Sample	Location	Mineral	$\delta^{13}C_{PDB}$	Error $\delta^{13}C_{PDB}$	$\delta^{18}O_{PDB}$	Error $\delta^{18}O_{PDB}$	$\delta^{18}O_{SMOW}$	Error $\delta^{18}O_{SMOW}$
HT4	Dalpe	Dolomite	1.06	0.05	-7.80	0.05	22.82	0.05
HT10	Verzasca	Calcite	0.24	0.05	-12.79	0.05	17.68	0.05
HT11	Verzasca	Calcite	-0.44	0.05	-9.42	0.05	21.15	0.05
HT15	Narèt	Calcite	2.65	0.05	-8.05	0.05	22.57	0.05
HT16	Narèt	Calcite	3.09	0.05	-7.79	0.05	22.83	0.05
HT17	Narèt	Calcite	2.80	0.05	-10.21	0.05	20.33	0.05
HT23	Someo	Calcite	2.02	0.04	-10.10	0.04	20.45	0.04
HT26	Crevola	Dolomite	-0.23	0.05	-3.66	0.05	27.09	0.05
HT28	Crevola	Dolomite	1.37	0.06	-4.27	0.06	26.47	0.06

Figure 4.1 shows the data grouped into the areas of highest and lowest degree of metamorphism and separates dolomite from calcite. HT10 and HT11 have undergone the highest degree of metamorphism and show a downward shift in $\delta^{13}C_{PDB}$ and a slight downward shift in $\delta^{18}O_{SMOW}$, when compared to samples from areas of lower metamorphic grade.

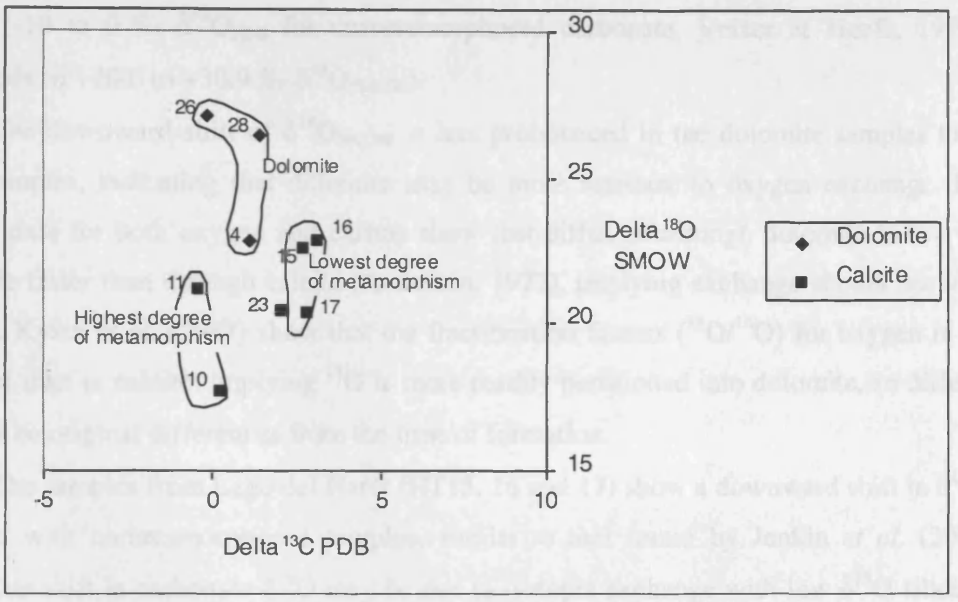

Figure 4.1 $\delta^{18}O$ and $\delta^{13}C$ data. The numbers denote the sample number (HTx; see Table 4.1 for locations).

4.1.2 *Comparison with Published Carbon and Oxygen Data and its Implications*

Figure 4.2 shows the analysed values compared with previously published values for unmetamorphosed Triassic carbonates to assess the possibility of fluid infiltration.

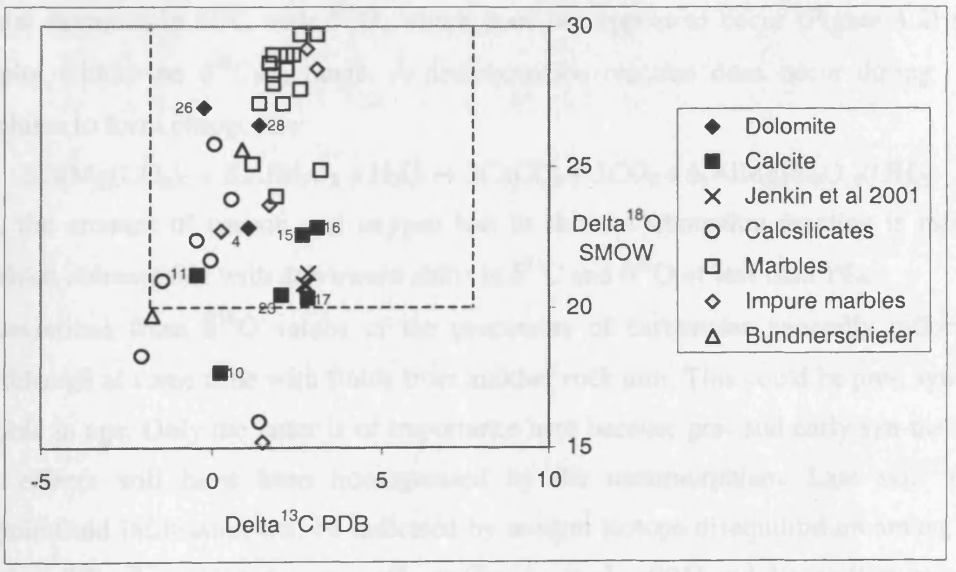

Figure 4.2 Graph to show variation in $\delta^{18}O_{SMOW}$ and $\delta^{13}C_{PDB}$ for Alpine carbonate samples. Data are from this study (solid symbols), Baertschi (1957) (open symbols; the samples are all from around Lago del Narèt) and Jenkin *et al.* (2001). The area enclosed by the dashed lines represents unmetamorphosed Triassic carbonate values for limestone; data are from Veizer & Hoefs (1976). Veizer & Hoefs (1976) give $\delta^{18}O_{PDB}$ data and these were converted to $\delta^{18}O_{SMOW}$ using the following equation: $\delta^{18}O_{SMOW} = ((\delta^{18}O_{PDB} \times 1.03086) + 30.86)$.

Most of these samples fit well within the limits of $\delta^{13}C_{PDB}$ for Triassic carbonates (-2 to +6.8 $\delta^{13}C_{PDB}$; Veizer & Hoefs, 1976), however, some of the measured $\delta^{18}O_{SMOW}$ values are slightly

lower (-10 to 0 ‰ $\delta^{18}O_{PDB}$ for unmetamorphosed carbonate, Veizer & Hoefs, 1976; which corresponds to +20.6 to +30.9 ‰ $\delta^{18}O_{SMOW}$).

The downward shift of $\delta^{18}O_{SMOW}$ is less pronounced in the dolomite samples than in the calcite samples, indicating that dolomite may be more resistant to oxygen exchange. However, diffusion data for both oxygen and carbon show that diffusion through dolomite is two orders of magnitude faster than through calcite (Anderson, 1972), implying exchange should occur faster in dolomite. Kyser *et al.* (1987) show that the fractionation factors ($^{18}O/^{16}O$) for oxygen in dolomite are higher than in calcite; implying ^{18}O is more readily partitioned into dolomite, so differences in $\delta^{18}O$ may be original differences from the time of formation.

The samples from Lago del Narèt (HT15, 16 and 17) show a downward shift in $\delta^{18}O$, when compared with unmetamorphosed samples, similar to that found by Jenkin *et al.* (2001), who suggest this shift in carbonate $\delta^{18}O$ may be due to isotopic exchange with low $\delta^{18}O$ silicates (such as quartz). As most of the samples are impure marbles (Appendix 1), it is possible that the shift in $\delta^{18}O$ is due to exchange with low $\delta^{18}O$ silicate material. In general, Figure 4.2 shows that impure marbles and calcsilicates have lower $\delta^{18}O$ than pure marbles suggesting exchange with silicates may be taking place. This decrease in $\delta^{18}O$ could also be achieved by exchange with fluids. Another possibility for the downward shift in $\delta^{18}O$ is *via* decarbonation reactions with a coincidental decrease in $\delta^{13}C$ with $\delta^{18}O$, which does not appear to occur (Figure 4.2) as all the samples plot within the $\delta^{13}C_{PDB}$ range. A decarbonation reaction does occur during prograde metamorphism to form phlogopite:

$$3CaMg(CO_3)_2 + KAlSi_3O_8 + H_2O \rightarrow 3CaCO_3 + 3CO_2 + KAlMg_3Si_3O_{10}(OH)_2$$

However, the amount of carbon and oxygen lost in this decarbonation reaction is insignificant (~10%) which corresponds with downward shifts in $\delta^{13}C$ and $\delta^{18}O$ of less than 1‰.

Deviations from $\delta^{18}O$ values of the precursors of carbonates generally reflect oxygen isotope exchange at some time with fluids from another rock unit. This could be pre-, syn- or post-metamorphic in age. Only the latter is of importance here because pre- and early syn-metamorphic exchange effects will have been homogenised by the metamorphism. Late syn- and post-metamorphic fluid infiltration will be indicated by oxygen isotope disequilibrium among different minerals that differ from closed-system effects (Jenkin *et al.*, 1994) and disequilibrium within the same mineral in monomineralic rocks on small length scales. Oxygen diffusion should be a good indicator of fluid flow through carbonate rocks, as the exchange of oxygen isotopes between a water-based fluid and a carbonate should produce isotopically light samples in comparison with unaltered samples. Oxygen isotope exchange between a carbonate and a fluid is more likely to occur as diffusion of oxygen is faster at lower temperatures, in comparison with the diffusion of metallic elements (compare Farver & Yund 1998 with Farver & Yund 1996).

Other indications of a lack of fluid flow come from petrology and cathodoluminescence. The samples used in this study avoid the effects of retrograde alteration (no or very limited

alteration to chlorite in biotite or phlogopite and no, or very limited, sericitisation in feldspars), have no late fractures and the primary minerals contain no or very few fluid inclusions (see Table 1.1 and Appendix 1).

Graham *et al.* (1998) believe that yellow luminescing calcite maps out fluid infiltration pathways in high-grade marbles. Cathodoluminescence (for example, HT16 shown in Figure 4.3) shows no indicators of fluid flow through any of the samples (these indicators include yellow luminescing calcite along grain boundaries, fracture planes and in speckled exsolution patches). Any fluid infiltration and decarbonation associated with the formation of the phlogopite would have taken place before the peak of metamorphism and not affected the retrograde effects being examined. The samples used in this study are very close to being closed system rocks.

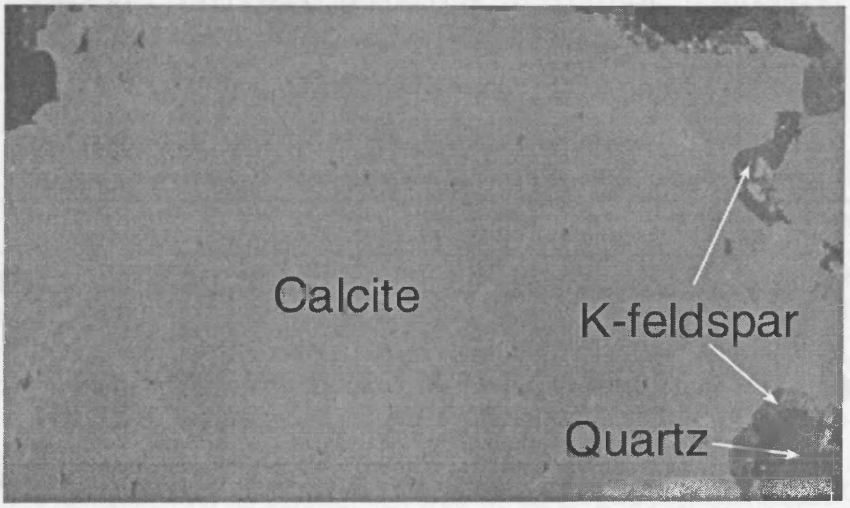

Figure 4.3 Cathodoluminescence image of HT16. Field of view 1 cm. The photomicrograph shows orange luminescing calcite, black/brown luminescing quartz and blue luminescing K-feldspar.

4.2 Mineral Rb-Sr data

Mineral separate Rb-Sr data are given in Table 4.2. Rb-Sr dating work was carried out a NIGL (see Appendix 2 for details) and analyses of the NBS 987 standard gave 0.710187 (± 3, 2 SD, n = 11).

The calcites were found to have low Rb contents (< 0.5 ppm) and a value of zero is assumed where Rb was undetected. Almost all the calcite $^{87}Sr/^{86}Sr$ ratios are significantly higher than Triassic seawater values (0.7075 to 0.7079; Koepnick *et al.* 1990) indicating Sr isotope exchange with a high $^{87}Sr/^{86}Sr$ phase since deposition, probably during metamorphism. This will be discussed more fully in Chapter 5 (Section 5.4.3 and subsequent sections).

The phlogopites and muscovites have high Rb/Sr ratios and low Sr contents. The high Rb/Sr ratios result in precise measured ages with errors generally below 0.5 Ma.

Table 4.2 Mineral Rb-Sr isotope data.

Sample	HT4	HT26	HT28	HT11
Location	Dalpe	Crevola	Crevola	Verzasca
Carbonate	Dolomite	Dolomite	Dolomite	Calcite
Mica	Muscovite	Phlogopite	Phlogopite	Muscovite
Carbonate				
$^{87}Sr/^{86}Sr$	0.708509±5	0.709804±6	0.708644±5	0.707956±6
$^{87}Rb/^{86}Sr$	0.00	~0.01	0.01	~0.01
Rb (ppm)	0.5	0	0.2	0
Sr (ppm)	329	40	73	546
Mica Values				
$^{87}Sr/^{86}Sr$	0.711324±5	0.724473±5	0.711419±9	0.708622±7
$^{87}Rb/^{86}Sr$	11.81	72.87	13.66	2.50
Rb (ppm)	336	286	173	83
Sr (ppm)	82	11	37	96
Ages (Ma)[×]				
Mica/Cc[‡]	16.8 ± 0.2	14.2 ± 0.2	14.0 ± 1.0	18.8 ± 0.2

Continued...

Sample	HT15	HT15	HT16	HT17	HT23
Location	Narèt	Narèt	Narèt	Narèt	Someo
Carbonate	Calcite	Calcite	Calcite	Calcite	Calcite
Mica	Phlogopite	Phlogopite	Muscovite	Phlogopite	Phlogopite
Carbonate					
$^{87}Sr/^{86}Sr$	0.715119±5	0.715119±5	0.717481±5	0.718609±7	0.709500±10
$^{87}Rb/^{86}Sr$	0.00	0.00	0.00	0.01	0.01
Rb (ppm)	0.2	0.2	0.0	0.4	0
Sr (ppm)	337	337	131	110	416
Mica Values					
$^{87}Sr/^{86}Sr$	1.148923±22	0.776637±7		0.775524±7	0.736870±7
$^{87}Rb/^{86}Sr$	1769.56	287.89			103.62
Rb (ppm)	938	613		720	211
Sr (ppm)	2	6		9	6
Ages (Ma)[×]					
Mica/Cc[‡]		17.3 ± 0.7		17.8 ± 0.2	18.5 ± 0.1
> 1000 μm	17.3 ± 0.2				

Continued...

Sample	HT23*	HT23*	HT23*	HT23*	HT23*
Location	Someo	Someo	Someo	Someo	Someo
Carbonate	Calcite	Calcite	Calcite	Calcite	Calcite
Mica	Phlogopite	Phlogopite	Phlogopite	Phlogopite	Phlogopite
Carbonate					
$^{87}Sr/^{86}Sr$	0.709500±10	0.709500±10	0.709500±10	0.709500±10	0.709500±10
$^{87}Rb/^{86}Sr$	0.01	0.01	0.01	0.01	0.01
Rb (ppm)	0	0	0	0	0
Sr (ppm)	416	416	416	416	416
Mica Values					
$^{87}Sr/^{86}Sr$	0.711092±6	0.718584±10	0.723597±5	0.742185±6	0.749356±7
$^{87}Rb/^{86}Sr$	6.2	34.3	53.3	131.6	162.4
Rb (ppm)	135	216	232	252	258
Sr (ppm)	63	18	13	6	5
Ages (Ma)[×]					
75 - 200 µm	18.1 ± 1.1				
300 - 350 µm		18.7 ± 0.2			
350 - 600 µm			18.6 ± 0.2		
600 -1000 µm				17.5 ± 0.1	
>1000 µm					17.3 ± 0.1

[×] Errors in the age incorporate a 0.5 % error on $^{87}Rb/^{86}Sr$ and the quoted error on $^{87}Sr/^{86}Sr$.
[‡] Unless otherwise specified, separates are 100-250 µm.
* Phlogopite separates are from a dissolution experiment (Section 4.2.3 and Appendix 2).

Figure 4.4 shows an isochron diagram for the mica separate data for HT23 given in Table 4.2. The mineral ages were calculated using the calcite data to estimate initial $^{87}Sr/^{86}Sr$ ratios. For these micas, the high Rb/Sr ratio means that the choice of initial ratio does not affect the calculated age. Mica-calcite ages are considered the most meaningful as calcite represents the largest reservoir of Sr in these rocks. The isochron, of the grain size separates from HT23 (Figure 4.4) gives an age of 17.3 ± 0.6 Ma (with an initial $^{87}Sr/^{86}Sr$ ratio of 0.70988±76), which is controlled by the micas with the highest Rb/Sr ratios.

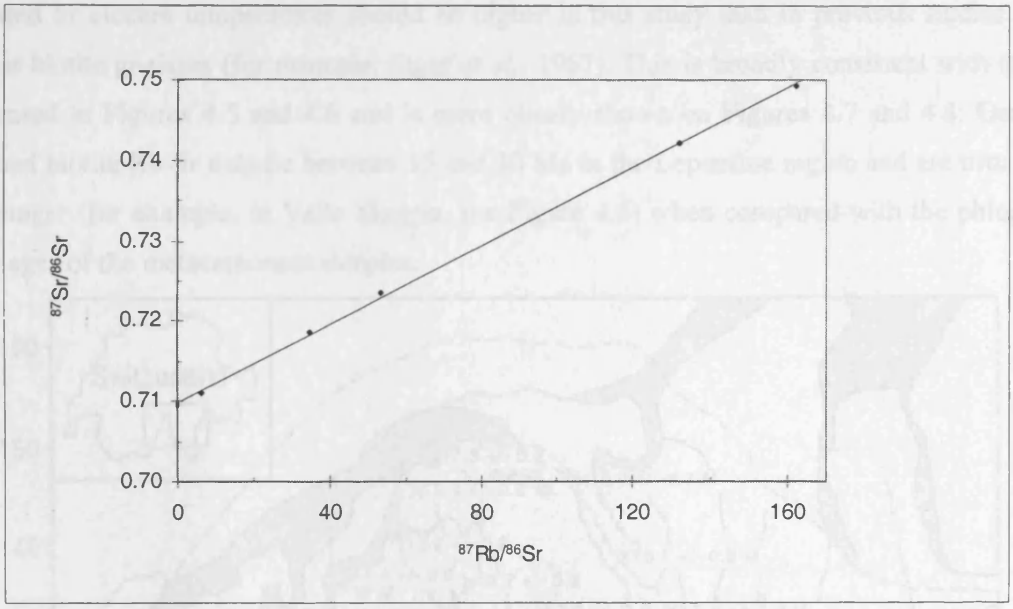

Figure 4.4 Isochron plot for the HT23 phlogopite separates. The six data points (five mica and one calcite) produce a measured age of 17.3 ± 0.6 Ma. MSWD = 190.

Figure 4.5 shows the distribution of measured ages from this work. These ages will be discussed further in Section 4.2.2, comparing these results with previously published data.

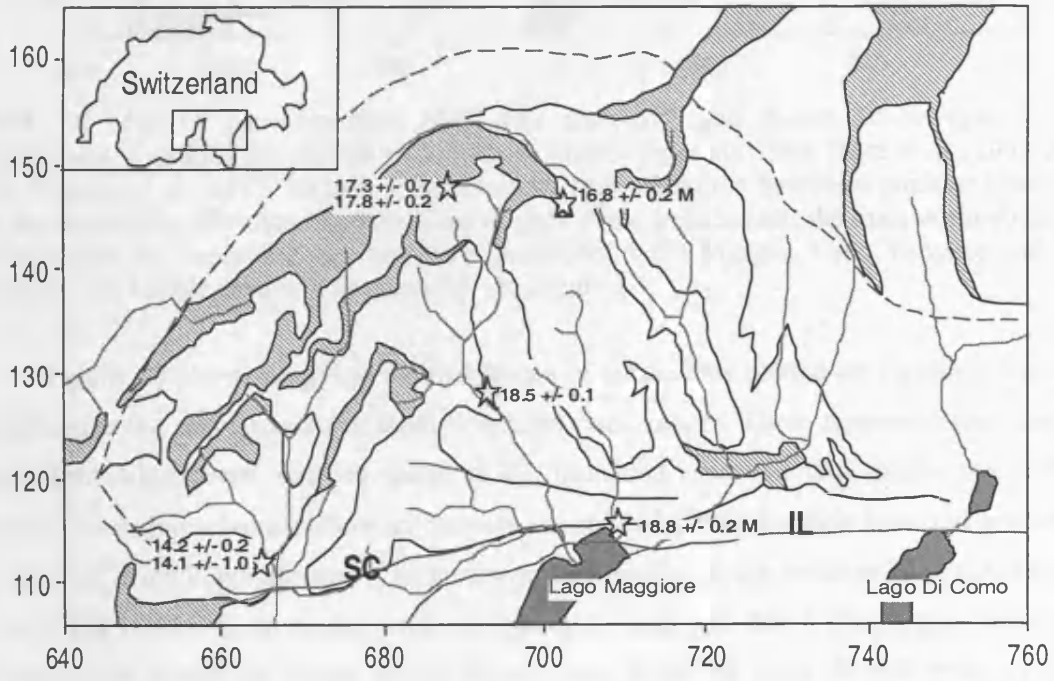

Figure 4.5 Map of the Lepontine Alps with phlogopite and muscovite (marked M on the diagram) Rb-Sr ages (in Ma) from this work superimposed. See Figure 1.1 for details of the map.

4.2.1 *Comparison with Published Rb-Sr Data*

Dahl (1996) suggests that an Mg- and F-rich mica would tend to have a higher Sr closure temperature (and therefore age) than biotite, which would tend to be Fe-richer and F-poorer. The phlogopites from the metacarbonates are Mg- (with > 80 % phlogopite end-member) and F-rich

(20-35% F^- on the OH^- site; see Appendix 4 for electron microprobe data) suggesting that any calculated Sr closure temperatures should be higher in this study than in previous studies on the adjacent biotite gneisses (for example, Jäger *et al.*, 1967). This is broadly consistent with the data represented in Figures 4.5 and 4.6 and is more clearly shown on Figures 4.7 and 4.8. Generally published biotite Rb-Sr data lie between 15 and 20 Ma in the Lepontine region and are usually 1-2 Ma younger (for example, in Valle Maggia, see Figure 4.8) when compared with the phlogopite-calcite ages of the metacarbonate samples.

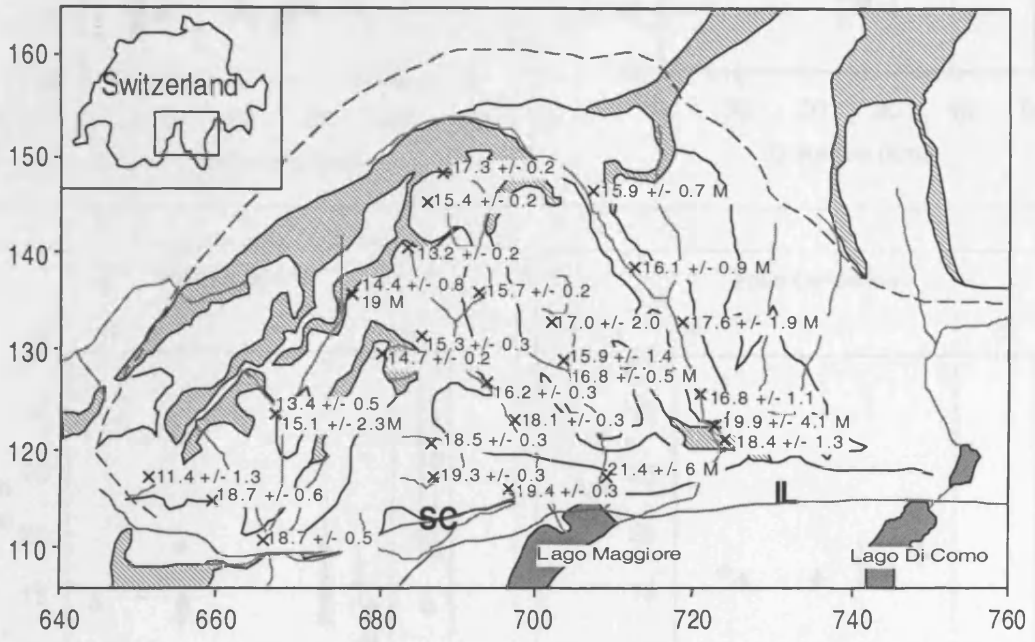

Figure 4.6 Map of the Lepontine Alps with muscovite and biotite Rb-Sr ages (in Ma) superimposed, locations are marked with × (from Armstrong *et* al., 1966; Jäger *et* al., 1967; Jäger, 1970; Wagner *et al.*, 1977; Steiner, 1984; Hurford 1986) from the basement gneisses (muscovite ages are denoted by M following the measured age). From west to east, the main north-south river valleys within the Lepontine Alps are Valle Antigorio, Valle Maggia, Valle Verzasca and Valle Leventina. For further details of the diagram, see Figure 1.1.

Figure 4.7 shows graphical representations of all the data plotted on Figures 4.5 and 4.6, separated into the four main north-south orientated river valleys. These representations show the spatial distribution, from north to south, of the measured ages. All four graphs (for different minerals and dating schemes) show an increase in age towards the Insubric Line and towards the northern part of the Lepontine area. The minimum ages tend to cluster between 20 and 30 km south of the 155 N gridline (zero on the *x*-axis of Figures 4.7 and 4.8). The Valle Maggia data will be examined more closely in Figure 4.8. Muscovite ages from this work fit well with previously measured ages (Valle Leventina and Valle Verzasca).

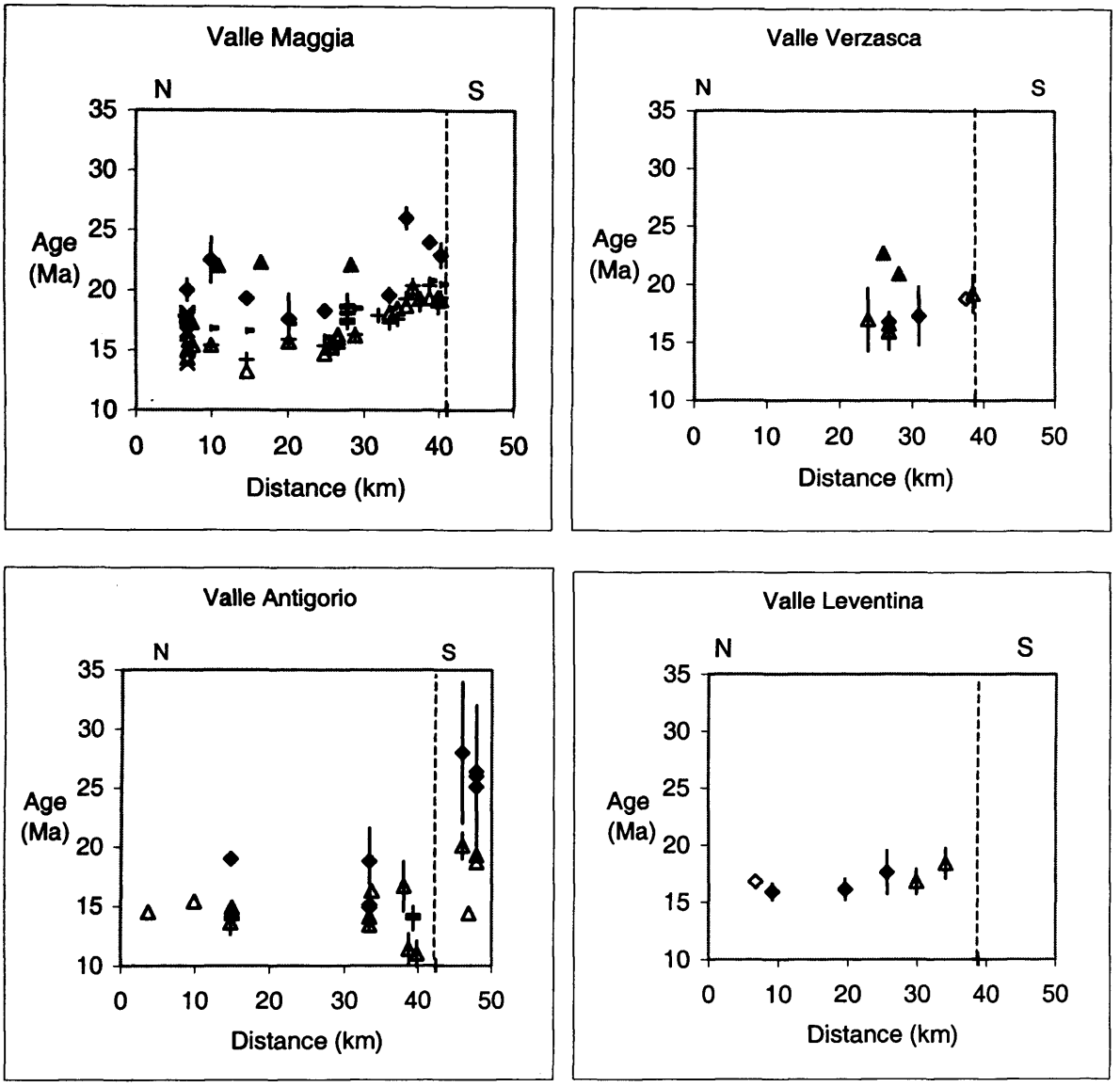

Figure 4.7 Graphical representations of measured mineral ages in Valle Maggia, Valle Verzasca, Valle Antigorio and Valle Leventina. Muscovite K-Ar, biotite Rb-Sr and biotite K-Ar data are from Hurford (1986); Steiner 1984; Jäger *et al.*, 1967 and Armstrong *et al.*, 1966 (where error bars are not shown, the error is within the size of the symbol). The dashed line marks the Insubric Line, the southern limit of the Lepontine Alps, and zero on the *x*-axis represents the 155 N gridline (Swiss National Grid). Key: Δ Biotite Rb-Sr; ♦ Muscovite Rb-Sr; ◊ Muscovite Rb-Sr (this work); — Phlogopite Rb-Sr (this work); × Phlogopite Rb-Sr (Jenkin *et al.*, 2001); + Biotite K-Ar; - Muscovite K-Ar; ▲ Monazite U-Pb (Köppel *et al.*, 1980).

Figure 4.7 shows two anomalously young biotite Rb-Sr ages in Valle Antigorio, (from Wagner *et al.*, 1997; $x = 40$), when compared with the overall trend, within the Lepontine Alps, of increasing measured ages towards the Insubric Line. These data points are from the west of Valle Antigorio and the micas may have been subjected to re-activation by movement on the Simplon-Centovalli fault, which has experienced movement since ~35 Ma to ~3 Ma (Selverstone, 1999).

Figure 4.8 shows the age data for Valle Maggia, without the muscovite Rb-Sr data, for clarity. The monazite U-Pb data are from Köppel *et al.* (1980) and date the onset of cooling in Valle Maggia; these data are consistently around 22 Ma for the northern and central parts of Valle Maggia. The Hurford (1986) data show the oldest muscovite and biotite K-Ar and biotite Rb-Sr

ages at the Insubric Line, which decrease towards central Valle Maggia and increase again in the north. These older Rb-Sr muscovite and biotite ages imply that cooling started earlier in the north and south when compared to the central region of Valle Maggia. A similar increase in age towards the south can be found in the data for the other river valleys (Figure 4.7). Cooling rates appear to be faster in the central region of Valle Maggia with minerals cooling through their closure temperatures at similar ages.

Figure 4.8 shows an apparently anomalous age, a phlogopite Rb-Sr age (from Jenkin *et al.*, 2001; $x = 6.8$), which is considerably younger than the other phlogopite ages and the biotite Rb-Sr ages in that region (all these data points come from Lago del Narèt, within 1 km of each other). This anomalous age is for a 120-160 μm grain size fraction, taken from the centre of the phlogopite band. All other phlogopite-calcite ages from this region have a minimum diameter of around 250 μm for their grain size fractions and have fairly consistent ages (Jenkin *et al.*, 2001 Table 6, and Table 4.2 in this work), suggesting this grain size fraction has undergone greater Sr loss. Phlogopite Rb-Sr ages are generally older than the biotite Rb-Sr ages, suggesting generally higher closure temperatures for phlogopite Rb-Sr, as predicted from crystal chemical data (Dahl, 1996).

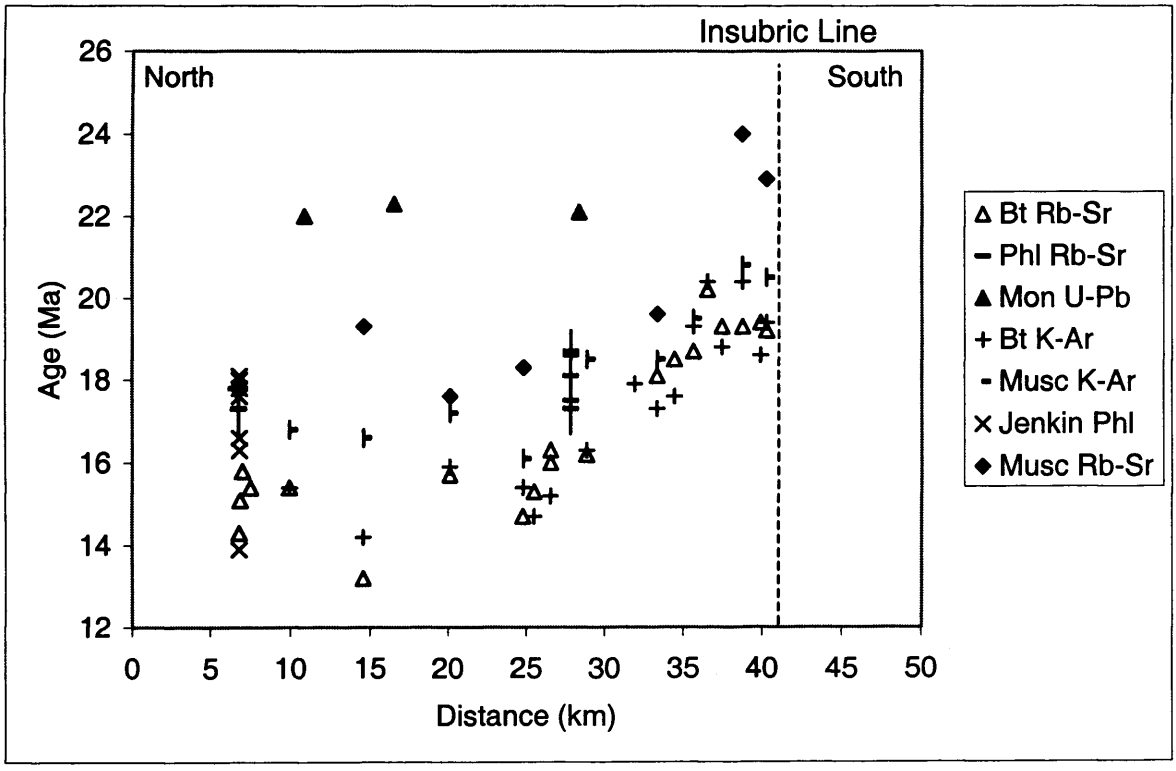

Figure 4.8 Graphical representation of measured mineral ages in Valle Maggia. Muscovite K-Ar, biotite Rb-Sr and biotite K-Ar data are from Hurford, 1986 and Steiner, 1984 (where error bars are not shown, the error is within the size of the symbol, i.e. 0.2 Ma or less); further phlogopite Rb-Sr data are from Jenkin *et al.*, 2001; Monazite U-Pb data are from Köppel *et al.*, 1980. Zero on the *x*-axis represents the 155 N gridline (Swiss National Grid).

Biotite K-Ar and Rb-Sr ages follow the same spatial distribution, although there appears to be a wider scatter in ages for Rb-Sr than K-Ar. This suggests that there may be more variability in

the Rb-Sr closure temperature than the K-Ar closure temperature. A possible reason for this is that any Ar produced diffuses faster (and may travel further into the surrounding rock) and therefore be more likely to undergo equilibration with an infinite reservoir, as in the Dodson (1973) model, giving more consistent closure ages. Figure 4.9 shows the diffusion of argon, rubidium and strontium through fluorophlogopite. Assuming biotite behaves in the same way as fluorophlogopite, these relationships should remain the same. Argon diffuses the most rapidly at all temperatures, with rubidium diffusing faster than strontium at very high temperatures, which changes at 1000 °C, so that strontium diffusion is faster. In micas, Rb replaces K in interlayer sites, both of which have similar ionic radii and ionic charges (1.49 and 1.38 Å respectively for a +1 charged ion), whereas the strontium ion has a much smaller radius (1.16 Å) and has a different ionic charge (+2). The small size of the strontium ion means it is too small for the K site and allows rapid diffusion through the crystal lattice.

A larger range in Rb-Sr ages could also be due to the variability in the size of the reservoir with which the Sr can exchange. For Ar, exchange always takes place with an infinite reservoir, as the Ar does not partition into any other minerals and any Ar produced leaves the rock. However, Sr may exchange between different minerals within the rock, such as calcite, K-feldspar and plagioclase and the amount of exchange that takes place depends upon how much of each mineral is present and their respective Sr concentrations (Jenkin *et al.*, 1995).

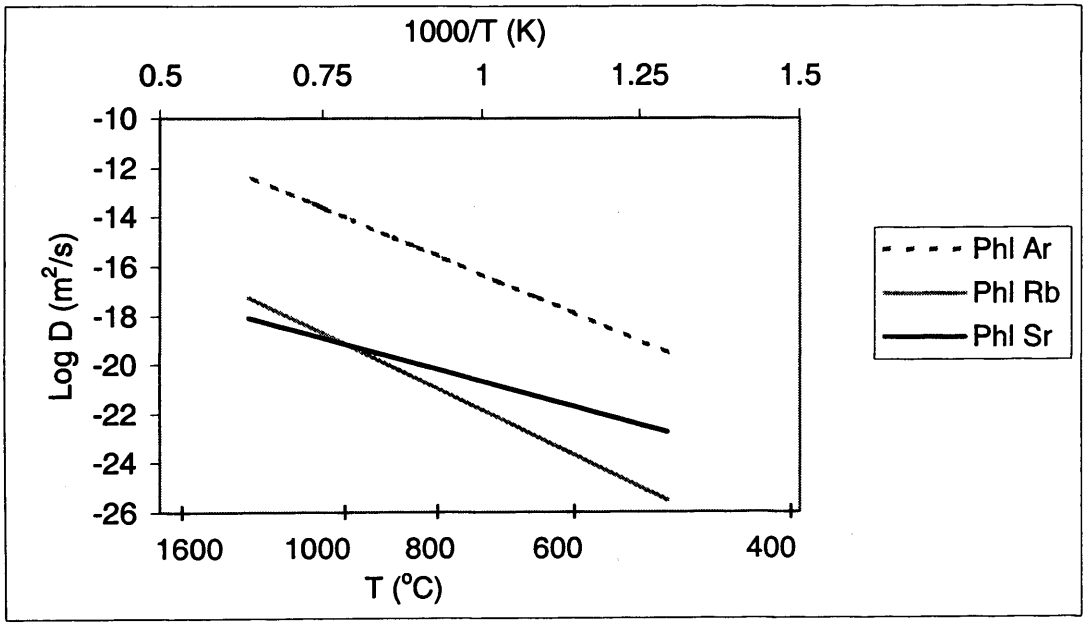

Figure 4.9 Arrhenius plot to show the relative diffusivities of argon, rubidium and strontium in fluorophlogopite. The Arrhenius relations are from Hammouda & Arnaud (in press), Hammouda & Cherniak (in press) and Hammouda & Cherniak (2000) respectively.

4.2.2 *The Age-Grain Size Relationship (A Dissolution Experiment)*

Whole grains of phlogopite were separated from HT23 (which contains calcite and phlogopite only, see Appendix 1), by dissolving the calcite in ethanoic acid. This experiment

contrasts with the bulk mica samples (Table 4.2) analysed are for micas from bulk, crushed samples and separated using a magnetic separator. For details of the experiment see Appendix 2.

The phlogopite collected from the dissolution was sieved to give grain size fractions, which were dated using Rb-Sr. The ages for the HT23 phlogopite separates are given in Table 4.2 and these are plotted against their respective grain size fractions (Figure 4.10; see Appendix 2 for details of the grain size fractions and the determination of the mean grain size). The model Sr closure temperature in biotite appears to be higher than that in phlogopite (Figure 4.10), although both of these should be viewed as semi-empirical due to the assumptions in producing the diffusion coefficients and therefore could be incorrect, although the general shape would remain the same.

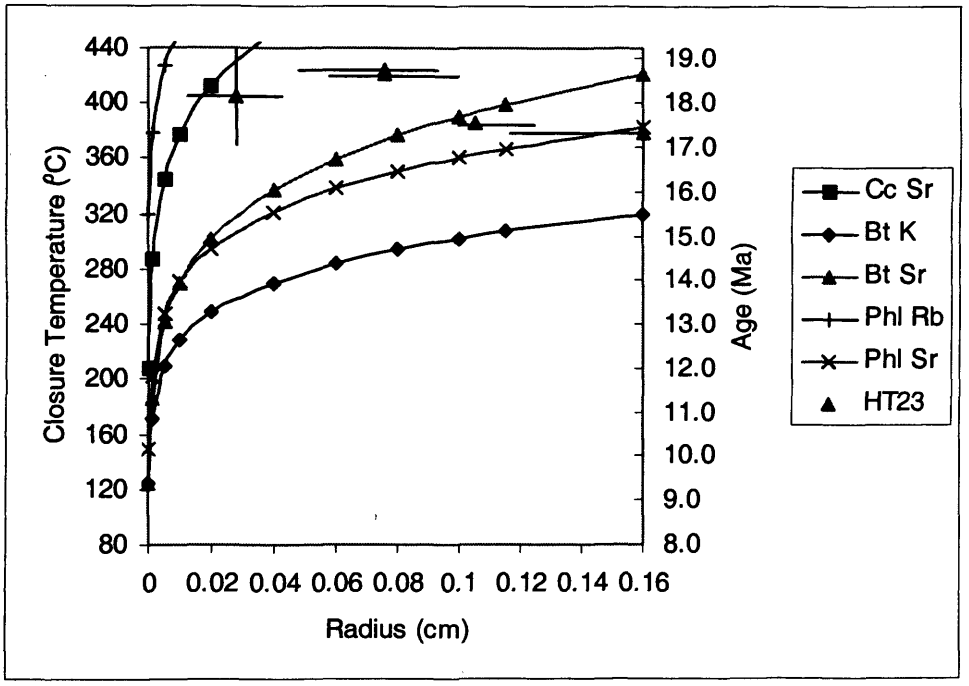

Figure 4.10 Rb-Sr ages for HT23 phlogopite separates. The grain size fraction is plotted against the measured age. The ages for HT23 are plotted against the weighted mean for the grain diameter and the error bars represent the variation in the diameter for the grain size fraction. The diffusion coefficients used in calculating the closure temperatures are from Amirkhanov *et al.* (1978) for biotite K, Cherniak (1997) for calcite Sr, Hammouda & Cherniak (2000) for phlogopite Sr, Hammouda & Cherniak (in press) for phlogopite Rb and Jenkin (1997) for biotite Sr. The curves on Figure 4.8 show biotite, phlogopite and calcite closure temperatures and phlogopite closure ages as a function of grain size for a Dodson (1973) infinite reservoir model for Sr diffusion. The calcite model assumes spherical grains and the mica models assume the grains behave as infinite cylinders. The closure age (t_c) is related to the calculated closure temperature (T_c) using the temperature (T_i) and time (t_i) of metamorphism (after Jenkin *et al.*, 2001): $t_c = t_i - [(T_i - T_c)/(dT/dT)]$, where T_i = 625 °C, t_i = 25 Ma and dT/dt = 32 °C/Ma, the overall cooling rate for Valle Maggia, calculated from Hurford (1986). However, as the cooling rate itself is partly dependent upon on assumptions about the closure temperatures of micas, the positions of these curves may only be considered as approximations, although the general form of the curves should not be affected.

The phlogopites do not show a simple age-grain size relationship, with ages increasing, then decreasing with decreasing grain size (Figure 4.10). The coarsest grains give an age of ~17 Ma, which increases to ~18.7 Ma in the 200-300 μm grain size fraction. The ages for the larger grain size fractions are anomalously low and are not within error of either of the modelled mica Sr

curves. However, there is an increase in age in the intermediate grain size fractions and these are close to the Sr biotite and phlogopite curves and an anomalously old age in the finest grain size fraction. An increase in age with decreasing grain size is unexpected, according to the Dodson (1973) model.

Figure 4.11 tries to determine the cause of age changes between the phlogopite grain size fractions. From the decay equation (Equation 2.2), an increased $^{87}Sr/^{86}Sr$ ratio or a lowered $^{87}Rb/^{86}Sr$ ratio (or a combination of these two factors) promotes increased measured ages.

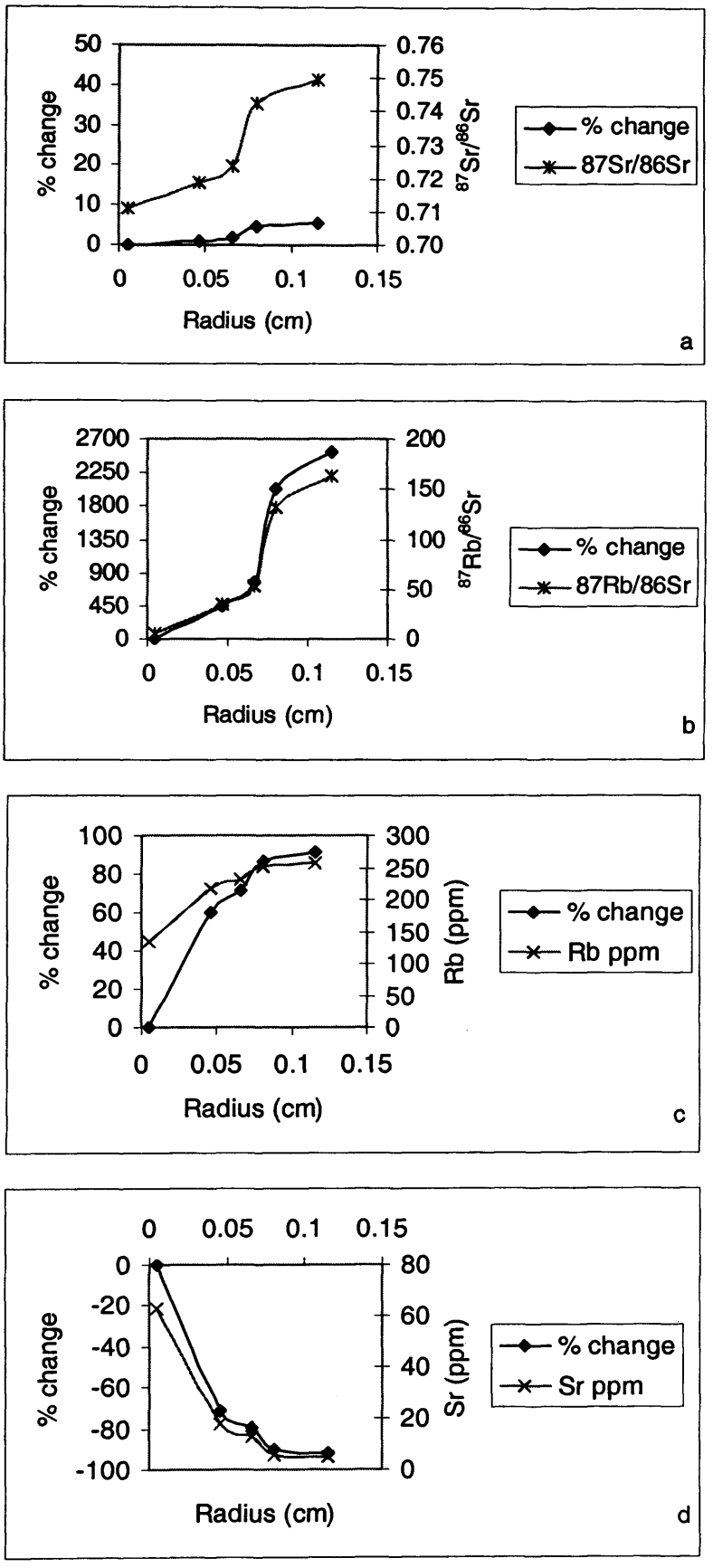

Figure 4.11 Graphs to show the variation in **a** $^{87}Sr/^{86}Sr$, **b** $^{87}Rb/^{86}Sr$, **c** Rb concentration and **d** Sr concentration for the HT23 mica grain size separates. The percentage change in all these graphs is plotted relative to the value for the smallest radius of the grain size fraction (sieve measurements).

Figure 4.11a shows the variation in $^{87}Sr/^{86}Sr$ with grain size. The percentage change shows that the $^{87}Sr/^{86}Sr$ ratios are relatively constant between the grain size fractions; however, there is a slight increase in $^{87}Sr/^{86}Sr$, which corresponds with the youngest measured ages for HT23 (those from the largest grain size fractions). Figure 4.11b shows the variation in $^{87}Rb/^{86}Sr$ with grain size. The percentage change shows that the $^{87}Rb/^{86}Sr$ ratio varies widely between the grain size fractions, with a massive decrease in Rb concentration for the oldest ages recorded. Both the percentage change and the actual $^{87}Rb/^{86}Sr$ ratios show a decrease, which corresponds with the oldest measured ages for HT23, suggesting the $^{87}Rb/^{86}Sr$ ratio is controlling the measured age. The $^{87}Rb/^{86}Sr$ ratio depends upon the relative concentrations of Rb and Sr. The reduction in the $^{87}Rb/^{86}Sr$ ratio corresponds with a decrease in Rb concentration and an increase in Sr concentration. The reduction in Rb concentration (Figure 4.11c) for the oldest measured ages is coincident with a slight decrease in $^{87}Sr/^{86}Sr$ (Figure 4.11), reducing the amount of ^{87}Rb more than the decrease in ^{87}Sr, so that the apparent age increases (similar to results from Jenkin *et al.*, 2001). The loss of ^{87}Rb must have occurred during cooling, since loss of Rb prior to cooling would result in lower production of ^{87}Sr and there would be no effect on the age. The loss of Rb may be a retrograde chemical exchange effect, which will be examined in Chapter 6. Figure 4.12 suggests that the largest grains are most able to retain their Rb, implying that Rb may be lost *via* diffusion from the edges of grains. These graphs may also reflect that there has been two generations of mica growth as there seems to be two trends in the data, one for the larger grains and one for the smaller grains.

Table 4.3 gives the Rb-Sr data for leaches from the dissolution experiment, showing that Rb is undetectable in the leaches, implying Rb is not lost during the dissolution.

Table 4.3 Rb-Sr data for leaches from the dissolution experiment.

	Rb (ppm)*	Sr (ppm)#	$^{87}Rb/^{86}Sr$	$^{87}Sr/^{86}Sr$
HT23 (1)	0.01	6	0.004817	0.710005±8
HT23 (2)	0.01	3	0.003333	0.709852±10

* Rb was undetected, so a value of 0.01 has been assumed.
\# 1 ml of ethanoic acid was used for each of the analyses. A value of 8 ppm in the leach would reflect a value of 416 ppm in the calcite.

Jenkin *et al.* (2001) give results for phlogopite-calcite separates from Lago del Narèt, with Rb-Sr ages ranging from 16.6 ± 0.2 to 18.0 ± 0.2 Ma within sample I.29 (Figure 4.12). Jenkin *et al.* (2001) also show that ages vary within the same outcrop, with phlogopite samples from less than 15 m away giving Rb-Sr ages as low as 13.9 ± 0.1 Ma; data from this study for Lago del Narèt are presented in Table 4.2 and fit within the age range quoted in Jenkin *et al.* (2001). The range of ages found by Jenkin *et al.* (2001) at Lago del Narèt and at Someo (Figure 4.12), in this study, suggests that a single value for the closure temperature of the phlogopite Rb-Sr system is incorrect.

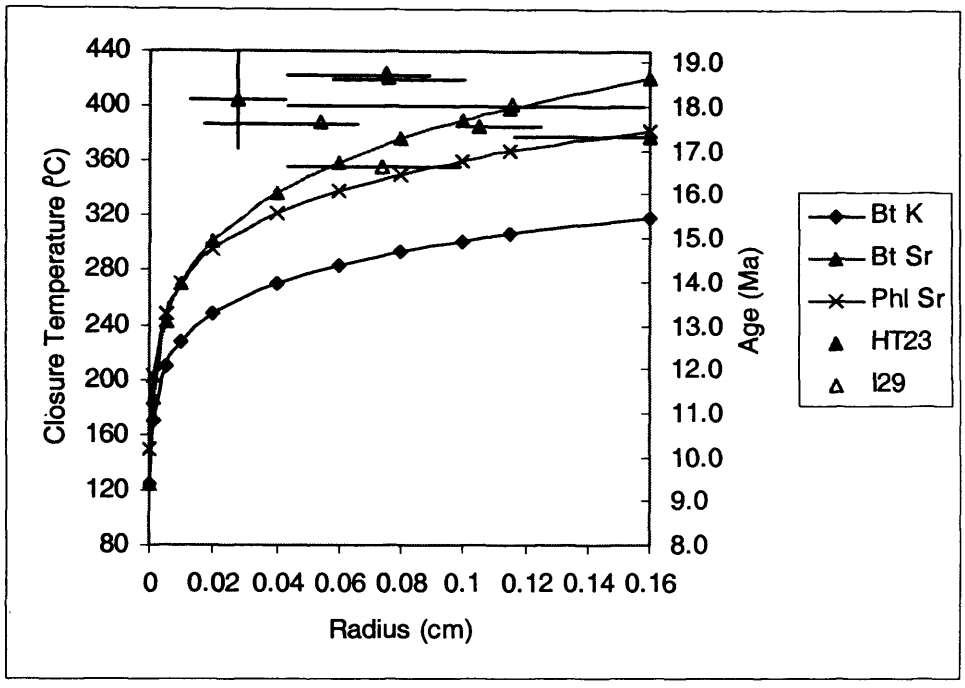

Figure 4.12 Rb-Sr ages at Someo (HT23) and at Lago del Narèt (I.29 from Jenkin *et al.*, 2001) for phlogopite separates. The grain size fraction is plotted against the measured age. The ages for HT23 are plotted against the weighted mean for the grain radius and the error bars represent the variation in the grain size fraction. The curves are as those used in Figure 4.8.

HT23 and I.29 come from different areas and have undergone different peak metamorphic conditions and subsequent cooling rates (see Sections 3.3.3, 3.3.4 and 3.3.5). This may partly explain the differences in the measured ages, as according to the Dodson (1973) closure temperature equation partly depends upon the cooling rate. Most of the measured ages are very similar to each other, although not within error (errors are ± 0.2 Ma, which are within the limit of the symbols, unless shown).

Jenkin *et al.* (1995) suggest an alternative to the Dodson (1973) closure temperature model, using a closed system Rb-Sr model. The Jenkin *et al.* (1995) model suggests that the closure temperature for a mineral pair will be between the Dodson (1973) closure temperatures of the two minerals in question, depending upon the proportions and Sr contents of the two phases. For a mica-calcite pair, the closure temperature would only equal the Dodson (1973) mica closure temperature for a low mica/calcite ratio and low $[Sr]_{mica}/[Sr]_{calcite}$ (Jenkin *et al.*, 2001). These conditions are met in this sample (HT23 contains phlogopite and calcite only, with $[Sr]_{mica}/[Sr]_{calcite} \approx 0.01$) suggesting the Rb-Sr dates should lie on or close to the Dodson (1973) mica Sr closure temperature curves. Figures 4.10 and 4.12 show the Rb-Sr ages clustering around the Sr biotite and phlogopite curves, although often these data are not within error of the Dodson curves, implying that the Dodson closure temperature model is incorrect.

4.2.3 *Implications of Rb-Sr Data*

The phlogopite-calcite and muscovite-calcite Rb-Sr ages are consistent with trends found in the previously published data (Figures 4.6 to 4.8). The phlogopite-calcite ages are older than the

biotite gneiss ages suggesting the phlogopite Sr closure temperature is higher than the biotite Sr closure temperature. However, the modelled curves (after Dodson, 1973) suggest that the biotite Sr closure temperature is higher than the phlogopite Sr closure temperature (Figures 4.10 and 4.12), although the biotite Sr data are an estimate (from Jenkin, 1997), which may be inaccurate. The modelled closure temperature curves can be discounted as the general cooling rate used in the calculation is itself partly dependent upon assumptions about the closure temperatures of micas and the positions of these curves may only be considered as approximations (although their relative positions will remain the same, if the diffusion data are correct).

The difference between the biotite and phlogopite Rb-Sr ages could also be due to a mineral mode effect. Samples from Hurford (1986) are mainly biotite / muscovite feldspar gneisses, samples of Matorello gneiss from Steiner (1984a), described in Steiner (1984b), contain biotite, hornblende, K-feldspar, quartz and epidote ± plagioclase ± titanite ± zircon. Whereas the phlogopite separates, in this study, come from marbles, which contain varying amounts of calcite ± quartz ± K-feldspar ± muscovite ± dolomite ± apatite ± plagioclase. Steiner (1984b) gives whole rock and mica Sr concentrations, for the samples around Lago del Narèt, which suggest that biotite contains ~ 5 % of the Sr present. From the same region, in the marbles from this study, the phlogopite present contains 0 and 0.8% of the Sr in HT15 and HT17 respectively. Differing rock types, from the same region, are producing different mica ages suggesting that the mineral mode and Sr content is an important factor in producing a closure temperature age. In these marble samples, the majority of the strontium resides in the calcite, whereas in the gneiss samples any strontium present resides in the feldspars and micas. Also different minerals have different diffusion characteristics and therefore, cause variations in closure temperature (as discussed in Chapter 2). Jenkin *et al.* (1995) have shown that in bi-mineralic rocks with the same cooling histories, but with distinct mineral modes, the age difference can be > 100 Ma for slowly cooled rocks. All other things being equal the rock which has a smaller percentage of its Sr in the mica, will produce a lower age.

The phlogopite data show a range of ages within individual samples, as shown in Section 4.2.3. This range of ages is inconsistent with the assumption that the biotite/phlogopite closure temperature for the Rb-Sr is 300 °C, or any single temperature. Part of this variation may be attributed to grain size. However, Section 4.2.3 suggests that the age-grain size relationship is not as straightforward as Dodson (1973) implies. Dodson (1973) suggests that closure temperature and measured age should decrease with grain size and this appears to be correct (Figure 4.5) with mica separate ages clustering around the phlogopite and biotite Sr curves, although not always within error.

4.3 Summary

Petrological, cathodoluminescence and carbon and oxygen stable isotope data suggest that the samples being studied have not been affected by fluid infiltration or the exchange of isotopes

with fluids. This implies that the down-temperature isotopic and chemical exchange effects examined in Chapters 5 and 6 occur with little or no fluid present.

Table 4.2 quotes measured phlogopite-calcite Rb-Sr ages. These measured ages are demonstrably lower than the ages thought to represent onset of cooling from the peak of metamorphism (~ 25 Ma for Lago del Narèt, in the north of the Maggia nappe; after Hurford, 1986) implying loss of ^{87}Sr from the phlogopite (in order to produce a lowered measured age). This fits with the measured diffusion data of Hammouda & Cherniak (2000 and in press) who suggest that Sr diffusion is faster than Rb diffusion in fluorophlogopites (Figure 4.9).

Figures 4.3 and 4.4 show phlogopite and biotite gneiss Rb-Sr ages. The differences between these ages can be explained if phlogopite has a higher Sr closer temperature than biotite (due to mineral composition effects) or by rock mineral mode differences (Section 4.2.4, after Jenkin *et al.*, 1995).

Figure 4.10 shows that there is an age – grain size relationship for the mica Rb-Sr system, although this relationship may not be as straightforward as Dodson (1973) suggests. The anomalies present (increased measured age with decreasing grain size) correspond with a decrease in Rb concentration in the mica. The preferential loss of ^{87}Rb over ^{87}Sr could cause the increase in apparent age seen with decreasing grain size. However, this does not fit with the diffusion data for synthetic fluorophlogopite (Hammouda & Cherniak; 2000 and in press), which suggest Sr diffuses more rapidly, making phlogopite more susceptible to Sr loss, except at very high temperatures. Any loss of Rb must have occurred after the onset of cooling, otherwise there would be a corresponding reduction in ^{87}Sr production and therefore, a lower measured age. The mica separate ages lie close to the Sr phlogopite and biotite curves (Figure 4.10), as suggested by the closed system model of Jenkin *et al.* (1995).

Chapter 5

Strontium Isotopic Exchange

5.1 Introduction

The low Rb-Sr closure temperatures of micas are thought to be due to down temperature re-equilibration of Sr isotopes *via* diffusion during cooling (Dodson, 1973; Giletti, 1991a and Jenkin *et al.*, 1995), however, recrystallisation or reaction with fluids may also contribute in some cases (see Section 2.3). Although diffusion is thought to be the dominant process controlling isotopic re-equilibration in the Rb-Sr system, the precise mechanism for producing closure ages is unknown. Dodson (1973) focused on the effect of volume diffusion within mineral grains, assuming equilibration with a hypothetical infinite reservoir. However, Jenkin *et al.* (1995) and Jenkin (1997) suggest the interdiffusion of Sr isotopes among minerals in a finite reservoir may be more realistic in the case of a closed system rock. As the mechanism of Sr isotope (^{87}Sr with ^{86}Sr) re-equilibration is poorly understood, our ability to make use of mica closure temperature ages is limited, making tectonic reconstructions from cooling curves unreliable.

This chapter will examine the exchange of Sr isotopes using LA-ICP-MS (Laser Ablation Inductively Coupled Plasma Mass Spectrometry) in two simple phlogopite-bearing marbles from the central Swiss Alps, in order to constrain the mechanism of isotopic exchange and, therefore, the process of isotopic closure in mica-bearing rocks. LA-ICP-MS traverses were completed across individual calcite grains to assess the impact of volume diffusion within grains. It is expected that the phlogopite in the samples will be the source for ^{87}Sr and this will exchange with ^{86}Sr present in the calcite. The mechanism for this exchange is expected to be a combination of volume and grain boundary diffusion (c.f. Jenkin *et al.* 1995) and the amount of exchange will be controlled by the mineral mode, the grain size and the Sr concentration of different minerals.

5.2 Samples Investigated

Two samples have been investigated for the effects of Sr isotope exchange, HT15 (from Lago del Narèt) and HT23 (from Someo, approximately 25 km south of Lago del Narèt) as shown in Figure 5.1.

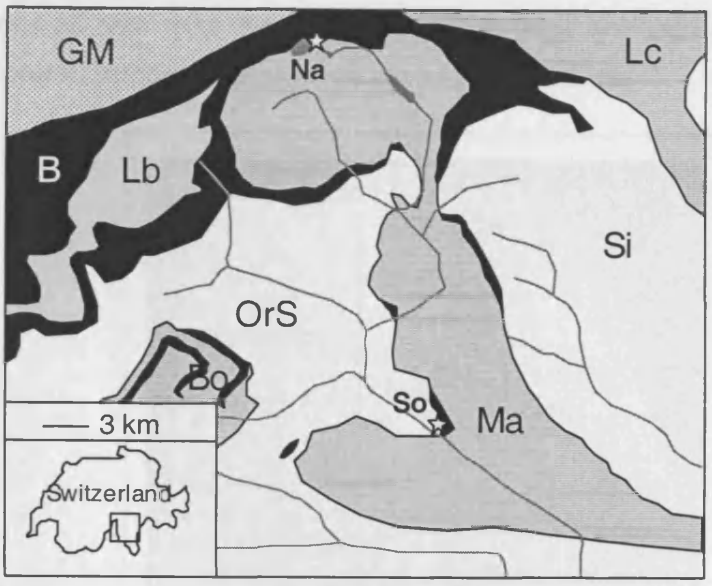

Figure 5.1 Location map for Someo (So) and Lago del Narèt (Na) showing the local Pennine nappes: Ma = Maggia, Bo = Bosco Series, Lb = Lebendun Series, OrS = Orsalia Series, Si = Simano, Lc = Lucomagno Gneiss and B = Bündnerschiefer (Mesozoic metasediments) and the Helvetic Gotthard Massif (GM). After Spicher (1980).

5.2.1 *Thermal History*

In the Lago del Narèt region, cooling starts at approximately 25 Ma (extrapolation to peak temperature of 575°C, Rb-Sr age measurements by Steiner (1984a) of 22.7 ± 2.0 Ma for muscovite and 16.5 ± 1.2 Ma for biotite in Jenkin *et al.*, 2001). Phlogopite-calcite Rb-Sr gives ages of 17-18 Ma (see Section 4.1), implying that more than 7 Ma of radiogenic ^{87}Sr has been lost from the phlogopites since the onset of cooling.

At Someo, the phlogopite-calcite Rb-Sr ages are around 17-18 Ma (see Section 4.1). Previous muscovite K-Ar and biotite Rb-Sr ages of 18.5 ± 0.2 and 16.2 ± 0.3 Ma respectively (Hurford, 1986) produce a cooling rate of 22 °C/Ma. Other cooling curves (Section 3.3.5) from the northern and central parts of the Maggia Valley, (Hurford, 1986 and 1991), show a sharp increase in cooling rate above 350 °C, suggesting an age of 23 Ma for the peak of metamorphism around Someo, which is consistent with the southward decrease in age of peak metamorphism of other studies. However, extrapolating the average of these cooling curves to the peak metamorphic temperature (Figure 3.7) suggests an age of ~28 Ma for the peak of metamorphism at ~625°C (after Todd & Engi, 1997). Köppel *et al.* (1980) give concordant monazite U-Pb ages of 20-30 Ma for the Central Alps, suggesting a metamorphic peak at this time. More details of the regional geology and isotopic work completed in this study can be found in Chapters 3 and 4 respectively.

5.2.2 *Samples*

HT23 is a calcite marble (calcite MgO = 1-4 wt%) with a 2 cm phlogopite / calcite band at the base which grades into calcite marble. Sections (Figures 5.2 and 5.3) are approximately 600

μm thick and cover an area from the phlogopite-calcite band into calcite-marble. Phlogopite averages 1 mm diameter, perpendicular to *c*, and calcite averages 5 mm.

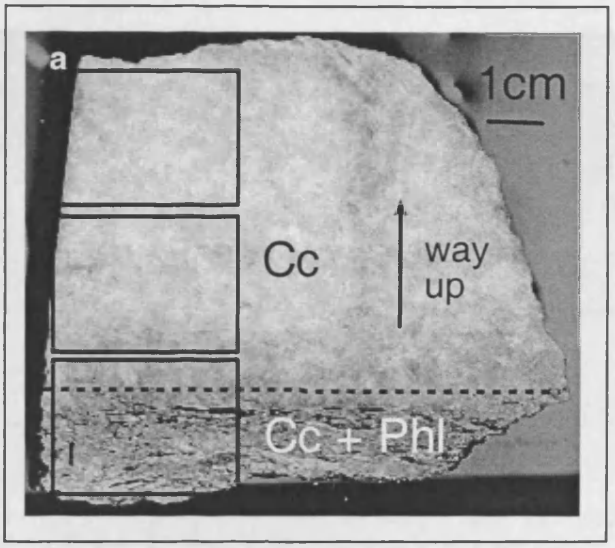

Figure 5.2 HT23, from Someo. The dashed line represents the margin of the phlogopite / calcite band, the rectangles define the area of the thick sections. The other margin of the phlogopite band lies close to the edge of the sample.

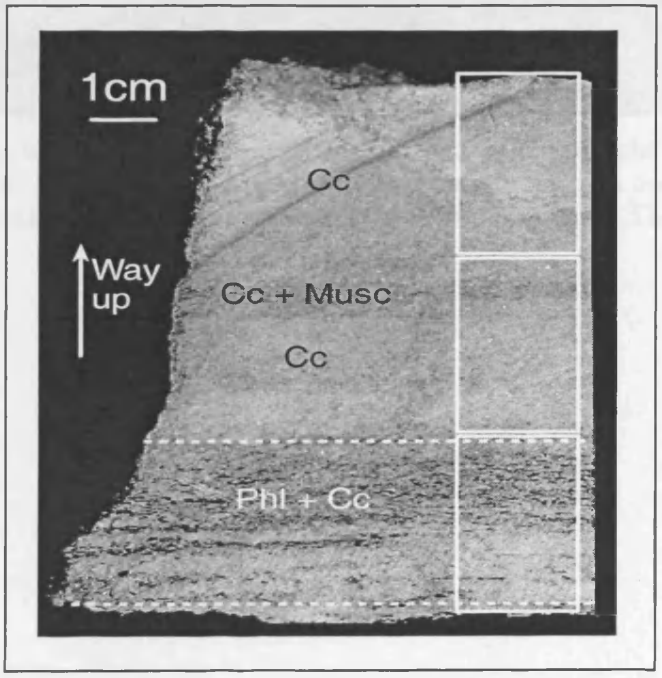

Figure 5.3 HT15, from Lago del Narèt. The dashed lines represent the boundaries of the phlogopite / calcite band, the rectangles define the area of the thick sections. In HT15, there is a thin muscovite band, this band never exceeds 3 mm thick and is discontinuous.

HT15 is a calcite marble (calcite MgO = 1-3 wt%) with a 3.6 cm phlogopite / calcite band near the base with a minor muscovite layer 3 cm away from the phlogopite band (Figure 5.7). There are also minor amounts of K-feldspar (4%) and quartz (3%) scattered throughout the sample. Cathodoluminescence imaging shows that minor dolomite exsolution has occurred, but no grains of

dolomite have been found in the sample. Calcite grains are 1-2 mm across, quartz and K-feldspar average 0.5 mm, phlogopite averages 1 mm diameter and muscovite 0.6 mm, perpendicular to *c*.

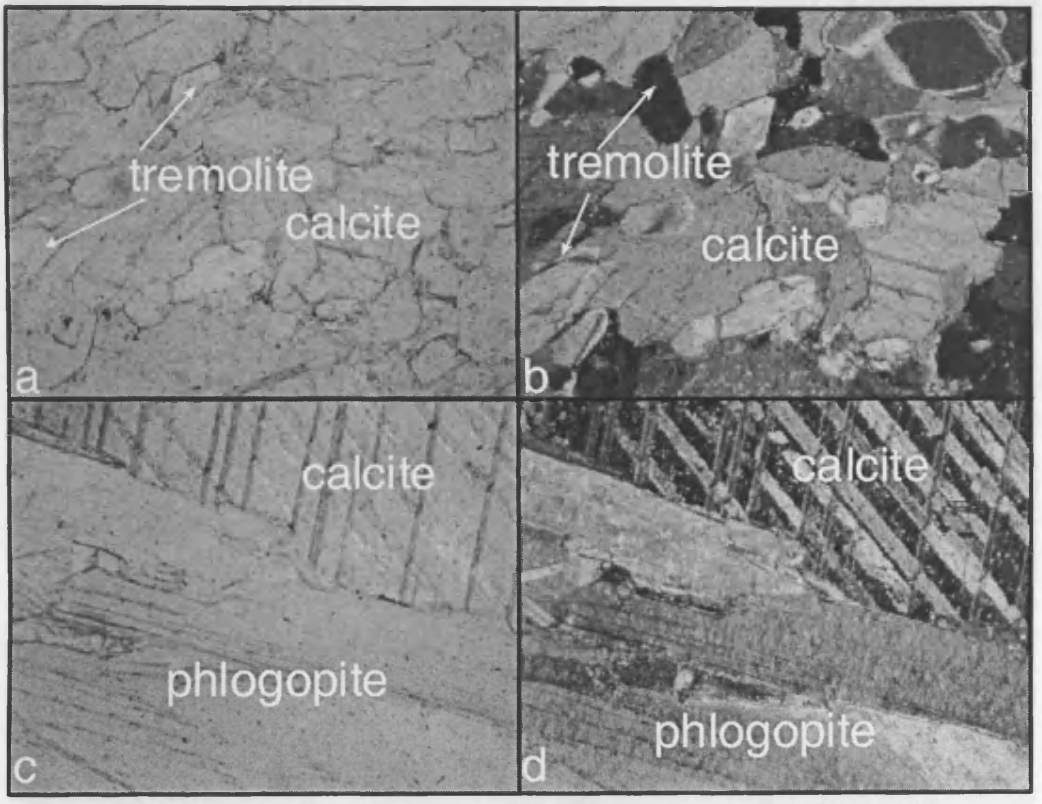

Figure 5.4 Photomigraphs of HT23 in plane polarised and cross-polarised light. 5.4a and b show calcite with small grains of tremolite, these grains are found outside the area used to produce the $^{87}Sr/^{86}Sr$ profiles in the calcite. 5.4 c and d show one side of the mica band. The field of view is approximately 3 mm.

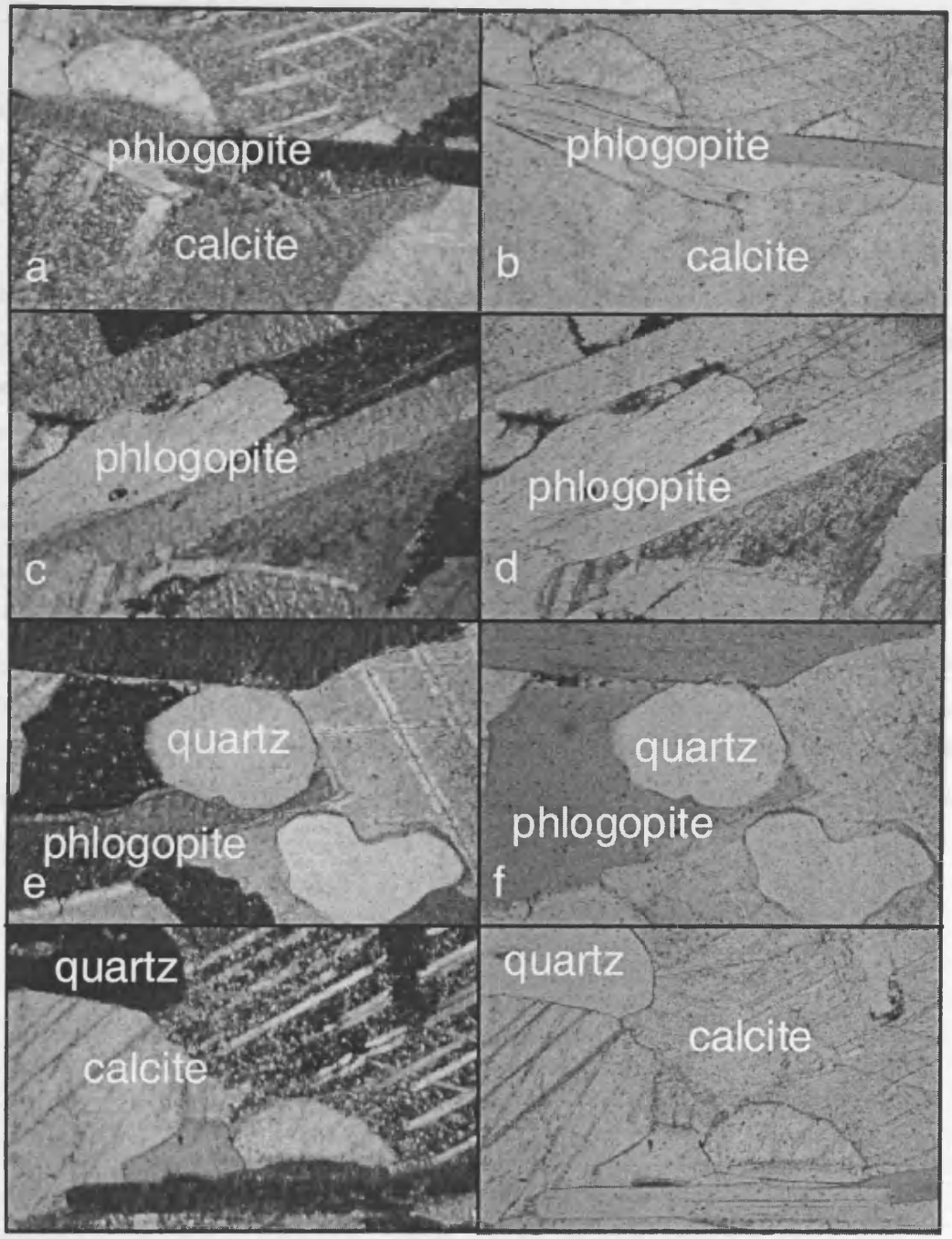

Figure 5.5 Photomigraphs of HT15 in cross-polarised and plane polarised light. 5.5a, b, c and d show calcite and phlogopite. 5.5e, f, g and h show calcite, phlogopite and quartz. The field of view is approximately 3 mm.

5.3 The LA-ICP-MS Technique

The applications of multi-collector LA-ICP-MS are discussed in Halliday *et al.* (1998) and further details of Sr analysis by LA-ICP-MS can be found in Christensen *et al.* 1995 (with reference to feldspars) and in Appendix 3. Other strontium isotope studies have been completed on marine carbonates and these include; Putten *et al.* (2000) on *Mytilus Edulis*, Sinclair *et al.* (1998) on modern corals and Bailey (2001) on belemnites for the Sr seawater curve in the Jurassic.

5.3.1 *Advantages of LA-ICP-MS*

LA-ICP-MS is a relatively new technique, but is increasingly replacing TIMS (thermal ionisation mass spectrometry) for precise isotope ratio measurements due to its sensitivity, precision, accuracy and high spatial resolution (Becker & Dietze, 2000). Laser ablation microsampling coupled with multi-collector ICP-MS requires little sample preparation and allows rapid analysis of solid-state samples (each analysis takes a few minutes). *In situ* analyses are conducted and these analyses can be related to each other spatially, in terms of rim *versus* core in individual grains and from one mineral grain to another, allowing the production of isotope ratio profiles. The samples used were thick, polished sections, however, blocks of clean hand specimen may also be used. The whole process is rapid compared to conventional geochemistry involving crushing, mineral separation, isotope dilution and then mass spectrometry. There is also less chance of sample contamination, although there may be scattered ablated particles in the sample chamber.

5.3.2 *LA-ICP-MS: Conditions and Precision*

For a full description of the apparatus, see Appendix 3. Analyses were carried out with a 266nm Nd: YAG UV laser at the NERC Isotope Geoscience Laboratory in conjunction with a static Faraday collection procedure on a VG Elemental P54 ICP-MS (see Table 5.1 for conditions). Ablation occurs in a sealed sample chamber and ablated material is entrained in an Ar gas stream, and then passed into the ionisation chamber.

Table 5.1 Conditions for LA-ICP-MS.

Parameter	Conditions
Sample	600 μm thick microprobe section
Laser energy	50% power (250 mJ)
Laser spot size	95 μm diameter
Dwell time	1 s
Mode	Line of spots or continuous raster
Scan speed	40 μms^{-1}
Laser pulse rate	10 Hz
Masses monitored	83, 84, 85, 86, 87, 88
Interferences	^{86}Kr on ^{86}Sr ^{87}Rb on ^{87}Sr

The analyses were completed as a line traverse of ablation spots, following a desired zonal region of the crystal, and the mean of all the ablation spots was taken to give the ratio for the analysis (and therefore, the zone). Where possible, several traverses were analysed, following the shape of the grain, from the rim to the core (Figure 5.6). At the centre of the grain a raster of spots was completed.

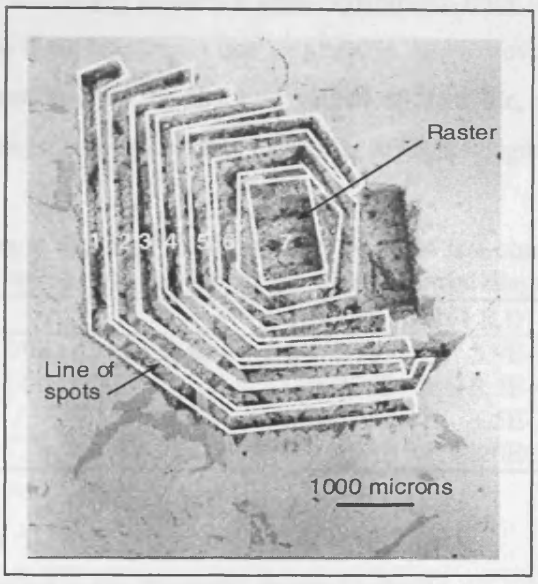

Figure 5.6 An example SEM image of laser ablation pits for grain 23-2A (2.5 mm from edge to centre of the raster). A concentric pattern for the analyses was used to achieve a large enough volume of ablated calcite for the individual analysis (approximately 0.06 mm^3 of carbonate was needed for each analysis). For this reason, fewer analyses were carried out on smaller grains and a raster of spots had to be completed at the centre of the grains. The numbers 1 to 7 refer to the analysis number (23)x, see Appendix 3; analyses 4 and 7 were aborted due to problems with the plasma.

The calcite samples analysed contain approximately 400 ppm Sr and each calcite analysis requires the ablation of approximately 0.06 mm^3 of sample (which contains approximately 60 ng Sr). Most analysis laser pits were 0.1 to 0.2 mm wide by 0.1 to 0.3 mm deep requiring a typical analysis length of 2 to 10 mm. For this reason, on smaller grains and towards grain cores on larger grains, the analysis took the form of a raster of spots, as a large enough volume of sample could not be achieved for the analysis by completing several concentric analyses. Throughout the analyses, ^{85}Rb was monitored to ensure no phlogopite or other Rb-bearing phases were analysed during the ablation (the background level of $^{85}Rb/^{86}Sr$ = 0.0067 for the NBS 987 standard solution and significant variation from this suggests analysis of a Rb-bearing silicate phase). The $^{87}Sr/^{86}Sr$ ratios were corrected for mass bias and Kr and Rb interferences (see Appendix 3).

Table 5.2 Standard data from all analyses performed. NBS 987 is the Sr standard and NBS 987/984 is a combined Sr and Rb standard, with their concentrations given in ppb.

Standard solution	$^{87}Sr/^{86}Sr$	± (1 S.D)	n
NBS 987 (100 ppb)	0.710260	4.9E-05	17
NBS 987 (200 ppb)	0.710277	2.8E-05	47
NBS 987 (300 ppb)	0.710314	1.6E-05	15
NBS 987/984 (200/42 ppb)	0.710153	5.5E-05	8

Throughout the analyses the NBS 987 standard solutions were used to check the consistency of the measurements, with a standard analysed after every fourth analysis; the actual value of the Sr standard is 0.71024 (NIGL laboratory results). The measured standard gave 0.71028 (Table 5.2) and results remained stable throughout the analyses, with errors in the fifth place, and analyses were therefore corrected to the NBS 987 value (0.71024). The disagreements between the

two standard values (Table 5.2) imply there is a small systematic error in the Rb correction, which may arise from errors in the mass bias correction (Appendix 3). However, as the analyses are used in examining a trend and not strictly for absolute values of $^{87}Sr/^{86}Sr$, and as the calcite samples studied contain very little Rb (< 1 ppm Rb), this particular error is insignificant (Table 5.3).

Table 5.3 Standard and sample data for $^{87}Rb/^{86}Sr$. NBS 987/984 is a combined Sr and Rb standard, with their concentrations given in ppb. See Appendix 3 for isochron diagram and discussion.

	$^{87}Rb/^{86}Sr$	± (1 S.D)	n
NBS 987/984 (200/42 ppb)	5.160565	3.9E-3	8
NBS 987 (100 ppb)	0.002782	8.3E-4	15
HT15	0.163989	1.5E-1	42
HT23	0.011381	3.0E-3	22

5.4 LA-ICP-MS Traverses

The Sr isotope traverses were measured perpendicular to the mica band and assuming this band is continuous, this reduces the geometry to one dimension. Sr isotopes were measured within individual grains across the sections to examine the change in $^{87}Sr/^{86}Sr$ ratio with distance from the phlogopite band. Assuming the two samples described in this chapter have operated as closed systems (Section 4.1.2) the phlogopite will only be able to exchange Sr isotopes with other minerals in the sample. All these Sr-bearing phases have estimated closure temperatures greater than the phlogopite closure temperature for Sr isotope exchange (Section 2.4.3) so the effective phlogopite closure temperature will correspond with the next highest mineral Rb-Sr closure temperature (an assumption from Giletti, 1991a). However, in contrast, Jenkin *et al.* (1995) predict that for phlogopite surrounded by a large volume of calcite, the effective phlogopite closure temperature is the same as the closure temperature for phlogopite in an infinite reservoir.

It is likely that ^{87}Sr and ^{86}Sr are exchanging between the phlogopite band (where ^{87}Sr is produced) and calcite grains; in both samples calcite represents a large proportion of the specimen, so would be a good candidate as an infinite reservoir for ^{87}Sr during cooling. In both HT23 and HT15 calcite provides 99.9% of the total Sr present in the rock. However, other Rb bearing phases are potential sources for radiogenic ^{87}Sr; in HT15 these are muscovite and K-feldspar.

5.4.1 *Theory*

Figure 5.7 shows a first approximation of results expected from Sr isotope exchange within a single calcite grain. After diffusion has occurred, there will be high $^{87}Sr/^{86}Sr$ at the rim of the grain and low $^{87}Sr/^{86}Sr$ in the core. It is expected that the isotopic profiles in phlogopite will show the opposite effects with low $^{87}Sr/^{86}Sr$ rims and high $^{87}Sr/^{86}Sr$ cores as, in a closed system, the ^{86}Sr must be diffusing in the opposite sense, although there may be more complex zonation as diffusion through mica is anisotropic (diffusion perpendicular to the *c-axis* is expected to be faster than diffusion parallel to the *c-axis,* Giletti 1991b; Hammouda & Cherniak, 2000).

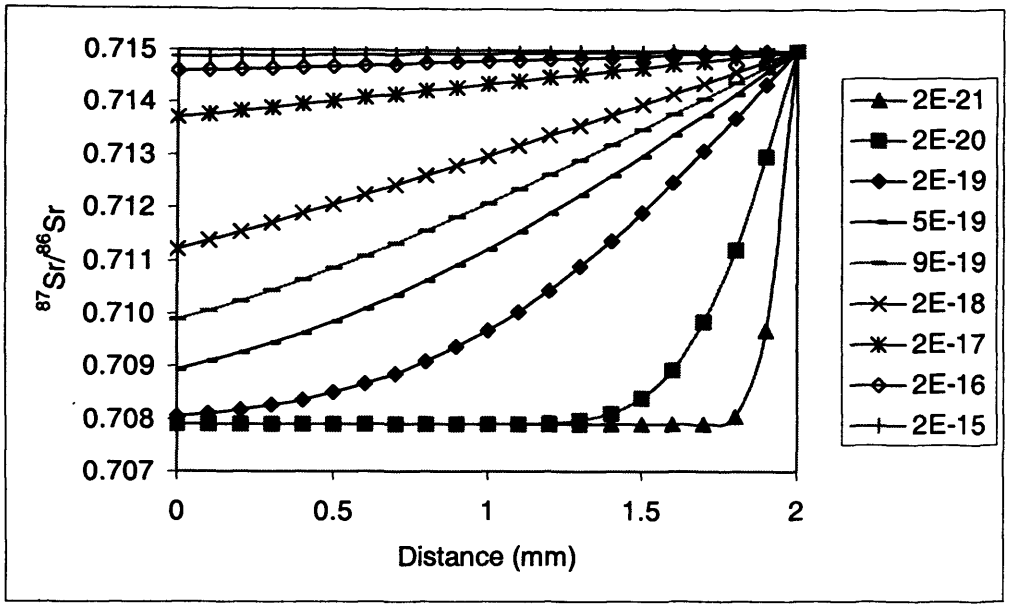

Figure 5.7 Predicted results for Sr isotope exchange within single 4 mm diameter calcite grains (zero being the centre of the grain) using the Crank (1975, number 6.60) equation for diffusion in a sphere, assuming ^{87}Sr is supplied by an infinite reservoir. As calcite should gain ^{87}Sr from the phlogopite, it is predicted that there will be high $^{87}Sr/^{86}Sr$ at the rims and they may initially have Triassic carbonate values towards the cores of calcite grains (around 0.7075 to 0.7079, Koepnick *et al.*, 1990). The rim value is based upon the production of 5 Ma of ^{87}Sr in a phlogopite grain ($^{87}Rb/^{86}Sr = 104$) adjacent to the calcite, assuming all the ^{87}Sr produced leaves the mica and that the mica $^{87}Sr/^{86}Sr$ does not change throughout the period of diffusion. The curves are denoted by the diffusion coefficient used in their calculation, at 600 °C; Cherniak (1997) gives a diffusion coefficient of 2×10^{-21} m^2s^{-1}.

The kind of variation shown in Figure 5.7 may be expected in grains close to the phlogopite band (high at the rim, with low values towards the core). For this model, even with rapid diffusion (Figure 5.7), there is a marked difference in $^{87}Sr/^{86}Sr$ between the rim and the core of the grain.

With greater distance from the phlogopite band, there may be less variation from the rim to the core (i.e. the whole profile will display values closer to bulk calcite from pure marble layers) of the grain as, assuming a combination of volume and grain boundary diffusion in metamorphic rocks, Sr isotopic exchange is expected to operate over a length-scale of millimetres to centimetres in the order of 10^6 years (Joesten, 1991). For example, a grain further away from the phlogopite band may only display the effects of 1 Ma addition of ^{87}Sr (i.e. have a lower rim value), as a grain further away will receive less ^{87}Sr, even though diffusion has been occurring for 6 Ma.

At a certain distance from the phlogopite band, no Sr diffusion effects will be seen and the grains should equal bulk calcite values. If no previous diagenetic effects or equilibration have occurred, the calcite should approach Triassic values ($^{87}Sr/^{86}Sr$ 0.7075 to 0.7079; Koepnick *et al.*, 1990), as the original limestones, which now form the marble outcrops, are Triassic in age (see Chapter 3).

5.4.2 *Grain Traverses*

Traverses were completed across individual calcite grains to assess the impact of volume diffusion within grains (Figure 5.6). From the rim to the core, adjacent analyses are within error of each other (Figure 5.8) and do not show a systematic variation as predicted from volume diffusion (Figures 5.7) across the grains within the limit of the precision. The average $^{87}Sr/^{86}Sr$ ratios, of all the zones in individual grains, are reported in Table 5.4, with errors propagated from the analyses.

Table 5.4 Bulk calcite laser ablation ICP-MS data[a].

Grain	Distance (cm) from centre of mica band	Average $^{87}Sr/^{86}Sr$	Propagated Standard Deviation (1 SD)[b]	Standard Deviation of means (1 SD)	Number of zones in the grain
23-1, C	-0.5	0.70941	4E-5	4E-5	1
A	-0.2	0.70942	4E-5	8E-5[c]	6
B	0.3	0.70944	5E-5	7E-5[c]	3
F	0.5	0.70929	5E-5	5E-5	2
G	1.1	0.70894	5E-5	1E-4[c]	2
I	1.3	0.70880	6E-5	6E-5	1
H	1.5	0.70849	6E-5	6E-5	1
23-2, C	1.9	0.70847	4E-5	4E-5	4
B	2.8	0.70845	6E-5	5E-5	4
A	3.9	0.70841	3E-5	5E-5	5
15-1, G	-1.6	0.71578	7E-4	5E-3[c]	2
F	-1.4	0.71599	6E-4	2E-3[c]	2
H	-0.5	0.71612	4E-5	4E-5	1
I	0.0	0.71616	4E-5	7E-5[c]	2
C	1.0	0.71594	6E-5	6E-5	1
B	1.5	0.71588	4E-5	4E-5	1
15-2, A	2.1	0.71565	5E-5	1E-4[c]	2
B	2.6	0.71525	4E-5	4E-5	1
C	3.2	0.71510	4E-5	4E-5	1
D	3.6	0.71510	3E-5	3E-5	1
F	4.6	0.71488	4E-5	4E-5	1
G	5.1	0.71497	3E-5	3E-5	1
H	5.4	0.71494	4E-5	5E-5[c]	2
15-3, A	5.8	0.71475	7E-5	7E-5	1
B	6.0	0.71471	7E-5	7E-5	1
D	7.0	0.71470	6E-5	4E-5	3
G	8.2	0.71463	4E-5	4E-5	1
H	8.9	0.71463	5E-5	5E-5	1

[a] A full data table for individual analyses can be found in Appendix 3.

[b] The propagated error is calculated by using: $\sigma = \sqrt{\sigma_a^2 + \sigma_b^2} + ...$, i.e. propagating through the errors on individual analyses.

[c] The standard deviation exceeds the expected propagated error, implying that the sample is heterogeneous, see Figure 5.8.

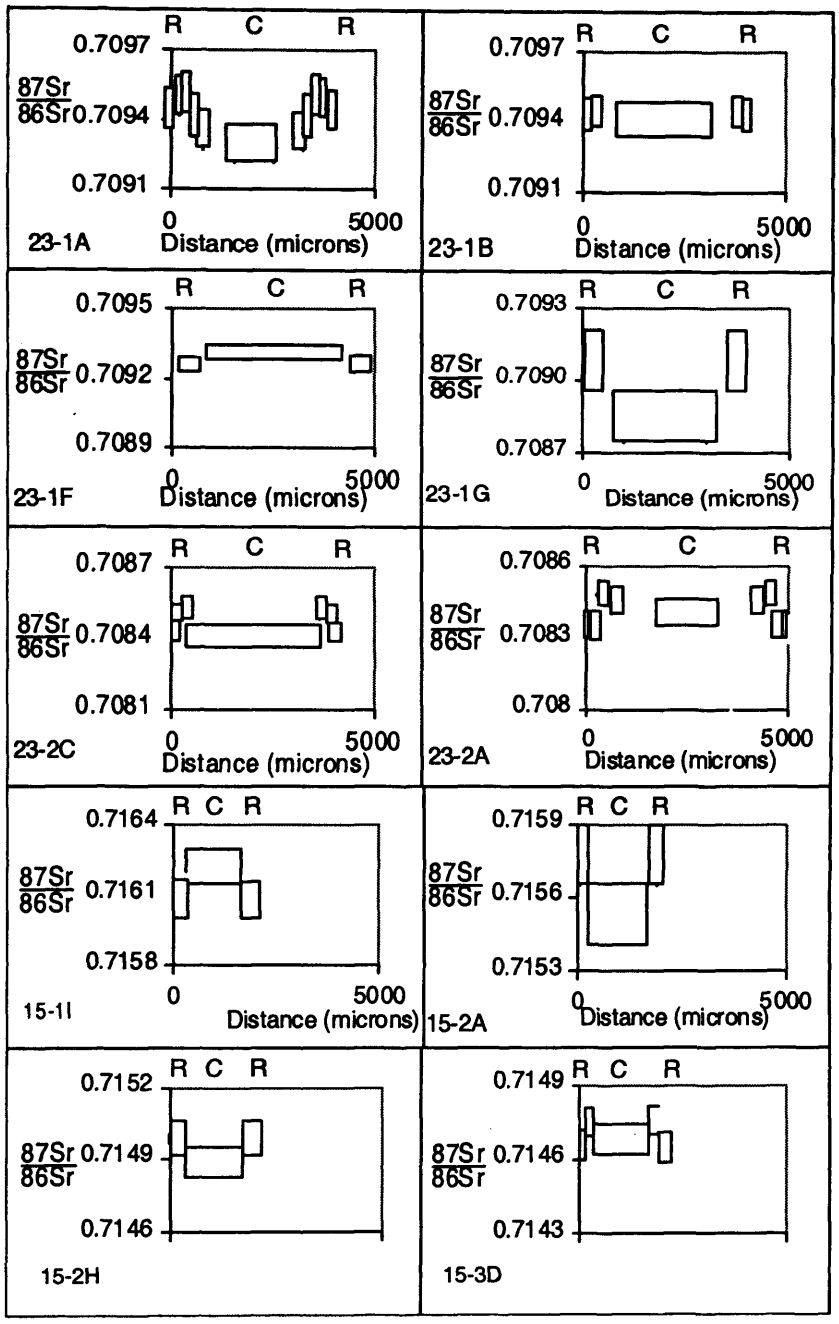

Figure 5.8 Laser ablation ICP-MS traverses across grains, plotted as mirror images around the centre of the grain. Most of the graphs show the analyses are well within one standard error of each other (error bars are one standard error). The exceptions are 23-1A (in the phlogopite band) and 23-1G (just outside the phlogopite band). The boxes represent the width of the analysis plotted against the analytical error; R and C denote the rims and cores of the grains respectively. The graphs are plotted on the same *x* and *y* scale for ease of comparison.

The traverse of 23-1A implies more radiogenic Sr is present towards the rim of the grain, decreasing toward the core. This grain was in the phlogopite band, where rim to core variation was expected.

These within grain profiles are not as expected. Figure 5.7 shows a systematic variation from high values at the rim to low values in the core, whereas the actual profiles (Figure 5.8) show a greater variability with either flat profiles or profiles which increase towards the centre of the grain (e.g. HT15-1I) as well as those which decrease towards the centre (although these do overlap

within error). Comparison of these flat measured profiles (Figure 5.8) with the theoretical profiles (Figure 5.7) implies that the diffusion rate through grains is very rapid (in the order of 2×10^{-15} m^2s^{-1}). The measured profiles may be flat due to the influence of rapid diffusion pathways through the grains, such as fractures or cleavage planes. The profiles (Figure 5.8) are all above Triassic values ($^{87}Sr/^{86}Sr$ 0.7075 to 0.7079; Koepnick *et al.* 1990) in the cores of the grains and this may be due to an equilibration event, for example the peak of metamorphism, which occurred before the present $^{87}Sr/^{86}Sr$ profiles started to form in the grains. Alternatively, these profiles could mean that diffusion through the grains is very slow, so there is no noticeable affect on the $^{87}Sr/^{86}Sr$ from one part of the grain to another.

5.4.3 *HT23 Traverse (Someo) and Interpretation*

The $^{87}Sr/^{86}Sr$ measurements range from 0.70944 in the phlogopite band decreasing to 0.70841 over a distance of 2 cm (Figure 5.9). Previous analysis gave a value of 0.70950 (bulk calcite from within the phlogopite band, see Section 4.1; and would be expected to be closer in value to the calcite in the phlogopite band than values in the calcite outside the phlogopite band).

The value of 0.70841 (from the base of the profile) is taken to be the background level of $^{87}Sr/^{86}Sr$ within the calcite. This value is higher than previously measured Triassic carbonate $^{87}Sr/^{86}Sr$ (0.7075 to 0.7079; Koepnick *et al.* 1990) and, assuming a closed system, suggests a major isotopic re-equilibration event has occurred during metamorphism. The rocks around Someo have been subjected to complete reworking by the Alpine amphibolite grade metamorphism (shown by concordant U-Pb monazite, Köppel *et al.* 1980) but have not been overprinted by any later geological events, so 0.70841 can be taken as the background level of $^{87}Sr/^{86}Sr$ in the calcite. Therefore, the slope in the profile is an effect of down-temperature exchange.

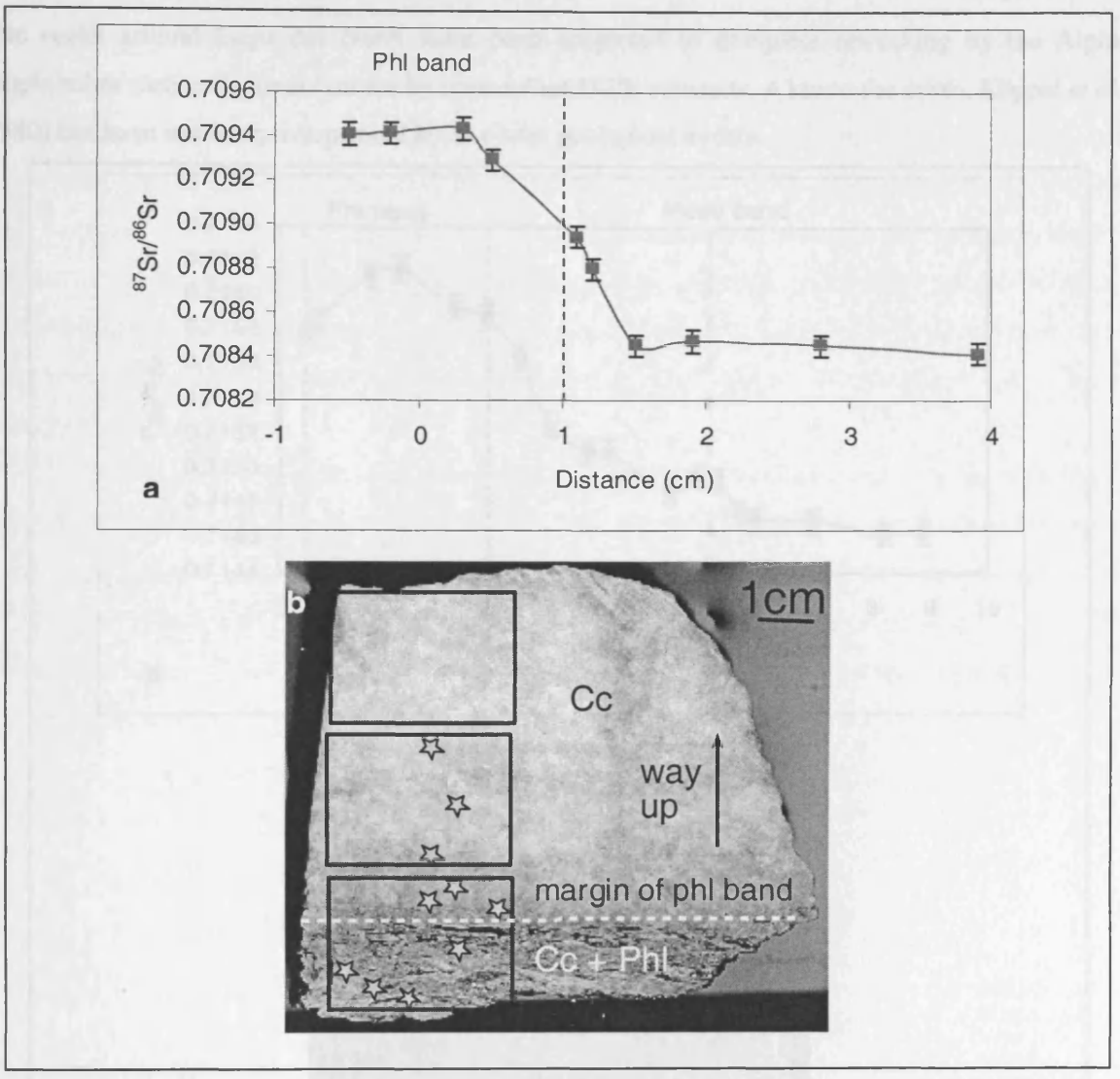

Figure 5.9 a) $^{87}Sr/^{86}Sr$ isotope ratio traverse from sample HT23, Someo. **b)** Locations of laser ablation spots (each star represents one or more analyses on one grain) and the dashed line represents the margin of the phlogopite band.

5.4.4 *HT15 Traverse (Lago del Narèt) and Interpretation*

Calcite $^{87}Sr/^{86}Sr$ ranges from 0.71616 in the phlogopite band, decreasing over a distance of 6 cm to 0.71463. Previous analysis of a whole rock calcite mineral separate gave 0.71512 (sample taken a few cm away from the mica band) and a calculated whole rock $^{87}Rb/^{86}Sr$ of 0.38. Other samples collected from Lago del Narèt give similar results; HT16 (30 m to the west) gives a bulk calcite $^{87}Sr/^{86}Sr$ ratio of 0.71748 and HT17 (10 m to the east) gives a bulk calcite $^{87}Sr/^{86}Sr$ ratio of 0.71861 and a calculated whole rock $^{87}Rb/^{86}Sr$ of 1.94 (the $^{87}Sr/^{86}Sr$ data are quoted in Section 4.1). Samples from a previous study at Lago del Narèt, from within the same outcrop, (I.28 and I.29 from Jenkin *et al.*, 2001) give calcite $^{87}Sr/^{86}Sr$ ratios ranging from 0.71321 to 0.72363.

The value of 0.71463 is assumed to be the background level of $^{87}Sr/^{86}Sr$ (from the base of the profile) within the calcite of HT15. This value is considerably higher than previously measured Triassic carbonate $^{87}Sr/^{86}Sr$ (0.7075 to 0.7079; Koepnick *et al.*, 1990) and, assuming a closed system, again suggests a major isotopic re-equilibration event has occurred during metamorphism.

The rocks around Lago del Narèt have been subjected to complete reworking by the Alpine amphibolite metamorphism (shown by concordant U-Pb monazite, 4 km to the south, Köppel *et al.*, 1980) but have not been overprinted by any later geological events.

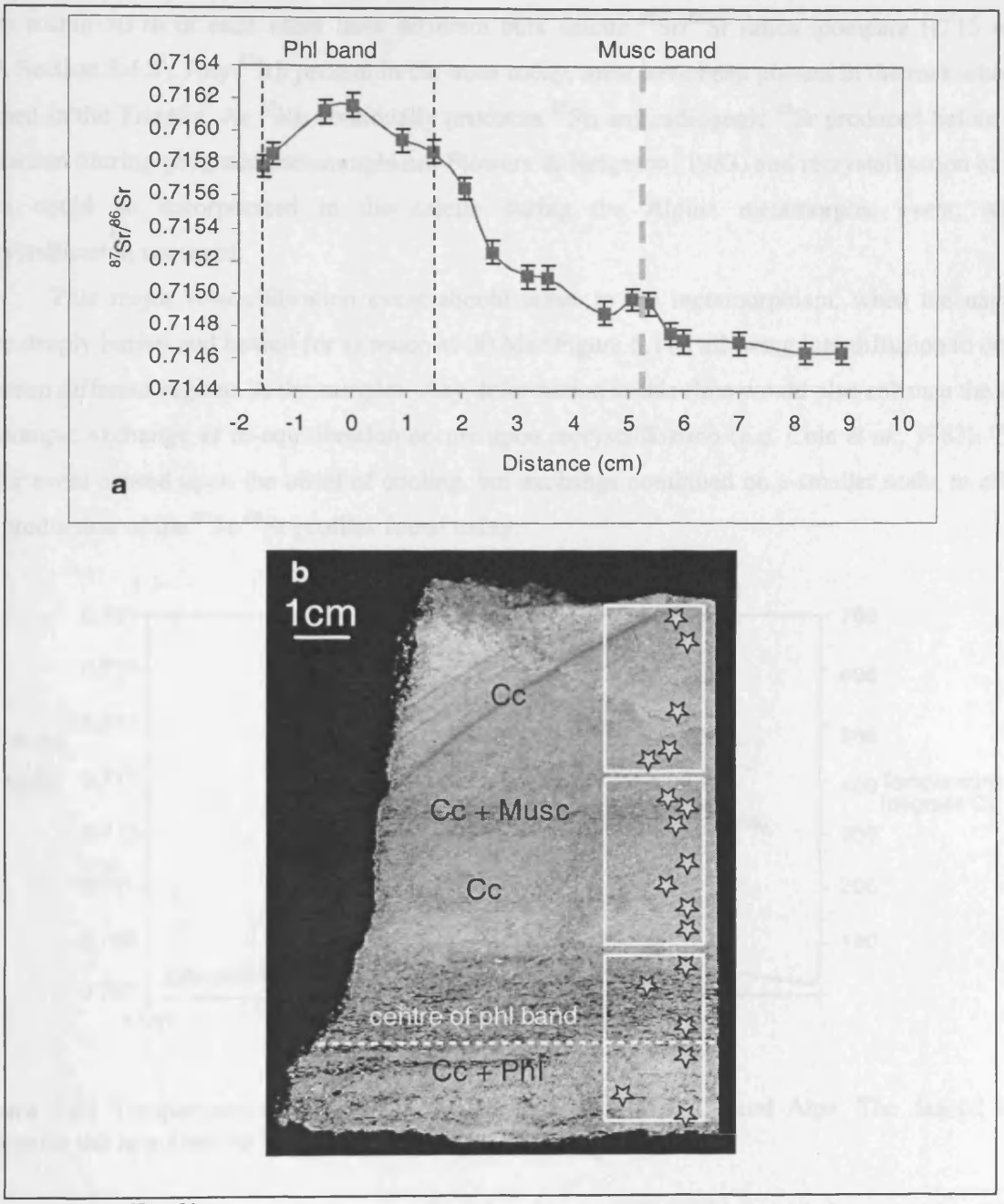

Figure 5.10 a) $^{87}Sr/^{86}Sr$ isotope ratio traverse from sample HT15, Lago del Narèt and **b)** Locations of laser ablation spots (each star represents one or more analyses on one grain) and the dashed line represents the centre of the phlogopite band.

5.4.5 *Equilibration Events*

HT15 and HT23 have both undergone major centimetre-scale equilibration calculated to be in the region of 0.5 m; but following this have behaved as closed systems. This calculation is based upon the ^{87}Rb present in the region of the phlogopite band producing ^{87}Sr between the time of rock formation (approximately 245 Ma) and the onset of cooling (approximately 25 Ma) and calculating how far the $^{87}Sr/^{86}Sr$ must be distributed in order to increase Triassic carbonate values to those of

the present day background levels. The calculation of $^{87}Sr/^{86}Sr$ production is based upon present day values for the mica band (based upon the values in Table 5.5).

The maximum distance for the re-equilibration must be less than 50 m as samples collected from within 50 m of each other have different bulk calcite $^{87}Sr/^{86}Sr$ ratios (compare HT15 with I.29, Section 5.4.8). Any ^{87}Rb present in the mica today, must have been present in the rock when it formed in the Triassic. As ^{87}Rb continually produces ^{87}Sr, any radiogenic ^{87}Sr produced before the formation (during prograde metamorphism; Flowers & Helgeson, 1983) and recrystallisation of the mica could be incorporated in the calcite during the Alpine metamorphic event, when recrystallisation occurred.

This major re-equilibration event should relate to the metamorphism, when the nappes were deeply buried and heated for as much as 30 Ma (Figure 5.11), allowing interdiffusion to occur between different regions in the samples. Any deformation at this time would also enhance the rate of isotopic exchange as re-equilibration occurs upon recrystallisation (e.g. Cole *et al.*, 1983). This major event ceased upon the onset of cooling, but exchange continued on a smaller scale, to allow the production of the $^{87}Sr/^{86}Sr$ profiles found today.

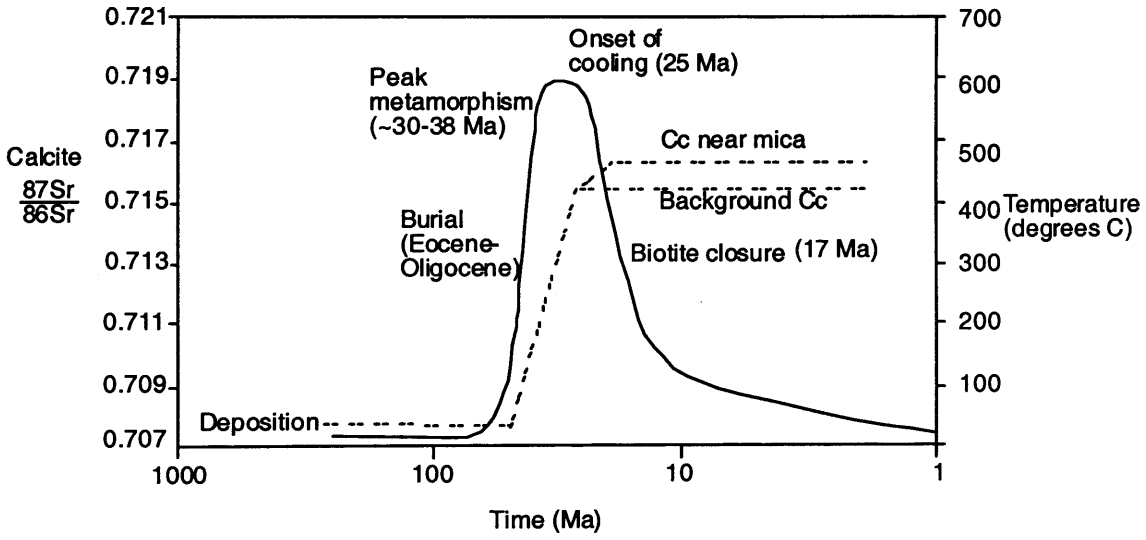

Figure 5.11 Temperature-time diagram for the marbles of the Central Alps. The dashed line represents the hypothetical $^{87}Sr/^{86}Sr$ evolution in the calcite.

However, these profiles might not have achieved full equilibrium during metamorphism and therefore, there would be no flat background level of $^{87}Sr/^{86}Sr$ as ^{87}Sr would build up in the region of the mica before, during and after metamorphism. This modelling assumes that a flat background level is reached during metamorphism, from which the present day $^{87}Sr/^{86}Sr$ profile build up upon cooling from the peak of metamorphism.

5.4.6 *The area under a curve*

In both HT23 and HT15, the area underneath the profile defines how much $^{87}Sr/^{86}Sr$ has been added to the calcite since the equilibration event. The profile is caused by ^{87}Sr entering the

calcite from the mica, increasing the calcite and decreasing the mica $^{87}Sr/^{86}Sr$ ratio. The area under the curve can be used to calculate an age and if this age is added to the calculated mica age, should give the age of the equilibration event (i.e. mica age + age calculated from $^{87}Sr/^{86}Sr$ in the calcite = age of equilibration).

The area under a curve can be found using the trapezium rule, where the curve is divided into several trapezia. The area of a single trapezium is the average height of the two parallel sides multiplied by the distance between them, so the area beneath a curve is the sum of the trapezia. For example, the area of a trapezium defined can be found:

$$\text{Area} = \text{Width} \times \frac{\text{Height}_a + \text{Height}_b}{2} \qquad (5.1)$$

The area of the grey-shaded trapezium in Figure 5.12 can be found by substituting the following values (where 0.71463 is the background $^{87}Sr/^{86}Sr$ value):

$$\text{Area} = 0.5 \times \frac{(0.716118 - 0.714634) + (0.71616 - 0.714634)}{2} \qquad (5.2)$$

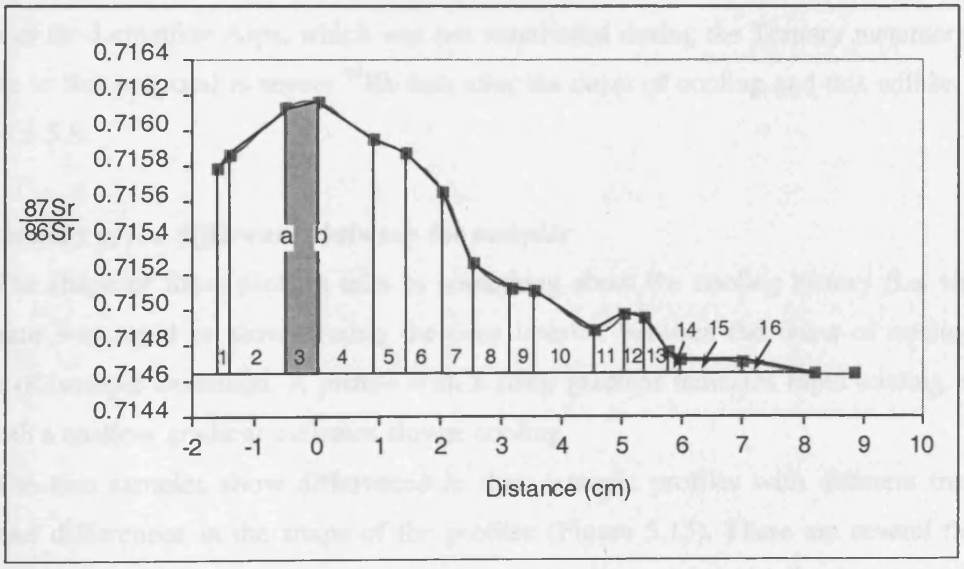

Figure 5.12 Illustration of the trapezium rule for the HT15 $^{87}Sr/^{86}Sr$ graph. The area of the shaded trapezium is found in Equation 5.2.

The total area beneath HT15 is 0.004443 ± 0.00041 and the area beneath HT23 is 0.001261 ± 0.00018 (both minus background calcite $^{87}Sr/^{86}Sr$ and for half the profile length; i.e. from the centre of the phlogopite band to the edge of the profile). The errors are found using the propagated standard errors in Table 5.4. These calculations show that approximately 3 times as much $^{87}Sr/^{86}Sr$ has been added to the calcite in HT15 and this can also be seen in Figure 5.9. This is probably due to the more radiogenic nature of the phlogopite in HT15. However, these areas also correspond to the time elapsed between the equilibration event and the time of isotopic closure of the minerals.

The $^{87}Rb/^{86}Sr$ values used to calculate ages are a function of the $^{87}Rb/^{86}Sr$ ratios of both the phlogopite and the calcite in the mica band, weighted for their mass proportions. These values are given in Table 5.5.

The age corresponding to the area under the curve for HT23 is 12.9 ± 1.9 Ma. Adding this age to the mica age produces an age of 30.1 ± 1.9 Ma (propagated error) for the equilibration event. This age implies a peak of metamorphism between 20 and 30 Ma, in agreement with concordant U-Pb ages of around 23 Ma and the age derived from the cooling rates discussed in Section 3.3.4. This method of calculating ages has the potential to be an important new method for determining peak metamorphic ages.

For HT15 the area produced gives 69.9 ± 6.5 Ma (calculated using the data in Table 5.5), suggesting that the equilibration event for HT15 did not occur during the Tertiary metamorphism. The age produced for HT15 is comparable to some of the ages for peak metamorphism in the basement gneisses of the Western Alps (see Chapter 3).

When added to the phlogopite age (Chapter 4 and Table 5.4), the ages produced above should give the age of the isotopic equilibration event discussed in Section 5.4.5. The age produced for the equilibration event at Lago del Narèt is 87.2 ± 6.54 Ma (propagated error) for HT15. This age does not appear to be meaningful in terms of Alpine evolution (Chapter 3), but taken at face value might suggest that there may have been an early phase of high temperature metamorphism in the north of the Lepontine Alps, which was not reactivated during the Tertiary metamorphism. An alternative to this proposal is severe ^{87}Rb loss after the onset of cooling and this will be examined in Section 5.5.8.

5.4.7 *Summary of the differences between the samples*

The shape of these profiles tells us something about the cooling history (i.e. whether the cooling rate was rapid or slow) during the time interval between the onset of cooling and the cessation of isotopic exchange. A profile with a steep gradient indicates rapid cooling, whereas a profile with a shallow gradient indicates slower cooling.

The two samples show differences in their isotopic profiles with different maxima and minima and differences in the shape of the profiles (Figure 5.13). There are several factors that could contribute to this including grain size, the width of the mica band (implying a mode effect, see Section 2.4.4), how much Rb the phlogopite contains and therefore, how much radiogenic Sr is available, the peak temperature, the cooling rate and the influence of other phases in the specimen, which would also imply a mode effect (Table 5.5).

HT15 has a longer profile with higher maximum and minimum (0.71463 to 0.71616) values of $^{87}Sr/^{86}Sr$ than HT23 and possible reasons for this are discussed below. There is more phlogopite in HT15 and it contains more ^{87}Rb, which would have produced more radiogenic ^{87}Sr to diffuse into the calcite during cooling (giving higher $^{87}Sr/^{86}Sr$ ratios). HT15 also has a smaller average grain size for calcite, implying that there will be a greater influence from grain boundary

diffusion on the bulk diffusion coefficient (see Section 5.5.1). This implies there is a greater volume of grain boundaries in HT15 and therefore, for a given temperature, diffusion should be faster through HT15 than HT23, allowing ^{87}Sr to penetrate further into the sample over any given time (Section 2.3.5).

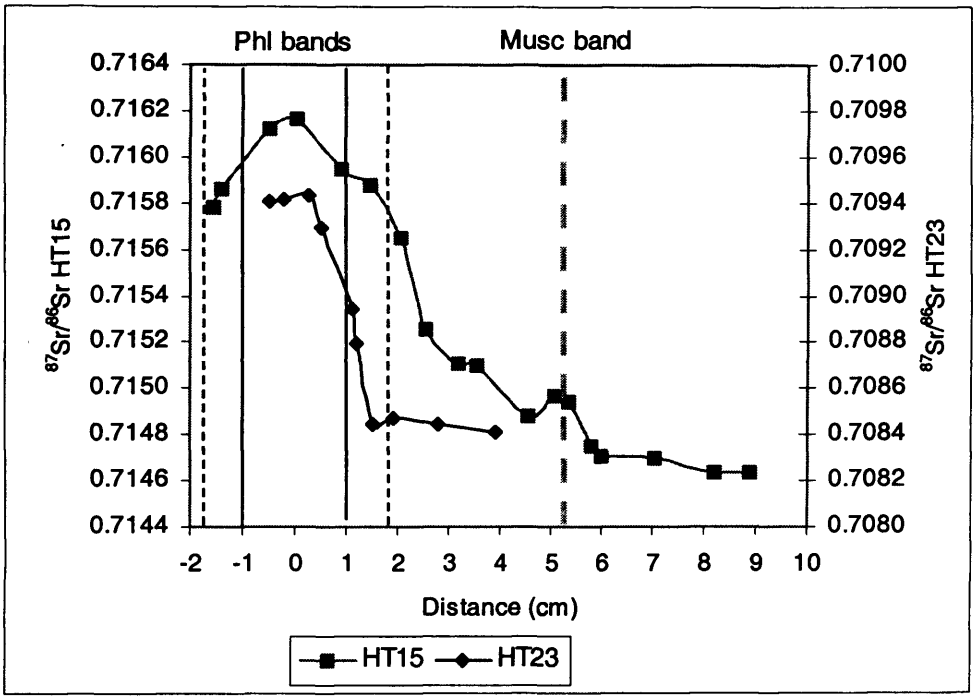

Figure 5.13 $^{87}Sr/^{86}Sr$ ratio profiles redrawn to plot on the same scale axes. It shows the area of the phlogopite band for both HT15 (fine dashed lines) and HT23 (solid lines) and the grey dashed line shows the location of the muscovite band in HT15. The calcite analyses in close proximity to the muscovite band show elevated $^{87}Sr/^{86}Sr$ ratios, implying muscovite is also contributing to the Sr budget of HT15.

In terms of temperature, higher temperatures promote faster diffusion and, all other factor being equal, the Sr will diffuse further out into the surrounding rock, producing a long, graded profile (Figure 5.14). At lower temperatures, diffusion will be less rapid and the Sr will not penetrate as far into the surrounding rock, giving a steeper profile with high Sr concentrations near the mica band.

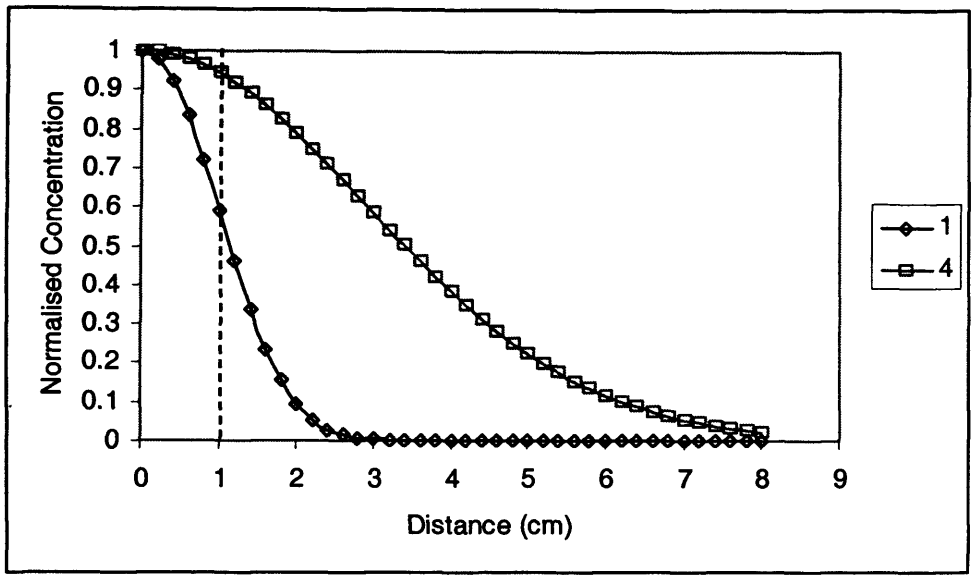

Figure 5.14 Simple diffusion model (using Crank, 1975; equation 2.15) to show the effect of altering the diffusion coefficient. The dashed line denotes the extent of the source (of concentration = 1), 1 and 4 represent values of $2(Dt^{½})$, a modelling parameter explained in Section 5.5.2. Assuming the time (t) the model is run for remains constant, a higher value of $2(Dt^{½})$ represents a faster diffusion coefficient.

HT15 also contains small amounts of K-feldspar and muscovite, which may release ^{87}Sr and therefore, contribute to the ^{87}Sr budget of the specimen. Figure 5.10a shows the HT15 profile and illustrates that the muscovite band does have a minor influence on the calcite $^{87}Sr/^{86}Sr$ ratio. Although no isotopic study has been completed, ion microprobe work (see Section 6.4) suggests that Sr is also mobile in K-feldspar during cooling (however, Sr T_c = 680 °C for a 1 mm radius grain, using the diffusion coefficient of Giletti (1991a) and the closure temperature model of Dodson (1973)), but these effects should be negligible due to high closure temperature of K-feldspar. Muscovite is thought to have a closure temperature of around 500 °C (Jäger *et al.*, 1967), so muscovite would be expected to contribute to any ^{87}Sr added to the calcite. Any contribution from the muscovite will be smaller than that from the phlogopite as there is a smaller proportion of muscovite in the sample and the muscovite contains less Rb.

The ages produced by the areas underneath the curves imply that the two areas have undergone different degrees of metamorphism at different stages. At Lago del Narèt, not considering the possibility of Rb loss from the mica, there seems to have been a very early equilibration event and then a very slow cooling, which allowed diffusion of ^{87}Sr from the mica and caused the build-up of $^{87}Sr/^{86}Sr$ in the calcite. At Someo, there is a later equilibration event, at ~ 30 Ma and then slow cooling to allow the build-up of ^{87}Sr in the calcite within the region of the mica band. Table 5.5 shows that there is a difference in the peak (Tertiary) metamorphic temperature between the two areas. Someo achieved a higher metamorphic peak temperature allowing re-homogenisation of $^{87}Sr/^{86}Sr$ between the mica and the calcite and then a long period of cooling which caused the build-up of $^{87}Sr/^{86}Sr$ in the calcite within the mica band.

Table 5.5 Properties of HT15, HT23 and I.29.

Property	**HT23**	**HT15**	**[a]I.29**
Location	Someo	Lago del Narèt	Lago del Narèt
Bulk measured age Phl-Cc (Ma)	17.20 ± 0.43[b]	17.3 ± 0.7 [c]	17.8 ± 0.2 to 18.1 ± 0.2
[d] Overall cooling rate (°C/Ma)	22	32	32
[d] Onset of cooling (Ma)	28	25	25
[e] Peak metamorphic temperature (°C)	625	575	575
[e] Peak metamorphic pressure (kb)	>6.5	6-6.5	6-6.5
Half-width of phl band (cm)	1	1.8	1
[f] Cc grain size (cm)	0.5	0.1-0.2	0.15-0.2
[f] Cc Sr (ppm)	416	337	109
[f] Cc $^{87}Sr/^{86}Sr$	0.70859 (phl band)	0.71509 (bulk)	0.71321 to 0.72000
[f] Phl Rb (ppm)	211	938	723 to 889
[f] Phl $^{87}Rb/^{86}Sr$	104	1769	3611 to 9635
[f] Phl $^{87}Sr/^{86}Sr$	0.73687	1.14892	1.56651 to 3.18527
[g] Musc Rb (ppm)	n/a	683	n/a
[g] Musc $^{87}Rb/^{86}Sr$	n/a	234	n/a
[g] Musc $^{87}Sr/^{86}Sr$	n/a	0.78987	n/a
% Cc in phl band	83	77	81
% Phl in phl band	17	23	19
[h] Bulk $^{87}Rb/^{86}Sr$ (phl band)	6.859487	2.485533	4.414863
[h] Bulk $^{87}Sr/^{86}Sr$ (phl band)	0.710425	0.716564	0.721239
[h] Bulk $^{87}Rb/^{86}Sr$ (Musc band)		0.991648	
[h] Bulk $^{87}Sr/^{86}Sr$ (Musc band)		0.715202	

[a] Data are from Jenkin *et al.*, 2001.
[b] Age based upon all phlogopite separates (Table 4.1) except the > 1000 μm value.
[c] Age based upon all phlogopite separates (Table 4.1).
[d] Cooling rates and the onset of cooling have been calculated from work by Steiner (1984) and Hurford (1986) in Sections 3.3.5 and 5.2.1.
[e] Peak metamorphic temperatures and pressures are from Todd & Engi (1997).
[f] Calcite and phlogopite isotopic ratios and Rb and Sr concentrations refer to Chapter 4.
[g] The data for muscovite in HT15 is from a similar sample (I.28). I.28 and I.29 were analysed by Jenkin *et al.*, (2001).
[h] Calculated using the method for determining isotopic abundance given in Faure (1986), based upon the % abundance of the two minerals in the mica band (from point counts).

5.4.8 *Comparison with earlier work*

Jenkin *et al.* (2001) give a calcite $^{87}Sr/^{86}Sr$ traverse (I.29) from Lago del Narèt (collected approximately 20 m away from HT15). This traverse was collected by microdrilling of several calcite grains at intervals on either side of the phlogopite band and selective dissolution of calcite in the powder. Figure 5.15 shows HT15 and I.29 plotted on the same scale. This diagram shows that the two profiles die-out over the same length-scale even though the mica bands are of different thicknesses (approximately 5 cm) and both have a minimum $^{87}Sr/^{86}Sr$ value greater than Triassic carbonate values, suggesting a complete homogenisation event. As these samples are from the same area, they have been subjected to the same re-homogenisation event and cooling rates and the same length-scale for exchange should be expected. The difference between the minimum values of the two samples indicates that the effects of the re-homogenisation event do not operate over

length-scales of several metres (i.e. the maximum distance for re-homogenisation is less than 20 m). The calcite in I.29 has accumulated more radiogenic ^{87}Sr through the period of cooling from peak temperature and this is because the phlogopite in I.29 is more radiogenic than that in HT15 (phlogopite in I.29 $^{87}Sr/^{86}Sr$ = 1.5 to 3.2, $^{87}Rb/^{86}Sr$ = 3611 to 9635; in HT15 $^{87}Sr/^{86}Sr$ = 0.78, $^{87}Rb/^{86}Sr$ = 288).

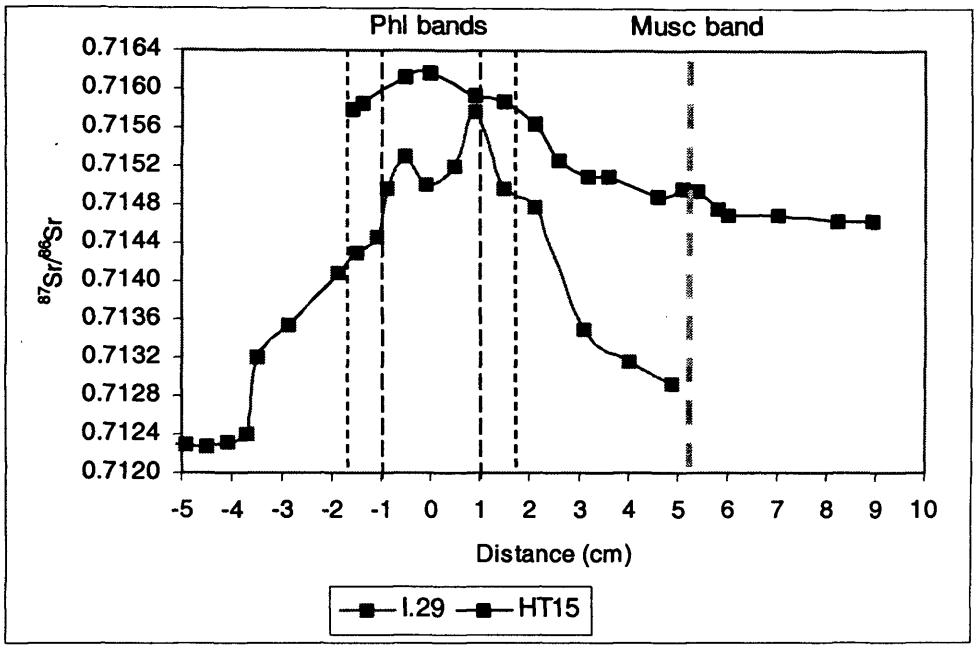

Figure 5.15 $^{87}Sr/^{86}Sr$ ratio profiles redrawn to plot on the same scale axes. It shows the area of the phlogopite band for both HT15 (fine dashed lines) and I.29 (long dashed lines) and the thick, grey dashed line shows the location of the muscovite band in HT15.

The total area beneath I.29 (for half the profile) is 0.00804 ± 0.000148 (minus background calcite $^{87}Sr/^{86}Sr$ of 0.71227). Comparing this value with that of HT15 shows that approximately twice as much $^{87}Sr/^{86}Sr$ has been added to the calcite in I.29 and this can be seen in Figure 5.15. The profile in I.29 was developed in 128 ± 2.4 Ma (Rb values are taken from Table 5.5), which is considerably larger than that for the HT15 profile (69.9 ± 6.5 Ma) and is also geologically unreasonable. As the two samples come from the same location, a similar cooling history and age for development of the $^{87}Sr/^{86}Sr$ profile would be expected.

However, both samples appear to have undergone severe ^{87}Rb loss, see Jenkin *et al.* (2001) and Chapter 6. As a first approximation, assuming the micas closed to exchange at 25 Ma and the background value from the laser study is the initial $^{87}Sr/^{86}Sr$ ratio, the $^{87}Rb/^{86}Sr$ ratios needed are much higher than those found in the phlogopite band. For HT15, the $^{87}Rb/^{86}Sr$ should be 4.53 (almost double that found in the mica band) and for I.29 the $^{87}Rb/^{86}Sr$ ratio should be 21.04 (almost five times greater than the value found in the mica band). This Rb loss suggests that the samples are either violating closed-system behaviour (which petrological and stable isotope data suggest they are not) or Rb is leaving the mica in preference for another mineral, for example K-feldspar and this option will be examined in Chapter 6.

I.29 also shows loss of elemental strontium from the region of the mica band (Figure 5.16, from Jenkin *et al.*, 2001), with the lowest Sr concentrations being found in the region of the highest $^{87}Sr/^{86}Sr$ ratios.

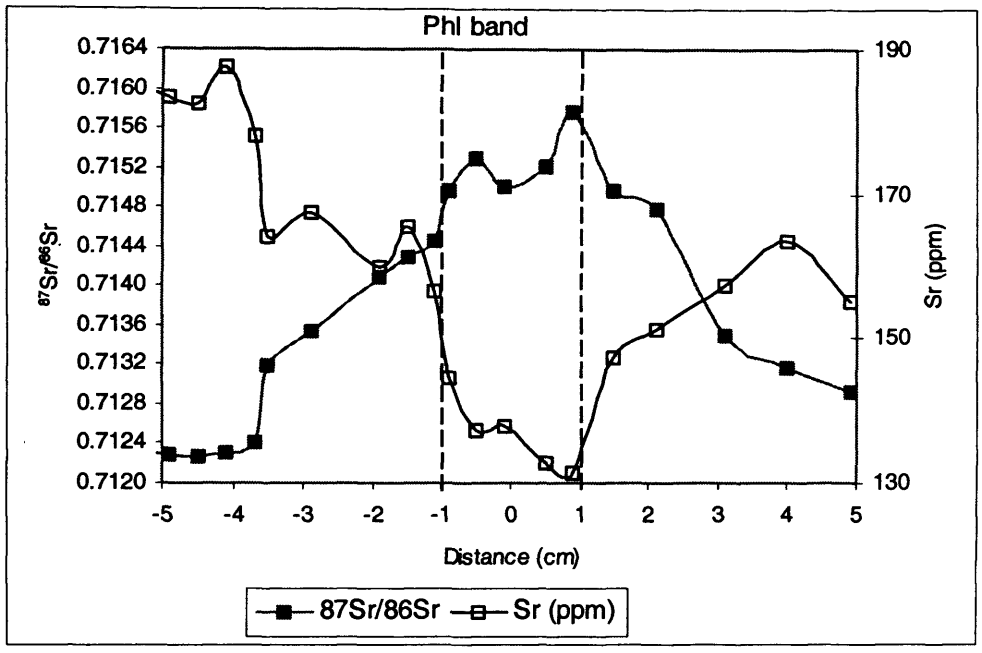

Figure 5.16 Strontium isotope and elemental concentration data for the I.29 traverse (from Jenkin *et al.*, 2001).

Figure 5.16 suggests that all Sr isotopes are mobile before closure, allowing isotopic exchange, which causes the increase in the $^{87}Sr/^{86}Sr$ ratio and simultaneously allows the decrease in Sr concentration (i.e. the loss of other Sr isotopes). The effects of chemical exchange among calcite and the other minerals present in the samples will be examined further in Chapter 6.

5.4.9 *Conclusion from $^{87}Sr/^{86}Sr$ profiles*

Figure 5.13 shows HT15 and HT23 plotted on the same scale axes and this clearly illustrates the differences between the maxima and minima of the profiles. These profiles imply that there is Sr isotope movement between minerals and different regions of the sample, as there are elevated calcite $^{87}Sr/^{86}Sr$ ratios in the phlogopite band which decrease with distance away from the margins of the band (this is also a mode effect, see Figures 5.9b and 5.10b, as the phlogopite content decreases towards the margins of the phlogopite bands). These profiles imply that ^{87}Sr is entering the calcite from the mica, as the calcite shows elevated $^{87}Sr/^{86}Sr$ ratios within and close to the mica bands (for both phlogopite and muscovite). In Figure 5.10a, the phlogopite band shows a greater effect on calcite $^{87}Sr/^{86}Sr$ ratios than the muscovite band, this again could imply a mode effect, as there is less muscovite present in the sample. It may also be due to differences in diffusivity through different types of mica (compare Jenkin (1997) with Hammouda & Cherniak (2000) and Hammouda & Cherniak (in press)) and their Rb concentrations. Figure 5.8 shows the individual grain traverses and these imply that diffusion through the grains is rapid as, apart from 23-1A, there are no significant differences in $^{87}Sr/^{86}Sr$ between the rims and cores of grains. This

suggests that either volume diffusion through the grains is more rapid than that predicted by experiment or that the twin and cleavage planes within the calcite are acting as rapid diffusion pathways through the grains (making diffusion rates through the grains similar to those for grain boundary diffusion), see Lee (1995). Another possibility is that the profiles occur on such a small scale that the differences are not recorded by the size of the laser spots.

5.5 Diffusion modelling of Sr isotope traverses

If the measured profiles (Figures 5.9b and 5.10b) can be fitted to a model, then we are closer to understanding what the profile means in terms of the mechanism of isotopic exchange. It is assumed that the exchange in these rocks has been *via* a combination of volume and grain boundary diffusion. Assuming that the measured Sr diffusion coefficients in calcite (Cherniak, 1997) are correct a diffusion model, which can reproduce the analytical results will confirm that isotopic exchange occurs *via* diffusion. Previous studies have been unable to prove the models of Dodson (1973) and this study should provide the mechanism through which down-temperature exchange occurs.

Two approaches were taken in modelling of the isotope traverses, both modelling the exchange of Sr isotopes between mica bands and the surrounding calcite. The first method uses an analytical solution from Crank (1975) that describes the diffusion of a substance initially confined to a central region (a step function) and is a useful first approximation. However, this method assumes an isothermal model. Dividing the area of $^{87}Sr/^{86}Sr$ under the curve by the width of the phlogopite band generates the step function. The second approach uses finite difference modelling (Smith, 1965), and allows easy modelling of more complex situations, such as additional mica bands and varying temperature. With this second technique, the starting concentrations are the same throughout the traverse (i.e. the background level of $^{87}Sr/^{86}Sr$ in the calcite, formed during recrystallisation) and with time, more ^{87}Sr is added to the calcite within the region of the mica bands. This allows for the production of more radiogenic Sr with time, which then diffuses out into the surrounding calcite. This model also has limitations, which will be discussed in Section 5.5.6.

5.5.1 *Strontium Diffusion Coefficients*

Cherniak (1997) derived an Arrhenius relation experimentally for strontium volume diffusion in calcite under dry conditions. This Arrhenius relation was obtained for measurements from a temperature range of 440-800°C, which encompasses the peak metamorphic temperature for the Lepontine Alps. Cherniak (1997) gives the following equation:

$$D_{VOLSr} = 2.1 \times 10^{-13} \exp\left(\frac{-132}{RT}\right) \qquad (5.3)$$

Where:

D_{VOLSr} is the Sr volume diffusion coefficient (m^2s^{-1})

R is the gas constant (8.31451 $JK^{-1}mol^{-1}$)

T is the temperature (K)

D_{BULK} is found by combining D_{VOL} and D_{GB} (Equation 5.4 and Table 5.6), the bulk, volume and grain boundary diffusion coefficients respectively. No data have been published regarding the rate of grain boundary diffusion of Sr in calcite, however, Farver & Yund (1996, 1998) have published data on both calcium and oxygen showing that grain boundary diffusion is approximately six orders of magnitude faster than volume diffusion. Ca^{2+}, Sr^{2+} and O^{2-} have ionic radii of 1.00, 1.16 and 1.35 Å respectively and Sr replaces Ca in the $CaCO_3$ lattice, so similarities in their style and rate of diffusion should be expected. In producing D_{BULK}, it is assumed Sr behaves in the same way as calcium and oxygen and D_{GB} is assumed to be six orders of magnitude faster than D_{VOL}.

$$D_{BULK} = D_{GB}\left(\frac{\delta}{d}\right) + D_{VOL}\left(1 - \frac{\delta}{d}\right) \qquad (5.4)$$

Where:

δ/d is the proportion of grain boundaries by volume.

D_{BULK}, D_{VOL} and D_{GB} are the bulk, volume and grain boundary diffusion coefficients.

Table 5.6 Bulk diffusion coefficients for peak metamorphic temperatures.

Location	[a] Temperature (°C)	D_{VOLSr} (m^2s^{-1})	D_{GBSr} (m^2s^{-1})	[c] δ/d	D_{BULK} (m^2s^{-1})
Narèt	575	[b] 1.55×10^{-21}	1.55×10^{-15}	9.00×10^{-5}	1.41×10^{-19}
Someo	625	[b] 4.41×10^{-21}	4.41×10^{-15}	1.80×10^{-5}	8.38×10^{-20}

[a] peak temperatures are from Todd & Engi (1997)

[b] volume diffusion coefficients are calculated from Cherniak (1997)

[c] δ/d is the proportion of grain boundaries. For derivation of δ/d, D_{GB} and D_{BULK}, see Equation 5.2 and text.

To estimate D_{BULK}, D_{VOL} and D_{GB} are weighted for the proportion of grain boundaries by volume (δ/d) in the sample. Assuming straight grain boundaries in 1 cm^3 ($1 \times 10^{-6} m^3$) of sample, for cubic grains, and an effective grain boundary width of 30 nm (Farver & Yund, 1996), the volume of the grain boundaries can be estimated (i.e. the area of one plane = $10^{-4} m^3$; the volume of one plane, which represents four grain boundaries between individual grains, = $30 \times 10^{-9} \times 10^{-4}$ = $3 \times 10^{-12} m^3$; the total volume = $1 \times 10^{-6} m^3$), as we know the average calcite grain size (see Table 5.5). For example, assuming a cubic grain size of 5 mm, there will be six planes, which form grain boundaries in 1 cm^3 of sample (see Figures 5.17 and 5.18); the total volume of grain boundaries is, therefore, $1.8 \times 10^{-11} m^3$. In Figure 5.17, three of the planes are internal and there are six external planes (although these are treated as half the value, as they form the external boundary of the 1 cm^3

of sample). In Figure 5.18, all six planes are within the 1 cm^3 of sample, and the volume of grain boundaries remains the same as in Figure 5.17.

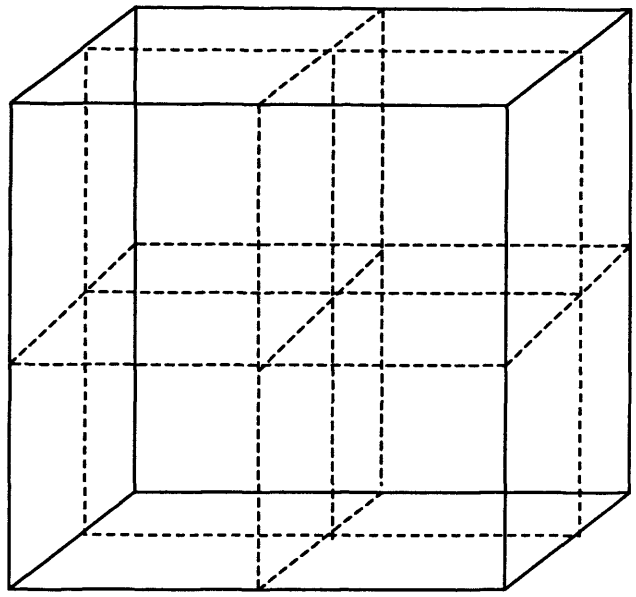

Figure 5.17 Illustration of grain boundaries (dashed lines) entirely within 1 cm^3 of sample, if these grains are 5 mm in diameter, then the faces of the cube also represent grain boundaries, which would contribute half their width to this area of sample and the other half to adjacent cubes. This actually represents $3 + (1/2 \times 6) = 6$ grain boundaries.

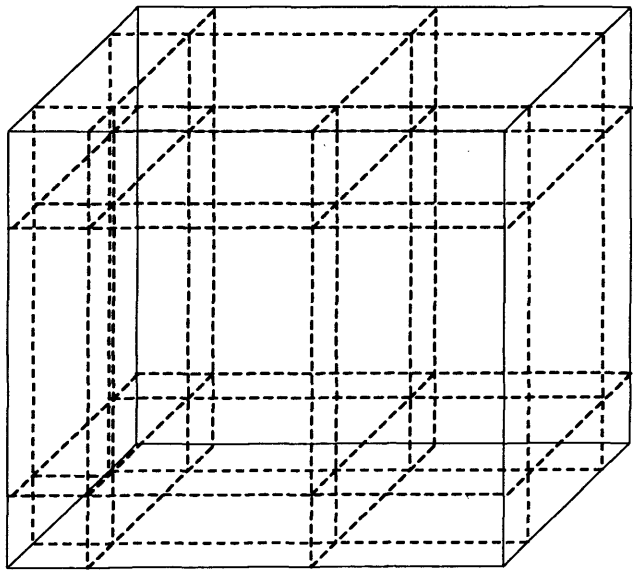

Figure 5.18 Illustration of grain boundaries (dashed lines) entirely within 1 cm^3 of sample, if the grains are 5mm in diameter, then the faces of the cube are entirely within grains.

The bulk diffusion coefficients calculated here have assumed no partitioning (i.e. elements or isotopes have no preference for one mineral over another) and that the grain boundaries between calcite grains are straight, making cubic grains. However, in nature grain shapes would be somewhere between cubic and spherical (in these samples, the grains form a polygonal network of grain boundaries, approaching 120° triple junctions between grain boundaries) as there are no large voids in the samples and petrological examination shows interconnected grains. For a 1 cm^3 sphere

and a 1 cm^3 cube, the surface area/volume ratios are 0.716 and 6 respectively, showing that for the same volume of material, a spherical grain would have a smaller surface area and therefore a smaller volume of grain boundaries. As the grains in the study are somewhere between spherical and cubic, approximating their grain shapes to that of a cube will give an over estimation of the number of grain boundaries present.

5.5.2 *Strontium Production*

The amount of radiogenic daughter to be added is calculated as an $^{87}Sr/^{86}Sr$ ratio using the present day isotopic ratios of the phlogopite and the Rb-Sr decay equation (a variation on Equation 2.2):

$$\left(\frac{^{87}Sr}{^{86}Sr}\right)_{change} = \left(\frac{^{87}Rb}{^{86}Sr}\right) \times \left(e^{\lambda t} - 1\right) \qquad (5.5)$$

Where:

λ is the decay constant ($1.42 \times 10^{-11} yr^{-1}$, Steiger & Jäger, 1977)

t is the time step (years)

Equation 5.5 is used to find the $^{87}Sr/^{86}Sr$ produced for the amount of time specified using an $^{87}Rb/^{86}Sr$ calculated from Rb and Sr in the weighted proportions of phlogopite and calcite in the region of the phlogopite band (using the methodology outlined in Faure, 1986, p120).

This $^{87}Rb/^{86}Sr$ is then used to determine how much ^{87}Sr is produced in different length time-steps. Currently mica diffusion coefficients are poorly constrained for few elements, so it has been assumed that all the ^{87}Sr produced may leave the mica. The $^{87}Sr/^{86}Sr$ ratios produced can then be used to determine the amount of ^{87}Sr available for diffusion from the phlogopite band (as a $^{87}Sr/^{86}Sr$ ratio).

5.5.3 *The Crank Equation*

Crank (1975, Equation 2.15) gives the following:

$$C = \frac{1}{2} C_0 \left\{ \text{erf} \frac{h - x}{2\sqrt{Dt}} + \text{erf} \frac{h + x}{2\sqrt{Dt}} \right\} \qquad (5.6)$$

Where:

C is the concentration

$\mathbf{C_0}$ is the original concentration

D is the diffusion coefficient ($m^2 s^{-1}$)

t is time (s)

$-h < x < +h$ is the area within which the diffusing substance is originally confined, x is the distance over which the diffusing substance disperses and *erf* is the error function (tables of values for the

error function can be found in Crank, 1975). The profiles are symmetrical about $x = 0$ and the peak of the profile depends upon $(Dt/h^2)^{½}$, the greater the value of $(Dt/h^2)^{½}$ the lower the peak.

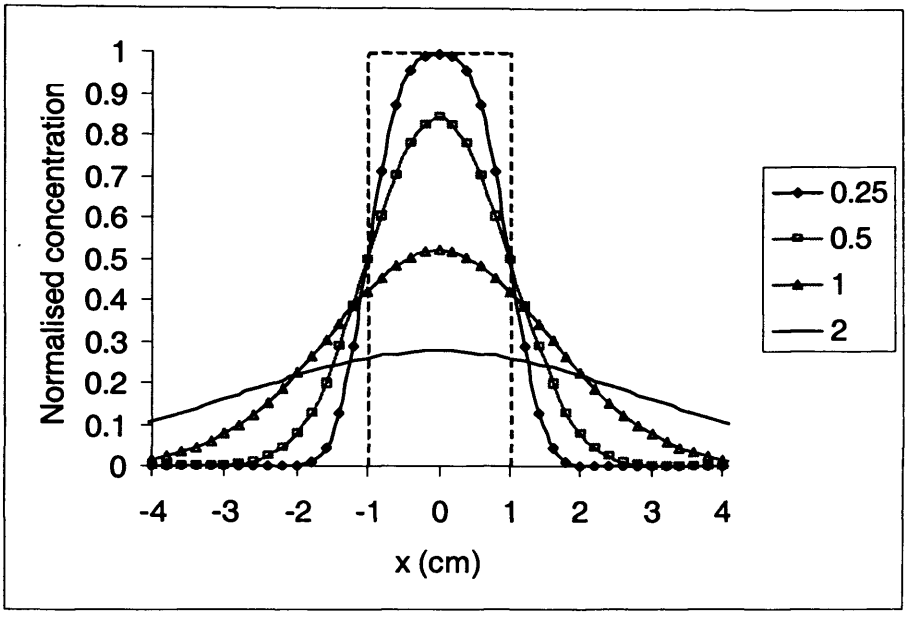

Figure 5.19 Concentration-distance curves for a source of limited extent (after Crank, 1975). The dashed line represents the initial step function and the curves are defined by values of $(Dt/h^2)^{½}$, i.e. for constant D and h the curves show increasing t.

In Figure 5.19 the *y*-axis is given as normalised concentration, which means the highest concentration is recalculated to equal one and the lowest concentration is equal to nought. All values for the concentration profile then lie between nought and one. The profile starts as a step function and over time produces a curve (the area under all these curves is the same) as the initial amount of substance diffuses into the surrounding region.

5.5.4 *The Measure of Fit*

The fit of the modelled profile to the analysed profile is assessed using the standard error of the estimate:

$$\text{Standard Error of the Estimate} = \sqrt{\frac{\sum_{i=1}^{i=n}(O_i - E_i)^2}{(n-2)}} \qquad (5.7)$$

Where:

O is the observed value (analysed value)

E is the expected value (modelled value)

n is the number of analysis points

The lower the value of the standard error, the closer the fit of the model to the analysed results. The best-fit models give the lowest value for the standard error of estimate for a given set of parameters.

5.5.5 Modelling using the Crank Equation

This method provides an analytical model of the Sr ratio profiles, however it does not take into account the gradual production of more ^{87}Sr through time *via* the decay of ^{87}Rb. These models are isothermal, as the value for the diffusion coefficient cannot be changed with cooling rate (in reality the temperature decreases with time from the peak metamorphic event) and the total amount of ^{87}Sr produced must be specified before running the model. The total time for the diffusion can be calculated from $(Dt/h^2)^{½}$ as D_{BULK} can be specified and h is a constant (the mica band half-width). The area of $^{87}Sr/^{86}Sr$in the initial step function is equal to the area under the analysed profile.

Figure 5.20 shows the best-fit isothermal model for HT23. This model gives a reasonably good fit, with an overall value for the standard error of the estimate = 0.000101 (0.000109 within the phlogopite band and 0.000121 outside the phlogopite band) and the area beneath the modelled curve equals the area beneath the analysed profile (0.001261). The diffusion coefficient produced by this model is very close to that calculated in Table 5.6 ($5.43 \times 10^{-20} m^2 s^{-1}$ compared with $8.38 \times 10^{-20} m^2 s^{-1}$).

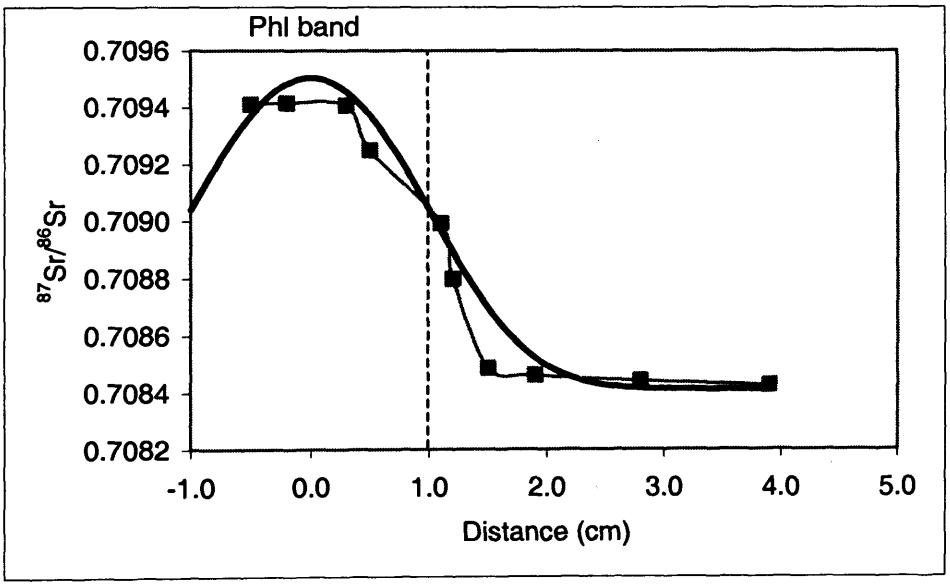

Figure 5.20 HT23 Crank diffusion model, for this model, $(Dt/h^2)^{½} = 0.47$, with an age of 12.9 Ma. This gives a bulk diffusion coefficient of $5.43 \times 10^{-20} m^2 s^{-1}$. The dashed line represents the limit of the phlogopite band.

Figure 5.21 shows a best-fit isothermal model for HT15. This model gives a very good fit, with an overall value for the standard error of the estimate = 0.000095 (0.000058 within the phlogopite band and 0.000114 outside the phlogopite band) and the area beneath the modelled curve equals the area beneath the analysed profile. The value for the standard error of the estimate

is very similar to the value for the analytical error, suggesting the fit of this model is very reasonable. The diffusion coefficient produced by this model is very close to that calculated in Table 5.6 ($1.09 \times 10^{-19} m^2 s^{-1}$ compared with $1.41 \times 10^{-19} m^2 s^{-1}$).

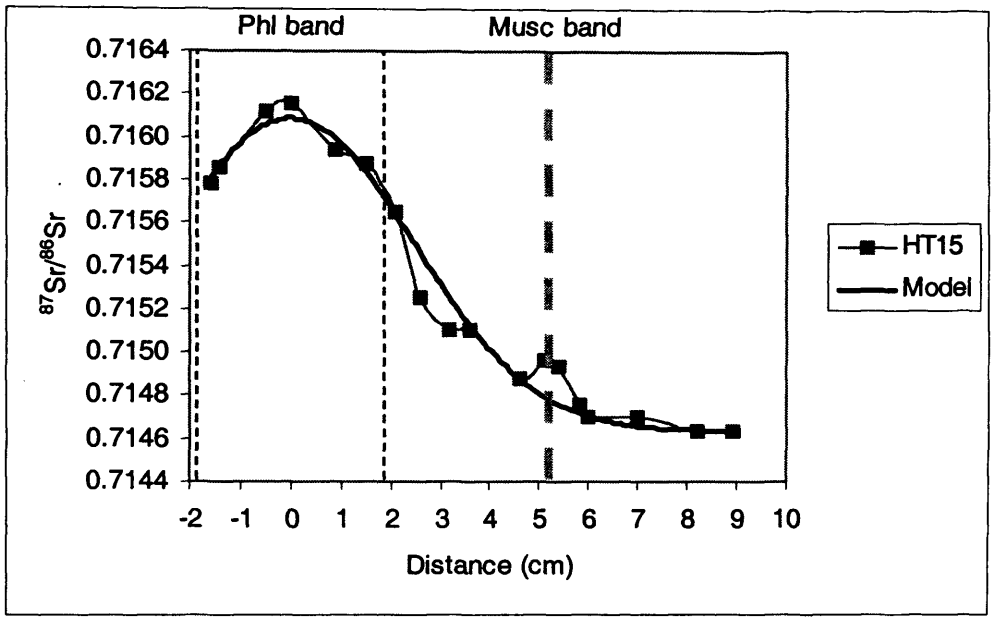

Figure 5.21 HT15 Crank diffusion model, for this model, $(Dt/h^2)^{1/2} = 0.861$, with an age of 69.9 Ma. This model gives bulk diffusion coefficient of $1.09 \times 10^{-19} m^2 s^{-1}$. The dashed lines represent the limits of the phlogopite band and the grey line represents the muscovite band.

These two models produce very good fits for the analytical data (Figures 5.20 and 5.21). The models assume a high, static starting concentration of $^{87}Sr/^{86}Sr$, which then diffuses out into the surrounding calcite. However, in reality, ^{87}Sr is produced through time and diffuses out of the mica and into the calcite as it is produced. For HT15, the effects of the muscovite band on the $^{87}Sr/^{86}Sr$ ratio profile cannot be accounted for as there is no way to add in a second mica band. The diffusion coefficient changes with time from the onset of cooling, as the rate of diffusion decreases with decreasing temperature. For these reasons, the Crank diffusion models should be used as a first approximation and finite difference modelling has been completed on the two samples.

5.5.6 *Finite Difference Modelling*

With this method, the profiles can be modelled to take into account the temperature and diffusion coefficient decrease and the production of ^{87}Sr from the phlogopite in a series of discrete time steps. For HT15, the muscovite band can also be modelled. Every new $^{87}Sr/^{86}Sr$ ratio produced depends upon those calculated previously and a profile can be created in 2D-space, in terms of distance and time. The explicit finite difference model is explained mathematically in Crank (1975, p.136 onwards) and in Smith (1965, Chapter 1) and takes the form of a grid:

Distance Steps (*i*) →

Time Steps (j) ↓

	x_1	x_2	x_3	x_4
t_0	A_0	B_0	C_0	D_0
t_1	A_1	B_1	C_1	D_1
t_2	A_2	B_2	C_2	D_2
t_3	A_3	B_3	C_3	D_3

Figure 5.22 A grid to show the basic finite difference model. The values in the first column represent the time-step (i.e. t = 0, t = 1 etc) and as such, the values in the first row represent the starting concentrations (i.e. at t = 0, the concentrations are A_0, B_0, C_0, D_0) at distances progressively further away from the source of the diffusing substance.

In Figure 5.22, the starting concentrations are represented by A_0, B_0, C_0 and D_0 and the time steps are represented by rows t_1, t_2 and t_3 (Δt and Δx remain constant throughout). For example, the derivation of B_1 uses the following equation:

$$B_{t_1} = B_{t_0} + r\left(A_{t_0} - 2B_{t_0} + C_{t_0}\right) \qquad (5.8)$$

In general,

$$x_i, t_j = x_i, t_{j-1} + r\left(x_{i-1}, t_{j-1} - 2x_i, t_{j-1} + x_{i+1}, t_{j-1}\right) \qquad (5.9)$$

Where:

$$r = \delta T/(\delta X)^2$$

T and **X** are dimensionless variables: $\mathbf{T} = Dt/l^2$ and $\mathbf{X} = x/l$, where D is the diffusion coefficient (m^2/s), t is the time step (s), l is the half-width of the mica band (m) and x is the distance step (m). Smith (1965) shows that the value of r = 0.5 is critical. Below this value the finite difference solutions agree with the analytical solutions reasonably well, but above this value oscillations develop and the solution becomes unstable as the rounding errors increase without limit. At values approaching r = 1, the finite difference model bears no resemblance to the analytical solution. The limitation on the value of r imposes restrictions on δT for any value of δX and as such, large numbers of small time steps have to be used to keep $r < 0.5$, for geological values of the diffusion coefficient.

Column x_1 represents the central point about which the profile is symmetrical and as such, Equation 5.8 changes to:

$$A_{t_1} = A_{t_0} + r\left(2B_{t_0} - 2A_{t_0}\right) \qquad (5.10)$$

In general,

$$x_i, t_j = x_i, t_{j-1} + r\left(2x_{i+1}, t_{j-1} - 2x_i, t_{j-1}\right) \qquad (5.11)$$

To add more radiogenic daughter element, a set amount (z, equivalent to the amount of ^{87}Sr produced in the time step and weighted for the proportion of Sr in phlogopite and in calcite) is

added to each previous row in rows $t_{0.5}$, $t_{1.5}$ and $t_{2.5}$ (Figure 5.23). These new values in $t_{0.5}$, $t_{1.5}$ and $t_{2.5}$ are then used to calculate the subsequent concentrations, i.e. use row $t_{0.5}$ to calculate the values in t_1, row $t_{1.5}$ to calculate the values in t_2 etc (within the limit of the mica band). The radiogenic daughter is only added to the columns within the limit of *l*, the distance over which the mica is present and then allowed to diffuse into the rest of the modelled rock.

Distance Step (*i*) →

Time Step (*j*) ↓

	x_1	x_2	x_3	x_4	x_5	x_6
t_0	A_0	B_0	C_0	D_0	E_0	F_0
$t_{0.5}$	A_0+z	B_0+z	C_0+z			
t_1	A_1	B_1	C_1	D_1	E_1	F_1
$t_{1.5}$	A_1+z	B_1+z	C_1+z			
t_2	A_2	B_2	C_2	D_2	E_2	F_2
$t_{2.5}$	A_2+z	B_2+z	C_2+z			
t_3	A_3	B_3	C_3	D_3	E_3	F_3

Figure 5.23 A grid representing the finite difference model with the addition of radiogenic daughter (z) after each time step. Columns x_1 to x_3 are all within the mica band.

In Figure 5.23, columns x_4, x_5 and x_6 represent the area outside the mica band. For example, the values in D_1 are calculated using:

$$D_1 = D_0 + r((C_0 + z) - 2D_0 + E_0) \qquad (5.12)$$

In general,

$$x_i, t_j = x_i, t_{j-1} + r(x_{i-1}, t_{j-0.5} - 2x_i, t_{j-1} + x_{i+1}, t_{j-1}) \qquad (5.13)$$

With the finite difference model the initial concentration profile is flat and with time, more ^{87}Sr is added to the calcite within the limit of *l*, which then diffuses into the surrounding calcite.

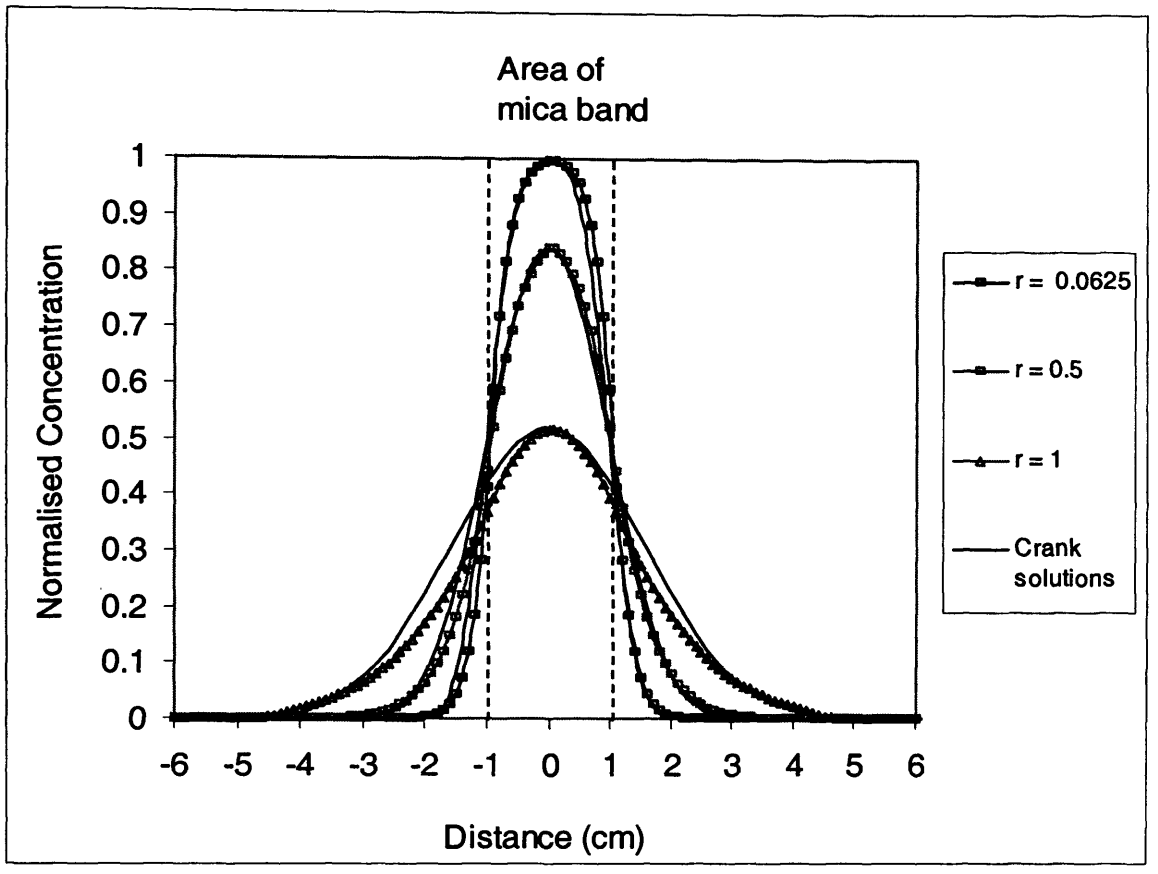

Figure 5.24 Finite difference model for the Crank (1975) solution. This is a simple model, which assumes 0.001 $^{87}Sr/^{86}Sr$ is added after each time step. The different models are denoted by their r values, the higher the value of r, the greater number of times steps is required to produce a high peak.

Figure 5.24 shows a finite difference model for the Crank source of limited extent model given in Figure 5.19. This figure shows that results very similar to those generated by the Crank model can be achieved with the finite difference model. The parameter r (in the finite difference model = Dt/x^2 (the square of the values which define the curves in Figure 5.19. To achieve different values of r, the diffusion coefficient and the time step must be changed.

5.5.7 Finite Difference Models for HT23

Figure 5.25 shows an isothermal finite difference model. The model runs for approximately 12 Ma from the onset of cooling, with a diffusion coefficient of 8.38×10^{-20} m^2s^{-1} (Table 5.6). The model produces a good degree of fit and has exactly the same area as the measured profile. The overall SEE for the model is 0.000093 and the age produced by the finite difference model is 12.3 Ma. There is a slight discrepancy between the finite difference age (calculated from the number of time steps taken to achieve the model result) and the age calculated from the area under the curve (12.3 Ma compared with 12.9 Ma). Increasing the number of distance steps can reduce this discrepancy in age. This model produces a worse fit than that of the Crank model (Figure 5.20), suggesting either the diffusion or the cooling rate parameter is incorrect.

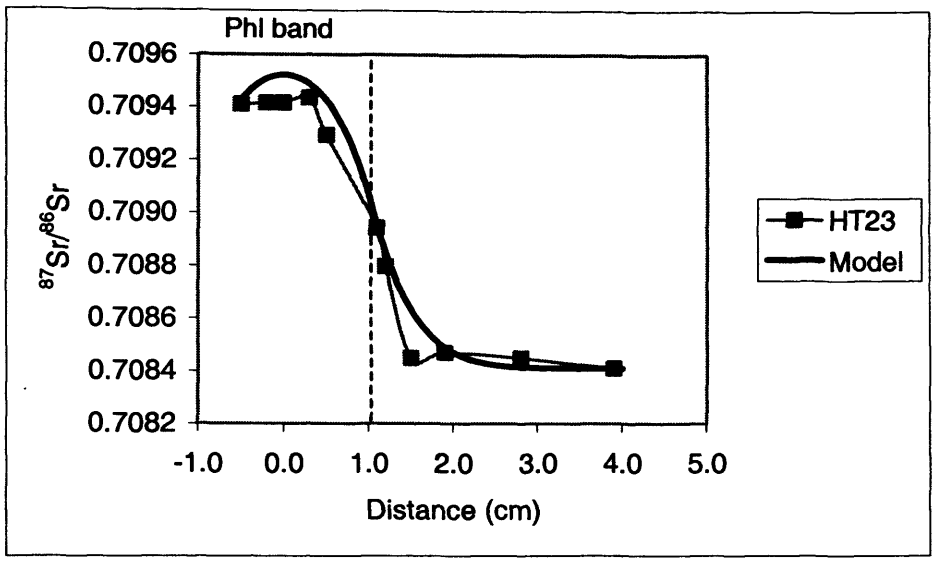

Figure 5.25 Isothermal finite difference models for HT23. The model equates the area under the model curve with the area under the measured curve. The mica band width is 2 cm, the diffusion coefficient is constant at $8.38 \times 10^{-20} m^2 s^{-1}$ and r is kept constant at 0.000263. The initial profile is flat and starts at $^{87}Sr/^{86}Sr = 0.70841$, with $^{87}Rb/^{86}Sr$ of 6.86 in the band.

Figure 5.26 shows a finite difference model produced for a constant cooling rate of 32°C/Ma, decreasing the diffusion rate with time from the peak metamorphic temperature. These models use a constant cooling rate of 32°C/Ma, starting at a temperature of 625 °C and varies the time step, the amount of $^{87}Sr/^{86}Sr$ added to the region of the mica band and the diffusion coefficient accordingly. 32°C/Ma is the cooling rate inferred for the Lepontine region (see Chapter 3).

The model produces a lower degree of fit, but is closer in area to the analysed profile. The overall SEE for the model is 0.000235 and produces an age of 12.4 Ma. It is possible that lowering the cooling rate will improve the model fit and this is examined in Table 5.7.

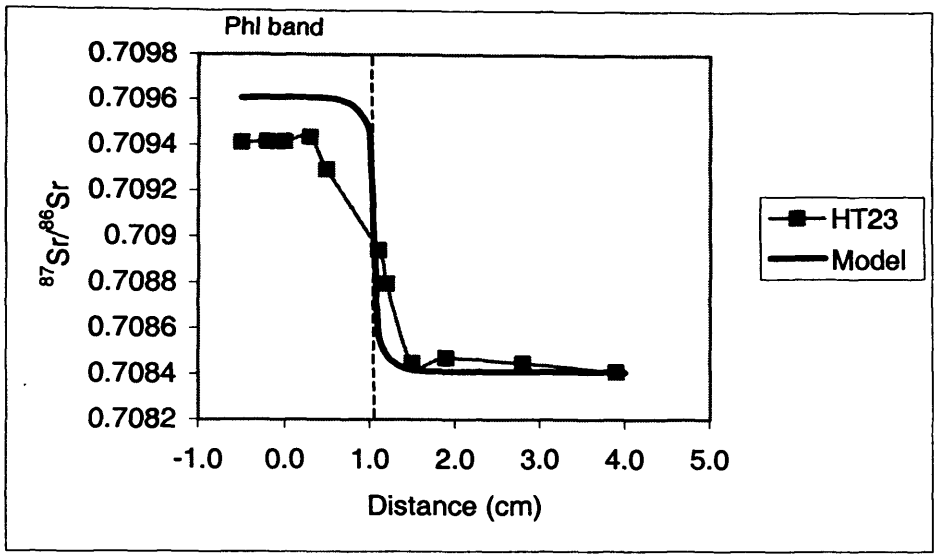

Figure 5.26 Finite difference model for HT23, using a cooling rate of 32 °C/Ma. The model equates the area under the model curve with the area under the measured curve. The mica band width is 2 cm, the diffusion coefficient starts at 8.38 × $10^{-20}m^2s^{-1}$ (then varies according to the cooling rate) and r is kept constant at 0.000263. The initial profile is flat and at $^{87}Sr/^{86}Sr$ = 0.70841, with $^{87}Rb/^{86}Sr$ of 6.86 in the band.

Figure 5.27 shows a finite difference model produced for a constant cooling rate of 22°C/Ma, decreasing the diffusion rate with time from the peak metamorphic temperature. This model use a constant cooling rate of 22°C/Ma, starting at a temperature of 625 °C and varies the time step, the amount of $^{87}Sr/^{86}Sr$ added to the region of the mica band and the diffusion coefficient accordingly. 22°C/Ma is the local cooling rate inferred from work by Hurford (1986), see Chapter 3).

The model produces a lower degree of fit, but has the same area as the analysed profile. The overall SEE for the model is 0.000214 and produces an age of 12.3 Ma.

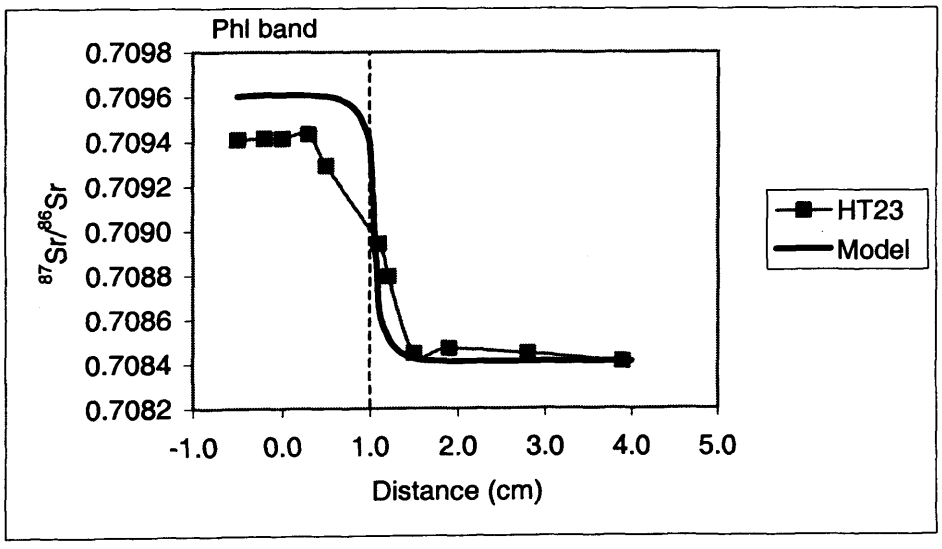

Figure 5.27 Finite difference model for HT23, using a cooling rate of 22 °C/Ma. The model equates the area under the model curve with the area under the measured curve. The mica band width is 2 cm, the diffusion coefficient starts at 8.38 × $10^{-20}m^2s^{-1}$ (then varies according to the cooling rate) and r is kept constant at 0.000263. The initial profile is flat and at $^{87}Sr/^{86}Sr$ = 0.70841 with $^{87}Rb/^{86}Sr$ of 6.86 in the band.

Table 5.7 Standard error of the estimate for different cooling rates, starting with a diffusion rate of $8.38 \times 10^{-20} m^2 s^{-1}$ at 625 °C, fitting the area produced by the model curve to the area produced by the analysed profile.

Cooling Rate (°C/Ma)	Overall	Within Phl Band	Outside Phl Band	Area
32	0.000235	0.000322	0.000243	0.001258
28	0.000232	0.000323	0.000235	0.001261
24	0.000220	0.000322	0.000213	0.001261
22	0.000214	0.000317	0.000203	0.001260
20	0.000205	0.000313	0.000187	0.001257
16	0.000189	0.000314	0.000148	0.001262
Isothermal	0.000093	0.000123	0.000099	0.001261

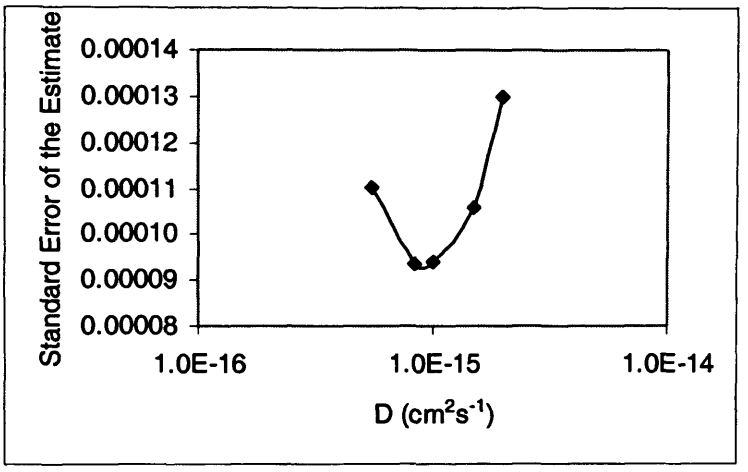

Figure 5.28 Graph of SEE versus diffusion coefficient for the isothermal models for HT23.

Table 5.7 shows that the isothermal model produces the best-fit for HT23. However, in reality, the sample has undergone cooling from the peak metamorphic temperature. Previously, it has been suggested that the overall cooling rate for the Lepontine Alps is 32 °C/Ma and work by Hurford (1986) suggests a local cooling rate of 22 °C/Ma for the area around Someo (central Valle Maggia). The lower cooling rate produces a better fit, suggesting that 22°C/Ma is an appropriate cooling rate for the central Lepontine. Figure 5.28 suggests that the best-fit for the curve is generated by a diffusion coefficient of $8.38 \times 10^{-20} m^2 s^{-1}$.

It is also possible to vary the magnitude of the diffusion coefficient, however, values either side of the current model value give worse fits for the same area under the modelled curve as the measured profile. For example, using a cooling rate of 22°C/Ma, diffusion rates of $1 \times 10^{-19} m^2 s^{-1}$ and $5.5 \times 10^{-20} m^2 s^{-1}$ at 625 °C, give SEEs of 0.000214 and 0.000228, the same as or worse than the value quoted in Table 5.7 for a cooling rate of 22 °C/Ma.

The finite difference age associated with this model is 12.3 Ma, suggesting the onset of cooling began at 29.7 Ma (12.3 + 17.4 Ma) in central Valle Maggia, in agreement with Hurford (1986).

5.5.8 *Finite Difference Models for HT15*

All the finite difference models for HT15 have been created assuming Rb loss and the present-day $^{87}Sr/^{86}Sr$ ratio for the mica band has been used to calculate the $^{87}Rb/^{86}Sr$ ratio for 8 Ma of ^{87}Sr production (i.e. the assumed age for the onset of cooling, after Hurford, 1986 minus the mica age = 25 – 17 = 8 Ma). The $^{87}Rb/^{86}Sr$ ratio assumed is 21.72, which suggests severe ^{87}Rb loss, which is probably occurring with the exchange of ^{87}Sr and ^{86}Sr between the mica and the calcite.

Figure 5.29 shows isothermal finite difference models for a diffusion coefficient of 1.41×10^{-19} m^2s^{-1} (given in Table 5.5). The model shows the profile produced if the model is allowed to run until the curve is the same as the analytical result. The model produces a model age of 7.69 Ma, but the fit between the model and the analysed result is poor (SEE = 0.000620).

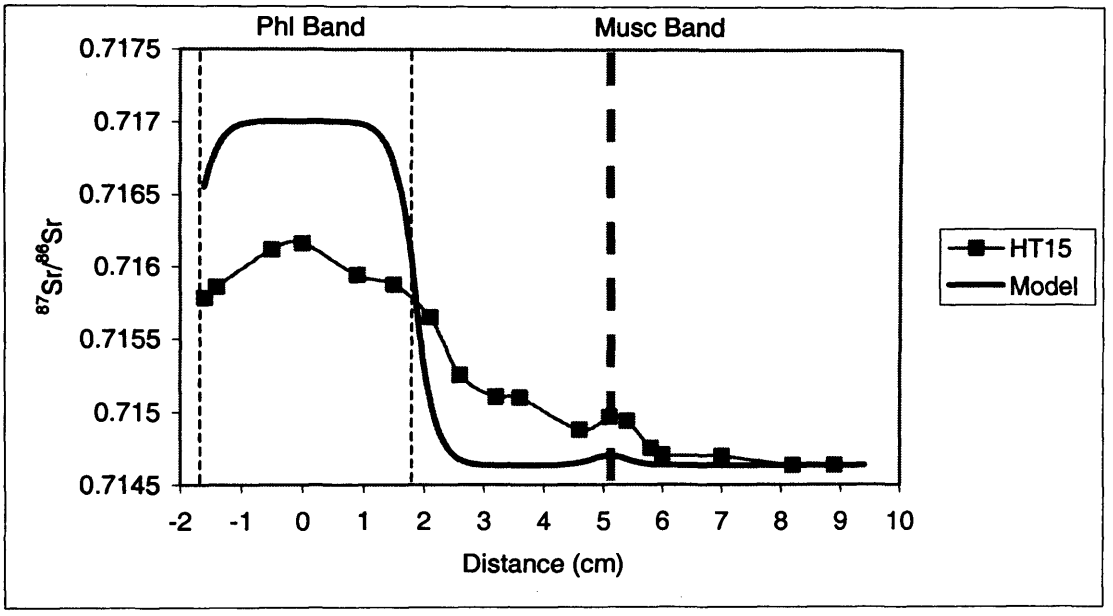

Figure 5.29 Isothermal finite difference models for HT15. The model equates the area under the model curve with the area under the measured curve. The mica band width is 3.6 cm, the diffusion coefficient is constant at $1.41 \times 10^{-19} m^2s^{-1}$ and r is kept constant at 0.000137. The initial profile is flat and starts at $^{87}Sr/^{86}Sr = 0.714634$, with $^{87}Rb/^{86}Sr = 2.49$ in the phlogopite band and $^{87}Rb/^{86}Sr = 0.99$ in the muscovite band.

However, isothermal models do not reflect reality and the following models have been produced assuming that diffusion slows according to the local cooling rate. Figure 5.30 shows models created using a diffusion coefficient of $1.41 \times 10^{-19} m^2s^{-1}$ and a cooling rate of 32 °C/Ma. The model shows the profile produced if the model is allowed to run until the curve is the same as the analytical result. The model produces a model age of 7.7 Ma but the fit between the model and the analysed result is poor (SEE = 0.000731).

Both of these models are flat-topped and produce very poor fits in the region between the two mica bands. This is because the $^{87}Sr/^{86}Sr$ builds up in the region of the mica band, but the diffusion coefficient is too slow to allow the strontium to diffuse into the surrounding calcite. The overall shape of the diffusion profile is produced by the diffusion coefficient and the shape of these two profiles suggests that the diffusion coefficient should be faster.

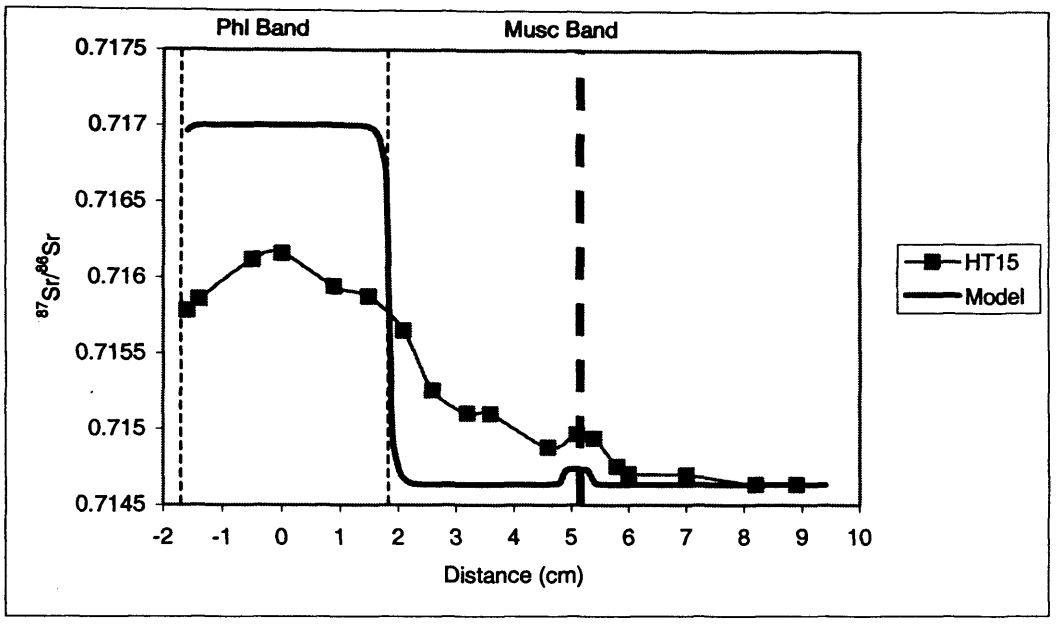

Figure 5.30 Finite difference models for HT15. The model equates the area under the model curve with the area under the measured curve. The mica band width is 3.6 cm, the diffusion coefficient is $1.41 \times 10^{-19} m^2 s^{-1}$ at 575 °C, decreasing with a cooling rate of 32°C/Ma and r is kept constant at 0.000137. The initial profile is flat and starts at $^{87}Sr/^{86}Sr = 0.714634$, with $^{87}Rb/^{86}Sr = 2.49$ in the phlogopite band and $^{87}Rb/^{86}Sr = 0.99$ in the muscovite band.

A faster rate of diffusion could be achieved by a greater number of grain boundaries or a faster rate of volume diffusion. The shape of the profiles given in Figures 5.29 and 5.30 suggest that a faster diffusion coefficient should be used in the finite difference models to achieve a better fit with the measured data. To increase the rate of diffusion, cleavage and twin planes, which form rapid diffusion pathways, can be considered. Assuming 30 rapid diffusion pathways per grain, the total volume of diffusion pathways in the sample = 9.9×10^{-10} m^3 (compare with Table 5.6 and Section 5.5.1, for HT15). This volume gives a δ/d value of 0.00099 and produces a diffusion coefficient of $1.41 \times 10^{-18} m^2 s^{-1}$ at 575 °C, a factor of ten faster than the previous D_{BULK}.

Figure 5.31 shows models created using a cooling rate of 32 °C/Ma with different diffusion coefficients (based upon the diffusion coefficient of 1.41×10^{-19} $m^2 s^{-1}$ at 575 °C). Model 1 uses a diffusion coefficient of 1.41×10^{-18} $m^2 s^{-1}$, Model 2 is for a diffusion coefficient of 1.41×10^{-17} $m^2 s^{-1}$ and Model 3 is for a diffusion coefficient of 1.41×10^{-16} $m^2 s^{-1}$. All three models run until the area beneath the curve is equal to the area beneath the analytical result. Models 1, 2, and 3 produce SEEs of 0.000664, 0.000481 and 0.000227 and finite difference model ages of 7.72 Ma, 7.69 Ma and 8.05 Ma respectively.

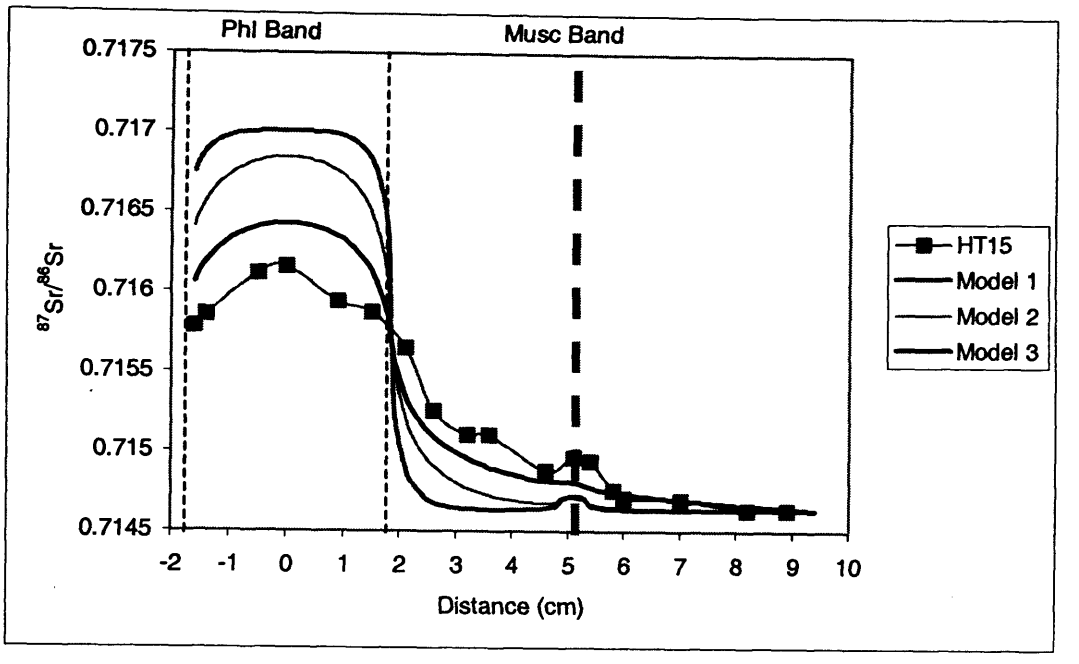

Figure 5.31 Finite difference models for HT15. Model 1 is for a diffusion coefficient of $1.41 \times 10^{-18} m^2 s^{-1}$, Model 2 is for a diffusion coefficient of $1.41 \times 10^{-17} m^2 s^{-1}$ and Model 3 is for a diffusion coefficient of $1.41 \times 10^{-16} m^2 s^{-1}$. The mica band width is 3.6 cm, the diffusion coefficient decrease with temperature with a cooling rate of 32°C/Ma and r is kept constant at 0.000137. The initial profile is flat and starts at $^{87}Sr/^{86}Sr = 0.714634$, with $^{87}Rb/^{86}Sr = 2.49$ in the phlogopite band and $^{87}Rb/^{86}Sr = 0.99$ in the muscovite band.

As shown on Figure 5.31, the faster the diffusion coefficient, the closer the model is to the analytical result. Another way of producing a better fit between the model and the analysed result is to decrease the cooling rate. With a lowered cooling rate, the diffusion remains at a higher rate for longer, allowing more $^{87}Sr/^{86}Sr$ to leave the region of the mica band in any given time step.

Figure 5.32 shows finite difference models for a diffusion coefficient of $1.41 \times 10^{-16} m^2 s^{-1}$ at 575 °C varying diffusion rate between 20 and 32 °C/Ma. At this faster diffusion rate, the best-fit model is produced by a cooling rate of 22 °C/Ma, as seen in Table 5.8 which shows the SEE and ages produced by all the models shown in Figure 5.32.

Table 5.8 Standard error of the estimate for different cooling rates, starting with a diffusion rate of $1.41 \times 10^{-16} m^2 s^{-1}$ at 625 °C.

Cooling Rate (°C/Ma)	Overall	Within Phl Band	Outside Phl Band	Area	Area Age (years)	FD Age (years)
32	0.000227	0.000382	0.000155	0.00247	7.99E+06	8.05E+06
28	0.000166	0.000270	0.000122	0.00247	8.01E+06	8.16E+06
24	0.000093	0.000108	0.000095	0.00245	7.96E+06	8.24E+06
22	0.000075	0.000062	0.000086	0.00245	7.93E+06	8.31E+06
20	0.000165	0.000267	0.000123	0.00247	8.00E+06	8.15E+06

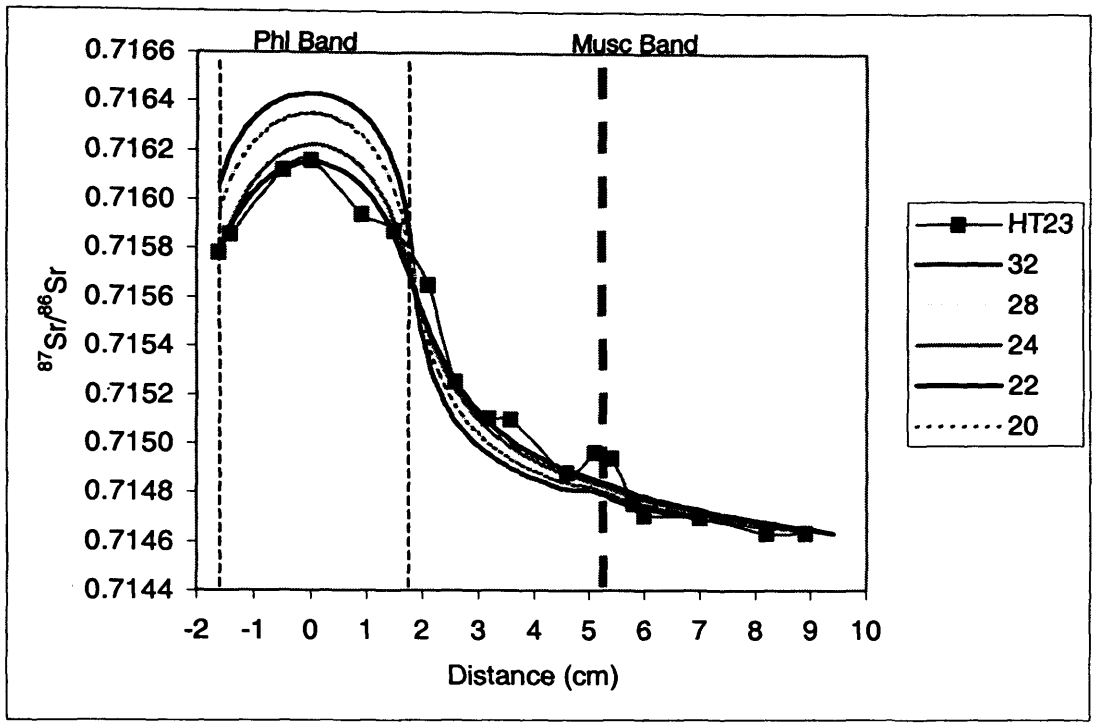

Figure 5.32 Finite difference models for HT15. The mica band width is 3.6 cm, the diffusion coefficient is 1.41 × $10^{-16}m^2s^{-1}$ at 575 °C, decreasing with different cooling rates of 20 °C/Ma, 22 °C/Ma, 24 °C/Ma, 28 °C/Ma or 32 °C/Ma and r is kept constant at 0.000137. The initial profile is flat and starts at $^{87}Sr/^{86}Sr$ = 0.714634, with $^{87}Rb/^{86}Sr$ = 2.49 in the phlogopite band and $^{87}Rb/^{86}Sr$ = 0.99 in the muscovite band.

Previously, it has been suggested that the overall cooling rate for the Lepontine Alps is 32 °C/Ma and work by Hurford (1986) suggests a local cooling rate of 32 °C/Ma for the area around Lago del Narèt (northern Valle Maggia). However, the lower cooling rate of 22 °C/Ma produces a better fit, suggesting that it is a more appropriate cooling rate for the northern Lepontine.

5.6 Discussion

5.6.1 *Dodson's Modelling*

The Dodson (1973) model suggests equilibration of Sr isotopes within an infinite reservoir. However, this study and the work of Jenkin *et al.* (1995) and Jenkin (1997) suggest re-equilibration between two or more minerals *via* the interdiffusion of Sr isotopes in a finite reservoir may be more realistic (in the case of a closed system rock). The measured $^{87}Sr/^{86}Sr$ profiles suggest a major re-equilibration event has taken place at the peak of metamorphism, which produced the present day background values in the calcite. This re-equilibration event occurred on a scale of centimetres to metres. Between the onset of cooling and the closure of the mica, Sr isotopes have exchanged between the micas and the calcite over a distance of several centimetres.

5.6.2 *Diffusion Coefficients*

This study has confirmed that Sr isotope exchange can be modelled using a combination of volume and grain boundary diffusion. The data for individual grains (Figure 5.9), suggest that the diffusion through grains is rapid, as almost flat profiles are produced. This implies either volume diffusion is very rapid or the movement of Sr through the grains is along rapid diffusion pathways (such as cleavage and twin planes). The models produced in Sections 5.5.7 and 5.5.8 suggest that the rate of diffusion required to produce the measured profiles can be up to 100 times greater than the diffusion coefficients calculated by Cherniak (1997). The rate of the bulk diffusion coefficient is affected by the grain size and the number of rapid diffusion pathways, which pass through the grains. Rapid diffusion pathways take the form of grain boundaries, cleavage and twin planes and fractures, which act in a similar way to grain boundaries, with a faster diffusion coefficient than that of volume diffusion. This implies that the number of microstructures present within grains has a direct influence on the rate of diffusion and microstructural features should always be considered in modelling using diffusion coefficients.

5.6.3 *What Happens in Terms of Measured Age?*

The concentration profiles (Figures 5.10 and 5.11) show that there is a concentration gradient within the calcite in terms of $^{87}Sr/^{86}Sr$ ratios. Calcite $^{87}Sr/^{86}Sr$ ratios are high within the phlogopite band and decrease with distance away from the mica. As the specimen is behaving as a closed system, the implication of this analytical study and the modelling results is that ^{87}Sr is leaving the phlogopite and entering the calcite. Calcite is gaining ^{87}Sr, so the slope of a two point isochron would change (in a closed system) depending upon where in the rock the calcite is sampled. Figure 5.33 shows a two point isochron, with the possible exchange paths for ^{87}Sr and ^{86}Sr. This implies that the down-temperature exchange of Sr isotopes between phlogopite and calcite causes the production of a lower than expected measured age (based upon a two point isochron) than would be expected if no exchange had taken place. However, the effect on the age is fairly small, for HT15 it is 0.4 Ma (within the error on the measured age) and for HT23 it is 0.7 Ma (using the mica separate data and comparing the difference in age between calcite in the mica band with calcite outside the mica band).

If ^{87}Sr is exchanging with ^{86}Sr then the implication is that ^{86}Sr must be entering the mica during isotopic exchange. As HT23 is bi-mineralic the only place for ^{87}Sr to come from is the phlogopite band and if calcite is losing ^{86}Sr, it must be going into the phlogopite to maintain mass balance. In HT15 the calcite gains additional ^{87}Sr from the muscovite present.

Modelling results show it is possible to achieve ^{87}Sr-^{86}Sr exchange over a period of several million years via a combination of volume and grain boundary diffusion. Sr is transferred from one area of the sample to another via grain boundary diffusion and then enters and diffuses through the grains via a combination of volume diffusion and "grain boundary" diffusion along twin and cleavage planes.

Overall cooling rates calculated from closure temperature ages in the Central Alps typically give rates of 25-35 °C/Ma and the models reflect these cooling rates.

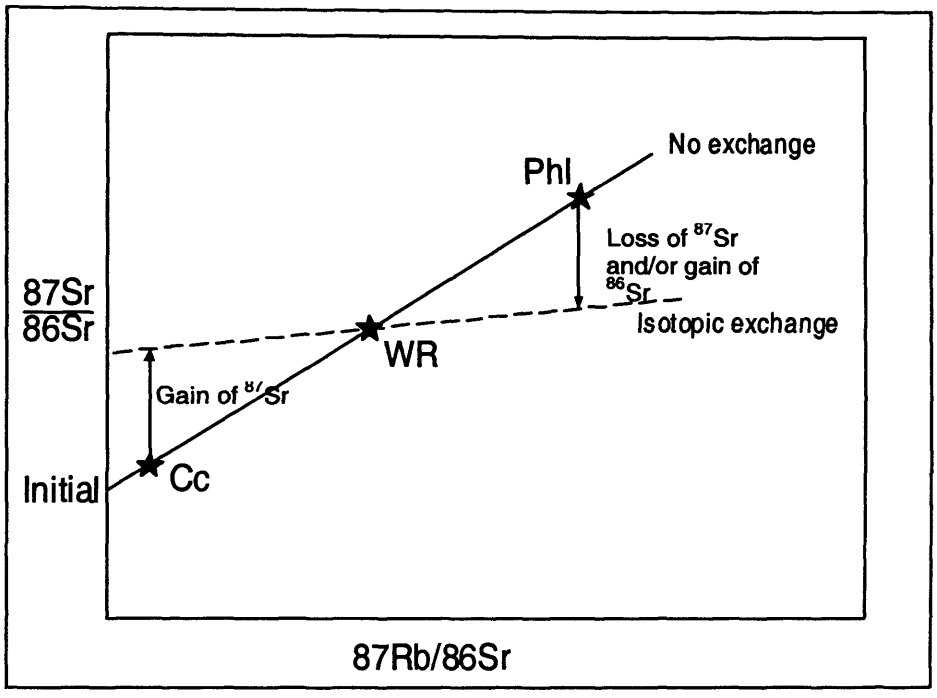

Figure 5.33 Isochron diagram to show the effects of strontium isotopic exchange on measured age.

5.6.4 *Applications*

The areas beneath the measured curves (Figures 5.10 and 5.11) correspond to the time interval between the onset of cooling (after the homogenisation event) and the phlogopite closure temperature age. Provided the system as a whole remains closed geochronologically (i.e. no Rb gain or loss, as in HT15), this method could potentially be used to determine cooling rates independently, which correspond to the time interval between the onset of cooling and the closure temperature of the mica phase. The shape of the curve relates to the cooling history of the sample, i.e. the cooling rate, which will control the distance the $^{87}Sr/^{86}Sr$ diffuses out of the mica band.

5.7 Conclusions

The laser ablation ICP-MS traverses indicate that exchange of strontium isotopes occurs between mica (both phlogopite and muscovite) and calcite during cooling from the peak of metamorphism. The following imply that the calculation of closure temperatures in the Rb-Sr system is more complex than the Dodson (1973) infinite reservoir model suggests:

- The $^{87}Sr/^{86}Sr$ traverses indicate that the length-scale of exchange is a few centimetres over several million years, implying exchange within a finite reservoir.
- The length-scale of exchange varies with the amount of radiogenic ^{87}Sr available in the mica, the size of the calcite grains and the mineral modes.

- Modelling indicates a combination of volume and grain boundary diffusion is a suitable mechanism for exchange between mica and calcite.

These points show that Sr isotopic exchange among minerals is dependent upon the rate of diffusion within and between different grains, the mineral grain sizes, the Sr concentration within different minerals and mineral mode. The exchange of strontium isotopes between phlogopite and calcite will alter the slope of a two point isochron to give a lower measured age than one calculated from minerals, which have not undergone isotopic exchange. More commonly dated rocks, such as biotite-bearing pelites and gneisses, should show similar effects.

Chapter 6

Chemical Exchange in the Rb-Sr Dating System.

6.1 Introduction

Determination of cooling and exhumation rates of metamorphic terranes depends on knowing closure temperatures for different geochronological systems. Closure temperatures have conventionally been assumed to relate to the effective cessation of isotopic exchange (for example, Sr isotopes in the Rb-Sr system) during cooling. However, results presented below suggest that the down-temperature *chemical* exchange of elements involved in dating schemes may also be important in controlling closure temperatures of radiometric systems.

Giletti (1991a), Jenkin *et al.* (1995), Jenkin (1997) and this work (Chapter 5) have modelled down-temperature exchange of Sr isotopes among minerals. However, in slowly cooled rocks there is the additional potential for down temperature exchange of elements, for example, the chemical exchange of Mg and Fe between biotite and garnet forms a geo-thermometer (Ferry & Spear, 1978). Previously Jenkin *et* al. (2001) found and have discussed chemical exchange within the calcite-phlogopite-feldspar system. Chemical exchange within the Rb-Sr system, as a rock cools, will cause variations in measured age, since the age depends upon both Rb and Sr contents. Ganguly & Ruiz (1986) discussed a thermodynamic model for closure temperatures in the Rb-Sr system, which suggested a wide variety of results for closure temperatures for the same mineral pairs if they experienced different cooling rates and chemical conditions in the host rock.

Chapter 5 discussed the down-temperature exchange of Sr isotopes in slowly cooled rocks and its effects on measured age. This chapter deals with the down-temperature chemical exchange of elements involved in dating schemes (specifically in the Rb-Sr system; for example, Rb with K, or Sr with Ca) and their control on closure temperatures of radiometric systems. Modelling the effects of down-temperature chemical exchange is possible using experimentally derived partition coefficients, which determine the preference of one mineral over another for each element. The down-temperature re-equilibration of isotopes and elements, principally those in the Rb-Sr dating system, is investigated by ion microprobe and laser ablation traverses across calcite, micas and feldspars in Alpine metacarbonate samples. Understanding the causes and effects of chemical and isotopic exchange produces better models of closure temperatures and, therefore, improves the constraints placed on the uplift rates of mountain belts.

6.2 Modelling

Here the potential effects of chemical exchange on mica ages for a simple phlogopite-K-feldspar and a more complex phlogopite-K-feldspar-muscovite rock are investigated, using experimentally derived partition coefficients. Within the Rb-Sr system (in these rocks), there is the potential for exchange of Rb (with K) between micas and K-feldspar and Sr (with Ca) among

calcite, micas and feldspars. Modelling work has been completed using experimentally derived partition coefficients

6.2.1 *Partitioning behaviour in the Phlogopite-K-Feldspar, Rb-K system*

Experimental data for phlogopite and sanidine (Beswick, 1973) suggest the partitioning of Rb and K changes so that, in cooling closed systems, Rb in feldspar should decrease and Rb in mica increase. Assuming that a phlogopite-sanidine system approximates a phlogopite-K-feldspar system, the exchange during cooling of a metamorphic rock can be predicted. The aim of this modelling is to examine the distribution of Rb atoms among phases using partition coefficients between vapour, muscovite, phlogopite and sanidine.

Partition coefficients describe the preference for a certain species by one mineral over another (i.e. they describe which minerals are likely to lose and which are likely to gain certain species with changing conditions). In the general form (where P is the partition coefficient, $[A_x]$ is the concentration of species x in mineral A and $[B_x]$ is the concentration of species x in mineral B):

$$P^{A}/_{B} = \frac{[A_x]}{[B_x]} \qquad (6.1)$$

The experimentally derived partition coefficients for mineral-vapour pairs (Beswick, 1973) are combined to give mineral-mineral partition coefficients. For example, the phlogopite-K-feldspar system where P refers to the partition coefficient, phl = phlogopite, fsp = K-feldspar, V = vapour:

$$P^{phl}/_{fsp} = \frac{P^{phl}/_{V}}{P^{fsp}/_{V}} \qquad (6.2)$$

In terms of natural logs:

$$\ln P^{phl}/_{fsp} = \ln P^{phl}/_{V} - \ln P^{fsp}/_{V} \qquad (6.3)$$

Using certain known (measurable) values, such as; partitioning behaviour (Figure 6.1), mineral mode, whole rock concentration and temperature and assuming an equilibrium relationship, the amount of Rb in specified minerals can be determined per formula unit (p.f.u.) and hence their Rb concentration (in ppm).

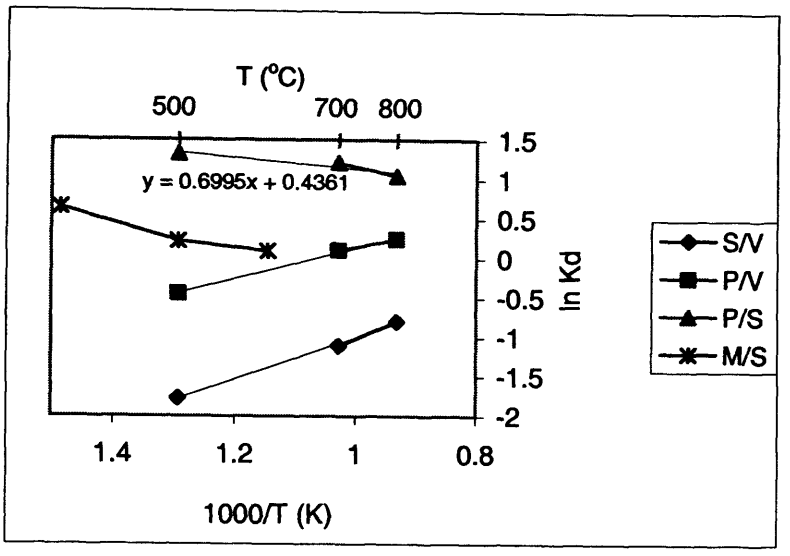

Figure 6.1 Graph to show the Rb/K partitioning behaviour between sanidine (S), phlogopite (P), muscovite (M) and vapour (V); data are from Beswick (1973) for sanidine and phlogopite and from Volfinger (1976) for muscovite. The regression equation given describes the phlogopite/sanidine partitioning behaviour in terms of 1000/T.

Figure 6.1 shows that partitioning varies widely at low temperatures and tends towards zero at high temperatures. Generally the partitioning of elements between phases decreases as temperature increases (Spear, 1993); in other words ln P tends towards zero as temperature increases. This occurs because, as the temperature increases, the energetic distinction between different elements becomes smaller and minerals display less of a preference for one element over another, Spear (1993). At lower temperatures partitioning behaviour becomes significant and, in a slowly cooled terrane, will affect what occurs to any element or radiogenic daughter product lost from minerals.

6.2.3 *Modelling the Phlogopite-K-feldspar System*

The aim of this section is to produce a model, which defines what happens to the Rb concentration of minerals with decreasing temperature. Table 6.1 shows some of the data used to calculate Rb p.f.u. of a phase.

Table 6.1 Values used in the Rb-K partitioning calculations.

Phase	Chemical formula	Molecular weight (g)	Molar volume*	Volume Fraction#	Rb + K (p.f.u.)§
Calcite	$CaCO_3$	100.09	36.93	A	0
Phlogopite	$KMg_3(Si_3AlO_{10})(OH,F)_2$	419.25	149.73	B	1
K-feldspar	$KAlSi_3O_8$	278.33	108.72	C	1
Biotite	$K(Mg,Fe)_3(Si_3AlO_{10})(OH,F)_2$	433.53	140.30	D	1
Muscovite	$KAl_2(Si_3AlO_{10})(OH,F)_2$	398.51	141.32	E	1

* Molar volumes are taken from Deer, Howie & Zussman (1963).
# Volume fractions and the total volume of material are all known from point counts and the volume fraction is calculated using: volume fraction A = (A/(A+B+C+D+E+F).
§ The number of atoms of Rb + K in an ideal formula unit of the phase.

The partitioning relationships used here have been investigated over a temperature range of 500 to 800 °C for phlogopite/sanidine (Beswick, 1973) and 400 to 600 °C for muscovite/sanidine (Volfinger, 1976), shown in Table 6.2.

Table 6.2 Partition coefficients of Rb/K between phlogopite, sanidine and vapour (Beswick, 1973) and muscovite, sanidine and vapour (Volfinger, 1976).

Temperature (°C)	400	500	600	700	800
P/v*		0.64		1.11	1.28
S/v*		0.17		0.33	0.45
P/S*		3.76		3.36	2.84
M/S*	1.9	1.25	1.1		
P/S (B)#		4.13		3.21	2.95

*P = phlogopite, S = sanidine, v = vapour, M = muscovite.
#P/S (B) Beswick's regressed data (not used in calculations).

Differences between the relationships quoted in Beswick (1973) and the one used in this study are due to using the P/S values rather than the P/S(B) values quoted in Table 6.2 (i.e. using Beswick's actual experimental data as the regressed data seems to contain errors). The partition relationships used are expressed in terms of natural logs.

Table 6.3 Symbols commonly used in formulae.

Symbol	Definition
$tRbK_{(phase)}$	Number of Rb+K atoms per formula unit of mineral.
$tRbK_{sys}$	Number of Rb+K atoms in the system
$Rb_{(phase)}$	Number Rb atoms per formula unit of mineral
$P^{x/y}$	Partition coefficient x/y
Vf	Volume fraction
Mf	Mole fraction (number of moles normalised to 1)
Rb_{sys}	Rb in the system
Atomic mass Rb	85.4678

The partitioning relationship of K and Rb between phlogopite and K-feldspar is governed by (after Beswick, 1973):

$$\ln P^{phl}/_{fsp} = \frac{699.5}{T} + 0.4361 \qquad (6.4)$$

Where T is the temperature in Kelvin. This equation is derived from data in Table 6.2 and within this relationship:

$$P^{phl}/_{fsp} = \frac{\left(\frac{Rb}{K}\right)_{phl}}{\left(\frac{Rb}{K}\right)_{fsp}} \qquad (6.5)$$

and

$$P^{fsp}/_{phl} = \frac{\left(\frac{Rb}{K}\right)_{fsp}}{\left(\frac{Rb}{K}\right)_{phl}} = \frac{1}{P^{phl}/_{fsp}} \qquad (6.6)$$

From Equation 6.6:

$$\left(\frac{Rb}{K}\right)_{fsp} = P^{fsp}/_{phl} \times \left(\frac{Rb}{K}\right)_{phl} \qquad (6.7)$$

The Rb and K contents of a phase are related to the total Rb+K of each phase (see Table 6.1), for example,

$$K_{phl} = tRbK_{phl} - Rb_{phl} \qquad (6.8)$$

and

$$K_{fsp} = tRbK_{fsp} - Rb_{fsp} \qquad (6.9)$$

Substituting 6.8 and 6.9 into Equation 6.7 gives the partitioning relationship in terms of Rb content,

$$\frac{Rb_{fsp}}{tRbK_{fsp} - Rb_{fsp}} = P^{fsp}/_{phl} \times \frac{Rb_{phl}}{tRbK_{phl} - Rb_{phl}} \qquad (6.10)$$

Rearranging and simplifying Equation 6.10 gives Rb_{fsp} (Rb p.f.u. feldspar) in terms of Rb_{phl} (Rb p.f.u. phlogopite).

$$Rb_{fsp} = \frac{\left(P^{fsp}/_{phl} \times Rb_{phl} \times tRbK_{fsp}\right)}{\left(tRbK_{phl} - Rb_{phl}\right) + \left(P^{fsp}/_{phl} \times Rb_{phl}\right)} \qquad (6.11)$$

Equation 6.11 is then used to calculate the Rb concentration per formula unit of K-feldspar, solving for Rb_{phl} by iteration, using the constraint that Rb_{sys} is exactly equal to Rb'_{sys} (see Equations 6.15 and 6.16).

To calculate the amount of Rb in the system, the number of moles and the mole fraction of both phases need to be found (using K-feldspar as an example):

$$\text{no moles}_{fsp} = \frac{Vf_{fsp} \times \text{total volume}}{\text{molar volume}_{fsp}} \qquad (6.12)$$

Normalising the number of moles to one, gives the mole fraction:

$$Mf_{fsp} = \frac{\text{no. moles}_{fsp}}{\text{total no. moles}} \qquad (6.13)$$

Using $tRbK_{phase}$ and the mole fractions, the total Rb and K in the system can be calculated:

$$tRbK_{sys} = (Mf \times tRbK)_{fsp} + (Mf \times tRbK)_{phl} \qquad (6.14)$$

$tRbK_{phase}$ is known from the molecular formula of the mineral, assuming that Rb can only exchange with K in both feldspar and mica. To solve for the Rb p.f.u. of both phases, the amount of Rb in the system needs to be calculated and this can be accomplished in two ways:

$$Rb'_{sys} = (Mf \times Rb)_{fsp} + (Mf \times Rb)_{phl} \qquad (6.15)$$

and,

$$Rb_{sys} = Rbno._{sys} \times tRbK_{sys} \qquad (6.16)$$

The easiest way to solve all these equations is in the form of a spreadsheet, solving for Rb'_{sys} by finding Rb_{phl} and $Rbno._{sys}$ (the number of Rb atoms in the system, found by iteration) with the constraint that Rb_{sys} must equal Rb'_{sys}. To calculate the Rb concentrations in ppm, mass fractions need to be used (using K-feldspar as an example):

$$\text{mass}\, Rb_{fsp} = Rb_{fsp} \times \text{atomic weight Rb} \qquad (6.17)$$

Equation 6.17 gives the mass of Rb per formula unit of feldspar in grams and,

$$\text{mass}_{fsp} = \text{molecular mass}_{fsp} \times \text{no. moles}_{fsp} \qquad (6.18)$$

Equation 6.18 gives the mass of one formula unit of feldspar in grams. Equation 6.19 returns the Rb concentration of the phase in ppm.

$$Rb\,ppm_{fsp} = 1000000 \times \left(\frac{\text{mass}\, Rb_{fsp}}{\text{mass}_{fsp}} \right) \qquad (6.19)$$

Multiplying the value returned in Equation 6.19 by the mass fraction of the phase normalises the Rb concentration to the whole rock Rb concentration:

$$\text{whole rock Rb ppm} = (Mf_{fsp} \times Rb\,ppm_{fsp}) + (Mf_{phl} \times Rb\,ppm_{phl}) \qquad (6.20)$$

The whole rock Rb concentration is used as a constraint so that the whole rock Rb ppm value calculated equals the Rb ppm input value (assuming a closed system). The whole rock concentration value is set by the user to be consistent with realistic rocks.

The spreadsheet can be further modified by the addition of more phases, for example, muscovite, again using sanidine as an approximation for orthoclase, with data derived from Volfinger (1976):

$$\ln P^{musc/fsp} = \ln\left(\frac{Rb/K_{musc}}{Rb/K_{fsp}}\right) = \frac{1526.4}{T} - 1.6643 \quad (6.21)$$

Equation 6.22 shows the relationship between K-feldspar and vapour, which can be used to calculate the Rb concentration in an aqueous vapour, a possible pore-space phase (derived from Beswick, 1973):

$$\ln P^{fsp/v} = \ln\left(\frac{Rb/K_{fsp}}{Rb/K_{v}}\right) = -\frac{2649.1}{T} + 1.6464 \quad (6.22)$$

Equations 6.4 to 6.20 can be modified to represent the partitioning between muscovite and K-feldspar (using the relationship expressed in 6.21) and added to the spreadsheet. These relationships are then used to calculate the Rb content of each mineral.

6.3 Results of Modelling

Using the spreadsheet, variations in mineral Rb concentration, at equilibrium, can be calculated. Temperatures, whole rock Rb concentrations and mineral modes in these examples are chosen to be consistent with samples collected from the amphibolite facies marbles of the Lepontine Alps, Central Swiss Alps.

6.3.1 *Three-phase System (Phlogopite/K-feldspar/Calcite)*

The three-phase system models are based upon rocks containing ~90% calcite, with varying amounts of phlogopite and K-feldspar. In these models, phlogopite and K-feldspar are assumed to be the only phases capable of bearing Rb in their mineral lattices.

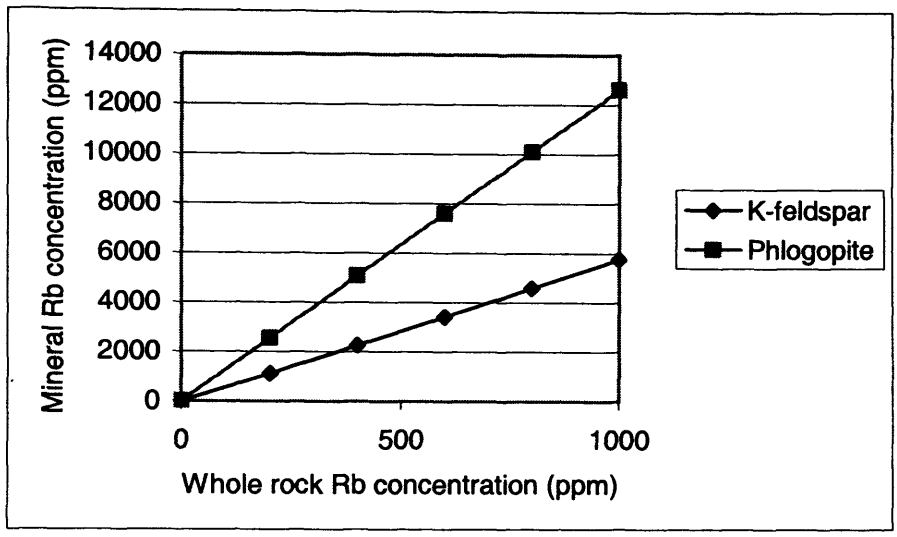

Figure 6.2 Mineral Rb concentrations calculated at 600 °C, with volume fractions of 0.06 for phlogopite 0.04 for K-feldspar and 0.9 for calcite.

Figure 6.2 shows the varying mineral Rb concentration with varying whole rock concentration at high temperatures. As the whole rock Rb concentration increases, the Rb concentration in the individual minerals increases. Due to the partitioning behaviour (Equation 6.3) between phlogopite and K-feldspar, Rb is more likely to reside in phlogopite than in K-feldspar giving the mica the higher Rb concentration for any given temperature.

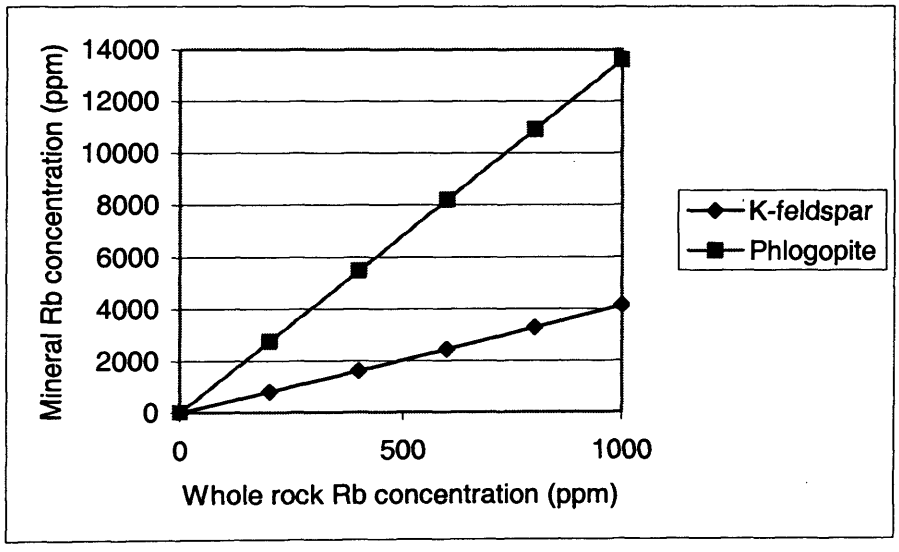

Figure 6.3 Mineral Rb concentrations calculated at 300 °C, with volume fractions of 0.06 for phlogopite, 0.04 for K-feldspar and 0.9 for calcite.

At 300 °C (Figure 6.3), for the same whole rock Rb concentrations, phlogopite contains more and K-feldspar contains less Rb than at 600°C. The greater difference in Rb concentration between the two minerals occurs because partitioning becomes more significant at lower temperatures.

Figure 6.4 shows the effect of varying the mineral mode on mineral Rb concentration, keeping the temperature and whole rock Rb concentration constant.

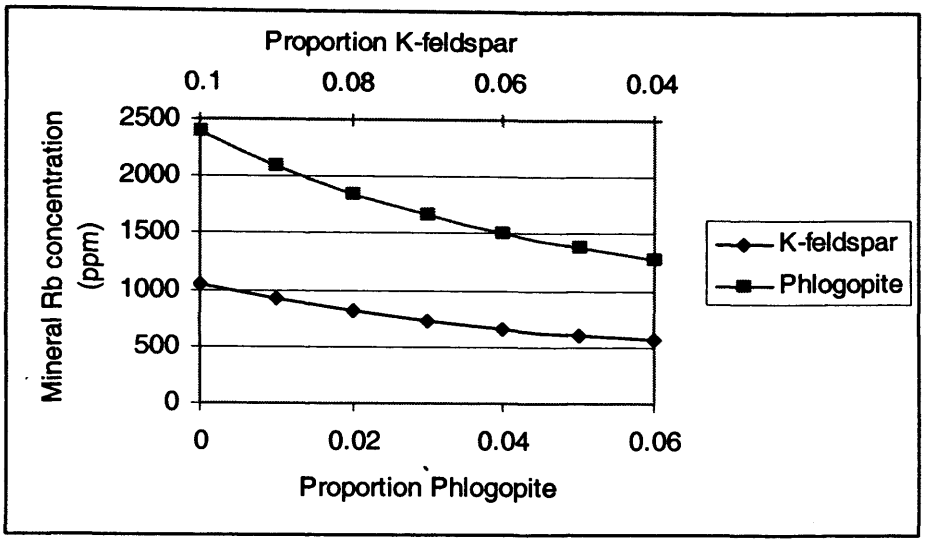

Figure 6.4 Varying the mineral modes at constant temperature (600 °C) and whole rock Rb concentration of 100 ppm (and assuming 90% of the rock is made up of calcite).

With increasing volume fraction of phlogopite, the Rb concentration of individual grains increases. As the volume fraction of phlogopite increases, its Rb concentration approaches that of the whole rock, as most of the Rb is held in the mica.

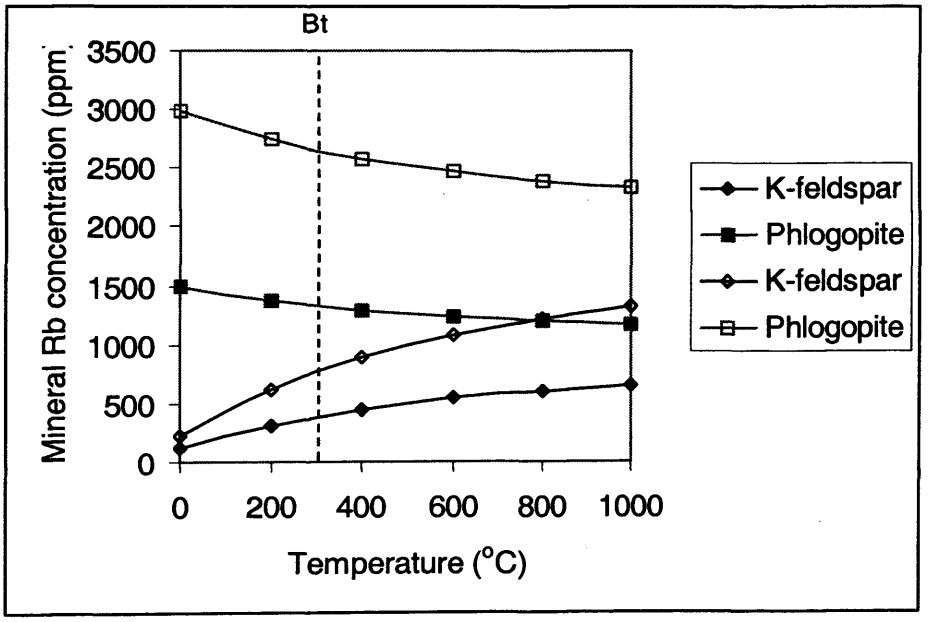

Figure 6.5 Plot of mineral Rb concentration with varying temperature and constant whole rock concentration 100 (solid symbols) or 200 (unfilled symbols) ppm and constant volume fraction of phlogopite (0.06), K-feldspar (0.04) and calcite (0.9). The biotite closure temperature (Rb-Sr) is marked at 300°C (dashed line).

Figure 6.5 shows that with decreasing temperature, the Rb concentration in phlogopite increases. Down-temperature equilibration of Rb and K in a phlogopite-K-feldspar rock should increase the Rb concentration in mica and decreases it in K-feldspar. This change with temperature would lower the slope of an isochron, and hence the measured age, of rocks that have undergone chemical

exchange. The amount of exchange that occurs, and therefore the change in age, is limited by the inter-diffusion of Rb and K between the two minerals.

6.3.2 *Summary of Three-phase Behaviour*

With increasing whole rock concentration, the Rb concentration of the two Rb-bearing minerals increases. The partitioning behaviour between phlogopite-K-feldspar dictates that more Rb resides in phlogopite than K-feldspar. With decreasing temperature, the Rb concentration in K-feldspar decreases as the Rb concentration in phlogopite increases. This exchange will decrease the age measured and lower the closure temperature compared to that calculated assuming exchange of Sr isotopes only, if the chemical exchange occurs after the isotopic exchange. The amount of Rb in the phlogopite increases with the K-feldspar/phlogopite ratio (Figure 6.4), so that the decrease in closure temperature will be greatest in K-feldspar rich rocks. These results add to previous suggestions that mica Rb-Sr ages vary with mineral mode and therefore, rock type (Jenkin *et al.*, 1995). This can be examined by looking at the results of dating work from the Swiss Alps, which show different mica Rb-Sr ages for different rock types (comparing Hunziker, 1992; Steiner, 1984a and unpublished work by this author, see Section 4.2.2).

6.3.3 *Four-phase System (Phlogopite, Muscovite, K-feldspar and Calcite)*

The four-phase system models are based upon rocks containing >80% calcite, with varying amounts of phlogopite, muscovite and K-feldspar. In these models the phlogopite, muscovite and K-feldspar are assumed to be the only phases capable of bearing Rb in their mineral lattices. This system represents samples found at Lago del Narèt, which contain two mica phases.

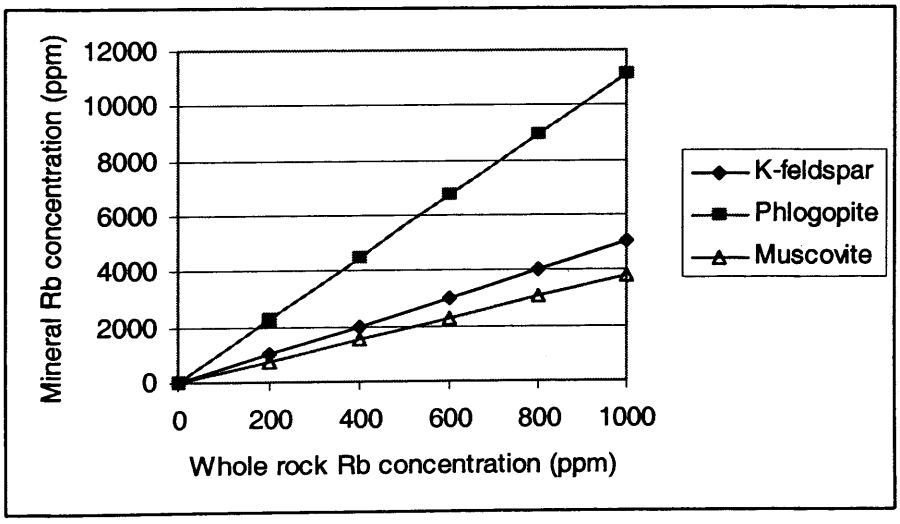

Figure 6.6 Mineral Rb concentrations calculated at 600 °C, with volume fractions of calcite (0.87), K-feldspar (0.04), phlogopite (0.06) and muscovite (0.03).

Figure 6.6 shows that as the whole rock concentration increases, the Rb concentration of the individual minerals increases. Due to the partitioning behaviour between the phases, Rb is more

highly concentrated within the phlogopite grains and is approximately equally concentrated in both muscovite and K-feldspar.

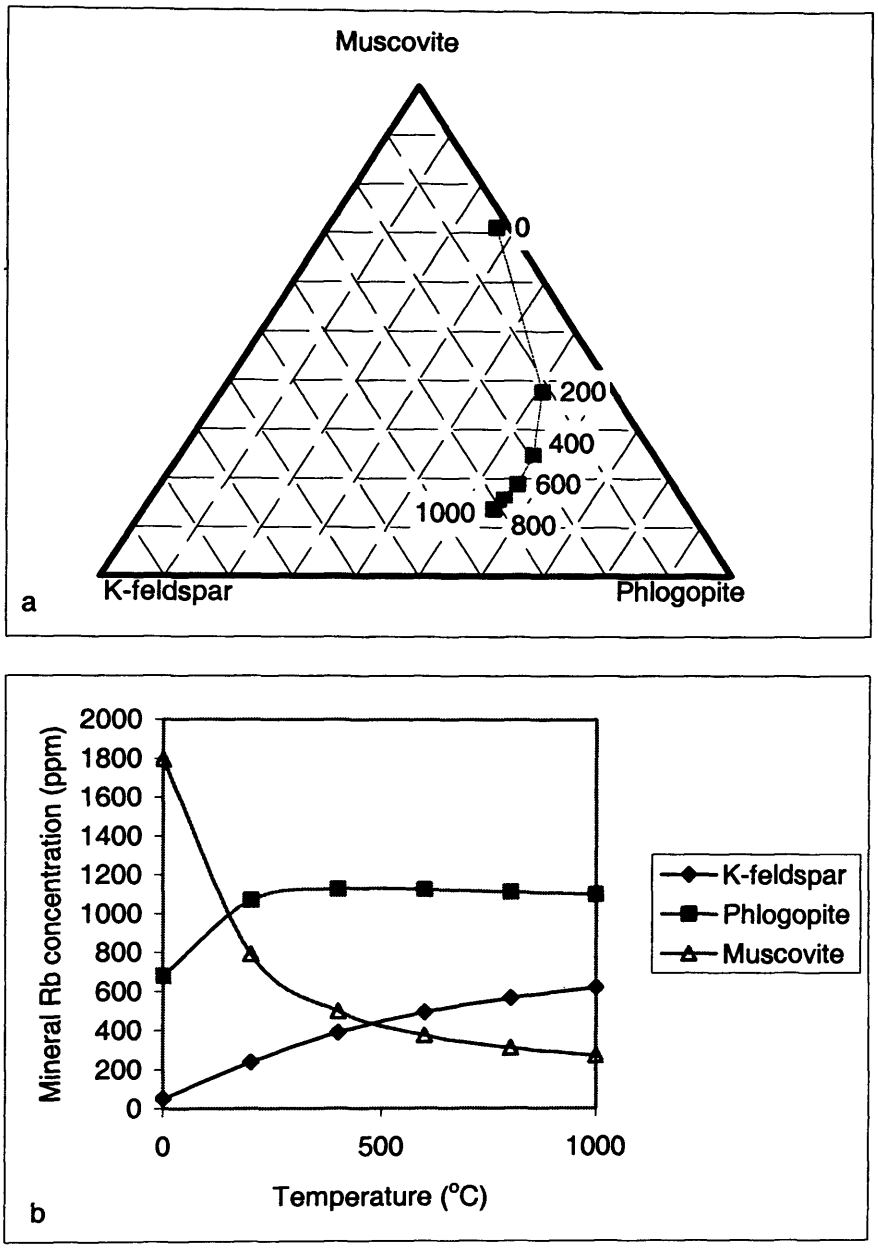

Figure 6.7 a) Triangular plot to show the effect on mineral Rb concentration (plotted as a proportion) of varying temperature (the apices of the plot mean that phase contains 100% of the Rb present) and **b)** plot of changing mineral Rb concentration with temperature. Both a and b have constant whole rock concentration (100 ppm) and constant volume fractions (taken from HT15) of calcite (0.87), K-feldspar (0.04), phlogopite (0.06) and muscovite (0.03). The numbers next to the data points represent the temperature in °C.

Figure 6.7 shows that with decreasing temperature the Rb concentration of K-feldspar decreases and that of muscovite increases. In phlogopite, the Rb concentration increases slightly between 1000 and 500°C and then decreases at lower temperatures. The partitioning behaviour of Rb and K between phlogopite and K-feldspar and between muscovite and K-feldspar, in cooling closed systems, changes so that generally Rb in K-feldspar decreases and Rb in the mica phases increases (except at the lowest temperatures for phlogopite). At the lowest temperatures the

difference in Rb concentration between phlogopite and K-feldspar decreases, which is not expected from the partitioning behaviour described by Beswick (1973). This implies that at lower temperatures, the muscovite partitioning relationship has the greatest influence on the chemical exchange (Figure 6.1, which shows that muscovite will have the greatest effect on Rb partitioning low temperatures).

Down-temperature equilibration of Rb and K increases the Rb present in the muscovite and phlogopite (until a point below the current estimates of phlogopite closure temperature) and lowers the Rb concentration of K-feldspar. This would lower the slope of an isochron plotted from data of rocks that have undergone chemical exchange.

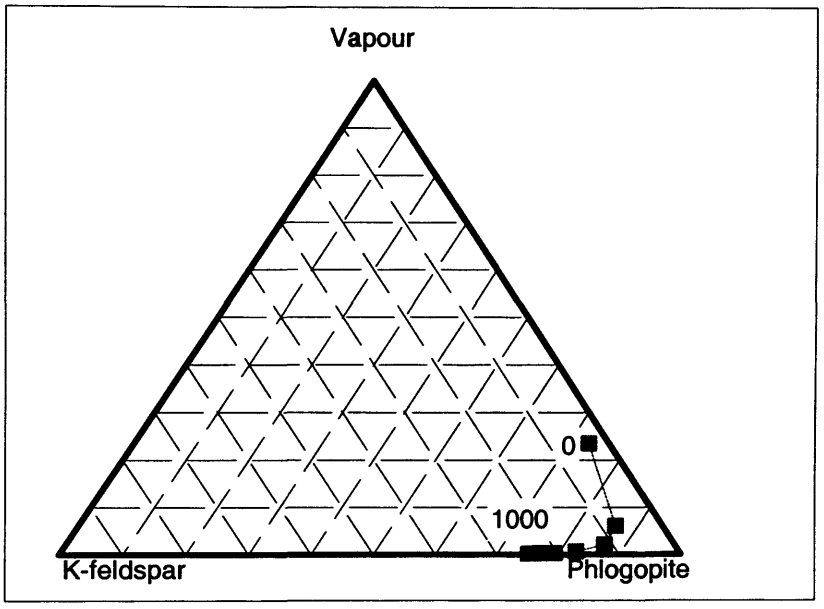

Figure 6.8 Triangular plot to show the effect on Rb concentration (plotted as a proportion) of varying temperature on Rb concentration in different phases, with constant whole rock concentration (100 ppm) and constant volume fractions (taken from HT15) of K-feldspar (0.04), phlogopite (0.06) and vapour (0.05).

Figure 6.8 shows that with decreasing temperature, more Rb is partitioned into the fluid phase (assuming the fluid phase is water with a molar volume of 24 cm^3mol^{-1}, a molar mass of 18.015g and a density of 0.75 gcm^{-3}). At the same time, Rb is being lost by the K-feldspar and gained by the phlogopite, in a similar way to the down-temperature exchange between K-feldspar and phlogopite shown in Figure 6.5. Below ~ 200 °C phlogopite begins to lose Rb.

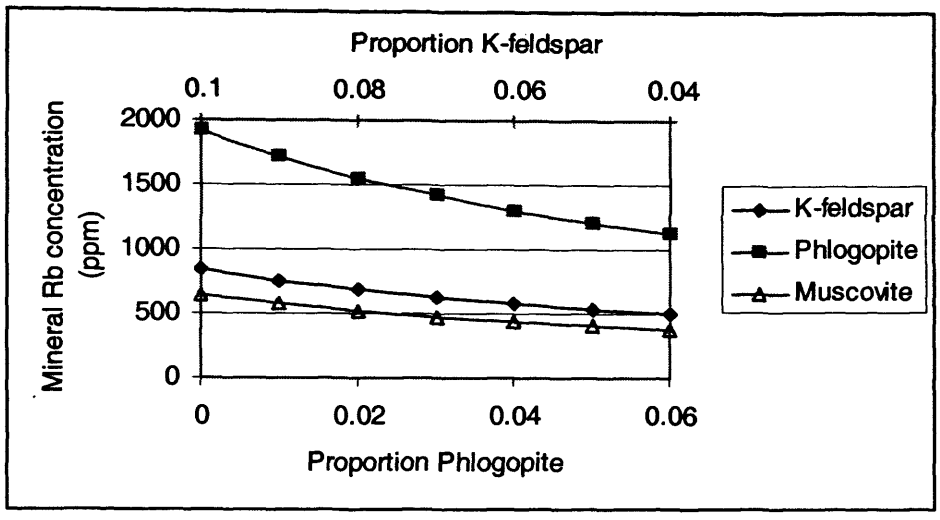

Figure 6.9 Varying mode of phlogopite and K-feldspar with constant muscovite (0.1) at 500°C and 100 ppm whole rock concentration.

With increasing volume fraction of phlogopite (Figure 6.9), the Rb concentration of individual grains decreases (as most Rb is held in the mica).

6.3.4 *Summary for a four-phase system.*

With increasing whole rock concentration, the Rb concentration of all three minerals increases. The partitioning behaviour between phlogopite-muscovite-K-feldspar dictates that more Rb resides in phlogopite than the other two minerals until ~ 200 °C where muscovite has the highest Rb concentration. Down-temperature exchange of Rb and K shows decreasing Rb concentration in K-feldspar with increasing Rb concentration in muscovite. Rb in phlogopite also increases but then decreases at lowest temperatures (below the biotite closure temperature). Increasing Rb in micas (and decreasing that in K-feldspar) will lower the slope of a Rb/Sr isochron, decreasing the age measured and lowering the closure temperature compared with that calculated assuming exchange of Sr isotopes only. The increase in Rb in the phlogopite increases with the K-feldspar/phlogopite ratio, so that the decrease in closure temperature will be greatest in K-feldspar rich rocks. These results add to previous suggestions that mica Rb-Sr ages vary with mineral mode and therefore, rock type (Jenkin *et al.*, 1995).

6.3.5 *Rb-K Interdiffusion*

The rate of exchange is controlled by the rate of K-Rb interdiffusion among the minerals involved in the exchange. There is no published data on K diffusion in phlogopite.

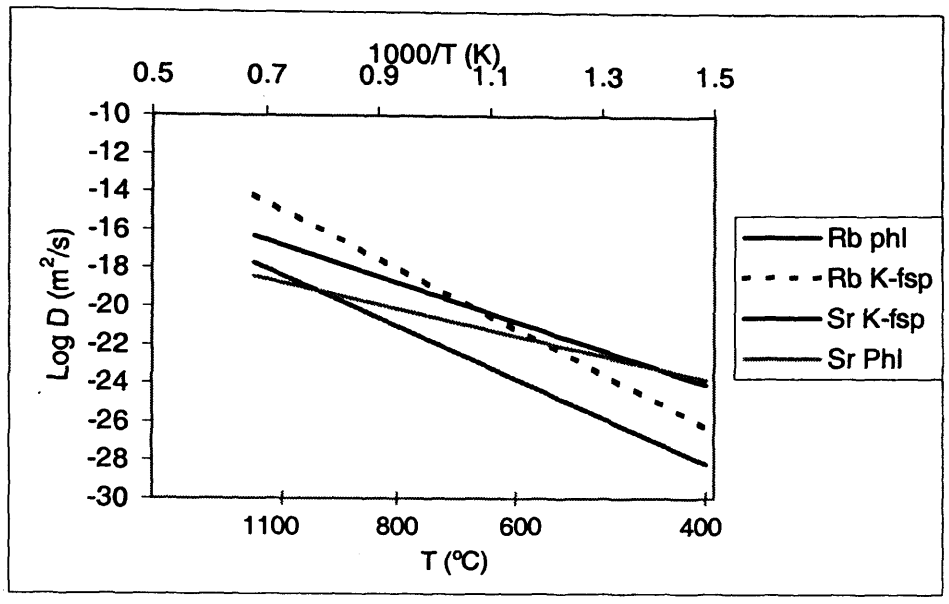

Figure 6.10 The rate of Rb and Sr diffusion through fluorophlogopite (parallel to the c-axis; Hammouda & Cherniak, in press and Hammouda & Cherniak, 2000 respectively) and Rb and Sr through orthoclase (Giletti, 1991).

Figure 6.10 shows an Arrhenius plot for Rb and K diffusion data in fluorophlogopite and orthoclase. This plot suggests that the rate of exchange of Rb and K between phlogopite and K-feldspar will be controlled by the rate of Rb diffusion in the mica at temperatures above 600 °C and by K-feldspar below 600 °C.

6.3.6 *Sr-Ca Exchange*

Similar models can be produced for Sr-Ca exchange between plagioclase and calcite. The diffusion of Sr-Ca between calcite and plagioclase behaves in such a way that there is little exchange between these two species, except at very high temperatures (> 600 °C, which is greater than the peak metamorphic temperature and lower than the Dodson (1973) closure temperature for all but the smallest plagioclase grains). This suggests that Sr/Ca exchange should not be taking place between calcite and plagioclase in the Lepontine marbles. There is also the possibility of exchange between calcite and K-feldspars.

6.3.7 *Implications of Modelling Results*

Down-temperature chemical exchange increases Rb in phlogopite (arrow 1) and decreases Rb in K-feldspar (arrow 2). This produces a lower slope for the Rb-Sr isochron and, therefore, a lower measured age. The effects of the chemical exchange (Rb with K) depend upon timing in relation to any isotopic exchange. Greater effects will be noticed if chemical exchange occurs after isotopic exchange has slowed and the isochron has started to develop. For the same temperature range, Sr diffuses one order of magnitude faster than Rb in the same type of mineral (see Figure 6.10, at around 600 °C). The effects of chemical exchange may not be noticed if it occurs while isotopic exchange is rapid enough to give both minerals similar $^{87}Sr/^{86}Sr$ ratios. Chemical exchange

enhances the effect of isotopic exchange, further lowering the measured age (Figure 6.11) and the closure temperature.

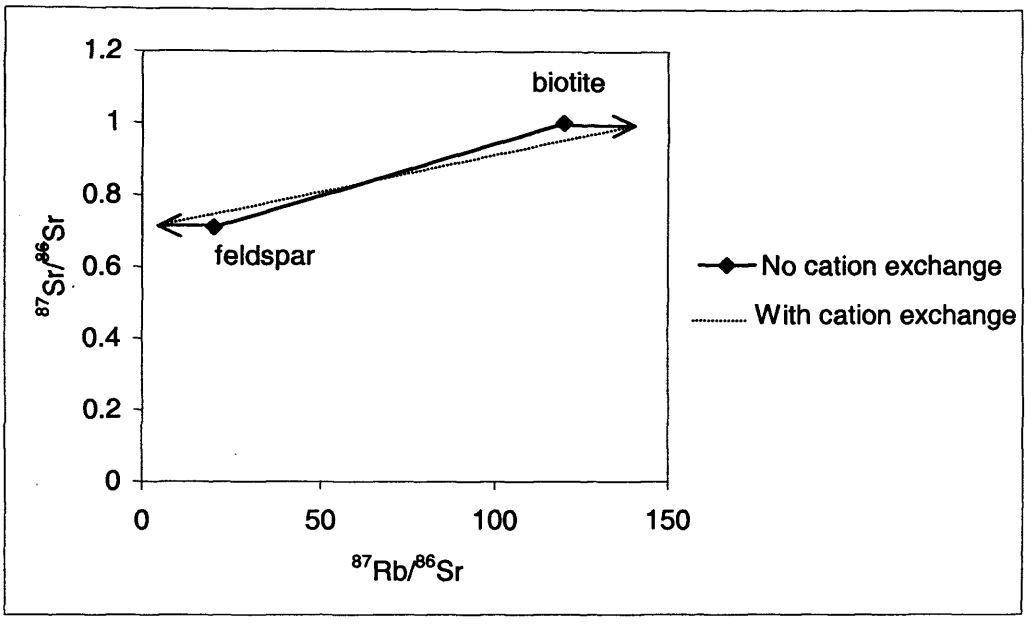

Figure 6.11 Rb-Sr isochron diagram to show alteration in measured age.

6.4 Electron and Ion microprobe traverses

Electron microprobe work was carried out at Leicester University on a JEOL 8600 S automated instrument. All ion microprobe work was carried out at the Ion Microprobe Facility at Edinburgh University on a Cameca ims-4f ion microprobe. For conditions and standards for electron and ion microprobe analyses and further microprobe data, see Appendix 4.

6.3.2 *Calcite - Results and Interpretation*

In Chapter 5, the exchange of Sr isotopes between calcite and micas was discussed. It was suggested that at the same time as ^{87}Sr increases in the calcite, other Sr isotopes move in the opposite sense. Here the exchange of elements in calcite is considered.

Figures 6.12 to 6.14 show calcite electron microprobe traverses. Microprobe traverses were taken across orange-luminescing calcite grains free from dolomite exsolution.

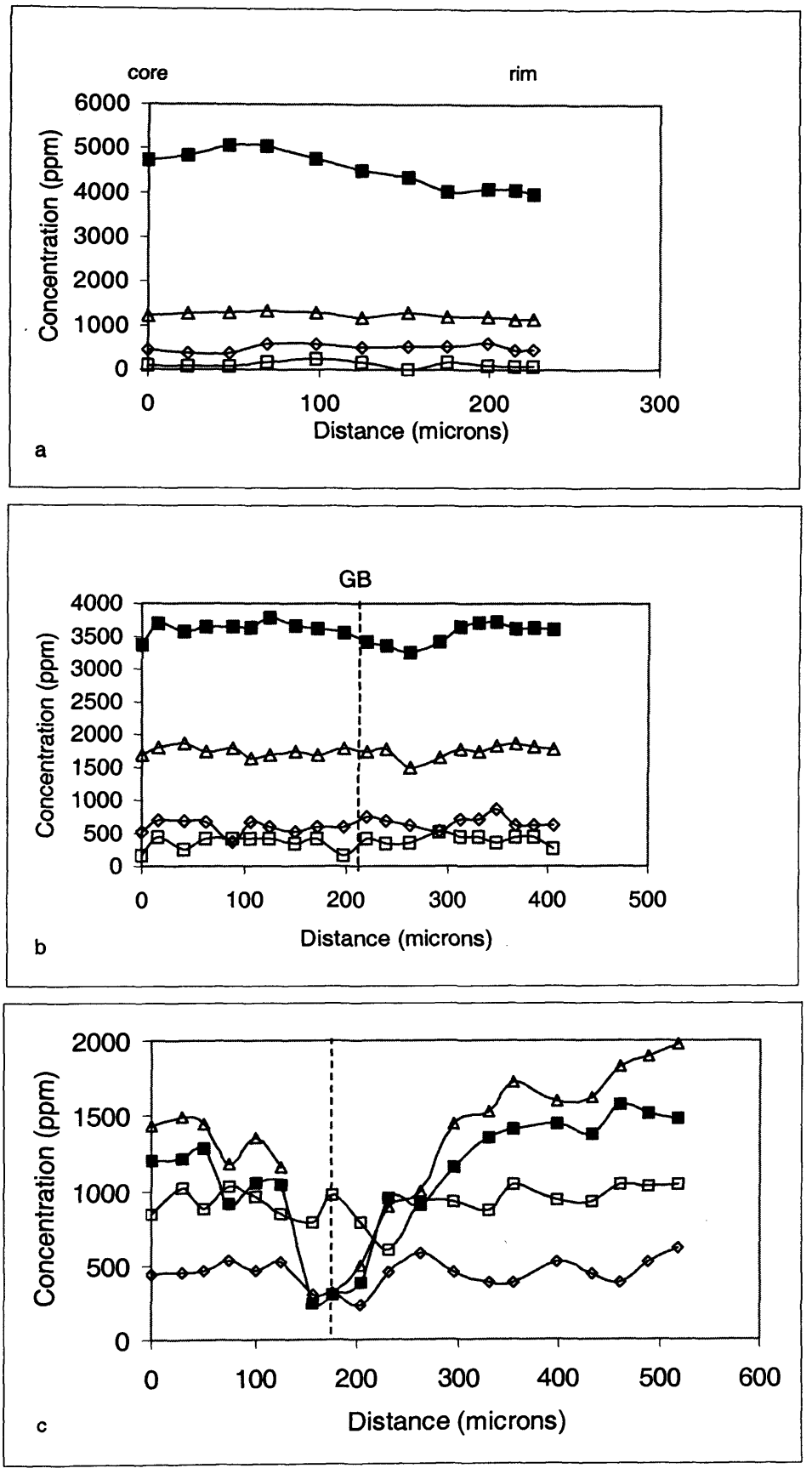

Figure 6.12 Calcite traverses from Lago del Narèt; **a** HT17, **b** HT15; and from Verzasca Dam, **c** HT11. Dashed lines mark grain boundaries. The symbols represent elemental concentrations (in ppm) across the grains ■ Mg, □ Sr, Δ Fe and ◊ Mn.

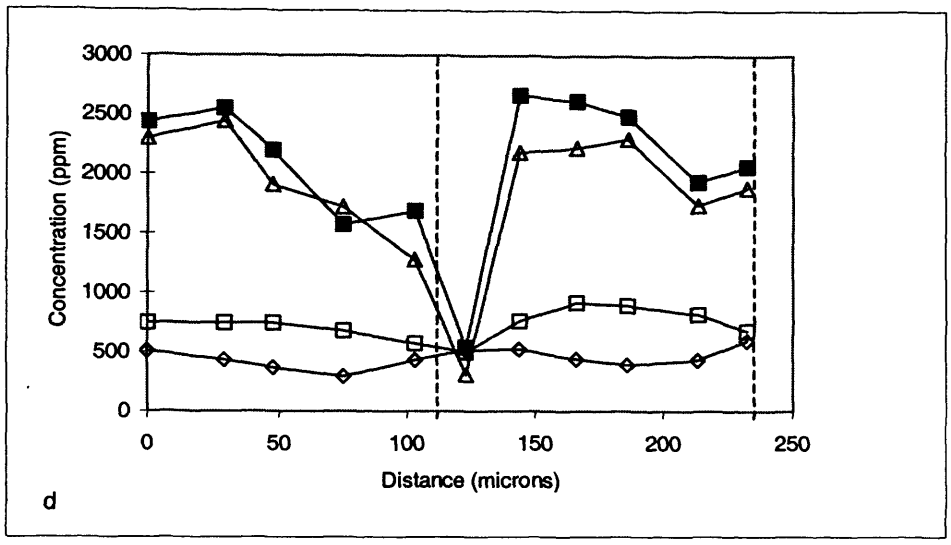

Figure 6.12 Calcite traverse from Verzasca Dam, **d** HT11. Dashed lines mark grain boundaries. The symbols represent elemental concentrations (in ppm) across the grains ■ Mg, □ Sr, Δ Fe and ◊ Mn.

Figures 6.12 and 6.13 are electron microprobe traverses across calcite grain boundaries. Figures 6.12a and b and 6.13 show relatively smooth concentration profiles from core to rim, whereas those of 6.12c and d are more uneven, but generally show the same results. These show a large decrease in Mg and Fe from core to rim, often in the order of 1000 ppm. The concentration of Mn appear to vary in the opposite sense with concentrations low the cores and higher at the rims of the grains. Sr appears to vary in the same way as Mg and Fe, but with a less pronounced variation between the rim and the core.

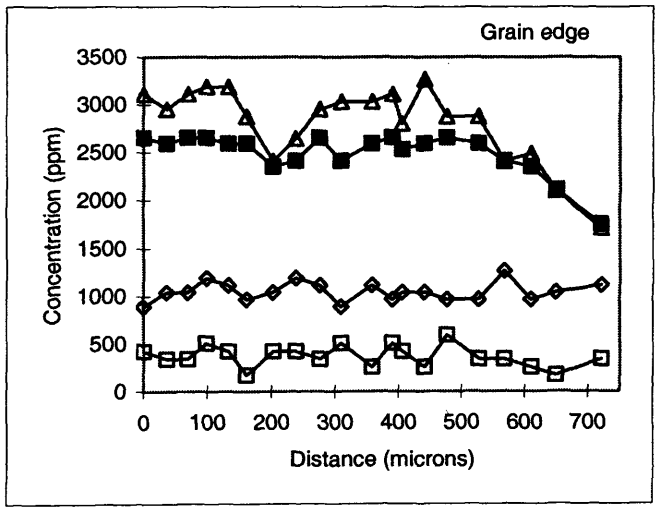

Figure 6.13 HT10 calcite traverse, Verzasca Dam. The symbols represent elemental concentrations (in ppm) across the grains ■ Mg, □ Sr, Δ Fe and ◊ Mn.

Figure 6.14 shows ion microprobe traverses across calcite grain boundaries. These four traverses indicate little or no change in Mn concentration across the profiles. There are major decreases in both Mg and Fe towards the grain boundaries, with decreases in concentration of up to 10000 ppm for Mg and 1000 ppm for Fe, for example in Figure 6.14b. Sr concentration also decreases towards the rims of grains, this being most pronounced in Figure 6.14b, which shows a

smooth Sr profile from 900 ppm in the core to 550 ppm at the rim of the grain. Similar effects are also seen in Figures 6.14a and 6.14c.

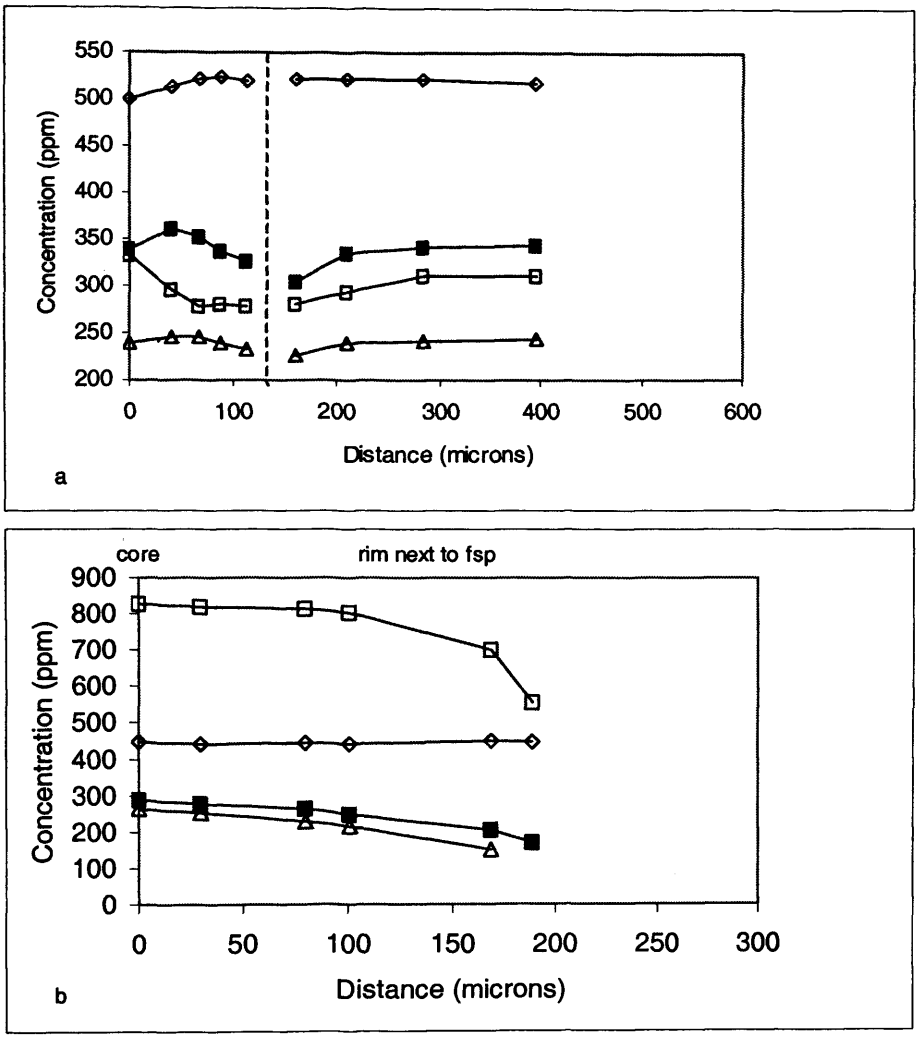

Figure 6.14 Calcite ion microprobe traverses of **a** HT15, from Lago del Narèt and **b** HT11, from Verzasca Dam (Mg and Fe concentrations are divided by 100 and 10 respectively).

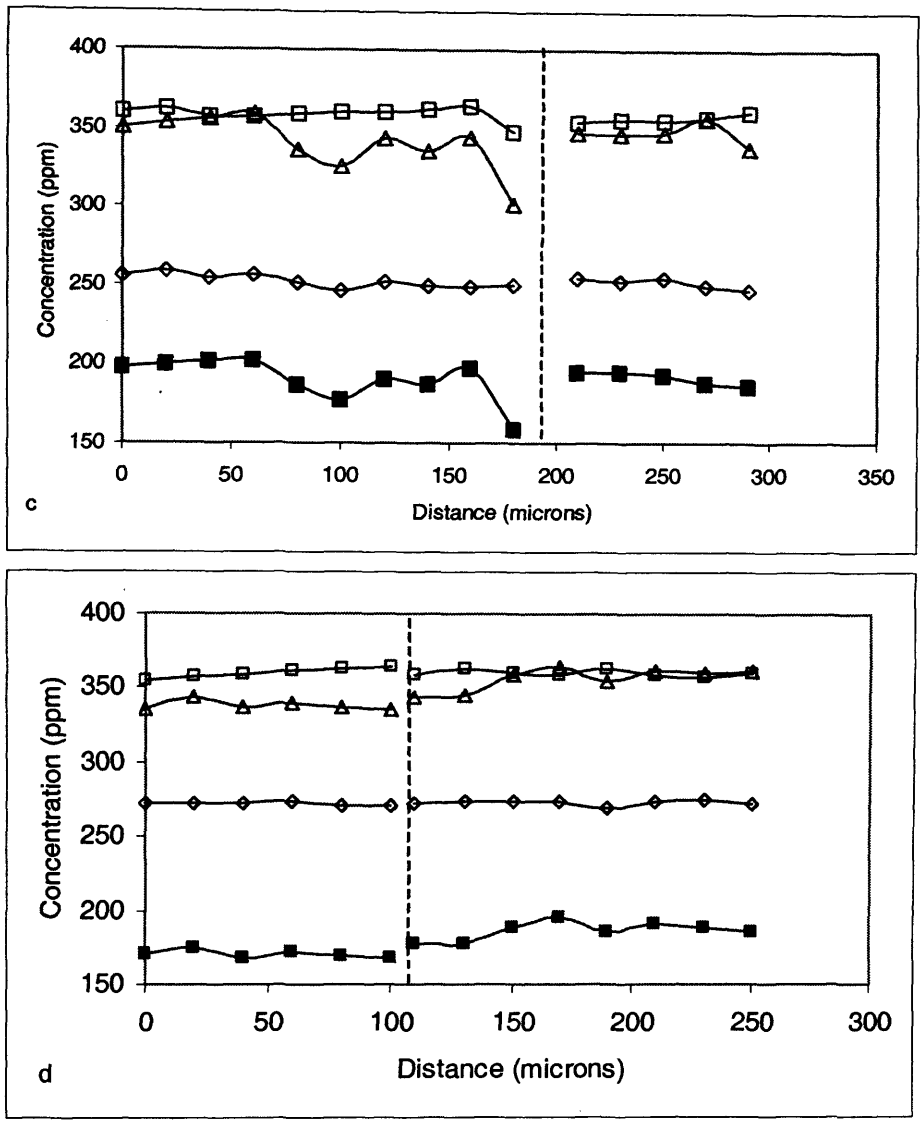

Figure 6.14 Calcite ion microprobe traverses of **c** and **d** HT23 from Someo (Mg and Fe concentrations are divided by 100 and 10 respectively).

The ion microprobe traverses confirm the variation in Fe, Mg and Sr from core to rim, but seem to disprove any variation in Mn as all the profiles are more or less flat, this is in disagreement with the data published by Jenkin *et al.* (2001) which shows distinct Mn increases towards the rim in two profiles.

Decreases in Mg and Fe would be expected if the rims of the grains were recording exchange with dolomite down to low temperatures (Anovitz & Essene, 1987). The Mg-content of the grains translates into an equilibration temperature (discussed in Appendix 4) and these suggest that the profile were developed in the temperature range 350-500°C (for the whole of the Lepontine Alps). Any Mg or Fe lost from the calcite may be preferentially partitioned into any phlogopite present. However, this may not produce a noticeable effect on the phlogopite profiles as the micas contain ~ 25 wt% MgO (~150000 ppm).

6.3.3 *Phlogopite and K-feldspar - Results and Interpretation*

Figures 6.16 and 6.17 show phlogopite and K-feldspar ion microprobe traverses.

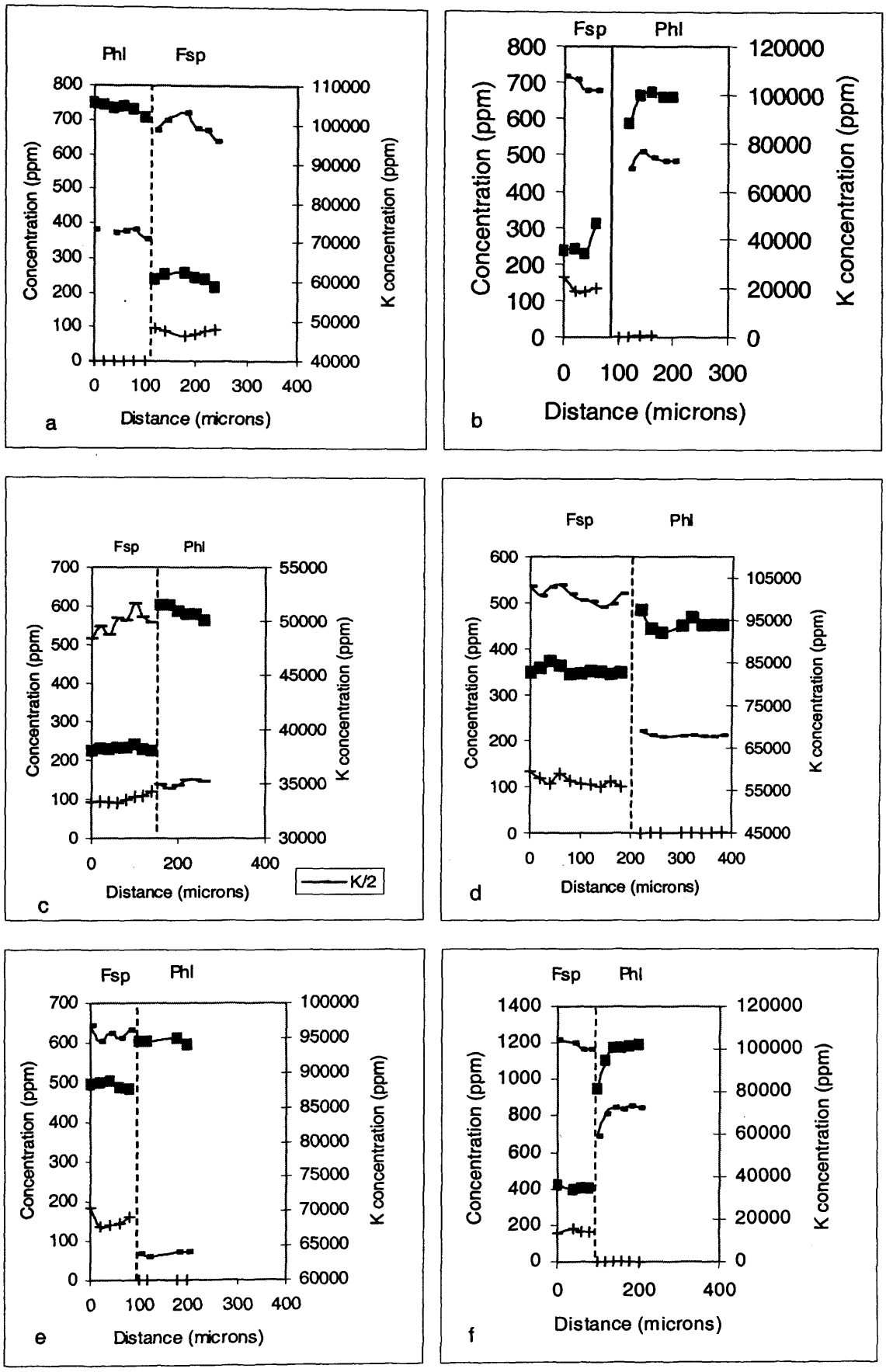

Figure 6.15 Ion microprobe traverses across adjacent phlogopite and K-feldspar grains; **a** HT17-132 (⊥c), **b** HT17-96 (⊥c), **c** HT17-114 (//c), **d** HT14-64 (⊥c), **e** HT16-27 (⊥c) and **f** HT16-40 (⊥c). The dashed lines mark the grain boundaries (data for these traverses can be found in Appendix 4). The symbols represent elemental concentrations (in ppm) across the grains ■ Rb, + Sr and – K.

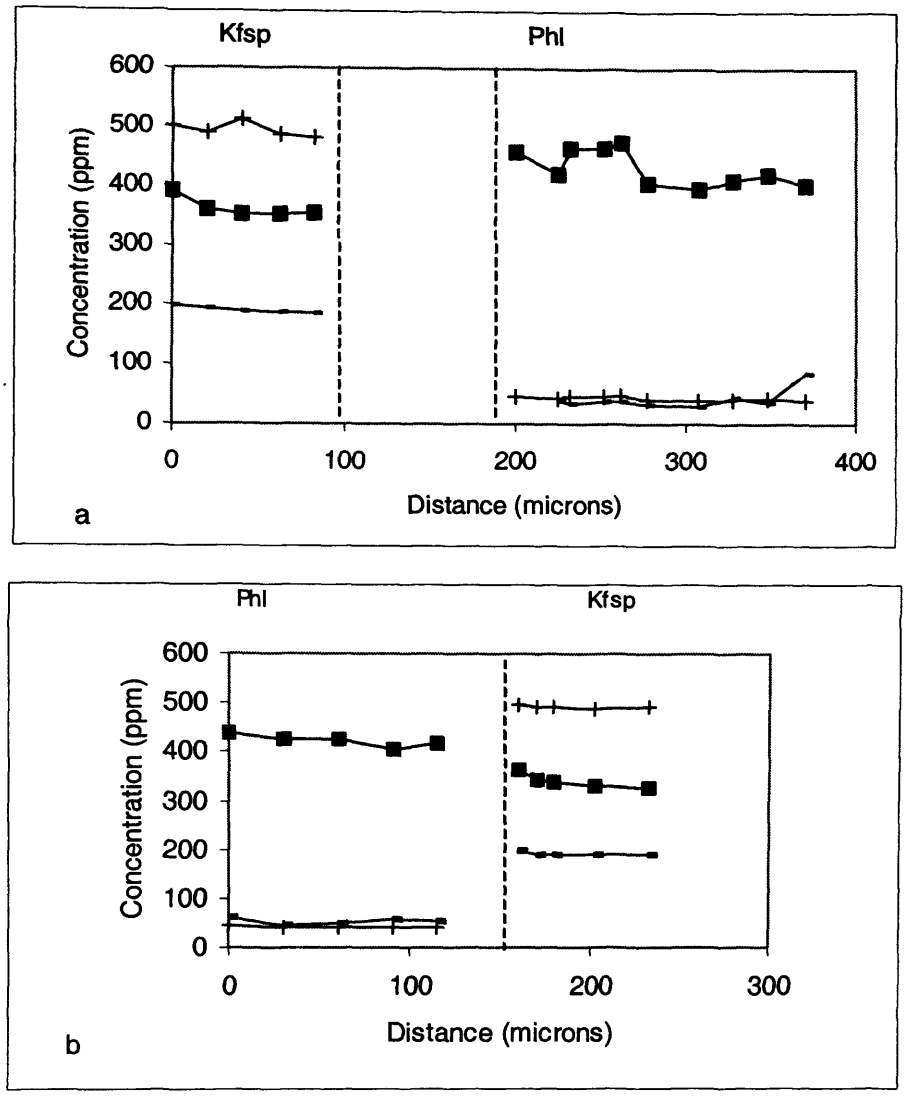

Figure 6.16 Ion microprobe traverses across adjacent phlogopite and K-feldspar grains; **a** *HT15-76 (//c)* and **b** *HT15-97 (//c). The dashed lines mark the grain boundaries (data for these* traverses can be found in Appendix 4). The symbols represent elemental concentrations (in ppm) across the grains ■ Rb, + Sr and – K.

The profiles in Figures 6.15 and 6.16 appear to give inconclusive results, with the behaviour of Rb, Sr and K being different in different grains of the same mineral and between grains of the same mineral in the same sample. For the majority of K-feldspar grains, Rb and K decrease and Sr increases towards the rims, suggesting that K-feldspar is losing Rb and K, but is acting as a sink for Sr during cooling. For the majority of phlogopite grains K decreases towards the rims and an equal number of profiles show Rb either increasing or decreasing. Using the Beswick (1973) partitioning equation (Equation 6.4) the equilibration temperatures for Rb-K exchange between phlogopite and K-feldspar can be calculated. For the data presented in Figures 6.15 and 6.16, an equilibration temperature between 330 and 410 °C is suggested, which shows down temperature exchange has taken place, even though the profiles show varying results.

Previous work by Jenkin *et al.* (2001) found that in phlogopite, Rb concentration decreased towards the rims of large grains and is low throughout small grains. Jenkin *et al.* (2001) also examined K-feldspar grains, which showed gradients of increasing K, Ba, Sr and Rb towards the

rims. However, modelling work (Section 6.3) suggests that phlogopite should gain Rb and lose K (assuming direct exchange between K and Rb) and K-feldspar should gain K and lose Rb in a closed cooling environment. However, the diffusion in K-feldspar is also controlled by K-Na exchange with plagioclase, which will affect the rate and amount of exchange.

A factor which may hamper the production of true exchange profiles is lack of knowledge about the 3D geometry of the grain in question. Asymmetry in the profiles may be produced by the traverses not running perpendicular to grain boundaries and it is not known how close the traverse is to grain boundaries above and below the plane of the section (Jenkin *et al.*, 2001). It is possible that anomalies in concentration profiles may be a function of how close the traverse is to another grain boundary out of the plane of the section.

6.4 Discussion and Conclusions

It has been shown that calcite, phlogopite and K-feldspar show zonations in trace and major elements. As discussed in previous chapters, any exchange is not thought to occur *via* metamorphic fluids and those zonations found today are believed to be formed on cooling from the peak metamorphic temperature. In the Lepontine Alps, the peak temperatures reached in excess of 575 °C, high enough to re-equilibrate pre-existing gradients and suffered prolonged deformation, allowing the formation of new gradients upon cooling.

The observed cation zonations indicate the complex nature of the chemical exchange during cooling of the rock. Multi-component chemical exchange among minerals must occur in a closed system, as by mass balance, any element leaving a mineral must be replaced by another. Due to partitioning behaviour, some of these exchange reactions may occur against the concentration gradient (for example, Rb entering phlogopite). Observed gradients indicate that; Mg, Fe and Sr are lost from calcite; Rb and K are lost and Sr is gained in K-feldspar; K is lost from phlogopite and Rb movement occurs, but exchanges into and out of different phlogopite grains. This loss of Rb and K at the grain boundaries may be an indication of alteration at the grain edges. Jenkin *et al.* (2001) suggest that exchange experienced by the calcite may be coupled with exchange in any dolomite present, although Mg and Fe may be partitioned into the phlogopite and Sr isotope exchange occurs between phlogopite and calcite as discussed in Chapter 5. Mineral concentrations, coupled with partitioning data indicate that exchange has occurred during cooling from peak temperature to a closure temperature of ~300-400 °C.

The results from Chapter 5 indicated that isotopic exchange occurs such that the $^{87}Sr/^{86}Sr$ ratio of calcite increases. However, it appears that exchange of elemental strontium occurs in the opposite sense, with calcite traverses showing Sr-poor rims, indicating that chemical and isotopic exchange are decoupled from each other, as suggested by Jenkin *et al.* (2001).

Chapter 7

Conclusions and Suggestions for Future Work

7.1 Conclusions from the Study

Petrological, cathodoluminescence and carbon and oxygen stable isotope data suggest that the samples being studied have not been affected by fluid infiltration or the exchange of isotopes with fluids to any great extent. This implies that the down-temperature isotopic and chemical exchange effects examined occur with little or no fluid present.

The measured phlogopite-calcite Rb-Sr ages are considerably lower than the ages thought to represent onset of cooling from the peak of metamorphism (~ 25 Ma for Lago del Narèt, in the north of the Maggia nappe; after Hurford, 1986) implying loss of ^{87}Sr from the phlogopite (in order to produce a lowered measured age). This loss of Sr agrees with the measured diffusion data of Hammouda & Cherniak (2000 and in press) who suggest that Sr diffusion is faster than Rb diffusion in fluorophlogopite.

A comparison of the phlogopite-calcite Rb-Sr ages with the biotite gneiss ages produced by previous authors (the biotite gneisses give 1-2 Ma younger ages) suggests that phlogopite has a higher Sr closure temperature than biotite. This difference in closure temperature is explained by the differences in mineral composition and by differences in the mineral modes between phlogopite- and biotite-bearing rock samples (Section 4.2.4, after Jenkin *et al.*, 1995).

The age – grain size relationship for the mica Rb-Sr system may not be as straightforward as Dodson (1973) suggests. The anomalies presented (increased measured age with decreasing grain size) correspond with a decrease in Rb concentration in the mica. The preferential loss of ^{87}Rb over ^{87}Sr could cause the increase in apparent age seen with decreasing grain size. However, this does not fit with the diffusion data for synthetic fluorophlogopite (Hammouda & Cherniak; 2000 and in press), which suggest Sr diffuses more rapidly, making phlogopite more susceptible to Sr loss, except at very high temperatures, although this will also depend on whether the element has another reservoir to be absorbed into. Therefore, any loss of Rb must have occurred after the onset of cooling, otherwise there would be a corresponding reduction in ^{87}Sr production and therefore, a lower measured age. Further evidence of Rb loss is found in sample HT15 (Chapter 5) where more ^{87}Sr has been produced (and gained by the calcite) than it is possible to produce from the Rb present within the mica band, in this case Rb can be lost to the K-feldspar present in the sample.

The Jenkin *et al.* (1995) model suggests that the closure temperature of a mineral pair (in a closed system) will be between the Dodson (1973) closure temperatures of the minerals in question, depending upon the proportions and Sr contents of the two phases. The phlogopite-calcite ages produced in this study lie close to the modelled Sr phlogopite and biotite curves for closure temperature versus grain size, as suggested by the closed system model of Jenkin *et al.* (1995).

The laser ablation ICP-MS traverses indicate that exchange of strontium isotopes occurs between mica (both phlogopite and muscovite) and calcite during cooling from the peak of metamorphism. However, the calculation of closure temperatures in the Rb-Sr system is more complex than the Dodson (1973) infinite reservoir model suggests. The $^{87}Sr/^{86}Sr$ traverses indicate that the length-scale of exchange is a few centimetres over several million years, implying exchange within a finite reservoir. The length-scale of exchange varies with the size of the calcite grains and the mineral modes. Modelling of the $^{87}Sr/^{86}Sr$ traverses indicates a combination of volume and grain boundary diffusion is a suitable mechanism for the exchange of Sr isotopes between mica and calcite.

It has been shown that calcite, phlogopite and K-feldspar show zonations in trace and major elements. As discussed in previous chapters, any exchange is not thought to occur *via* metamorphic fluids and those zonations found today are believed to be formed on cooling from the peak metamorphic temperature. In the Lepontine Alps, the peak temperatures reached in excess of 575 °C, high enough to re-equilibrate pre-existing isotopic/chemical gradients and the rocks underwent severe deformation, allowing the formation of new isotopic/chemical gradients upon cooling.

The observed cation zonations indicate the complex nature of the chemical exchange during cooling of the rock. Multi-component chemical exchange among minerals occurs in a closed system, as by mass balance, any element leaving a mineral must be replaced by another. Due to partitioning behaviour, some of these exchange reactions may occur against the concentration gradient (for example, Rb entering phlogopite). Observed gradients indicate that; Mg, Fe and Sr are lost from calcite; Rb and K are lost and Sr is gained in K-feldspar; K is lost from phlogopite and Rb movement occurs, but exchanges into and out of different phlogopite grains. Jenkin *et al.* (2001) suggest that exchange experienced by the calcite may be coupled with exchange in any dolomite present. The results from Chapter 5 indicated that isotopic exchange occurs such that the $^{87}Sr/^{86}Sr$ ratio of calcite increases. However, it appears that exchange of elemental strontium occurs in the opposite sense, with calcite traverses showing Sr-poor rims, indicating that chemical and isotopic exchange are decoupled from each other, as suggested by Jenkin *et al.* (2001). This suggests that calcite is behaving as a Sr sink and in this case may act as an infinite reservoir for strontium (after Dodson, 1973).

Sr isotopic exchange among minerals is dependent upon the rate of diffusion within and between different grains, the mineral grain sizes, the Sr concentration within different minerals and mineral mode. The exchange of strontium isotopes between phlogopite and calcite will alter the slope of a two point isochron to give a lower measured age than one calculated from minerals, which have not undergone isotopic exchange. More commonly dated rocks, such as biotite-bearing pelites and gneisses, should show similar effects.

7.2 Implications

7.2.1 *Diffusion Coefficients*

This study has confirmed that Sr isotope exchange can be modelled using a combination of volume and grain boundary diffusion. The $^{87}Sr/^{86}Sr$ data for individual grains (Figure 5.7), suggests that the diffusion through grains is rapid, as almost flat profiles are produced. This implies either volume diffusion is very rapid or the movement of Sr through the grains is along rapid diffusion pathways (such as fractures). The models produced in Sections 5.5.7 and 5.5.8 suggest that the rate of diffusion required to produce the measured profiles can be up to 100 times greater than the diffusion coefficients calculated by Cherniak (1997). The rate of the bulk diffusion coefficient is affected by the grain size and the number of rapid diffusion pathways, which pass through the grains. Rapid diffusion pathways take the form of grain boundaries, cleavage and twin planes and fractures, which act in a similar way to grain boundaries, with a faster diffusion coefficient than that of volume diffusion. The number of microstructures present within grains has a direct influence on the rate of diffusion and microstructural features should always be considered in modelling using diffusion coefficients.

Modelling results show it is possible to achieve ^{87}Sr-^{86}Sr exchange over a period of several million years via a combination of volume and grain boundary diffusion. Sr is transferred from one area of the sample to another via grain boundary diffusion and then enters and diffuses through the grains via a combination of volume diffusion and "grain boundary" diffusion along twin and cleavage planes.

Diffusion coefficients are important factors in chemical exchange as the rate of exchange can only progress at the diffusion rate of the slowest moving species. In modelling chemical exchange the partitioning behaviour of elements among minerals is also important as this controls which species has a preference for which mineral and can change with temperature.

7.2.2 *Dodson's Modelling*

The Dodson (1973) model suggests equilibration of Sr isotopes within an infinite reservoir. However, this study and the work of Jenkin *et al.* (1995) and Jenkin (1997) suggest re-equilibration between two or more minerals *via* the interdiffusion of Sr isotopes in a finite reservoir may be more realistic (in the case of a closed system rock). The measured $^{87}Sr/^{86}Sr$ profiles suggest a major re-equilibration event has taken place at the peak of metamorphism, which produced the present day background values in the calcite. This re-equilibration event occurred on a scale of centimetres to metres. Between the onset of cooling and the closure of the mica, Sr isotopes have exchanged between the micas and the calcite over a distance of several centimetres within this finite reservoir.

Chemical exchange also occurs in these rocks and is controlled by the interdiffusion of species among minerals and their partitioning behaviour. Modelling of chemical exchange tells us how much of each species is expected to exchange, but in reality, the profiles across grains do not

always reflect the modelling and may have retained some of their pre-metamorphic profiles (for example, in K-feldspar, which may not reach its re-equilibration temperature in some areas of the Lepontine Alps).

7.2.3 *What Happens in Terms of Measured Age?*

The $^{87}Sr/^{86}Sr$ profiles (Figures 5.8 and 5.9) show that there is a concentration gradient within the calcite in terms of $^{87}Sr/^{86}Sr$ ratios. Calcite $^{87}Sr/^{86}Sr$ ratios are high within the phlogopite band and decrease with distance away from the mica. As the specimen is behaving as a closed system, the implication of this analytical study and the modelling results is that ^{87}Sr is leaving the phlogopite and entering the calcite. Calcite is gaining ^{87}Sr, so the slope of a two point isochron would change (in a closed system) depending upon where in the rock the calcite is sampled. This implies that the down-temperature exchange of Sr isotopes between phlogopite and calcite can cause the production of a lower than expected measured age (based upon a two point isochron) than would be expected if no exchange had taken place. However, the effect on the age is fairly small, for HT15 it is 0.4 Ma (within the error on the measured age) and for HT23 it is 0.7 Ma (using the mica separate data and comparing the difference in age between calcite in the mica band with calcite outside the mica band), suggesting the Dodson (1973) approximation is justified.

If ^{87}Sr is exchanging with ^{86}Sr then the implication is that ^{86}Sr must be entering the mica during isotopic exchange. As HT23 is bi-mineralic the only place for ^{87}Sr to come from is the phlogopite band and if calcite is losing ^{86}Sr, it must be going into the phlogopite to maintain mass balance.

Chemical exchange is more difficult to predict. Modelling suggests down-temperature chemical exchange of Rb and K increases Rb in phlogopite and decreases Rb in K-feldspar. The chemical exchange of Rb and K is also affected by the mineral mode, so that in K-feldspar rich rocks, more Rb is partitioned into the phlogopite. The partitioning of more Rb into phlogopite will produce a lower slope for an Rb-Sr isochron and, therefore, a lower measured age (after Sr isotope exchange has ceased).

The effects of the chemical exchange (Rb with K) depend upon timing in relation to any isotopic exchange. Greater effects will be noticed if chemical exchange occurs after isotopic exchange has ceased and the isochron has started to develop. For the same temperature range, Sr (which is controlling the rate of isotopic diffusion) diffuses three orders of magnitude faster than Rb in the same type of mineral (see Figure 6.10). The effects of chemical exchange will not be noticed if it occurs while isotopic exchange is rapid enough to give both minerals similar $^{87}Sr/^{86}Sr$ ratios. Chemical exchange enhances the effect of isotopic exchange, further lowering the measured age (Figure 6.12) and the closure temperature.

7.3 Applications

The areas beneath the measured curves of $^{86}Sr/^{88}Sr$ ratio profiles in calcite around a mica band correspond to the time interval between the onset of cooling (after the homogenisation event) and the phlogopite closure temperature age. Provided the system as a whole remains closed geochronologically (i.e. no Rb gain or loss, as in HT15), this method could potentially be used to determine cooling rates independently, which correspond to the time interval between the onset of cooling and the closure temperature of the mica phase. The shape of the curve relates to the cooling history of the sample, i.e. the cooling rate, which will control the distance the $^{87}Sr/^{86}Sr$ diffuses out of the mica band.

This study implies that samples collected for geochronological studies must be chosen with care, showing that different grain size fractions of the same mineral can give different measured ages, depending upon the amount of exchange which has taken place.

7.4 Suggestions for Future Work

The LA-ICP-MS part of the study could have been improved by the further study of polyatomic species, which may cause isobaric interferences. When analysing solid carbonates, there is the potential for interferences from combinations of different calcium, iron, magnesium and manganese isotopes as part of carbon and oxygen polyatomic species (Table A3.2). These and other species may cause interferences in the mass range 83 to 88. A more thorough understanding of the effects of polyatomic isobaric interferences can be found by using a solid calcite standard (instead of Sr standard solutions) with a previously well constrained $^{87}Sr/^{86}Sr$ ratio (such as a modern sea shell; as in Bailey, 2001). This approach was important to the Bailey (2001) study as it was concerned with absolute $^{86}Sr/^{88}Sr$ ratios for strontium isotope stratigraphy, however for this study it is the relative value of the $^{86}Sr/^{88}Sr$ ratio that is important. The aim of this study was to use different techniques to examine strontium isotopic exchange and not to refine the LA-ICP-MS technique, however, isobaric interferences should be considered in future isotopic LA-ICP-MS studies of calcite.

It may also be possible to modify the LA-ICP-MS procedure so the laser is used to sample the sample and then this ablated material is collected as a solution. This allows the close spatial distribution of analyses and the removal of potential contaminants in the solution before analysis. However, this would add to the length of each analysis, removing one of the advantages of the technique.

A further LA-ICP-MS study could be initiated to look at a large single crystal of calcite, which either contains or has been next to a source of ^{87}Sr to examine the effects of diffusion and Sr isotope exchange within a single grain of calcite. It may be possible to collect such a specimen from a carbonatite source rock, although it would be essential to have some constraints upon the eruptive and cooling history (and an idea of the potential for fluid flow) of the rock body.

References

Agard P., Goffe B., Touret J. L. R., and Vidal O. (2000) Retrograde mineral and fluid evolution in high-pressure metapelites (Schistes lustres unit, Western Alps). *Contributions to Mineralogy and Petrology* **140**, 296-315.

Ahrens L. H. (1952) The use of ionisation potentials. Part 1. Ionic radii of the elements. *Geochimica et Cosmochimica Acta* **2**, 155-169.

Amato J. M., Johnson C. M., Baumgartner L. P., and Beard B. L. (1999) Rapid exhumation of the Zermatt-Saas ophiolite deduced from high-precision Sm-Nd and Rb-Sr geochronology. *Earth and Planetary Science Letters* **171**, 425-438.

Amirkhanov K. I., Batyrmurzayev A. S., Omarova M. R., and Gadzhiyev S. Z. (1978) Potassium diffusion from minerals of the mica group. *Transactions (Doklady) of the U.S.S.R. Academy of Sciences: Earth Science Sections* **243**(1-6), 196-196.

Anderson T. F. (1972) Self-diffusion of Carbon and Oxygen in Dolomite. *Journal of Geophysical Research* **77**, 857-861.

Anovitz L. M. and Essene E. J. (1987) Phase equilibria in the system $CaCO_3$-$MgCO_3$-$FeCO_3$. *Journal of Petrology* **28**, 389-414.

Armstrong R. L., Jaeger E., and Eberhardt. (1966) A comparison of K-Ar and Rb-Sr ages on Alpine biotites. *Earth and Planetary Science Letters* **1**, 13-19.

Arnaud N. O. and Kelley S. P. (1995) Evidence for excess argon during high-pressure metamorphism in the Dora Maira Massif (western Alps, Italy), using an ultraviolet laser ablation microprobe ^{40}Ar-^{39}Ar technique. *Contributions to Mineralogy and Petrology* **121**, 1-11.

Baertschi P. (1957) Messung und Deutung relativer Haeufigkeitsvariationen von ^{18}O und ^{13}C in Karbonatgesteinen und mineralein. *Schweizerische Mineralogische und Petrographische Mitteilungen* **37**(1), 73-152.

Becker J. S. and Dietze H.-J. (2000) Precise and accurate isotope ratio measurements by ICP-MS. *Fresenius Journal of Analytical Chemistry* **368**, 23-30.

Beswick A. E. (1973) An experimental study of alkali metal distributions in feldspars and micas. *Geochimica et Cosmochimica Acta* **37**, 183-208.

Bailey T. (2001) Applications of Strontium Isotope Stratigraphy: The Potential of Laser Micro-sampling., Royal Holloway, University of London.

Brady J. B. (1983) Intergranular diffusion in metamorphic rocks. *American Journal of Science* **283A**, 181-200.

Cherniak D. J. and Ryerson F. J. (1993) A study of Strontium diffusion in apatite using Rutherford Backscattering spectroscopy and ion implantation. *Geochimica et Cosmochimica Acta* **57**(19), 4653-4662.

Cherniak D. J. (1997) An experimental study of Sr and Pb diffusion in calcite and implications for carbonate diagenesis and metamorphism. *Geochimica et Cosomochimica Acta* **61**, 4173-4179.

Cherniak D. J. and Watson E. B. (2000) Pb diffusion in zircon. *Chemical Geology* **172**, 5-24.

Christensen J. N., Halliday A. N., Lee D.-C., and Hall C. M. (1995) *In situ* Sr isotopic analysis by laser ablation. *Earth and Planetary Science Letters* **136**, 79-85.

Cliff R. A. (1985) Isotopic dating in metamorphic belts. *Journal of the Geological Society, London* **142**, 97-110.

Cole D. R., Ohmoto H., and Lasaga A. C. (1983) Isotopic exchange in mineral-fluid systems. I. Theoretical evaluation of oxygen isotopic exchange accompanying surface reactions and diffusion. *Geochimica et Cosmochimica Acta* **47**, 1681-1693.

Coward M. P., Dietrich D., and Park R. G. (1989) *Alpine Tectonics.* Vol. 45. Geological Society of London.

Crank J. (1975) *The Mathematics of Diffusion.* Oxford University Press.

Dahl P. S. (1996) The crystal chemical basis for Ar retention in micas: inferences from interlayer partitioning and implications for geochronology. *Contributions to Mineralogy and Petrology* **123**, 22-29.

Deer W. A., Howie R. A., and Zussman J. (1963) *An Introduction to the Rock Forming Minerals.* Longman Scientific and Technical.

Del Moro A. D., Puxeddu M., and Bozolo F. R. d. (1982) Rb-Sr and K-Ar ages in minerals at temperatures of 300-400 oC from deep wells in the Larderello geothermal field (Italy). *Contributions to Mineralogy and Petrology* **81**, 340-349.

Dercourt J., Zonenshain L. P., Ricou L. E., Kazmin V. G., Pichon X. L., L.Knipper A., Grandjacquet C., Sbortshikov I. M., Geyssant J., Lepvrier C., Pechersky D. H., Boulin J., Sibuet J.-C., Savostin L. A., Sorokhtin O., Westphal M., Bazhenov M. L., Lauer J.-P., and Biju-Duval B. (1986) Geological evolution of the Tethys belt from the Atlantic to the Pamirs since the Lias. *Tectonophysics* **123**, 241-315.

Dewey J. F., Helman M. L., Turco E., Hutton D. H. W., and Knott S. D. (1989) Kinematics of the Western Mediterranean. In *Alpine Tectonics*, Vol. 45 (ed. M. P. Coward, D. Dietrich, and R. G. Park). Geological Society of London.

Dodson M. H. (1973) Closure temperature in cooling geochronological and petrological systems. *Contributions to Mineralogy and Petrology* **40**, 259-274.

Dodson M. H. (1979) Theory of cooling ages. In *Lectures in isotope geology* (ed. Jaeger), pp. 194-201.

Duchêne S., Blichert-Toft J., Luais B., Telouk P., Lardeux J.-M., and Albarede F. (1997) The Lu-Hf dating of garnets and the ages of the Alpine high-pressure metamorphism. *Nature* **387**, 586-589.

England P. and Molnar P. (1990) Surface uplift, uplift of rocks and exhumation of rocks. *Geology* **18**, 1173-1177.

Farver J. R. and Yund R. A. (1996) Volume and grain boundary diffusion of calcium in natural and hot-pressed calcite aggregates. *Contributions to Mineralogy and Petrology.* **123**, 77-91.

Farver J. R. and Yund R. A. (1998) Oxygen grain-boundary diffusion in natural and hot-pressed calcite aggregates. *Earth and Planetary Science Letters.* **161**, 189-200.

Faure G. (1986) *Principles of Isotope Geology.* John Wiley & Sons.

Ferry J. M. and Spear F. S. (1978) Experimental calibration of the partitioning of Fe and Mg between biotite and garnet. *Contributions to Mineralogy and Petrology.* **66**, 113-117.

Fisler D. K. and Cygan R. T. (1999) Diffusion of Ca and Mg in Calcite. *American Mineralogist* **84**, 1392-1399.

Flowers G. C. and Helgeson H. C. (1983) Equilibrium and mass transfer during progressive metamorphism of siliceous dolomites. *American Journal of Science* **283**, 230-286.

Foland K. A. (1974) Alkali diffusion in orthoclase. In *Geochemical transport and Kinetics*, Vol. 634 (ed. A. W. Hoffmann, B. J. Giletti, H. S. Yoder, and R. A. Yund). Carnegie Institution.

Frank W. (1987) Evolution of the Austroalpine elements in the Cretaceous. In *Geodynamics of the Eastern Alps.* (ed. H. W. Flugel and P. Faupl), pp. 279-406. Deuticke.

Freeman S. R., Inger S., Butler R. W. H., and Cliff R. A. (1997) Dating deformation using Rb-Sr in white mica: Greenschist facies deformation ages from the Entrelor shear zone, Italian Alps. *Tectonics* **16**(1), 57-76.

Ganguly J. & Ruiz J. (1986) Time-temperature relation of mineral isochrons: a thermodynamic model and illustrative examples for the Rb-Sr system. *Earth and Planetary Science Letters* **81**, 238-248.

Giletti B. J. (1974) Diffusion related to geochronology. In *Geochemical Transport and Kinetics.*, Vol. 634 (ed. Hofmann, Giletti, Yoder, and Yund), pp. 61-76. Carnegie Institution.

Giletti B. J. (1991a) Rb and Sr diffusion in alkali feldspars with implications for cooling histories of rocks. *Geochimica et Cosmochimica Acta* **55**, 1331-1343.

Giletti B. J. (1991b) Diffusion kinetics of Mg, Ca, Sr and Ba in albite and Sr in muscovite and biotite. *Eos: Transactions of the American Geophysical Union, Fall Meeting.*

Giletti B. J. and Casserly J. E. D. (1994) Sr diffusion kinetics in plagioclase feldspars. *Geochimica et Cosmochimica Acta* **58**, 3785-3793.

Graham C. M., Valley J. W., Eller J. M., and Wada H. (1998) Timescales and mechanisms of fluid infiltration in a marble: an ion microprobe study. *Contributions to Mineralogy and Petrology* **132**, 371-389.

Grujic D. and Mancktelow N. S. (1996) Structure of the northern Maggia and Lebuden nappes, Central Alps, Switzerland. *Eclogae Geologae Helvetica* **89**, 461-504.

Günthert A. W., Stern W. B., and Schwander H. (1996) The polycyclic evolution of the Penninic Maggia nappe, Central Alps: A summary report. *Schweizerische Mineralogische und Petrographische Mitteilungen* **76**, 1-22.

Halliday A. N., Lee D.-C., Christensen J. N., Rahkamper M., Wen Y., Luo X., Hall C. M., Ballentine C. J., Pettke T., and Stirling C. (1998) Applications of multiple collector-ICPMS to cosmochemistry, geochemistry and palaeoceanography. *Geochimica et Cosmochimica Acta* **62**(6), 919-940.

Hammouda T. and Cherniak D. (2000) Diffusion of Sr in fluorophlogopite determined by Rutherford backscatter spectrometry. *Earth and Planetary Science Letters* **178**(3-4), 339-349.

Hammouda T. and Arnaud N. (in press) Argon diffusion in fluorophlogopite and some comments about diffusion in micas. *Geochimica et Cosmochimica Acta.*

Hammouda T. and Cherniak D. J. (in press) Rubidium diffusion in fluorophlogopite and inferences concerning the relative mobility of tracers in sheet silicates. *Geochimica et Cosmochimica Acta.*

Hatcher R. D. (1995) *Structural Geology. Principles, Concepts and Problems.* Prentice Hall.

Heller F., Lowrie W., and Hirt A. M. (1989) A review of palaeomagnetic and magnetic anisotropy results from the Alps. In *Alpine Tectonics*, Vol. 45 (ed. M. P. Coward, D. Dietrich, and R. G. park). Geological Society of London.

Henderson P. (1982) *Inorganic Geochemistry.* Permagon.

Hess J. C. and Lippolt H. J. (1994) The thermochronological potential of age/grain size relations. *Abstracts of the Eighth international conference on Geochronology, Cosmochronology, and Isotope Geology*(8), 135.

Holness M. B. and Graham C. M. (1991) Equilibrium dihedral angles in the system H_2O-CO_2-NaCl-calcite and implications for fluid flow during metamorphism. *Contributions to Mineralogy and Petrology* **108**, 368-383.

Holness M. B. and Graham C. M. (1995) P-T-X effects on equilibrium carbonate-H_2O-CO_2-NaCl dihedral angles: constraints on carbonate permeability and the role of deformation during fluid infiltration. *Contributions to Mineralogy and Petrology* **119**, 301-313.

Hsü K. J. (1989) Time and place in Alpine Orogenesis - the Fermor Lecture. In *Alpine Tectonics*, Vol. 45 (ed. M. P. Coward, D. Dietrich, and R. G. Parks), pp. 421-443. Geological Society of London.

Hsü K. J. (1995) *The Geology of Switzerland: An introduction to tectonic facies.* Princeton University Press.

Hunziker J. C., Desmons J., and Hurford A. J. (1992) *Thirty-two years of geochronological work in the central and western Alps: A review in seven maps.*

Hurford A. J. (1986) Cooling and uplift patterns in the Lepontine Alps, south central Switzerland and an age of vertical movement on the Insubric fault line. *Contributions to Mineralogy and Petrology* **92**, 413-427.

Hurford A. J. (1991) Uplift and cooling pathways derived from fission track analysis and mica dating: a review . *Geologische Rundschau* **80**, 349-368.

Inger S., Ramsbottom W., Cliff R. A., and Rex D. C. (1996) Metamorphic evolution of the Sesia-Lanzo Zone, Western Alps: time constraints from multi-system geochronology. *Contributions to Mineralogy and Petrology* **154**, 152-168.

Jackson S. E. (2001) The application of Nd:YAG lasers in LA-ICP-MS. In *Laser-Ablation-ICPMS in the Earth Sciences. Principles and Applications.* Vol. 29 (ed. P. Sylvester), pp. 29-45. Mineralogical Association of Canada.

Jäger E., Niggli E., and Wenk E. (1967) Rb - Sr Altersbestimmungen an glimmern der Zentralapen. *Beiträge zur Geologischen karte des Schweiz. N. E.* **134**, 1-67.

Jäger E. (1973) Die alpine Orogenese im Lichte der radiometrischen Altersbestimmung. *Eclogae Geologicae Helvetiae* **66**(1), 11-21.

Jenkin G. R. T., Farrow C. M., Fallick A. E., and Higgins D. (1994) Oxygen isotope exchange and closure temperatures in cooling rocks. *Journal of Metamorphic Geology* **12**, 221-235.

Jenkin G. R. T., Rogers G., Fallick A. E., and Farrow C. M. (1995) Rb-Sr closure temperatures in bi-mineralic rocks: a mode effect and test for different diffusion models. *Chemical Geology* **122**(1-4), 227-240.

Jenkin G. R. T. (1997) Do cooling paths derived from mica Rb-Sr data reflect true cooling paths. *Geology* **25**, 907-910.

Jenkin G. R. T., Ellam R. M., Rogers G., and Stuart F. (2001) An investigation of closure temperature of the biotite Rb-Sr system: the importance of cation exchange. *Geochimica et Cosmochimica Acta* **65**(7), 1141-1160.

Joesten R. (1991) Grain-boundary diffusion kinetics in silicate and oxide minerals. In *Diffusion, Atomic Ordering, and Mass Transport. Selected Topics in Geochemistry.* Vol. 8 (ed. S. K. Saxena), pp. 567. Speinger-Verlag.

Kobe W. (1966) Struktur des Gebietes zwischen Gresso und Passo della Garina, Tessin. (mit Deutungsversuch der tektonisch-strukturellen Verhaeltnisse des Gebietes vom Valle di Vergeletto bis zum untersten Val Verzasca). *Eclogae Geologicae Helvetiae* **59** (2), 789-802.

Koepnick R. B., Denison R. E., Burke W. H., Hetherington E. H., and Dahl D. A. (1990) Construction of the Triassic and Jurassic portion of the Phanerozoic curve of seawater 87Sr/86Sr. *Chemical Geology* **80**, 327-349.

Köppel V. and Grünenfelder M. (1975) Concordant U-Pb ages of monazite and xenotime from the Central Alps and the timing of the high temperature Alpine metamorphism, a preliminary report. *Schweizerische Mineralogische und Petrographische.* **55**, 129-132.

Köppel V., Günthert A., and Grünenfelder M. (1980) Patterns of U-Pb zircon and monazite ages in polymetamorphic units of the Swiss Central Alps. *Schweizerische Mineralogische und Petrographische Mitteilungen.* **61**, 97-119.

Kyser T. K. (1987) Stable isotope geochemistry of low temperature processes. In *Short Course*, Vol. 13. Mineralogical Association of Canada.

Lee J. K. W. (1995) Multipath diffusion in geochronology. *Contributions to Mineralogy and Petrology.* **120**, 60-82.

Lemoine M. (1989) Extension synrift et failles transformantes jurassiques dans les Alpes Occidentales. *Canadienne Royale Academie du Science. Series II.* **309**, 1711-1716.

Ludwig K. R. (2001) Isoplot/Ex A geochronolgical toolkit for Microsoft Excel. Berkley Geochronology Centre.

Mancktelow N. S. (1992) Neogene lateral extension during convergence in the Central Alps; evidence from interrelated faulting and backfolding around the Simplonpass; Switzerland. *Tectonophysics* **215**, 295-317.

Manning J. R. (1968) Basic Concepts. In *Diffusion kinetics for atoms in crystals.*

Manning J. R. (1974) Diffusion kinetics and mechanisms in simple crystals. In *Geochemical transport and kinetics* (ed. A. W. Hofmann, B. J. Giletti, H. S. Yoder, and R. A. Yund), pp. 3-13. Carnegie Institution of Washington.

Meyre C., Capitani C. D., Zack T., and Frey M. (1999) Petrology of high-pressure metapelites from the Adula Nappe (Central Alps, Switzerland). *Journal of Petrology* **40**(1), 199-213.

Mezger K., Rawnsley S. R., Bohlen S. R., and Hanson G. N. (1991) U-Pb garnet, titanite, monazite and rutile ages: implications for the duration of high grade metamorphism and cooling histories. *Journal of Geology* **99**, 415-428.

Mullis J., Dubessy J., Poty B., and O'Neil J. R. (1994) Fluid regimes during the late stages of continental collision: Physical, chemical and stable isotope measurements of fluid inclusions in fissure quartz from a geotraverse through the Central Alps. *Geochimica et Cosmochimica Acta* **58**, 2239-2267.

Nicolaysen L. O. (1961) Graphic interpretation of discordant age measurements on metamorphic rocks. *Annuals of the New York Academy of Science* **91**, 198-206.

Nimis P. and Tromsdorff V. (2001) Revised thermobarometry of Alpe Arami and other garnet peridotites from the Central Alps. *Journal of Petrology* **42**, 103-115.

Nordstrom D. K. and Munoz J. L. (1986) *Geochemical Thermodynamics.* Blackwell Scientific Publications.

Paquette J. and Reeder R. J. (1995) Relationship between surface structure, growth mechanism and trace element incorporation in calcite. *Geochimica et Cosmochimica Acta* **59**, 735-749.

Perkins W. T. and Pearce N. J. G. (1995) Mineral microanalysis by laserprobe inductively coupled plasma mass spectrometry. In *Microprobe Techniques in the Earth Sciences.*, Vol. 6 (ed. P. J. Potts, J. F. W. Bowles, S. J. B. Reed, and M. R. Cave), pp. 419. Chapman and Hall.

Pfiffner A. (1992) Alpine Orogeny. In *A Continent Revealed: The European Geotraverse.* (ed. D. Blundell, R. Freeman, and S. Mueller), pp. 275. Cambridge University Press.

Purdy J. W. and Jäger E. (1976) K-Ar ages on rock forming minerals form the Central Alps. *Memorie degli Instituti do Geologica e Mineralogica dell'Universita di Padova* **30**, 32.

Purdy J. W. and Stadler H. A. (1973) K-Ar ages of fissure minerals from the Swiss Alps. *Schweizerische Mineralogische und Petrographische Mitteilungen* **53**, 79-98.

Putten E. V., Dehairs F., Keppens E., and Baeyens W. (2000) High resolution distribution of trace elements in the calcite shell layer of modern *Mytilus edulis*: Environmental and biological controls. *Geochimica et Cosmochimica Acta* **64**(6), 997-1011.

Reddy S. M., Kelly S. P., and Wheeler J. (1996) A 40Ar-39Ar laser probe study of micas from the Sesia zone, Italian Alps - implications for metamorphic and deformation histories. *Journal of Metamorphic Geology* **14**, 493-508.

Reddy S. M., Wheeler J., and Kelley S. P. (1994) The use if heterogeneous excess argon and argon loss to constrain thermal histories: laser $^{40}Ar/^{39}Ar$ dating of deformed micas from the Sesia Zone, Italian Alps. *Abstracts of the Eighth international conference on Geochronology, Cosmochronology, and isotope geology* **8**, 261.

Scambelluri M., Pennacchioni G., and Philppot P. (1998) Salt-rich aqueous fluids formed during eclogitization of metabasites in the Alpine continental crust (Austroalpine Mt. Emilius unit, Italian western Alps). *Lithos* **43**, 151-167.

Schaltegger U. and Corfu F. (1992) The age and source of late Hercynian magmatism in the central Alps: evidence from precise U-Pb ages and initial Hf isotopes. *Contributions to Mineralogy and Petrology* **111**, 329-344.

Selverstone J. (1999) Tectonometamorphic perspectives on drainage-basin-scale exhumation in the Eastern and Central Alps. *Geological Society of America, Abstracts with Programs* **31**, 297.

Sinclair D. J., Kinsley L. P. J., and Culloch M. T. M. (1998) High resolution analysis of trace elements in corals by laser ablation ICP-MS. *Geochimica et Cosmochimica Acta* **62**, 1889-1901.

Smith G. D. (1965) *Numerical solution of partial differential equations.* Oxford University Press.

Spear F. S. (1993) *Metamorphic phase equilibria and pressure-temperature-time paths.* Mineralogical Society of America.

Spicher A. (1980) Tektonische Karte der Schweiz. 1: 500000. Schweizerischen Geologischen Kommission.

Steck A. and Hunziker J-C. (1994) The Tertiary structural and thermal evolution of the central Alps, compressional and extensional structures in an orogenic belt. *Tectonophysics* **238**, 229-254.

Steiger R. H. and Jäger E. (1977) Subcommission on Geochronology: Convention on the use of decay constants in geo- and cosmochronology. *Earth and Planetary Science Letters* **36**(359-362).

Steiner von H. (1984a) Radiometrische Alterbestimmungen an Gesteinen der Maggia-Decke (Penninikum der Zentralalpen). *Schweizerische Mineralogische und Petrographische Mitteilungen* **64**, 227-259.

Steiner von H. (1984b) Mineralogische-petrographische, geochemische und isotopengeologische Untersuchungen an einem Meta-Lamprophyr und seinem granodioritischen Nebengestein (Matorello-Gneiss) aus der Maggia-Decke. *Schweizerische Mineralogische und Petrographische Mitteilungen* **64**, 261-271.

Sylvester P. (2001) *Laser-Ablation-ICPMS in the Earth Sciences. Principles and Applications.* Mineralogical Association of Canada.

Thirwall M. F. (1997) Thermal ionisation mass spectrometry (TIMS). In *Modern Analytical Geochemistry.* (ed. R. Gill), pp. 329. Addison Wesley Longman.

Todd C. S. and Engi M. (1997) Metamorphic field gradients in the Central Alps. *Journal of Metamorphic Geology* **15**, 513-530.

Trümpy R. (1980) *Geology of Switzerland: A guidebook. Part A: An outline of the Geology of Switzerland.* Wepf & Co.

Twiss R. J. and Moores E. M. (1992) *Structural Geology.* W. H. Freeman.

Vance D. and O'Nions R. K. (1992) Prograde and retrograde thermal histories from the Central Swiss Alps. *Earth and Planetary Science Letters* **114**, 113-129.

Veizer J. and Hoefs J. (1976) The nature of $^{18}O/^{16}O$ and $^{13}C/^{12}C$ secular trends in sedimentary carbonate rocks. *Geochimica et Cosmochimica Acta* **40**, 1387-1395.

Villa I. M. (1998) Isotopic Closure. *Terra Nova* **10**, 42-47.

Volfinger M. (1976) Effet de la temperature sur les distributions de Na, Rb, Cs entre la sanidine, la muscovite, la phlogopite et une solution hydrothermale sous une pression de 1 kb. *Geochimica et Cosmochimica Acta* **40**, 267-282

Wagner G. A., Reimer G. M., and Jaeger E. (1977) Cooling ages derived by apatite fission track, mica Rb-Sr and K-Ar dating: The uplift and cooling history of the Central Alps. *Memorie degli Instituti do Geologica e Mineralogica dell'Universita di Padova* **30**, 1-27.

Watson E. B. and Liang Y. (1995) A simple model for sector zoning in slowly grown crystals: Implications for growth rate and lattice diffusion, with emphasis on accessory minerals in crustal rocks. *American Mineralogist* **80**, 1179-1187.

White W. M., Albarede F., and Telouk P. (2000) High-precision analysis of Pb isotope ratios by multi-collector ICP-MS. *Chemical Geology* **167**, 257-270.

Appendix 1

Sample localities and descriptions.

Sample number: HT4
Grid reference: 702.60, 148.35
Field location: Dalpe. A dolomite marble quarry (disused). The marble forms part of a large anticlinal structure and was taken from the western face.
Sample description: Dolomite marble.
Dolomite 75%, 0.75 mm in, deformed cleavage.
Phlogopite 2%, 0.2 perpendicular to c.
Muscovite 8%, 0.2 perpendicular to c.
Quartz with fluid inclusions, 10%, 0.5mm in .
Small amounts of zoisite 1%, rutile 1% and altered feldspar 3%.
Irregular holes - suggesting the removal of gypsum (implying fluid flow).

Sample number: HT10
Grid reference: 708.80, 117.05
Field location: Valle Verzasca Dam. The sample was taken from marble band beneath the dam on the western side of the river. The site can be accessed by crossing the dam and descending a steep track.
Sample description: Marble.
Calcite 70%, 1-2.5 mm.
Feldspar 13%, is mainly plagioclase (0.5 mm in diameter), but there are a few isolated grains K-feldspar.
Muscovite, as small aggregates of grains, 1%.
Scapolite 2%, 1mm perpendicular to c.
Quartz 5%, with few fluid inclusions, 0.5 mm in diameter.
Small grains of oxides 6%, titanite 2% and apatite 1%.

Sample number: HT11
Grid reference: 708.85, 117.05
Field location: Valle Verzasca Dam. The sample was taken from marble band beneath the dam on the western side of the river. The site can be accessed by crossing the dam and descending a steep track.
Sample description: Marble.
Calcite, 45%, 0.5-1 mm.
Quartz 25%, 0.25 mm in diameter.
Zoisite 5%, 1 mm in diameter.
K-feldspar, 15% 0.5mm in diameter.
Muscovite 5%, 0.5 mm perpendicular to c.
Also small grains of titanite 1%, apatite 1% and oxides 3%.

Sample number: HT14
Grid reference: 687.50, 148.45
Field location: Lago del Narèt. Lago del Narèt is found at the northern most part of Valle Maggia. Samples were taken from the marble band which forms one edge of the road leading to the dam following the road up Val Sambuco from Fusio. The outcrop is bounded by gneiss and dips steeply to the north.
Sample description: Marble.
Calcite 60%, 1-4 mm in diameter.
Rounded quartz grains 20%, 0.5 mm, some fluid inclusions present.
Muscovite, 20%, 0.25-1 mm perpendicular to c.
Small amounts of rutile staining and isolated grains of altered feldspar.

Sample number: HT15
Grid reference: 687.55, 148.25
Field location: Lago del Narèt
Sample description: Marble.
Calcite 84%, up to 2 mm in diameter, some areas cloudy.
Quartz, 3%, 0.1-0.5mm in diameter, some fluid inclusions.
K-feldspar 4%, ~0.2 mm in diameter.
Phlogopite 6%, 0.5-2 mm perpendicular to c.
Muscovite 3%, 0.25-0.5 mm perpendicular to c..
Isolated grains of apatite, titanite and zircon.

Sample number: HT16
Grid reference: 687.35, 148.15
Field location: Lago del Narèt
Sample description: Marble.
Calcite , 65%, 0.5-3 mm in diameter.
Muscovite, 5%, 0.25-0.5 mm perpendicular to c.
Isolated phlogopite grains, 1 mm perpendicular to c, 5%.
Quartz 22%, 0.1-0.2 mm in diameter.
Also altered feldspar 1%, ~0.1 mm

Sample number: HT17
Grid reference: 687.55, 148.40
Field location: Lago del Narèt
Sample description: Marble.
Calcite 70%, some areas cloudy.
K-feldspar 10%, 0.2-0.5 mm in diameter.
Muscovite 2%, 0.1-0.5 mm perpendicular to c.
Phlogopite 7%, 0.1-1 mm perpendicular to c.
Quartz 10%, 0.1-0.2 mm, with some fluid inclusions.
Apatite 1%.

Sample number: HT20
Grid reference: 683.05, 145.15
Field location: Lago Bianco. Lago Bianco is accessed by cable car to Robiei from San Carlo in Val Bavona, then walking north along the footpath. The samples were taken from the west side of the lake.
Sample description: Marble.
Calcite 75%, 1-2 mm, some areas cloudy.
Isolated muscovite grains 8%, 0.2-0.5 mm perpendicular to c.
Isolated phlogopite grains, 2%, ~1 mm perpendicular to c.
Quartz 10%, 0.1-0.5 mm, with some fluid inclusions, some grains show strained extinction.
Apatite 1%, K-feldspar 1%.

Sample number: HT21
Grid reference: 682.93, 145.25
Field location: Lago Bianco
Sample description: Marble.
Dolomite 85%, 0.1-0.2 mm in diameter.
Calcite 14%, ~0.3 mm in diameter.
Isolated phlogopite grains, 1%, ~1 mm perpendicular to c.

Sample number: HT23
Grid reference: 694.25, 127.23
Field location: Someo. Park in the village, then take the footpath through the vineyard to the east of the village. Follow the footpath to the first wayside chapel, then take the first right and go through the vineyard to reach the marble outcrop.

Sample description: Marble.
Calcite 95%, 2-5 mm in diameter.
Phlogopite 5%, 1-2 mm perpendicular to c.

Sample number: HT26
Grid reference: 665.79, 112.10
Field location: Crevoladossola. This location is part of a working quarry (at the top of a very steep hill within Crevolà village) and permission should be sought from the drunken Italian workmen before entering the quarry (they do not take any safety precautions so I advise caution!). The samples are loose blocks from the eastern part of the quarry.
Sample description: Marble.
Dolomite 80%, ~0.2 mm in diameter.
Phlogopite 14%, ~0.5mm perpendicular to c, some of the phlogopite grains contain unidentified opaque black inclusions.
Muscovite 1%, ~1 mm in diameter.
Small amount of feldspar 2% and quartz 3%.

Sample number: HT28
Grid reference: 665.79, 112.10
Field location: Crevoladossola
Sample description: Marble.
Dolomite 80%, 0.2-0.5 mm in diameter.
Phlogopite 14%, 0.2-1 mm perpendicular to c.
Muscovite 1%, ~1 mm perpendicular to c.
Small amount of K-feldspar 2% and quartz 3%.

Sample number: HT29
Grid reference: 668.75, 124.25
Field location: Rozzaro. Samples were taken from a cliff, exposing Bündnerschiefer at the base. This exposure is found by following a track to the west, from the centre of the village through the wood and up the hill.
Sample description: Marble.
Calcite 80%, 0.25-0.5 mm, cloudy, some deformation.
Isolated grains of muscovite, 3%, 0.2 mm perpendicular to c.
Phlogopite , 2%, 0.5 mm perpendicular to c.
Quartz 10%, 0.1-0.5 mm in diameter.

Sample number: HT30
Grid reference: 668.75, 124.30
Field location: Rozzaro
Sample description: Calcsilicate marble.
Calcite 50%, ~1 mm in diameter, cloudy.
Quartz 25%, 0.1-0.5 mm in diameter.
K-feldspar 20%, 0.1-0.5 mm in diameter.
Muscovite 5%, 0.5 mm perpendicular to c.
Small amounts of oxides.

Sample number: HT31
Grid reference: 651.05, 117.17
Field location: Alte Kaserne. Alte Kaserne is near Gondo, the samples were taken from near a track which heads southward up the mountainside from Alte Kaserne.
Sample description: Marble.
Calcite 75%, shows some deformation, 1-4 mm in diameter.
Muscovite 5%, ~1 mm perpendicular to c.
Quartz, rounded, 15%, 0.1-0.5 mm in diameter, contains some fluid inclusions.
Small amounts of oxides.

Sample number: HT32
Grid reference: 651.05, 117.02
Field location: Alte Kaserne
Sample description: Marble.
Calcite 85%, 0.2-1 mm in diameter, some deformation.
Rounded quartz grains with fluid inclusions, 0.2 mm, 5%.
Biotite band, 8%, 0.1-1.5 mm perpendicular to c.
Isolated grains of muscovite 2%, 0.1-0.5 mm perpendicular to c.

Appendix 2

Mass Spectrometry

A2.1 Rb-Sr Analysis

Isotope dilution thermal ionisation mass spectrometry (TIMS) was used for the measurement of isotopic compositions of elements to provide absolute age determinations. Isotope dilution and mass spectrometry for Rb-Sr analysis was carried out at NIGL.

A2.1.1 Mineral Separation and Sizing

Samples (~2 kg) were crushed using a jaw crusher, until the chips were < 1 cm^3, then passed through a disk mill until the grains were separated. These grains were then washed in double distilled water to remove any fines. The samples were hand-picked for mica (phlogopite and muscovite) and carbonate (calcite or dolomite), which may bias the samples towards larger grains.

To separate unbroken mica grains from the phlogopite band, chips of a sample were leached in 10-30 ml fractions of 1M ethanoic acid. HT23 was chosen for this dissolution experiment, as it does not contain any other silicate phase (Appendix 1), so dissolving the calcite leaves a pure phlogopite separate. The calcite was dissolved using ethanoic acid *via* the following reaction:

$$2CH_3COOH + CaCO_3 \rightarrow Ca(CH_3COO)_2 + CO_2 + H_2O \quad (A2.1)$$

10 ml of 1M ethanoic acid contains 0.01 moles of acid, which will react with 0.005 moles of calcite. The molecular mass of calcite is 100.0892, so if the reaction goes to completion, 10 ml of acid should dissolve 0.5g of calcite. The starting weight of the sample was 10.79g, of which 2.21g was phlogopite and 8.58g was calcite, if the reaction (A2.1) goes to completion, it should take 171.6 ml of ethanoic acid. The total amount of acid used was 455 ml (due to problems breaking up the sample residue) and the leaches were run for a total time for 107.5 hours. All the leaches produced clear, colourless solutions. A previous leaching experiment (Jenkin *et al.*, 2001) showed that leaching of metacarbonate samples in 1M ethanoic acid does not substantially alter the isotopic composition of the phlogopite present, so this method can be used to provide phlogopite separates.

The phlogopite collected from the dissolution was sieved to give grain size fractions, which were then dated using Rb-Sr (Table A2.1 gives the sieve fractions and actual grain sizes). Part of each sieved fraction was then assessed, using a binocular microscope to determine the grain dimensions for plotting purposes. Mica grains are tabular and as such the largest dimension is often greater than the maximum dimension of the sieve, Figures A2.1 and A2.2 show the dimension of a phlogopite grain and a sieve mesh respectively (after G. R. T. Jenkin, unpublished results).

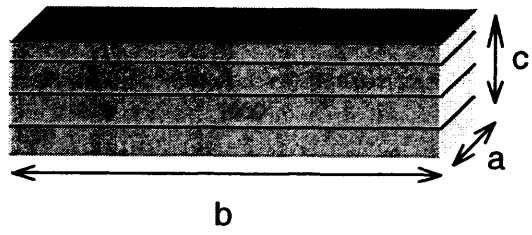

Figure A2.1 The dimensions of a typical mica grain; **a**, **b**, and **c** denote the three different dimensions.

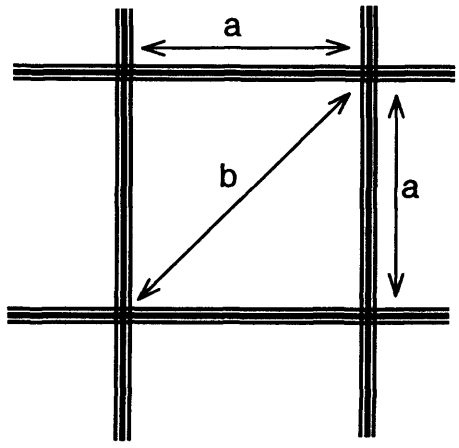

Figure A2.2 The dimensions of a sieve; **a** represents the sieve mesh size (for example 1000 microns), **b** represents the widest dimension of the sieve (for a 1000 micron mesh, this distance would be 1414 microns). However, the widest dimension of the mica grain may be perpendicular to the mesh and in this case, there is no limit to the maximum dimension of the mica grain, allowing some of the mica grains to be larger than the mesh size.

Table A2.1 shows the dimensions of the grains measured. Figure A2.3 shows the distribution of grain sizes for the phlogopite separates; the graph clearly shows overlap between the grain size fractions. The data show that there is considerable overlap between grain size fractions, often with grains being larger than the mesh dimensions.

Table A2.1 Sieve fractions of phlogopite for HT23.

Sieve mesh size (μm)	**n**	**Actual variation in size of grains (μm)[a]**	**Grain Length (μm) (weighted mean)[b]**
> 1000	5	1113-1875	1597
600-1000	5	950-1300	1050
350-600	10	550-1000	760
300-350	17	463-912	757
75-200	16	125-463	277

[a] Grain length is taken for the b dimension shown in Figure A2.1.
[b] These values are used in Figure 4.x. The average length in the b dimension (Figure A2.1) is weighted according to the mass of each grain

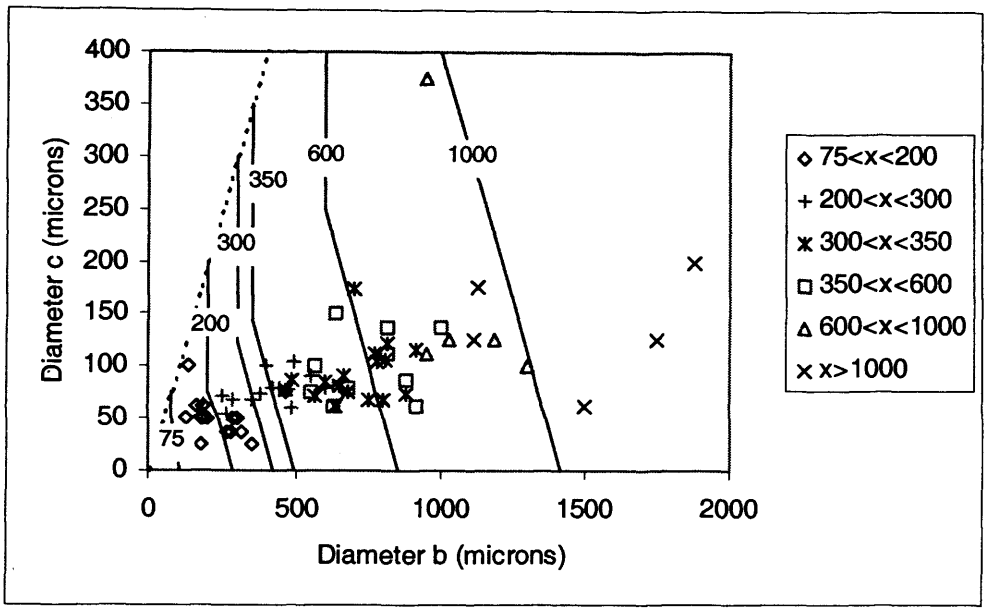

Figure A2.3 The black lines represent the ideal grain size boundaries for the largest dimension (i.e. b in Figure A2.2) for meshes of 75, 200, 300, 350, 600 and 1000 microns (marked on the plot). The dashed line represents b = c (Figure A2.2) for all mesh sizes. The data show that there is considerable overlap between the grain size fractions of HT23, often with grains being larger than the mesh dimensions (after G. R. T. Jenkin, unpublished results).

A2.1.2 Isotope Dilution

Mineral separates and standards (NBS 987 and BVH-01) were weighed into Savillex beakers (~0.2g), then washed with acetone. Mica samples were further leached with 1M ethanoic acid for one hour. Spike solutions were then added (Table A2.2).

Table A2.2 Spikes for Rb-Sr analysis (approximate weights).

Analysis type	^{87}Rb spike (g)	^{84}Sr spike (g)
Mica	0.6	0.02
Calcite	0.02	0.2
Leachate	None	0.02
Standard	0.6	0.2
Blank	None	0.02

The mica and the standard samples were heated overnight in Savillex bombs with a few drops of HF and 10 ml nitric acid and then dried down on digestion of the silicate material. 2 ml of 6 M HCl was added to convert the products to chloride. The carbonate was dissolved in 5 ml of 3 M ethanoic acid, on completion and then dried down. 1 ml of 2.5 M HCl was added to convert the products to chloride. 1 ml of 2.5 M HCl was added to both the blanks and the leachates. Sr and Rb were separated from solution using standard Dowex AG50W X12 cation exchange resin in quartz columns.

The Rb and Sr were separated using cation exchange columns, using the following method:

- Add 50 ml 6 M HCl to the columns. Drain and discard.
- Add 50 ml MQ H_2O to the columns. Drain and discard.

- Add 50 ml 6 M HCl to the columns. Drain and discard.
- Precondition the columns by adding 15 ml 2.5 M HCl. Drain and discard.
- Transfer the samples (dissolved in the 2 ml, 2.5 M HCl) to labelled centrifuge tubes, run the centrifuge for 5 minutes at 3000 rpm. At the same time, rinse the empty Savillex sample beakers with MQ H_2O and then leach on the hot plate with 1-2 ml 6M HCl.
- Pipette 1 ml of the sample solution onto the columns (using a clean pipette tip for each sample) and wash down with 2 ml of 2.5 M HCl.
- Add 17 ml 2.5 M HCl to the columns. Leave to drain and discard (this fraction contains elements such as Fe, Na, Mg and K).
- Wash the Savillex beakers with a few ml of 6 M HCl. Switch the glass beakers (which have been collecting the waste products) under the columns for the cleaned Savillex beakers.
- Add 4 ml 2.5 M HCl to the columns. This contains the Rb fraction. Collect the Rb in a clean, labelled Savillex sample beaker.
- Replace the glass beakers and add 15 ml 2.5 M HCl to the columns. Drain and discard (this fraction contains Ca).
- Label new, clean Savillex beakers for collection of Sr and put these under the columns. Add 10 ml 2.5 M HCl to the columns; this contains the Sr fraction.
- Dry down samples on a hot plate for storage. The sample should leave a small dark speck in the base of the beaker.

A2.1.3 Mass Spectrometry

For mass spectrometry, Sr samples were taken up in water and then loaded onto single Ta filaments with phosphoric acid. Rb samples were loaded onto triple Ta filaments. The Sr sample loading procedure is as follows:

- Place a Ta filament on the current generator. Using a clean pipette tip, load 1 µl of 1M H_3PO_4 onto the filament, set the current to 1 Amp and dry down to a small spot.
- Using the same pipette tip, take up 2-3 µl of MQ H2O and add to the sample beaker to dissolve the sample.
- Take up the dissolved sample and load onto the spot of H_3PO_4 and allow to dry down.
- Once the sample had dried to a small spot, turn the current up slowly (to ~ 2 Amps) until the filament glows a dull red. Hold the current at 2 Amps while the phosphoric fumes are liberated. The filaments can then be placed onto a magazine for running in the mass spectrometer.

For Rb, the procedure is slightly different, as double Ta filaments are used and no H_3PO_4 is required to load the sample. The current is turned up to 1 amp to dry and then the samples can be placed on the magazine for mass spectrometry. The samples were analysed using the Finnigan 262 multicollector mass spectrometer.

A2.1.4 *Blanks and Standards.*

Table A2.3 shows the standard and blank results. The sample analysis results can be found in Chapter 4. Rb blanks are not measured, as picogram blank levels should not affect the precision required for Rb concentrations. Sr blanks around 100-150 picograms are expected at NIGL. The effect of blanks can be found by looking at the % contribution of blank to your sample size (i.e. weight sample × concentration Sr in sample). If the blank contribution is <0.003% (which is the 2 S.D. reproducibility of the standard) then it is insignificant as we cannot quote the data to better than the over all reproducibility of the standard (i.e. blank contribution insignificant). However, regression analysis can tolerate a higher blank as we usually use 0.02% errors on the Sr isotope ratio in regressions to account for geological variation in samples. Thus the blank contribution needs to be < 0.2%, which it is except for three leachate analyses (blank/phlogopite ratios are within the region 0.002 – 0.1).

Table A2.3 Standard and blank data for Rb-Sr analysis.

	Result
NBS 987 Sr	0.710187
2 S.D.	0.000029
Number of analyses	11
Accepted NBS 987	0.71024±26
BHV-01	0.703465
2 S.D.	0.000017
Number of analyses	4
Accepted BHV-01	0.703427±42
Sr blank	420 pg
2 S.D.	120 pg
Number of analyses	3
Typical NIGL value	100±50 pg

A2.1.4 Errors

All the data points from the same sample should lie upon a straight line (an isochron) however, errors arising from the analysis of the samples may cause a poor fit to the isochron. These errors give rise to corresponding uncertainty in the estimate of the slope of an isochron line and, therefore, the age of the samples being dated. The uncertainty in the initial $^{87}Sr/^{86}Sr$ ratio will also be affected by the analytical errors associated with the data points.

Analytical error is the deviation of a measured value from its true value. Such errors may be; random errors, which have a normal distribution about the arithmetic mean of the measurements and approaches the true value as the number of measurements increases; or systematic errors which are consistent differences between the true value and a set of measurements, such that their arithmetic mean is displaced from the true value. Therefore random errors determine the precision of a set of measurements, whereas systematic errors determine their accuracy. Systematic errors in the measurement of $^{87}Sr/^{86}Sr$ and $^{87}Rb/^{86}Sr$ result in the similar errors in the initial $^{87}Sr/^{86}Sr$ ratio and the age derived from the isochron respectively.

All isochron diagrams (and measured ages) were created in Isoplot (Ludwig, 2001). The isochrons use Isoplot model 3, which assumes that the scatter in the data points is due to a combination of the assigned errors plus an unknown but normally distributed variation in the *y*-values.

A2.2 Carbon and Oxygen Analysis

Carbon and oxygen are both naturally occurring elements with more than one stable isotope; for these purposes ^{12}C and ^{13}C are measured (respectively ~98.9% and ~1.1% of naturally occurring carbon; Henderson, 1982) and ^{16}O and ^{18}O are measured (respectively ~99.7% and ~0.2% of naturally occurring oxygen; Henderson, 1982). These isotopes show the same chemical characteristics, but there are differences in isotopic partition due to differences in their isotopic masses. Carbon and oxygen isotope data are recorded as $\delta^{13}C_{PDB}$ and $\delta^{18}O_{SMOW}$ respectively.

Carbon and oxygen isotopes can be used to assess the impact of fluid infiltration on carbonate samples. In geochemical studies, the fractionation of stable isotopes is measured as the relative difference in the ratio of the isotopes in the samples being studied when compared with the ratio in the standard:

$$\delta_A = \left(\frac{R_A - R_{Std}}{R_{Std}} \right) \times 1000 \qquad \text{(A2.2)}$$

Where:

δ_A is the relative difference (expressed in parts per thousand or per mill).

R_A is the isotopic ratio in sample A.

R_{Std} is the isotopic ratio of the standard.

$^{18}O/^{16}O$ ratios are usually measured against Standard Mean Oceanic Water (SMOW) and $^{13}C/^{12}C$ are measured against a Cretaceous belemnite from the Peedee Formation (PDB).

Hilary Sloane carried out the carbon and oxygen analyses at NIGL on hand-picked carbonate samples. The dolomite samples were reacted at 25 °C for 60 hours and results were calculated using a fractionation factor of –1.01109. The calcite samples were reacted at 25 °C for 16 hours and results were calculated using a fractionation factor of –1.01025. Results of the carbonate oxygen and carbon isotope analyses are found in Chapter 4.

A2.3 Previously Published Geochronology from the Lepontine Alps

The data presented in Tables A2.4 and A2.5 are used to produce Figures 4.7 and 4.9 in Chapter 4, showing the spatial distribution of measured ages throughout the Central Alps.

Table A2.4 Summary of previously published mica Rb-Sr ages from Valle Maggia, Valle Verzasca, Valle Leventina and Valle Antigorio.

Sample	Elevation (m)	Co-ordinate (E)	Co-ordinate (N)	Distance (km)[a]	Musc Rb-Sr (Ma)	Error (Ma)	Bt Rb-Sr (Ma)	Error (Ma)	Phl Rb-Sr (Ma)	Error (Ma)	Location	Rock type	Paper
V. Maggia													
KAW 1877	~2076	683.300	145.080	9.920			15.4	0.2			Bianco	gneiss	Steiner 1984
HT17	~2310	687.550	148.400	6.600					17.8	0.2	Narèt	marble	This work
HT15	~2310	687.550	148.250	6.750					17.3	0.7	Narèt	marble	This work
HT15	~2310	687.550	148.250	6.750					17.3	0.2	Narèt	marble	This work
KAW 1875	~2310	687.187	147.625	7.375			17.3	0.2			Narèt	gneiss	Steiner 1984
I.29	~2310	687.450	148.200	6.800					17.8	0.2	Narèt	marble	Jenkin et al 2001
I.29	~2310	687.450	148.200	6.800					18.1	0.2	Narèt	marble	Jenkin et al 2001
I.29	~2310	687.450	148.200	6.800					18.0	0.2	Narèt	marble	Jenkin et al 2001
I.29	~2310	687.450	148.200	6.800					16.6	0.2	Narèt	marble	Jenkin et al 2001
I.29	~2310	687.450	148.200	6.800					17.6	0.2	Narèt	marble	Jenkin et al 2001
I.28	~2310		148.200	6.800					16.3	0.2	Narèt	marble	Jenkin et al 2001
I.28	~2310		148.200	6.800					13.9	0.1	Narèt	marble	Jenkin et al 2001
I.28	~2310		148.200	6.800	20.2	0.2					Narèt	marble	Jenkin et al 2001
KAW 1873	~1500	692.375	147.500	7.500			15.4	0.2			Sambuco	gneiss	Steiner 1984
KAW 1874	~2500	693.625	148.187	6.813			14.3	0.2			Scheggia	gneiss	Steiner 1984
KAW 1972	~2074	688.750	148.125	6.875			15.1	0.2			Laghetti	gneiss	Steiner 1984
KAW 1974	~2074	688.625	148.000	7.000			15.8	0.2			Laghetti	gneiss	Steiner 1984
KAW 1877	2090	683.300	145.080	9.920	22.5	1.9	15.4	0.2			Bianco	gneiss	Hurford 1986
KAW 1876	1060	684.040	140.450	14.550	19.3	0.3	13.2	0.2			Bavona	gneiss	Hurford 1986
KAW 1887	630	692.700	134.950	20.050	17.6	2.1	15.7	0.2			Menzonio	gneiss	Hurford 1986
KAW 1878	1550	680.780	130.260	24.740	18.3	0.3	14.7	0.2			Bosco G.	gneiss	Hurford 1986
KAW 1881	680	688.550	129.550	25.450			15.3	0.3			Linescio	gneiss	Hurford 1986
B7	~420	691.100	128.500	26.500			16	3.2			Riveo	gneiss	Armstrong 1966
KAW 1886	420	691.100	128.500	26.500			16.3	0.3			Riveo	gneiss	Hurford 1986
HT23	~500	694.250	127.230	27.770					18.1	1.1	Someo	marble	This work
HT23	~500	695.250	127.230	27.770					18.7	0.2	Someo	marble	This work
HT23	~500	696.250	127.230	27.770					18.6	0.2	Someo	marble	This work
HT23	~500	697.250	127.230	27.770					17.5	0.1	Someo	marble	This work
HT23	~500	698.250	127.230	27.770					17.3	0.1	Someo	marble	This work
KAW 1885	360	695.050	126.200	28.800			16.2	0.3			G. Someo	gneiss	Hurford 1986
KAW 1884	300	698.400	121.700	33.300	19.6	0.6	18.1	0.3			Moghegno	gneiss	Hurford 1986
KAW 1879	980	687.900	120.600	34.400			18.5	0.3			Vergeletto	gneiss	Hurford 1986
KAW 2100	630	699.925	119.425	35.575	26	0.9	18.7	0.2			Ronchi	gneiss	Hurford 1986
KAW 2104	1869	704.325	118.538	36.462			20.2	0.3			Trosa	gneiss	Hurford 1986
KAW 1880	960	689.600	117.600	37.400			19.3	0.3			Onserone	gneiss	Hurford 1986
KAW 2101	250	701.650	116.300	38.700	24	0.5	19.3	0.2			Brolla	gneiss	Hurford 1986
KAW 1883	220	701.330	115.800	39.200	22.4	0.2	19.4	0.2			Brolla	gneiss	Hurford 1986
KAW 1882	340	697.200	115.150	39.850			19.4	0.3			Intragna	gneiss	Hurford 1986
KAW 2103	250	699.375	114.775	40.225	22.9	1	19.2	0.2			Golino	gneiss	Hurford 1986
V. Antigorio													
KAW 311	2070	675.800	151.275	3.725			14.5	0.6			Cher	gneiss	Wagner 1977
KAW 1877	~2076	683.300	145.080	9.920			15.4	0.2			Bianco	gneiss	Steiner 1984
KAW 286	1670	675.000	140.180	14.820	19		13.6				Cascata T.	gneiss	Jäger 1970
KAW 286	1670	675.000	140.180	14.820			13.6	0.8			Cascata T.	gneiss	Wagner 1977
B28a	?	647.700	140.000	15.000			14.9	1			Cascata T.	gneiss	Jäger 1967
B28c	?	647.700	140.000	15.000			14.6	1			Cascata T.	gneiss	Jäger 1967
B28b	?	647.700	140.000	15.000			14.4	0.8			Cascata T.	gneiss	Jäger 1967
B4	520	668.850	121.600	33.400			14.1	0.6			Verampio	gneiss	Armstrong 1966
KAW 201	520	668.850	121.600	33.400	15.1						Verampio	gneiss	Jäger 1970
KAW 201	520	668.850	121.600	33.400			13.4				Verampio	gneiss	Jäger 1970
KAW 201	520	668.850	121.600	33.400			13.4	0.5			Verampio	gneiss	Wagner 1977

Sample	Elevation (m)	Co-ordinate (E)	Co-ordinate (N)	Distance (km) [a]	Musc Rb-Sr (Ma)	Error (Ma)	Bt Rb-Sr (Ma)	Error (Ma)	Phl Rb-Sr (Ma)	Error (Ma)	Location	Rock type	Paper
KAW 201	520	668.850	121.600	33.400	18.8	2.8					Baceno	gneiss	Jäger 1967
KAW 201	520	668.850	121.600	33.400	15.1	2.3					Baceno	gneiss	Jäger 1967
KAW 201	520	668.850	121.600	33.400	14.9	1.9					Baceno	gneiss	Jäger 1967
KAW 201	520	668.850	121.600	33.400			13.4	0.5			Baceno	gneiss	Jäger 1967
B32	~1100	684.800	121.350	33.650			16.3	1.9			Vergeletto	gneiss	Jäger 1967
B31	~1250	683.000	117.000	38.000			16.7	2.1			Onsernone	gneiss	Jäger 1967
KAW 159	860	653.960	116.300	38.700			11.4	1.3			Gondo	gneiss	Wagner 1977
KAW 160	1160	650.400	115.200	39.800			11	1.1			Alte Kas.	gneiss	Wagner 1977
HT26	~400	665.790	112.100	42.900					14.2	0.2	Crevola	Marble	This work
HT28	~400	665.790	112.100	42.900					14	1	Crevola	Marble	This work
KAW 83	~300	668.145	109.000	46.000	28	6	20.1	1.1			Beura	gneiss	Jäger 1967
KAW 372	500	662.200	108.150	46.850			14.4	0.6			Torno	gneiss	Wagner 1977
KAW 83	270	667.600	107.100	47.900			19.3	0.7			Croppo	gneiss	Armstrong 1966
KAW 82	270	667.600	107.100	47.900	26	6					Croppo	gneiss	Jäger 1967
KAW 82	270	667.600	107.100	47.900			18.7	0.6			Croppo	gneiss	Jäger 1967
KAW 82	270	667.600	107.100	47.900			18.7	0.6			Croppo	gneiss	Wagner 1977
P2b	~250	660.475	103.675	51.325	34.3	3.5					Villa	gneiss	Jäger 1967
P2a V. Verzasca	~250	660.475	103.675	51.325	33.6	3.3	19.7	1.7			Villa	gneiss	Jäger 1967
B12	~2400	702.230	131.150	23.850			17	2.7			V.Verzasca	gneiss	Jäger 1967
KAW 4	800	703.750	128.250	26.750	16.8	0.5					Brione	gneiss	Wagner 1977
KAW 4B	800	703.750	128.250	26.750			15.9	1.4			Brione	gneiss	Jäger 1967
KAW 4B	800	703.750	128.250	26.750			16.6	1.4			Brione	gneiss	Jäger 1967
KAW 4B	800	703.750	128.250	26.750			16	1.6			Brione	gneiss	Jäger 1967
KAW 6	530	707.900	124.050	30.950	17.3	2.5					Lavertezzo	gneiss	Wagner 1977
HT11	~500	708.800	117.500	37.500	18.8	0.2					Verzasca	Marble	This work
B8 V. Leventina	~425	708.800	116.500	38.500	30	28	19.2	1.6			Gordemo	gneiss	Jäger 1967
HT4	~1200	702.600	148.250	6.750	16.8	0.2					Dalpe	Marble	This work
KAW 140	700	707.030	145.870	9.130	15.9	0.7					Chiggiogna	gneiss	Wagner 1977
KAW 138	300	715.570	135.400	19.600	16.1	0.9					Pollegio	gneiss	Wagner 1977
KAW 137	300	719.690	129.410	25.590	17.6	1.9					Osogna	gneiss	Wagner 1977
KAW 75	~250	721.925	125.175	29.825			16.8	1.1			Claro	gneiss	Armstrong 1966
KAW 76	260	723.850	121.000	34.000			18.4	1.3			Castione	gneiss	Wagner 1977
B18	~350	722.700	119.800	35.200			19.4	2.3			Gorduno	gneiss	Jäger 1967

[a] Distance south of the 155 N gridline (Swiss National Grid).

Table A2.5 Summary of previously published mica K-Ar and monazite U-Pb ages from Valle Maggia and Valle Verzasca.

Sample	Elevation (m)	Co-ordinate (E)	Co-ordinate (N)	Distance (km) [a]	K-Ar (Ma)	Error (Ma)	K-Ar (Ma)	Error (Ma)	U-Pb (Ma)	Error (Ma)	Location	Rock type	Paper
V. Maggia													
FUSIO	~1200	694.060	144.160	10.840					22		Fusio	gneiss	Köppel 1980
RUSCADA	~900	695.450	138.550	16.450					22.3		Prato	gneiss	Köppel 1980
SOMEO	~500	694.650	126.730	28.270					22.1		Someo	gneiss	Köppel 1980
KAW 1877	2090	683.300	145.080	9.920	15.4	0.2	16.8	0.2			Bianco	gneiss	Hurford 1986
KAW 1876	1060	684.040	140.450	14.550	14.2	0.2	16.6	0.3			Bavona	gneiss	Hurford 1986
KAW 1887	630	692.700	134.950	20.050	15.9	0.2	17.2	0.2			Menzonio	gneiss	Hurford 1986
KAW 1878	1550	680.780	130.260	24.740	15.4	0.2	16.1	0.2			Bosco G.	gneiss	Hurford 1986
KAW 1881	680	688.550	129.550	25.450	14.7	0.2					Linescio	gneiss	Hurford 1986
KAW 1886	420	691.100	128.500	26.500	15.2	0.2					Riveo	gneiss	Hurford 1986
KAW 1885	360	695.050	126.200	28.800	16.3	0.2	18.5	0.2			G. Someo	gneiss	Hurford 1986

Sample	Elevation (m)	Co-ordinate (E)	Co-ordinate (N)	Distance (km) [a]	K-Ar (Ma)	Error (Ma)	K-Ar (Ma)	Error (Ma)	U-Pb (Ma)	Error (Ma)	Location	Rock type	Paper
KAW 1884	300	698.400	121.700	33.300	17.3	0.2	18.5	0.2			Moghegno	gneiss	Hurford 1986
KAW 2100	630	699.925	119.425	35.575	19.3	0.2	19.5	0.2			Ronchi	gneiss	Hurford 1986
KAW 2101	250	701.650	116.300	38.700	20.4	0.2	20.8	0.2			Brolla	gneiss	Hurford 1986
KAW 1883	220	701.330	115.800	39.200	19	0.2	19.3	0.3			Brolla	gneiss	Hurford 1986
KAW 2103 V. Verzasca	250	699.375	114.775	40.225	19.4	0.2	20.5	0.2			Golino	gneiss	Hurford 1986
KAW 4B	800	703.750	128.250	26.750					22.7		Brione	gneiss	Jäger 1967
BRI 2	~800	704.400	128.950	26.050					20.9		Brione	gneiss	Köppel 1980

[a] Distance south of the 155 N gridline (Swiss National Grid).

Appendix 3

Laser Ablation Inductively Coupled Plasma Mass Spectrometry

Perkins & Pearce (1995) describe the laser ablation ICP-MS instrument and technique and Halliday *et al.* (1998) give details of the further applications of multi-collector ICP-MS. Christensen *et al.* (1995) first demonstrated the application of LA-ICP-MS to $^{87}Sr/^{86}Sr$ ratios on a modern marine gastropod and a plagioclase phenocryst. More recently, Bailey (*unpublished PhD thesis*) has completed work using LA-ICP-MS to refine strontium isotope stratigraphy for the Jurassic. Further details of applications of LA-ICP-MS have been published by the Mineralogical Association of Canada in its Short Course series (Sylvester, 2001).

A3.1 The Instrument

A3.1.1 *Inductively Coupled Plasma – Mass Spectrometry*

ICP-MS instruments combine low detection limits with rapid analysis capability (Perkins & Pearce, 1995). The inductively coupled plasma is the ion source used in the instrument. It consists of an argon plasma, generated by a radio frequency field and propagated at the end of a plasma torch. Argon gas is introduced tangentially into the outer two tubes of the torch whilst the inner tube has a linear flow. The inner flow is usually referred to as the nebulizer, carrier or injector flow and transfers the sample to the plasma. The outer or coolant gas is required to keep the hot plasma away from the torch. The radio frequency field, which generates and sustains the plasma is produced by a load coil, which encircles the end of the plasma torch. An intense electromagnetic field is produced at the end of the torch inside the coil. To produce plasma, it is necessary to "seed" the argon gas with charged particles, which can be achieved by passing a high-voltage spark along the inner wall of the outermost tube of the torch. Argon ions and electrons are produced and these particles are swept along the inside of the coil and enter the induction region where they become coupled to the oscillating field. This process causes the production of more argon ions in the gas, i.e. argon plasma. This plasma is maintained as long as the radio frequency field provides the induction. A temperature of about 10000 K is achieved in the core of the plasma. The inner nebulizer gas flow punches a hole through the plasma and the sample is heated by radiation and conduction from the surrounding plasma. The function of the argon plasma is to excite positive ions from the sample atoms. The excited ions are then transferred into a mass spectrometer *via* an ion extraction interface.

A3.1.2 *Ion extractor interface*

The interface consists of two water-cooled metal cones, through which plasma gas and ions are extracted into the instrument *via* chambers of increasingly high vacuum. The plasma and ions

are accelerated through the first cone to produce a supersonic jet of gas in the expansion chamber. The second cone pierces the back of this jet and extracts a small proportion of the gaseous plasma and ions into the main body of the mass spectrometer. Once inside the main chamber, the residual gas is separated from the positive ions and pumped away. The remaining ions are extracted and focused into the mass spectrometer by a series of ion lenses.

A3.1.3 *Ion lenses*

The function of the ion lenses is to produce a beam of ions focused into the mass analyser. Ions, which travel at the same velocity but have different masses, will have different kinetic energies and their paths through the lenses will vary according to their mass/charge ratio. On leaving the ion lenses, the ion beam enters the mass analyser.

A3.1.4 *Mass analyser*

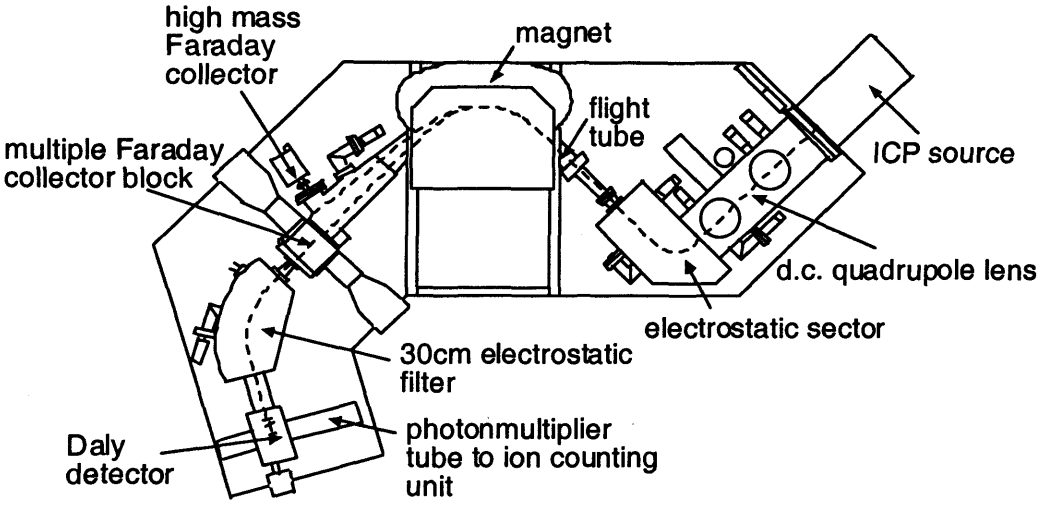

Figure A.3.1 Schematic outline of a VG Elemental Plasma 54 multiple collector inductively coupled plasma mass spectrometer (after Halliday *et al.* 1998). The dashed lines represent the ions, travelling from the ICP source to counting unit *via* the Faraday cups.

The mass analyser used was a VG Elemental Plasma 54 (illustrated in Figure A3.1), a double-focusing magnetic sector analyser. The principle behind this analysis is that in the presence of a magnetic field, a moving charge (ion) will travel in a curved path (Jackson *et al.*, 2001). The mass spectrometer also employs an electrostatic sector analyser, which focuses the ions according to their energy before entering the magnet. The analyser uses two curved conducting plates, over which a potential difference is applied, which steer ions along different paths according to their energy. When all the ions have the same kinetic energy, those with a lower mass will be more deflected by the magnetic field than ions with a heavier mass. The ions are then focused into a collector array of Faraday cups, which coincides with the ion focal plane and allow the simultaneous measurement of Sr ion beams. The detectors Low 3, Low 2, Low 1, Axial, High 1, High 2 and High 3 were used to collect the ion currents corresponding to atomic masses 83, 84, 85, 86, 87, 88 and 89 respectively. Mass 83 is measured to monitor the trace amounts of krypton

present in the gas supply, as krypton forms an isobaric interference with strontium at masses 84 and 86. Masses 84, 86, 87 and 88 measure strontium isotopes and mass 85 monitors ^{85}Rb to enable the correction for ^{87}Rb interference on ^{87}Sr.

A3.1.5 *Laser ablation*

Sample introduction involves the use of a laser to remove a portion of material from a solid sample, so generating microparticulate matter that is entrained in the carrier argon stream where it is ionised and injected into the plasma. The 266 nm Nd-YAG laser (VG Elemental Microprobe II) is generated using a rod of yttrium aluminium garnet doped with approximately 3wt% Nd_2O_3, typically with 500 mJ total power. A system of computer controlled optics and *x-y-z* stage is used to navigate around the sample.

A3.1.6 *Laser ablation and ICP-MS*

The ability of the laser to produce microparticulate material from solid samples makes it an ideal choice for sample introduction into an ICP. The plasma temperature is sufficiently high to volatilise solid particles and to produce ions. The laser output is normally arranged as a horizontal beam, which can be directed onto the sample surface using mirrors. The sample is enclosed in a circular fused silica cell through which argon can be passed and is located on an *x-y-z* stage, which is driven by computer controlled stepper motors. Simultaneous stage movement and laser firing allow the production of automated sampling patterns (individual spots, lines of spots and rasters of spots). Samples can be exchanged easily without shutting down the plasma source. The size of the sample is limited by the size of the sample chamber (it can accommodate most thin sections and small hand specimens) and can be viewed using transmitted and reflected light via a microscope-mounted video camera. The size of the craters formed by the ablation depends upon the type of material being ablated, its crystallographic orientation and the laser operating conditions.

A3.2 Operating Conditions

A3.2.1 *Sample Preparation*

Laser ablation analyses of calcite for $^{87}Sr/^{88}Sr$ were addressed in this study. Samples were prepared as 600 μm thick polished thin sections, which easily fit into the sample holder and allow a smooth, flat surface for the ablation.

A3.2.2 *Ablation Volume*

The spatial resolution of the analyses depends upon the amount of material it is necessary to ablate to produce the analysis of sufficient precision. A larger diameter of beam (or deeper ablation craters) will ablate more material, which reduces the spatial resolution but gives a greater ion signal and a generally higher precision.

The calcite samples analysed contain approximately 400 ppm Sr and each calcite analysis requires the ablation of approximately 0.06 mm^3 of sample (which contains approximately 60 ng Sr). Most analyses were 0.1 to 0.2 mm wide by 0.1 to 0.3 mm deep requiring a typical analysis length of 2 to 10 mm. For this reason, on smaller grains and towards grain cores on larger grains, the analysis took the form of a raster of spots as a large enough volume of sample could not be achieved for the analysis by completing several concentric analyses.

A3.2.3 *Data Output*

Isotope ratios were measured with an integration time of 2 seconds. Up to 100 individual integrations are taken and the mean and 2 standard errors of these is calculated to give one $^{87}Sr/^{86}Sr$ measurement (i.e. one analysis). The output from the mass spectrometer is in the form of raw counts (voltages) of masses from 82.5 to 89.5 (half-mass centring, i.e. for mass 83 the detector examines masses in the range 82.5 to 83.5). Uncorrected ratios of $^{86}Sr/^{88}Sr$, $^{84}Sr/^{86}Sr$ and $^{87}Sr/^{86}Sr$ are displayed on the computer screen during the analysis and can be printed out with the corrected ratios at the end of the analysis. These raw ratios are corrected for mass interferences and mass bias to give the true measured ratios.

A3.3.1 Data Correction

A3.3.2 *Interferences*

Christensen *et al.* (1995) describe mass interferences on $^{87}Sr/^{86}Sr$ measurements. At mass 87, ^{87}Rb interferes with ^{87}Sr and at low Rb concentrations this interference can be corrected for using the natural $^{85}Rb/^{87}Rb$ ($^{85}Rb/^{87}Rb_{nat}$) and the measured mass bias applied to this natural ratio. The Ar gas may also contain a small amount of ^{86}Kr and its contribution to ^{86}Sr can be corrected for by measuring a gas blank, which is then subtracted from the total mass 86 intensity calculations of $^{87}Sr/^{88}Sr$ (see Section A3.3.4) or by monitoring other Kr isotopes.

A3.3.3 *Mass Bias Corrections*

Mass bias affects isotopes of lighter elements more than heavier elements because, proportionally, the difference between their masses is greater. For example, hydrogen shows a greater mass bias effect than strontium as ^{2}H has twice the mass of ^{1}H, but ^{87}Sr is less than 1% heavier than ^{86}Sr, however, the effect is still present and has to be corrected for.

Mass bias results from space-charge effects in the low electrostatic field regions of the ICP-MS instrument (White *et al.*, 2000 and references therein). As the ion beam expands, lighter ions migrate to the exterior of the plasma and are focussed less efficiently into the mass analyser causing the preferential selection of heavier masses. This fractionation is mainly a function of the mass of the ion, so the isotopic fractionation of two elements of similar mass should be similar. In

the case of strontium isotopes, $^{86}Sr/^{88}Sr$ is used to produce the mass bias correction, after the subtraction of ^{86}Kr.

A3.3.4 *Equations for Mass Bias Calculations*

To correct for mass bias, ratios are corrected by calculating a mass fractionation factor from a measured ratio of a pair of stable isotopes of the element being determined (calculated using an accepted value for this ratio and a mass fractionation law). Internal normalisation can only be used when an element has at least three isotopes, at least two of which are non-radiogenic, for example, Sr, Nd, or Hf.

Table A3.1 Atomic weights and relative abundances for species analysed in Rb-Sr LA-ICP-MS.

Species	Atomic Mass [a]	Relative Abundance (%)[b]
^{83}Kr	82.914135	11.5
^{84}Sr	83.913430	0.56
^{85}Rb	84.911794	72.2
^{86}Kr	85.910616	17.3
^{86}Sr	85.909267	9.86
^{87}Sr	86.908884	7.00
^{87}Rb	86.909187	27.8
^{88}Sr	87.905619	82.6

[a] Atomic masses are based upon the Carbon 12 standard.
[b] Relative abundances are taken from Faure, 1986.

Christensen *et al.* (1995) first demonstrated the application of LA-ICP-MS to $^{87}Sr/^{86}Sr$ ratios. Mass bias correction was achieved by using a normalisation to $^{86}Sr/^{88}Sr$, employing the exponential law. The interference of ^{87}Rb on ^{87}Sr was determined by measurement of ^{85}Rb and applying a correction from the natural $^{85}Rb/^{87}Rb$ ratio and a mass bias correction determined from $^{86}Sr/^{88}Sr$. The interference on ^{86}Sr from Kr was corrected in a similar way by determination of ^{83}Kr. The standard procedure for $^{87}Sr/^{86}Sr$ mass bias correction at NIGL follows (abundances and atomic weights are taken from Table A3.1). To find the $^{87}Sr/^{86}Sr$ ratio corrected for Rb and Kr interference and mass bias, Equation (A3.1) is used:

$$\frac{^{87}Sr}{^{86}Sr_{cor}} = \frac{87_{cor}}{86_{cor}} \times \left[\left(\frac{^{86}Sr/^{88}Sr_{ab}}{^{86}Sr/^{88}Sr} \right)^{\frac{\ln(87/86)}{\ln(86/88)}} \right] \qquad \text{(A3.1)}$$

Subscripts in the equations refer to measured ratios (m), isotopic abundances (ab) and corrected values (cor). $^{87}Sr/^{86}Sr_{cor}$ is the $^{87}Sr/^{86}Sr$ ratio corrected for mass bias using an exponential law and for the interference from Rb and Kr. 87_{cor} (Equation A3.2) is the 87 peak intensity corrected for the interference of ^{87}Rb (i.e. it gives ^{87}Sr).

$$87_{cor} = 87 \text{ intensity} - \left(85 \text{ intensity} \times {}^{87}Rb/{}^{85}Rb_{ab}\right) \qquad \text{(A3.2)}$$

86_{cor} (Equation A3.3) uses the 83 peak intensity corrected for the interference of ^{86}Kr.

$$86_{cor} = 86\,\text{intensity} - \left(83\,\text{intensity} \times {}^{86}Kr/{}^{83}Kr_{ab}\right) \qquad \text{(A3.3)}$$

$^{86}Sr/^{88}Sr_{ab}$ (Equation A3.4) is the ratio of isotopic abundances for $^{86}Sr/^{88}Sr$.

$$^{86}Sr/^{88}Sr_{ab} = \frac{9.86}{82.6} = 0.1194 \qquad \text{(A3.4)}$$

$^{87}Rb/^{85}Rb_{ab}$ (Equation A3.5) is the ratio of isotopic abundances for $^{87}Rb/^{85}Rb$.

$$^{87}Rb/^{85}Rb_{ab} = \frac{27.86}{72.14} = 0.3861 \qquad \text{(A3.5)}$$

$^{86}Kr/^{83}Kr_{ab}$ (Equation A3.6) is the ratio of isotopic abundances for $^{86}Kr/^{83}Kr$.

$$^{86}Kr/^{83}Kr_{ab} = \frac{17.3}{11.5} = 1.504 \qquad \text{(A3.6)}$$

Equations A3.1 and A3.7 (below) use the masses of the different isotopes of strontium to give the mass bias correction factor.

$$\frac{\ln(87/86)}{\ln(86/88)} = \frac{\ln(86.908884/85.909267)}{\ln(85.909267/87.905619)} = -0.50359 \qquad \text{(A3.7)}$$

The peak intensities are measured in counts per second for atomic masses 83 to 89 and can be corrected for specific interferences (as in Equation A3.3) by subtracting the proportion of counts that correspond to that atomic interference (calculated from the natural isotopic ratios).

A3.3.5 *Isobaric Interferences for Polyatomic Species*

Polyatomic species can be formed in the plasma (from Krypton and Argon), from impurities in the sample and potentially from the instrument. When analysing solid carbonates, there is the potential for interferences from combinations of different calcium, iron, magnesium and manganese isotopes as part of carbon and oxygen polyatomic species (Table A3.2).

Table A3.2 Isobaric interferences for Rb and Sr isotopes.

Mass	Ca	Fe	Mg	Mn	Other
83	$^{42}Ca^{25}MgO$	$^{56}Fe^{27}Al$		$^{55}MnCO$	^{83}Kr
				$^{55}Mn^{28}Si$	
84	$^{40}CaCO_2$	$^{56}Fe^{28}Si$	$^{24}MgCO_3$	$^{55}Mn^{29}Si$	^{84}Kr
	$^{42}Ca^{26}MgO$	$^{56}FeCO$			
	$^{44}Ca^{24}MgO$	$^{57}Fe^{27}Al$			
85	$^{44}Ca^{25}MgO$	$^{56}Fe^{29}Si$		$^{55}Mn^{30}Si$	
86	$^{42}CaCO_2$	$^{56}Fe^{30}Si$			^{86}Kr
	$^{44}Ca^{26}MgO$				
87	$^{43}CaCO_2$				
88	$^{44}CaCO_2$				

These and other species may cause interferences at the masses shown, however Fe, Mg and Mn form a small part of the calcite composition (see Appendix 4) and are not expected to cause large interferences. A way discovering the potential impact of polyatomic isobaric interferences is by using a solid calcite standard (instead of Sr standard solutions) with a previously well constrained $^{86}Sr/^{88}Sr$ ratio (such as a modern shell; as in Bailey, *unpublished PhD thesis*). This approach was important to the Bailey (*unpublished PhD thesis*) study as it was concerned with absolute $^{86}Sr/^{88}Sr$ ratios, however for this study the relative value of the $^{86}Sr/^{88}Sr$ ratio is important. The aim of this study was to use different techniques to examine strontium isotopic exchange and not to refine the LA-ICP-MS techniques; isobaric interferences from these species may be determined by examining the mass peaks and should be considered in future isotopic LA-ICP-MS studies and would worthy of intensive study by themselves.

A3.3.6 *Calibration, Precision and Accuracy*

The precision of an analytical technique is a measure of the closeness of agreement within a set of results, regardless of whether the result is correct in absolute terms. The accuracy is a measure of how closely the result represents the true value. Therefore, a result may be precise, but not accurate and *vice versa.* The precision may be tested within the limits of the analyses, whereas the accuracy requires the measurement and comparison to previously analysed data (or data from another laboratory, for which standards are analysed).

Calibration relates an instrument signal to the magnitude of the physical parameter it represents (for example, the intensity of a spectral line) by measuring a series of samples of known composition, or standards, before it can be converted into an estimate of concentration. All analytical techniques depend upon comparison with a calibration standard. Any deviation in the

measured standard value from the known standard value can be used to correct the analytical results.

A3.4 LA-ICP-MS Data

Table A3.3 gives the standard data, which is also shown on Figure A3.2, analysed during the collection of LA-ICP-MS data at NIGL from 18th – 22nd September 2001. The standards are in the form of solutions and their concentrations are given in Table A3.3. The standard solutions were analysed at the start and end of each analysis day, after every four sample analyses and after any change in analytical conditions.

Table A3.3 Standard data for $^{87}Sr/^{86}Sr$ ratios.

Analysis Number [a]	Standard [b]	$^{87}Sr/^{86}Sr$	Standard Deviation
AN000918.001	NBS 987 300 ppb	0.710310	1.1E-05
AN000918.002	NBS 987 300 ppb	0.710328	7.1E-06
AN000918.003	NBS 987 300 ppb	0.710290	7.1E-06
AN000918.004	NBS 987 300 ppb	0.710290	6.4E-06
AN000918.004	NBS 987 300 ppb	0.710342	7.1E-06
AN000918.004	NBS 987 300 ppb	0.710338	7.8E-06
AN000918.005	NBS 987 300 ppb	0.710325	7.1E-06
AN000918.005	NBS 987 300 ppb	0.710325	7.1E-06
AN000918.012	NBS 987 300 ppb	0.710311	7.8E-06
AN000918.013	NBS 987 300 ppb	0.710318	9.2E-06
AN000918.014	NBS 987 300 ppb	0.710303	9.2E-06
AN000918.018	NBS 987 300 ppb	0.710298	8.5E-06
AN000918.019	NBS 987 300 ppb	0.710315	7.8E-06
AN000918.019	NBS 987 300 ppb	0.710322	8.5E-06
AN000918.019	NBS 987 300 ppb	0.710297	7.1E-06
Average [c]	NBS 987 300 ppb	0.710314	1.6E-05 [d]
AN000919.001	NBS 987 100 ppb	0.710174	1.8E-05
AN000919.002	NBS 987 100 ppb	0.710272	1.6E-05
Average [c]	NBS 987 100 ppb	0.710223	4.9E-05 [d]
AN000919.003	NBS 987 200 ppb	0.710315	1.1E-05
AN000919.004	NBS 987 200 ppb	0.710296	1.1E-05
AN000919.004	NBS 987 200 ppb	0.710272	1.3E-05
AN000919.005	NBS 987 200 ppb	0.710274	9.2E-06
AN000919.006	NBS 987 200 ppb	0.710292	1.2E-05
AN000919.007	NBS 987 200 ppb	0.710300	7.8E-06
AN000919.007	NBS 987 200 ppb	0.710281	8.5E-06
AN000919.007	NBS 987 200 ppb	0.710300	7.8E-06
AN000919.014	NBS 987 200 ppb	0.710271	7.8E-06
AN000919.015	NBS 987 200 ppb	0.710273	7.8E-06
AN000919.025	NBS 987 200 ppb	0.710306	9.9E-06
AN000919.026	NBS 987 200 ppb	0.710289	9.9E-06
AN000919.027	NBS 987 200 ppb	0.710318	1.1E-05
AN000919.033	NBS 987 200 ppb	0.710279	9.2E-06
AN000919.033	NBS 987 200 ppb	0.710271	7.8E-06
AN000919.033	NBS 987 200 ppb	0.710313	9.2E-06
Average [c]	NBS 987 200 ppb	0.710290	1.6E-05 [d]

Analysis Number [a]	Standard [b]	$^{87}Sr/^{86}Sr$	Standard Deviation
AN000920.001	NBS 987 200 ppb	0.710322	1.1E-05
AN000920.002	NBS 987 200 ppb	0.710304	9.9E-06
AN000920.003	NBS 987 200 ppb	0.710286	9.2E-06
AN000920.004	NBS 987 200 ppb	0.710274	9.9E-06
AN000920.015	NBS 987 200 ppb	0.710295	9.2E-06
AN000920.015	NBS 987 200 ppb	0.710324	9.2E-06
AN000920.015	NBS 987 200 ppb	0.710278	9.2E-06
AN000920.021	NBS 987 200 ppb	0.710283	1.1E-05
AN000920.022	NBS 987 200 ppb	0.710266	9.9E-06
AN000920.027	NBS 987 200 ppb	0.710318	9.2E-06
AN000920.028	NBS 987 200 ppb	0.710269	9.2E-06
AN000920.037	NBS 987 200 ppb	0.710307	9.9E-06
AN000920.038	NBS 987 200 ppb	0.710272	9.2E-06
AN000920.038	NBS 987 200 ppb	0.710254	9.2E-06
AN000920.038	NBS 987 200 ppb	0.710279	9.2E-06
Average [c]	NBS 987 200 ppb	0.710289	2.1E-05 [d]
AN000921.001	NBS 987 200 ppb	0.710260	9.9E-06
AN000921.002	NBS 987 200 ppb	0.710262	9.9E-06
AN000921.002	NBS 987 200 ppb	0.710231	8.5E-06
AN000921.002	NBS 987 200 ppb	0.710229	8.5E-06
AN000921.008	NBS 987 200 ppb	0.710287	9.2E-06
AN000921.009	NBS 987 200 ppb	0.710254	9.2E-06
AN000921.023	NBS 987 200 ppb	0.710230	8.5E-06
AN000921.023	NBS 987 200 ppb	0.710235	9.2E-06
AN000921.032	NBS 987 200 ppb	0.710183	8.5E-06
AN000921.033	NBS 987 200 ppb	0.710273	9.2E-06
AN000921.034	NBS 987 200 ppb	0.710243	9.2E-06
AN000921.042	NBS 987 200 ppb	0.710273	9.9E-06
AN000921.042	NBS 987 200 ppb	0.710244	9.2E-06
AN000921.042	NBS 987 200 ppb	0.710295	1.1E-05
Average [c]	NBS 987 200 ppb	0.710250	2.8E-05 [d]
AN000921.019	NBS 987/984 200/42 ppb	0.710081	1.3E-05
AN000921.019	NBS 987/984 200/42 ppb	0.710073	1.3E-05
AN000921.020	NBS 987/984 200/42 ppb	0.710253	1.3E-05
AN000921.021	NBS 987/984 200/42 ppb	0.710201	1.2E-05
AN000921.022	NBS 987/984 200/42 ppb	0.710159	1.3E-05
Average [c]	NBS 987/984 200/42 ppb	0.710153	6.9E-05 [d]
AN000922.002	NBS 987 100 ppb	0.710377	1.6E-05
AN000922.003	NBS 987 100 ppb	0.710281	1.3E-05
AN000922.004	NBS 987 100 ppb	0.710265	1.1E-05
AN000922.005	NBS 987 100 ppb	0.710299	1.3E-05
AN000922.012	NBS 987 100 ppb	0.710298	1.6E-05
AN000922.013	NBS 987 100 ppb	0.710283	1.3E-05
AN000922.020	NBS 987 100 ppb	0.710273	1.6E-05
AN000922.021	NBS 987 100 ppb	0.710192	1.6E-05
AN000922.022	NBS 987 100 ppb	0.710236	1.6E-05
AN000922.026	NBS 987 100 ppb	0.710284	1.8E-05
AN000922.028	NBS 987 100 ppb	0.710230	1.6E-05
AN000922.036	NBS 987 100 ppb	0.710249	1.3E-05
AN000922.037	NBS 987 100 ppb	0.710299	1.4E-05
AN000922.046	NBS 987 100 ppb	0.710194	2.0E-05
AN000922.047	NBS 987 100 ppb	0.710209	1.4E-05

Analysis Number [a]	Standard [b]	$^{87}Sr/^{86}Sr$	Standard Deviation
Average [c]	NBS 987 100 ppb	0.710265	4.7E-05 [d]
AN000922.001	NBS 987 200 ppb	0.710285	9.2E-06
AN000922.001	NBS 987 200 ppb	0.710259	8.5E-06
Average [c]	NBS 987 200 ppb	0.710272	1.3E-05 [d]
AN000922.023	NBS 987/984 200/42 ppb	0.710150	1.3E-05
AN000922.024	NBS 987/984 200/42 ppb	0.710160	1.4E-05
AN000922.025	NBS 987/984 200/42 ppb	0.710149	1.3E-05
Average [c]	NBS 987/984 200/42 ppb	0.710153	4.7E-06 [d]
Total Average	NBS 987/984 200/42 ppb	0.710153	4.9E-05
Total Average	NBS 987 100 ppb	0.710260	2.8E-05
Total Average	NBS 987 200 ppb	0.710277	1.6E-05
Total Average	NBS 987 300 ppb	0.710314	5.5E-05

[a] The NIGL analysis number.
[b] NBS 987 is a strontium standard, NBS 987/984 is a combined strontium and rubidium standard, and their concentrations are given in ppb.
[c] The daily average for that standard. The NIGL value (for repeat analyses) of NBS 987 and NBS 987/984 is 0.71024.
[d] The daily standard deviation of the analyses.

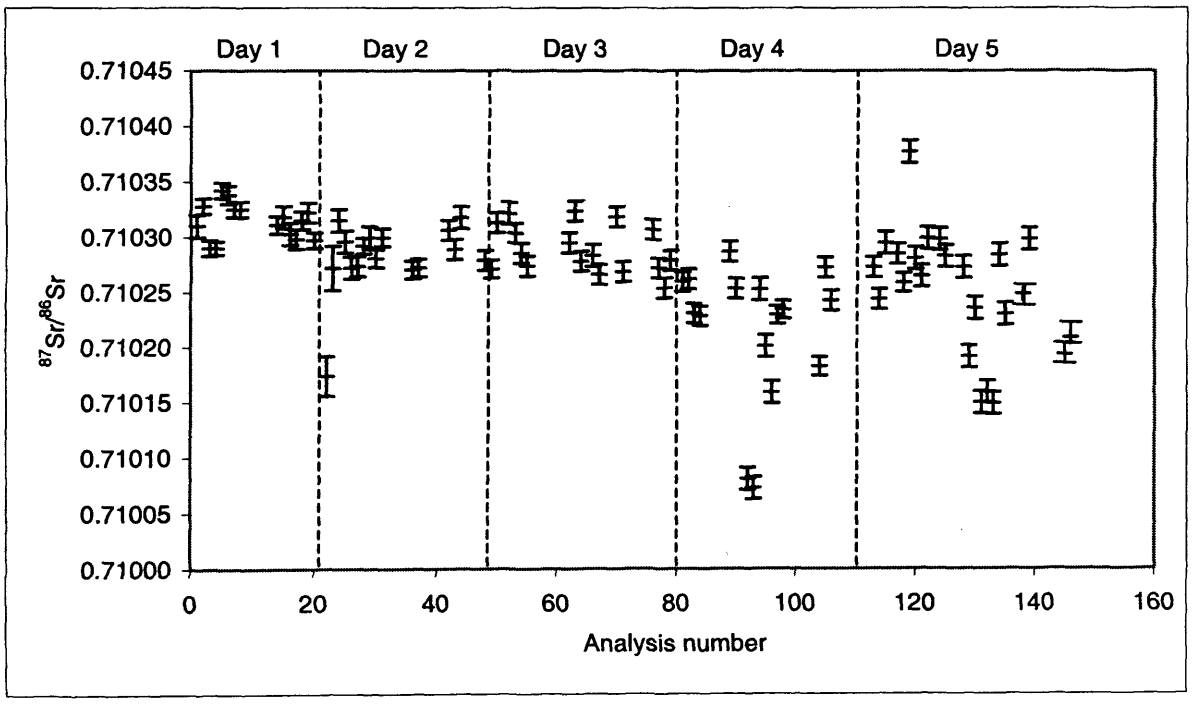

Figure A3.2 Standard data for the $^{87}Sr/^{86}Sr$ ratios of the NBS 987 and the NBS 987/984 standards, showing the daily variability in the standard measurements.

The accepted true $^{87}Sr/^{86}Sr$ ratios of the NBS 987 and the NBS 987/984 standards are 0.71024 (repeat NIGL laboratory results). Figure A3.2 shows the mass bias corrected values for the standards run over the five-day period of the experiment, daily and weekly averages for the standards are given in Table A3.3

Mass bias can be estimated by comparing the measured standard value with the true standard value, so any deviation from the true value is taken as a systematic error. Variations in the

measured standard values can be caused by the counting statistics (i.e. counts per second), which depend upon the acquisition time and ion fluxes. Counting statistics can be improved by the use of a more concentrated analyte, extending the time spent analysing each isotope and increasing the number of repetitive measurements (Monna *et al.*, 1998).

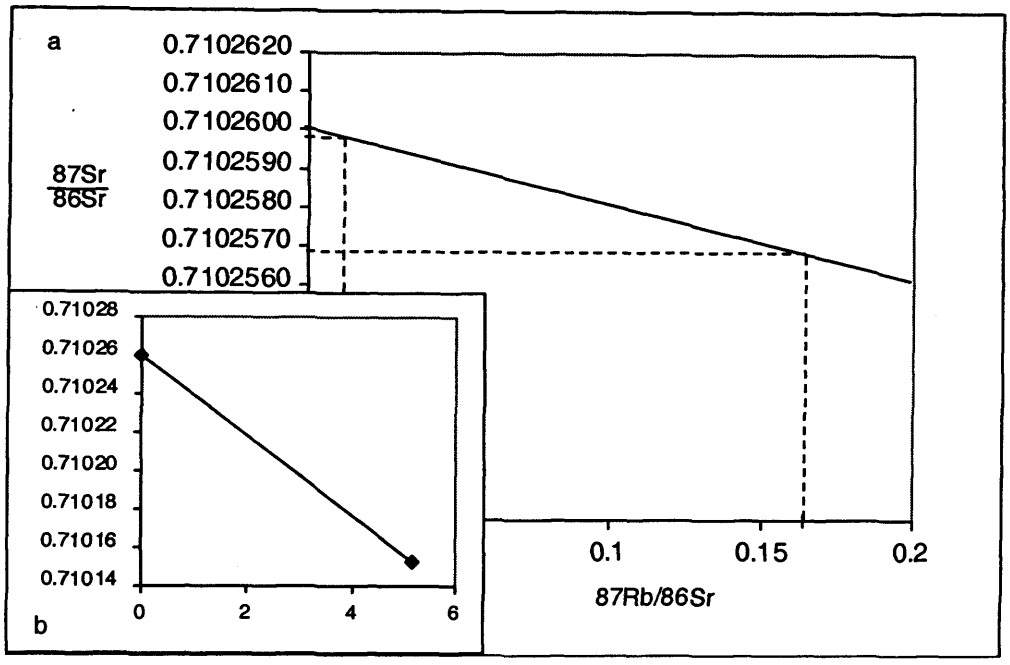

Figure A3.3 a) Expanded isochron diagram of the standard data presented in **b)**. The dashed lines represent the $^{87}Rb/^{86}Sr$ ratios of samples HT15 and HT23.

Figure A3.3 shows the amount of correction, which would be needed on the sample $^{87}Sr/^{86}Sr$ ratios to correct for the presence of ^{87}Rb in the solid. HT23 requires a very small correction of 2.5×10^{-7}, HT15 requires a larger correction of 3×10^{-6}. These corrections are smaller than the error on the analyses (see Tables A3.4 and A3.5).

Table A3.4 shows the $^{87}Sr/^{86}Sr$ ratios generated by LA-ICP-MS work on HT23 and HT15. A summary of this data is presented in Chapter 5, with graphs of selected grain traverses.

Table A3.4 $^{87}Sr/^{86}Sr$ ratios.

Grain	Analysis Number	Ablation Distance (cm)	Ablation Volume (mm^3)	Sr (volts)	Sr (ng)	83 Intensity	$^{85}Rb/^{86}Sr$*	$^{87}Sr/^{86}Sr$	Standard Deviation (1 SD)
23-1C	AN000920.020	-0.5	0.02	1.01	21	4E-5	0.00139	0.709410	3.9E-05
23-1A	AN000920.005	-0.2	0.06	1.05	62	6E-5	0.00077	0.709441	3.0E-05
23-1A	AN000920.007		0.06	0.77	62	4E-5	0.00081	0.709489	4.6E-05
23-1A	AN000920.008		0.11	1.04	100	6E-5	0.00045	0.709507	3.4E-05
23-1A	AN000920.009		0.05	0.98	52	4E-5	0.00083	0.709416	3.5E-05
23-1A	AN000920.010		0.05	0.99	52	4E-5	0.00074	0.709343	4.0E-05
23-1A	AN000920.013		0.05	0.97	52	4E-5	0.00052	0.709293	3.4E-05
Mean								0.709415	7.6E-05
Propagated Standard Error									3.6E-05
23-1B	AN000919.028	0.3	0.04	0.86	42	5E-5	0.00621	0.709439	1.1E-05
23-1B	AN000919.029		0.04	0.91	42	5E-5	0.00073	0.709447	6.4E-05

Grain	Analysis Number	Ablation Distance (cm)	Ablation Volume (mm^3)	Sr (volts)	Sr (ng)	83 Intensity	$^{85}Rb/^{86}Sr$*	$^{87}Sr/^{86}Sr$	Standard Deviation (1 SD)
23-1B	AN000919.032		0.01	0.96	10	6E-5	0.00041	0.709417	5.9E-05
Mean								0.709435	6.6E-05
Propagated Standard Error									5.1E-05
23-1F	AN000920.025	0.5	0.07	0.55	73	4E-5	0.00067	0.709271	4.3E-05
23-1F	AN000920.026		0.01	0.80	10	4E-5	0.00055	0.709314	5.2E-05
Mean								0.709293	2.2E-05
Propagated Standard Error									4.8E-05
23-1G	AN000920.032	1.1	0.08	0.92	83	7E-5	0.00030	0.708890	4.6E-05
23-1G	AN000920.033		0.08	0.95	83	5E-5	0.00042	0.709086	4.6E-05
Mean								0.708942	1.0E-04
Propagated Standard Error									4.8E-05
23-1I	AN000920.036	1.3	0.07	0.72	73	5E-5	0.00078	0.708796	6.1E-05
23-1H	AN000920.035	1.5	0.05	0.97	52	4E-5	0.00292	0.708486	5.8E-05
23-2C	AN000919.016	1.9	0.07	1.41	73	7E-5	0.00036	0.708444	4.2E-05
23-2C	AN000919.017		0.07	1.48	73	7E-5	0.00390	0.708496	3.9E-05
23-2C	AN000919.018		0.08	1.49	83	7E-5	0.03352	0.708525	4.1E-05
23-2C	AN000919.019		0.07	1.50	73	6E-5	0.00593	0.708414	4.0E-05
Mean								0.708470	4.3E-05
Propagated Standard Error									4.0E-05
23-2B	AN000919.008	2.8	0.06	1.14	62	6E-5	0.00225	0.708299	6.3E-05
23-2B	AN000919.010		0.06	1.26	62	8E-5	0.00114	0.708538	5.6E-05
23-2B	AN000919.011		0.04	1.28	42	8E-5	0.00268	0.708423	5.8E-05
23-2B	AN000919.012		0.06	1.31	62	9E-5	0.00711	0.708533	5.6E-05
Mean								0.708448	5.3E-05
Propagated Standard Error									5.8E-05
23-2A	AN000918.006	3.9	0.07	1.50	73	7E-5	0.02303	0.708356	3.5E-05
23-2A	AN000918.007		0.07	1.66	73	4E-5	0.01092	0.708356	3.0E-05
23-2A	AN000918.008		0.07	1.70	73	1E-4	0.00871	0.708478	3.0E-05
23-2A	AN000918.010		0.06	1.75	62	9E-5	0.00017	0.708457	2.6E-05
23-2A	AN000918.011		0.04	1.87	42	8E-5	0.00026	0.708409	2.7E-05
Mean								0.708411	5.0E-05
Propagated Standard Error									2.9E-05
15-1G	AN000921.003	-1.6	0.02	0.69	21	7E-5	0.55281	0.715265	5.0E-03
	AN000921.004		0.02	0.91	21	8E-5	0.33785	0.716569	2.0E-04
Mean								0.715781	6.5E-04
Propagated Standard Error									5.0E-03
15-1F	AN000921.006	-1.4	0.03	0.68	31	8E-5	0.0931	0.715436	1.2E-03
	AN000921.007		0.03	0.85	31	4E-5	0.0256	0.716555	1.2E-03
Mean								0.715995	5.5E-04
Propagated Standard Error									1.7E-03
15-1H	AN000921.018	-0.5	0.03	1.38	31	5E-5	0.00577	0.716118	4.4E-05

Grain	Analysis Number	Ablation Distance (cm)	Ablation Volume (mm^3)	Sr (volts)	Sr (ng)	83 Intensity	$^{85}Rb/^{86}Sr$*	$^{87}Sr/^{86}Sr$	Standard Deviation (1 SD)
15-1I	AN000921.024	0.0	0.03	1.20	31	7E-5	0.04571	0.716089	4.3E-05
15-1I	AN000921.026		0.07	1.29	73	6E-5	0.01514	0.716231	3.9E-05
Mean								0.716160	7.1E-05
Propagated Standard Error									4.1E-05
15-1C	AN000921.028	1.0	0.05	0.69	52	7E-5	0.01981	0.715942	6.1E-05
15-1B	AN000921.031	1.5	0.04	0.99	42	4E-5	0.02525	0.715875	3.9E-05
15-2A	AN000921.035	2.1	0.07	1.05	73	9E-5	0.02310	0.715771	5.1E-05
15-2A	AN000921.037		0.04	1.35	42	6E-5	0.01803	0.715530	4.2E-05
Mean								0.715650	1.2E-04
Propagated Standard Error									4.7E-05
15-2B	AN000921.038	2.6	0.04	0.99	42	6E-5	0.00306	0.715254	4.4E-05
15-2C	AN000921.039	3.2	0.04	1.04	42	4E-5	0.00233	0.715104	4.1E-05
15-2D	AN000921.040	3.6	0.04	1.08	42	5E-5	0.00191	0.715100	3.4E-05
15-2F	AN000921.041	4.6	0.04	1.04	42	6E-5	0.00259	0.714879	3.6E-05
15-2G	AN000922.011	5.1	0.05	1.12	52	8E-5	0.00699	0.714965	3.4E-05
15-2H	AN000922.014	5.4	0.08	1.16	83	6E-5	0.00072	0.714990	3.4E-05
15-2H	AN000922.015		0.08	1.19	83	8E-5	0.00235	0.714888	3.9E-05
Mean								0.714939	5.1E-05
Propagated Standard Error									3.7E-05
15-3A	AN000922.045	5.8	0.04	0.83	42	5E-5	0.00358	0.714753	7.1E-05
15-3B	AN000922.044	6.0	0.04	0.70	42	4E-5	0.00526	0.714705	6.6E-05
15-3D	AN000922.039	7.0	0.06	0.97	62	4E-5	0.00688	0.714659	5.4E-05
15-3D	AN000922.042		0.06	1.02	62	4E-5	0.00399	0.714750	5.5E-05
15-3D	AN000922.043		0.04	0.85	42	5E-5	0.00902	0.714680	6.4E-05
Mean								0.714696	3.9E-05
Propagated Standard Error									5.8E-05
15-3G	AN000922.033	8.2	0.04	1.09	42	5E-5	0.00259	0.714634	3.9E-05
15-3H	AN000922.030	8.9	0.06	1.03	62	6E-5	0.00428	0.714634	4.6E-05

*$^{85}Rb/^{86}Sr$ values for micas are around 10.48 (AN000922.016) and values for the NBS standards are ~0.002 for NBS 987 and ~1.8 for the NBS 987/984 mixed standard.

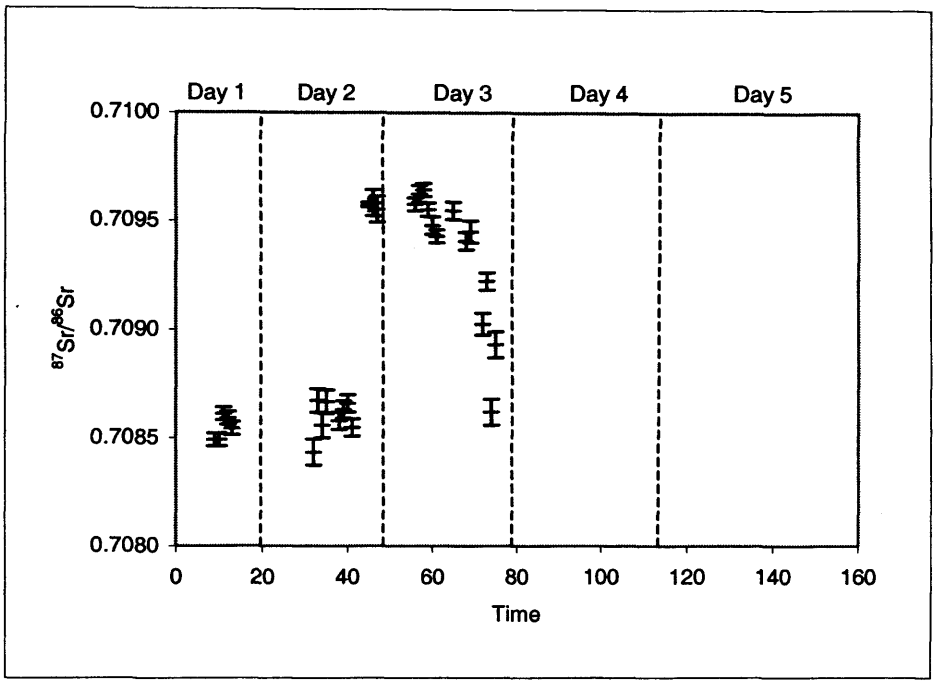

Figure A3.4 $^{87}Sr/^{86}Sr$ data for HT23, plotted against the relative time the analysis was measured.

The variable results shown on Figure A3.4 (Day 3) are genuine variations due to taking analyses from different parts of the sample.

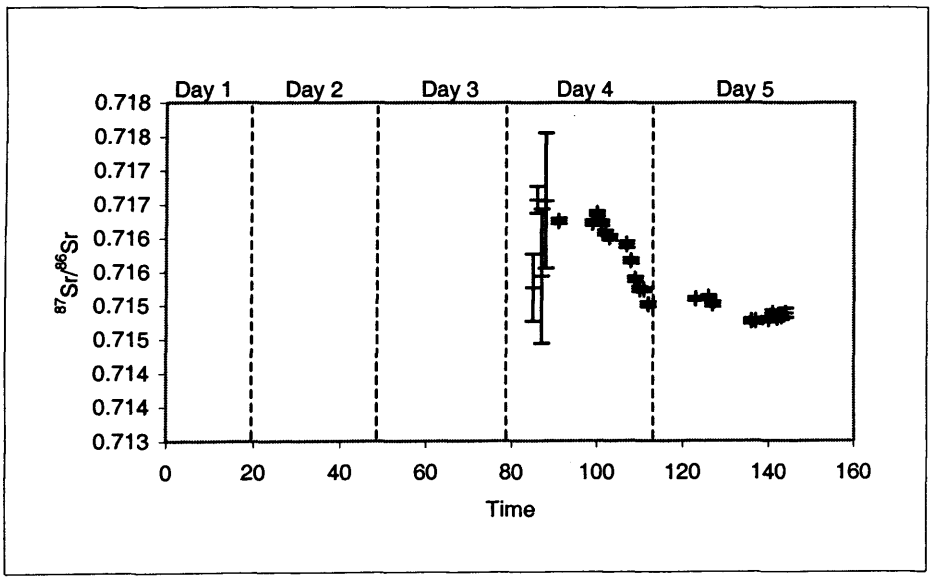

Figure A3.5 $^{87}Sr/^{86}Sr$ data for HT15, plotted against the relative time the analysis was measured.

Figure A3.5 shows large variations in analysed $^{87}Sr/^{86}Sr$, with large error bars (on Day 4) and there is a corresponding dip in the standard values (Figure A3.2), suggesting some sort of contamination at the start of Day 4, associated with sample exchange. After this initial variability, the standard values recover to previous levels.

Appendix 4

Electron and Ion Microprobe Data

A4.1 The Electron Microprobe

A4.1.1 *The Instrument*

Electron microprobe analyses were carried out at the Department of Geology, University of Leicester on a JEOL 8600 S automated instrument. Electron microprobe analysis is a technique capable of producing chemical analyses of microvolumes at the surface of polished solid samples using a fine beam of electrons to bombard the surface of the sample. The electron 'probe' generates X-rays whose wavelengths (or energies) are characteristic of the elements present in the sample. The intensities of the X-rays are a measure of the proportions of the elements present and the analysis may be quantified by reference to the X-ray intensities obtained from standard materials. Since the electron beam may be focussed to a diameter of less than 1 micron and penetrates the surface to a depth of only a few microns, analysis of very small sample volumes may be possible in suitable circumstances.

The electron microprobe in the Department of Geology is a JEOL 8600 S automated instrument. The wavelength-dispersive system comprises three crystal spectrometers, which allow the quantitative analysis of elements from atomic mass F upwards in the Periodic Table.

A4.1.2 *Accuracy and sensitivity*

X-ray intensities are measured by counting photons and the precision obtained is limited by statistical error. For major elements, errors of better than ± 1% are obtainable, however this depends upon other factors, such as uncertainties in the compositions of the standards and errors in the various corrections, which are applied to the raw data. As well as producing a characteristic X-ray pattern for each element, there is a continuous X-ray spectrum, which limits the detection of smaller peaks, owing to the presence of background counts. Detection limits are typically 100 pmm, but using longer counting times can reduce these.

A4.1.3 *Sample Preparation*

Electron microprobes only sample the near surface of the sample therefore samples need to be well polished so that surface irregularity does not affect the results. To achieve the best possible quantitative data the specimens must be polished to a 0.25 μm diamond finish. The specimens are prepared as polished thin sections or as polished blocks and mounted using Araldite or a similar vacuum compatible epoxy resin. The samples must be coated with a conducting surface; a 20 nm carbon coating is most commonly used, which has a minimal effect on X-ray intensities due to its low atomic number and (unlike gold) it does not add extra peaks to the X-ray spectrum. The

specimen holder is designed to accommodate 3 polished thin sections 48 - 50 mm in length and 28 mm in width.

Table A4.1 Electron microprobe conditions.

	Calcite	K-feldspar	Muscovite	Phlogopite
Accelerating voltage (kV)	15	15	15	15
Current (nA)	3	3	3	3
Beam diameter (μm)	15	10	10	10

A4.2 Electron Microprobe Data

Further electron microprobe data can be found on the CD appended to this thesis.

A4.2.1 *Calcite and Dolomite*

The average compositions of calcite and dolomite grains are presented in Table A4.2. The average calcite-dolomite solvus equilibration temperatures are also presented (after Annovitz & Essene, 1987). All the temperatures calculated are within the temperature range 320-450 °C, indicating that Ca and Mg have re-equilibrated between calcite and dolomite during cooling from the peak temperature. To achieve equilibration temperatures closer to the peak temperature, of approximately 600 °C (which would imply no down temperature chemical exchange), calcite Mg contents would have to approach 7 mol% $MgCO_3$. Dolomite compositions indicate equilibration with calcite at 350-450 °C (falling on the steep limb of the calcite-dolomite solvus, after Annovitz & Essene, 1987), which is consistent with the calcite data. Mg and Fe compositions are consistent within the same sample, indicating equilibration on at least the scale of a thin-section (~ 4 cm).

Table A4.2 Average compositions of carbonates, analysed by electron microprobe.

Sample	HT4		HT4		HT10		HT11		HT15	
Location	Dalpe		Dalpe		Verzasca		Narèt		Narèt	
	Dol		Cc		Cc		Cc		Cc	
n	14		11		35		12		50	
	Mean	SD	Mean	SD	Mean	SD	Mean	SD	Mean	SD
CaO	31.01	0.30	54.73	0.23	56.19	0.35	55.48	1.18	56.53	0.75
MgO	20.66	0.44	1.67	0.21	0.41	0.03	0.31	0.07	1.14	0.03
FeO	0.10	0.02	0.20	0.02	0.36	0.05	0.20	0.05	0.38	0.05
MnO	0.05	0.02	0.05	0.02	0.14	0.01	0.05	0.01	0.12	0.03
SrO	0.04	0.02	0.04	0.02	0.04	0.01	0.09	0.01	0.04	0.01
BaO	0.07	0.07	0.12	0.07	0.07	0.07	0.06	0.07	0.08	0.07
CO_2	48.07	0.73	43.16	0.20	42.77	0.35	43.79	1.12	41.69	0.83
Total	100.00	0.01	100.00	0.00	100.00	0.01	100.00	0.00	100.00	0.00
Fe	495	82	968	117	1740	243	968	249	1838	251
Mn	235	72	265	99	674	62	275	28	590	188
Sr	221	113	270	150	258	78	534	69	237	71
Ba	469	491	873	511	525	538	418	494	617	546
%$CaCO_3$	63.7	0. 4	96.9	0.4	98.6	0.7	98.9	0.8	97.5	0.8
%$MgCO_3$	35.8	0.4	2.5	0.3	0.1	0.1	0.4	0.1	1.6	0.1
%$FeCO_3$	0.1	0.1	0.1	0.1	0.1	0.0	0.1	0.1	0.1	0.1
T (°C)			399						322	

Continued...

Sample	HT16		HT17		HT21		HT23		HT26	
Location	Narèt		Narèt		Bianco		Someo		Crevola	
	Cc		Cc		Dol		Cc		Dol	
n	31		38		18		28		20	
	Mean	SD	Mean	SD	Mean	SD	Mean	SD	Mean	SD
CaO	54.25	0.52	56.23	1.74	31.59	0.35	52.68	0.42	31.23	0.19
MgO	1.11	0.12	1.86	1.18	20.99	0.23	2.16	0.12	21.08	0.15
FeO	0.27	0.01	0.30	0.09	0.18	0.02	0.43	0.02	0.55	0.05
MnO	0.02	0.01	0.07	0.00	0.18	0.01	0.04	0.01	0.02	0.01
SrO	0.02	0.01	0.02	0.00	0.01	0.00	0.04	0.01	0.01	0.01
BaO	0.07	0.07	0.06	0.06	0.09	0.07	0.07	0.07	0.06	0.07
CO_2	44.24	0.61	41.45	0.63	46.93	0.53	44.55	0.36	47.01	0.17
Total	100.00	0.00	100.00	0.00	100.00	0.01	100.00	0.01	100.00	0.01
Fe	1305	92	1487	443	870	116	2108	141	2685	261
Mn	105	66	341	25	905	84	202	52	110	43
Sr	155	100	119	50	73	58	281	73	95	81
Ba	548	503	423	440	665	528	509	516	477	513
%$CaCO_3$	97.7	0.7	96.7	0.6	63.6	0.5	95.9	0.6	63.1	0.4
%$MgCO_3$	1.7	0.1	2.7	0.3	35.7	0.3	3.3	0.1	35.9	0.3
%$FeCO_3$	0.3	0.1	0.4	0.1	0.1	0.1	0.5	0.1	0.8	0.1
T (°C)	322		416				456			

Continued...

Sample	HT28		HT29		HT30		HT32		HT34	
Location	Crevola		Rozzaro		Rozzaro		Kaserne		Crevola	
	Dol		Cc		Cc		Cc		Dol	
n	21		8		10		6		8	
	Mean	SD	Mean	SD	Mean	SD	Mean	SD	Mean	SD
CaO	31.39	0.22	54.03	0.17	54.23	0.70	53.80	0.55	30.25	0.36
MgO	21.27	0.10	2.21	0.24	1.89	0.28	1.03	0.05	20.80	0.12
FeO	0.11	0.01	0.22	0.02	0.17	0.08	0.56	0.04	0.56	0.02
MnO	0.01	0.01	0.03	0.01	0.07	0.01	0.19	0.01	0.11	0.02
SrO	0.01	0.00	0.04	0.01	0.05	0.02	0.04	0.01	0.02	0.01
BaO	0.08	0.07	0.10	0.06	0.09	0.08	0.15	0.06	0.10	0.07
CO_2	47.11	0.29	43.35	0.15	43.47	0.66	44.21	0.61	48.13	0.31
Total	100.00	0.01	100.00	0.01	99.99	0.01	100.00	0.01	100.00	0.01
Fe	532	53	1079	108	834	430	2742	232	2724	141
Mn	61	50	155	46	354	75	935	82	538	101
Sr	65	31	260	51	344	150	244	113	171	63
Ba	563	527	739	467	647	559	1044	434	713	498
$\%CaCO_3$	63.3	0.5	96.1	0.4	96.6	0.6	97.2	0.8	62.5	0.6
$\%MgCO_3$	36.2	0.2	3.3	0.4	2.8	0.2	1.6	0.1	36.7	0.2
$\%FeCO_3$	0.2	0.1	0.3	0.1	0.2	0.1	0.6	0.1	0.8	0.1
T (°C)			452		423		316			

Any chemical re-equilibration between calcite and dolomite during cooling is limited by the rate of Ca-Mg interdiffusion. The calcites contain very little Mg (~1 wt%) and the Ca-Mg interdiffusion coefficient will approximate to the Mg tracer diffusion coefficient.

Using the Dodson (1973) closure temperature formulation and tracer diffusion coefficients for Ca-Mg and Ca-Sr, the closure temperatures for chemical exchange can be determined (Table 6.2).

Table A4.3 Closure temperatures for the calcite Ca-Mg and Ca-Sr systems.

	Ca-Mg	Ca-Sr
Author	Fisler & Cygan, 1999	Cherniak, 1997
$\delta T/\delta t$ (°C/Ma)	32	32
Do (m^2s^{-1})	5.49×10^{-4}	2.10×10^{-9}
0.5 mm[a]	512	435
1 mm[a]	537	478

[a] Grain radius

The closure temperatures quoted in Table A4.3 are high when compared with those calculated from the electron microprobe data. Lower modelled closure temperatures can be achieved by either a faster diffusion coefficient or a slower cooling rate.

A faster diffusion coefficient can be determined using the analytical uncertainty given by the authors. For Mg tracer diffusion, Fisler & Cygan (1999) give an analytical uncertainty of a factor of 2.5: a diffusion coefficient 2.5 times faster than that in Table A4.3, produces lower closure temperatures of 497 °C for Ca-Mg and 416 °C for Ca-Sr for a 0.5 mm diameter grain. An increased rate of diffusion is consistent with the Sr isotope exchange model described in Section 5.5.7. To

reduce these closure temperatures further, a slower cooling rate is required. A closure temperature of ~450 °C can be achieved with a faster diffusion rate and a cooling rate of 2 °C/Ma; however, this cooling rate seems unreasonably low. Cherniak (1997) gives an error of ± 3.7 % for Sr diffusion, which does not appreciably change the diffusion parameter.

A4.2.2 *Calcite electron Microprobe Traverse Data*

Table A4.4 Calcite electron microprobe traverse data.

Sample	Distance (microns)	CaO	MgO	FeO	MnO	SrO	BaO	CO2	Total	O	Ca	Mg	Fe2	Mn	Sr	Ba	C	Total	Mg	Fe	Mn	Sr	Ba
HT11	0	55.7	0.4	0.3	0.1	0.1	0.0	43.4	100.0	3.00	1.00	0.01	0.00	0.00	0.00	0.00	0.99	2.01	2533	2332	446	846	179
HT11	30	56.1	0.4	0.3	0.1	0.1	0.2	42.8	100.0	3.00	1.01	0.01	0.00	0.00	0.00	0.00	0.99	2.02	2533	2410	446	1015	1612
HT11	50	57.9	0.4	0.3	0.1	0.1	0.0	41.2	100.0	3.00	1.06	0.01	0.00	0.00	0.00	0.00	0.96	2.04	2593	2254	446	846	179
HT11	74	57.0	0.3	0.2	0.1	0.1	0.2	42.1	100.0	3.00	1.04	0.01	0.00	0.00	0.00	0.00	0.98	2.03	1869	1866	520	1015	1612
HT11	126	55.9	0.4	0.2	0.1	0.1	0.0	43.3	100.0	3.00	1.01	0.01	0.00	0.00	0.00	0.00	0.99	2.01	2171	1866	520	846	358
HT11	156	57.6	0.1	0.5	0.0	0.1	0.0	41.7	100.0	3.00	1.05	0.00	0.01	0.00	0.00	0.00	0.97	2.03	482	3809	297	761	90
HT11	175	58.4	0.1	0.1	0.0	0.1	0.2	41.1	100.0	3.00	1.07	0.00	0.00	0.00	0.00	0.00	0.96	2.04	603	466	297	930	1612
HT11	203	57.8	0.1	0.1	0.0	0.1	0.1	41.8	100.0	3.00	1.05	0.00	0.00	0.00	0.00	0.00	0.97	2.03	784	777	223	761	627
HT11	232	57.2	0.3	0.2	0.1	0.1	0.2	42.0	100.0	3.00	1.04	0.01	0.00	0.00	0.00	0.00	0.97	2.03	1930	1399	446	592	1612
HT11	262	54.8	0.3	0.2	0.1	0.1	0.0	44.4	100.0	3.00	0.97	0.01	0.00	0.00	0.00	0.00	1.01	1.99	1930	1632	594	930	358
HT11	296	56.0	0.4	0.3	0.1	0.1	0.0	43.1	100.0	3.00	1.01	0.01	0.00	0.00	0.00	0.00	0.99	2.01	2412	2332	446	930	179
HT11	330	57.1	0.5	0.3	0.1	0.1	0.0	41.9	100.0	3.00	1.04	0.01	0.00	0.00	0.00	0.00	0.97	2.03	2774	2410	372	846	269
HT11	354	57.2	0.5	0.4	0.1	0.1	0.2	41.7	100.0	3.00	1.04	0.01	0.01	0.00	0.00	0.00	0.97	2.03	2895	2721	372	1015	1612
HT11	398	56.3	0.5	0.3	0.1	0.1	0.2	42.5	100.0	3.00	1.02	0.01	0.01	0.00	0.00	0.00	0.98	2.02	3015	2565	520	930	1612
HT11	433	55.5	0.5	0.3	0.1	0.1	0.0	43.5	100.0	3.00	0.99	0.01	0.01	0.00	0.00	0.00	0.99	2.01	2895	2643	446	930	90
HT11	461	57.5	0.5	0.4	0.1	0.1	0.0	41.4	100.0	3.00	1.05	0.01	0.01	0.00	0.00	0.00	0.96	2.04	3196	2876	372	1015	358
HT11	489	56.5	0.5	0.4	0.1	0.1	0.0	42.4	100.0	3.00	1.02	0.01	0.01	0.00	0.00	0.00	0.98	2.02	3136	3032	520	1015	358
HT11	519	57.3	0.5	0.4	0.1	0.1	0.2	41.4	100.0	3.00	1.05	0.01	0.01	0.00	0.00	0.00	0.97	2.04	3015	3109	594	1015	1612
Average		56.5	0.5	0.3	0.1	0.1	0.1	42.5	100.0		1.02	0.01	0.00	0.00	0.00	0.00	0.98	2.02	2807	2591	471	958	717
SD		0.9	0.1	0.1	0.0	0.0	0.1	1.0	0.0		0.02	0.00	0.00	0.00	0.00	0.00	0.01	0.01	378	419	86	56	639
%		1.5	13.5	16.2	18.2	5.9	89.2	2.3	0.0		2.42	13.74	19.18	0.00	0.00	141	1.37	0.67	13	16	18	6	89
HT11	0	55.9	0.4	0.3	0.1	0.1	0.2	43.0	100.0	3.00	1.01	0.01	0.00	0.00	0.00	0.00	0.99	2.01	2472	2332	520	761	1523
HT11	29	56.1	0.4	0.3	0.1	0.1	0.0	42.9	100.0	3.00	1.01	0.01	0.01	0.00	0.00	0.00	0.99	2.02	2593	2487	446	761	269
HT11	48	56.2	0.4	0.3	0.1	0.1	0.0	43.0	100.0	3.00	1.01	0.01	0.00	0.00	0.00	0.00	0.99	2.01	2231	1943	372	761	358
HT11	75	55.1	0.3	0.2	0.0	0.1	0.1	44.3	100.0	3.00	0.98	0.01	0.00	0.00	0.00	0.00	1.00	2.00	1568	1710	297	676	448
HT11	103	57.3	0.3	0.2	0.1	0.1	0.1	42.1	100.0	3.00	1.04	0.01	0.00	0.00	0.00	0.00	0.97	2.03	1749	1321	446	592	448
HT11	123	56.3	0.1	0.0	0.1	0.1	0.0	43.5	100.0	3.00	1.01	0.00	0.00	0.00	0.00	0.00	0.99	2.01	543	311	520	507	269
HT11	144	54.9	0.4	0.3	0.1	0.1	0.0	44.2	100.0	3.00	0.98	0.01	0.00	0.00	0.00	0.00	1.00	2.00	2653	2176	520	761	179
HT11	166	55.8	0.4	0.3	0.1	0.1	0.2	43.1	100.0	3.00	1.00	0.01	0.00	0.00	0.00	0.00	0.99	2.01	2653	2254	446	930	1523
HT11	186	52.2	0.4	0.3	0.1	0.1	0.0	47.0	100.0	3.00	0.91	0.01	0.00	0.00	0.00	0.00	1.04	1.96	2352	2176	372	846	90
HT11	213	56.9	0.3	0.2	0.1	0.1	0.2	42.3	100.0	3.00	1.03	0.01	0.00	0.00	0.00	0.00	0.98	2.02	1990	1788	446	846	1523
HT11	232	54.8	0.3	0.2	0.1	0.1	0.0	44.5	100.0	3.00	0.97	0.01	0.00	0.00	0.00	0.00	1.01	1.99	2050	1866	594	676	90
Average		55.1	0.3	0.2	0.1	0.1	0.1	44.1	100.0		0.98	0.01	0.00	0.00	0.00	0.00	1.00	2.00	2040	1762	483	761	612
SD		1.5	0.1	0.1	0.0	0.0	0.1	1.5	0.0		0.04	0.00	0.00	0.00	0.00	0.00	0.02	0.02	718	671	71	138	647
%		2.7	35.2	38.1	14.7	18.1	105.7	3.3	0.0		4.01	37.02	33.70	0.00	0.00	141.42	1.94	0.96	35	38	15	18	106

Sample	Distance (microns)	CaO	MgO	FeO	MnO	SrO	BaO	CO2	Total	O	Ca	Mg	Fe2	Mn	Sr	Ba	C	Total	Mg	Fe	Mn	Sr	Ba
HT17	0	56.2	1.6	0.3	0.1	0.0	0.0	41.8	100.0	3.00	1.02	0.04	0.00	0.00	0.00	0.00	0.97	2.03	9829	1943	446	85	90
HT17	23	55.3	1.7	0.3	0.1	0.0	0.0	42.7	100.0	3.00	0.99	0.04	0.00	0.00	0.00	0.00	0.98	2.02	10252	2099	372	85	90
HT17	47	55.6	1.8	0.3	0.1	0.0	0.2	42.1	100.0	3.00	1.01	0.05	0.00	0.00	0.00	0.00	0.97	2.03	10674	2099	372	85	1612
HT17	69	55.0	1.8	0.3	0.1	0.0	0.0	42.9	100.0	3.00	0.99	0.04	0.00	0.00	0.00	0.00	0.98	2.02	10734	2176	594	169	90
HT17	98	55.3	1.7	0.3	0.1	0.0	0.0	42.6	100.0	3.00	1.00	0.04	0.00	0.00	0.00	0.00	0.98	2.02	10071	2099	594	254	179
HT17	125	55.3	1.6	0.3	0.1	0.0	0.0	42.8	100.0	3.00	1.00	0.04	0.00	0.00	0.00	0.00	0.98	2.02	9528	1943	520	169	90
HT17	152	55.7	1.5	0.3	0.1	0.0	0.0	42.5	100.0	3.00	1.01	0.04	0.00	0.00	0.00	0.00	0.98	2.02	9166	2099	520	0	0
HT17	175	55.5	1.4	0.3	0.1	0.0	0.0	42.7	100.0	3.00	1.00	0.04	0.00	0.00	0.00	0.00	0.98	2.02	8503	1943	520	169	90
HT17	199	56.0	1.4	0.3	0.1	0.0	0.0	42.3	100.0	3.00	1.01	0.04	0.00	0.00	0.00	0.00	0.97	2.03	8563	1943	594	85	179
HT17	215	55.7	1.4	0.2	0.1	0.0	0.0	42.5	100.0	3.00	1.01	0.04	0.00	0.00	0.00	0.00	0.98	2.02	8563	1866	446	85	90
HT17	226	55.7	1.4	0.2	0.1	0.0	0.2	42.5	100.0	3.00	1.01	0.04	0.00	0.00	0.00	0.00	0.98	2.02	8382	1866	446	85	1612
Mean		55.7	1.5	0.3	0.1	0.0	0.0	42.5	100.0	3.0	1.0	0.0	0.0	0.0	0.0	0.0	1.0	2.0	8784.2	1943.3	507.7	98.7	343.3
Std dev		0.2	0.1	0.0	0.0	0.0	0.1	0.2	0.0	0.0	0.0	0.0	0.0	0.0	0.0	0.0	0.0	0.0	415.9	77.7	51.1	58.1	569.8
%		0.4	4.7	4.0	10.1	58.9	166.0	0.4	0.0	0.00	0.52	4.90	12.86	0.00	0.00	223.61	0.22	0.11	5	4	10	59	166
HT11	0	55.9	0.4	0.3	0.1	0.1	0.2	43.0	100.0	3.00	1.01	0.01	0.00	0.00	0.00	0.00	0.99	2.01	2472	2332	520	761	1523
HT11	29	56.1	0.4	0.3	0.1	0.1	0.0	42.9	100.0	3.00	1.01	0.01	0.01	0.00	0.00	0.00	0.99	2.02	2593	2487	446	761	269
HT11	48	56.2	0.4	0.3	0.1	0.1	0.0	43.0	100.0	3.00	1.01	0.01	0.00	0.00	0.00	0.00	0.99	2.01	2231	1943	372	761	358
HT11	75	55.1	0.3	0.2	0.0	0.1	0.1	44.3	100.0	3.00	0.98	0.01	0.00	0.00	0.00	0.00	1.00	2.00	1568	1710	297	676	448
HT11	103	57.3	0.3	0.2	0.1	0.1	0.1	42.1	100.0	3.00	1.04	0.01	0.00	0.00	0.00	0.00	0.97	2.03	1749	1321	446	592	448
HT11	123	56.3	0.1	0.0	0.1	0.1	0.0	43.5	100.0	3.00	1.01	0.00	0.00	0.00	0.00	0.00	0.99	2.01	543	311	520	507	269
HT11	144	54.9	0.4	0.3	0.1	0.1	0.0	44.2	100.0	3.00	0.98	0.01	0.00	0.00	0.00	0.00	1.00	2.00	2653	2176	520	761	179
HT11	166	55.8	0.4	0.3	0.1	0.1	0.2	43.1	100.0	3.00	1.00	0.01	0.00	0.00	0.00	0.00	0.99	2.01	2653	2254	446	930	1523
HT11	186	52.2	0.4	0.3	0.1	0.1	0.0	47.0	100.0	3.00	0.91	0.01	0.00	0.00	0.00	0.00	1.04	1.96	2352	2176	372	846	90
HT11	213	56.9	0.3	0.2	0.1	0.1	0.2	42.3	100.0	3.00	1.03	0.01	0.00	0.00	0.00	0.00	0.98	2.02	1990	1788	446	846	1523
HT11	232	54.8	0.3	0.2	0.1	0.1	0.0	44.5	100.0	3.00	0.97	0.01	0.00	0.00	0.00	0.00	1.01	1.99	2050	1866	594	676	90
Average		55.1	0.3	0.2	0.1	0.1	0.1	44.1	100.0		0.98	0.01	0.00	0.00	0.00	0.00	1.00	2.00	2040	1762	483	761	612
SD		1.5	0.1	0.1	0.0	0.0	0.1	1.5	0.0		0.04	0.00	0.00	0.00	0.00	0.00	0.02	0.02	718	671	71	138	647
%		2.7	35.2	38.1	14.7	18.1	105.7	3.3	0.0		4.01	37.02	33.70	0.00	0.00	141.42	1.94	0.96	35	38	15	18	106
HT10	0	56.3	0.4	0.4	0.1	0.1	0.0	42.7	100.0	3.00	1.02	0.01	0.01	0.00	0.00	0.00	0.98	2.02	2653	3109	892	423	269
HT10	36	56.4	0.4	0.4	0.1	0.0	0.2	42.4	100.0	3.00	1.02	0.01	0.01	0.00	0.00	0.00	0.98	2.02	2593	2954	1040	338	1612
HT10	69	56.3	0.4	0.4	0.1	0.0	0.0	42.7	100.0	3.00	1.02	0.01	0.01	0.00	0.00	0.00	0.98	2.02	2653	3109	1040	338	179
HT10	98	56.4	0.4	0.4	0.2	0.1	0.0	42.5	100.0	3.00	1.02	0.01	0.01	0.00	0.00	0.00	0.98	2.02	2653	3187	1189	507	90
HT10	132	56.1	0.4	0.4	0.2	0.1	0.0	42.8	100.0	3.00	1.01	0.01	0.01	0.00	0.00	0.00	0.98	2.02	2593	3187	1115	423	358
HT10	161	56.0	0.4	0.4	0.1	0.0	0.2	42.9	100.0	3.00	1.01	0.01	0.01	0.00	0.00	0.00	0.99	2.01	2593	2876	966	169	1612

Sample	Distance (microns)	CaO	MgO	FeO	MnO	SrO	BaO	CO2	Total	O	Ca	Mg	Fe2	Mn	Sr	Ba	C	Total	Mg	Fe	Mn	Sr	Ba
HT10	202	56.7	0.4	0.3	0.1	0.1	0.2	42.2	100.0	3.00	1.03	0.01	0.00	0.00	0.00	0.00	0.98	2.02	2352	2410	1040	423	1612
HT10	238	55.8	0.4	0.3	0.2	0.1	0.2	43.1	100.0	3.00	1.00	0.01	0.01	0.00	0.00	0.00	0.99	2.01	2412	2643	1189	423	1612
HT10	276	56.0	0.4	0.4	0.2	0.0	0.0	43.0	100.0	3.00	1.01	0.01	0.01	0.00	0.00	0.00	0.99	2.01	2653	2954	1115	338	179
HT10	309	55.7	0.4	0.4	0.1	0.1	0.2	43.2	100.0	3.00	1.00	0.01	0.01	0.00	0.00	0.00	0.99	2.01	2412	3032	892	507	1612
HT10	358	55.5	0.4	0.4	0.2	0.0	0.0	43.5	100.0	3.00	1.00	0.01	0.01	0.00	0.00	0.00	0.99	2.01	2593	3032	1115	254	269
HT10	390	57.1	0.4	0.4	0.1	0.1	0.0	41.9	100.0	3.00	1.04	0.01	0.01	0.00	0.00	0.00	0.97	2.03	2653	3109	966	507	90
HT10	406	55.9	0.4	0.4	0.1	0.1	0.0	43.1	100.0	3.00	1.01	0.01	0.01	0.00	0.00	0.00	0.99	2.01	2533	2798	1040	423	0
HT10	441	56.1	0.4	0.4	0.1	0.0	0.0	42.9	100.0	3.00	1.01	0.01	0.01	0.00	0.00	0.00	0.99	2.02	2593	3265	1040	254	179
HT10	477	56.0	0.4	0.4	0.1	0.1	0.2	42.8	100.0	3.00	1.01	0.01	0.01	0.00	0.00	0.00	0.99	2.02	2653	2876	966	592	1612
HT10	527	56.4	0.4	0.4	0.1	0.0	0.2	42.4	100.0	3.00	1.02	0.01	0.01	0.00	0.00	0.00	0.98	2.02	2593	2876	966	338	1612
HT10	567	56.3	0.4	0.3	0.2	0.0	0.0	42.8	100.0	3.00	1.02	0.01	0.00	0.00	0.00	0.00	0.98	2.02	2412	2410	1263	338	358
HT10	610	56.2	0.4	0.3	0.1	0.0	0.0	43.0	100.0	3.00	1.01	0.01	0.00	0.00	0.00	0.00	0.99	2.01	2352	2487	966	254	90
HT10	649	56.3	0.4	0.3	0.1	0.0	0.0	42.9	100.0	3.00	1.02	0.01	0.00	0.00	0.00	0.00	0.99	2.02	2111	2099	1040	169	0
HT10	721	56.4	0.3	0.2	0.2	0.0	0.0	42.9	100.0	3.00	1.02	0.01	0.00	0.00	0.00	0.00	0.99	2.01	1749	1710	1115	338	179
Mean	515	56.2	0.4	0.3	0.1	0.0	0.0	42.8	100.0		1.01	0.01	0.00	0.00	0.00	0.00	0.98	2.02	2424	2666	1048	347	439
Std dev	115	0.4	0.0	0.1	0.0	0.0	0.1	0.4	0.0		0.01	0.00	0.00	0.00	0.00	0.00	0.01	0.01	276	461	91	122	596
%	22	0.7	11.4	17.3	8.7	35.3	135.8	0.9	0.0		1.07	12.25	19.15	0.00	200.00	200.00	0.56	0.29	68677	17	9	35	136
HT15	0	55.9	1.2	0.4	0.1	0.0	0.0	42.5	100.0	3.00	1.01	0.03	0.01	0.00	0.00	0.00	0.98	2.02	7056	2721	520	169	269
HT15	16	57.9	1.2	0.4	0.1	0.1	0.0	40.4	100.0	3.00	1.07	0.03	0.01	0.00	0.00	0.00	0.95	2.05	7478	2798	669	423	179
HT15	41	56.8	1.2	0.4	0.1	0.0	0.2	41.3	100.0	3.00	1.04	0.03	0.01	0.00	0.00	0.00	0.96	2.04	7357	2954	669	254	1612
HT15	62	57.1	1.2	0.4	0.1	0.1	0.0	41.2	100.0	3.00	1.04	0.03	0.01	0.00	0.00	0.00	0.96	2.04	7478	2798	669	423	269
HT15	88	57.1	1.2	0.4	0.1	0.1	0.0	41.2	100.0	3.00	1.04	0.03	0.01	0.00	0.00	0.00	0.96	2.04	7478	2876	372	423	0
HT15	106	56.9	1.2	0.3	0.1	0.1	0.2	41.2	100.0	3.00	1.04	0.03	0.01	0.00	0.00	0.00	0.96	2.04	7478	2643	669	423	1612
HT15	124	57.9	1.3	0.4	0.1	0.1	0.0	40.3	100.0	3.00	1.07	0.03	0.01	0.00	0.00	0.00	0.95	2.05	7659	2721	594	423	90
HT15	149	57.3	1.2	0.4	0.1	0.0	0.0	40.9	100.0	3.00	1.05	0.03	0.01	0.00	0.00	0.00	0.96	2.04	7478	2798	520	338	90
HT15	171	57.2	1.2	0.4	0.1	0.1	0.1	41.1	100.0	3.00	1.05	0.03	0.01	0.00	0.00	0.00	0.96	2.04	7417	2721	594	423	448
HT15	197	57.5	1.2	0.4	0.1	0.0	0.0	40.8	100.0	3.00	1.06	0.03	0.01	0.00	0.00	0.00	0.95	2.05	7236	2876	594	169	269
HT15	220	57.2	1.2	0.4	0.1	0.1	0.0	41.1	100.0	3.00	1.05	0.03	0.01	0.00	0.00	0.00	0.96	2.04	6995	2798	743	423	90
HT15	239	57.1	1.1	0.4	0.1	0.0	0.2	41.1	100.0	3.00	1.05	0.03	0.01	0.00	0.00	0.00	0.96	2.04	6875	2798	669	338	1612
HT15	263	58.0	1.1	0.3	0.1	0.0	0.2	40.3	100.0	3.00	1.07	0.03	0.00	0.00	0.00	0.00	0.95	2.05	6573	2332	594	338	1612
HT15	292	57.8	1.2	0.3	0.1	0.1	0.0	40.5	100.0	3.00	1.06	0.03	0.01	0.00	0.00	0.00	0.95	2.05	6935	2565	520	507	269
HT15	313	59.0	1.2	0.4	0.1	0.1	0.1	39.3	100.0	3.00	1.10	0.03	0.01	0.00	0.00	0.00	0.93	2.07	7236	2721	669	423	448
HT15	331	59.1	1.2	0.3	0.1	0.1	0.0	39.2	100.0	3.00	1.10	0.03	0.01	0.00	0.00	0.00	0.93	2.07	7357	2643	669	423	269
HT15	349	58.8	1.2	0.4	0.1	0.0	0.0	39.5	100.0	3.00	1.09	0.03	0.01	0.00	0.00	0.00	0.94	2.07	7417	2798	817	338	90

Sample	Distance (microns)	CaO	MgO	FeO	MnO	SrO	BaO	CO2	Total	O	Ca	Mg	Fe2	Mn	Sr	Ba	C	Total	Mg	Fe	Mn	Sr	Ba
HT15	368	58.5	1.2	0.4	0.1	0.1	0.1	39.7	100.0	3.00	1.09	0.03	0.01	0.00	0.00	0.00	0.94	2.06	7236	2876	594	423	627
HT15	387	58.3	1.2	0.4	0.1	0.1	0.0	40.0	100.0	3.00	1.08	0.03	0.01	0.00	0.00	0.00	0.94	2.06	7297	2798	594	423	0
HT15	406	59.0	1.2	0.4	0.1	0.0	0.0	39.3	100.0	3.00	1.10	0.03	0.01	0.00	0.00	0.00	0.93	2.07	7176	2721	594	254	179
Mean		58.3	1.2	0.3	0.1	0.0	0.1	40.0	100.0	3.00	1.08	0.03	0.00	0.00	0.00	0.00	0.94	2.06	7110	2705	646	389	519
Std dev		0.7	0.0	0.0	0.0	0.0	0.1	0.7	0.0	0.00	0.02	0.00	0.00	0.00	0.00	0.00	0.01	0.01	248	151	82	68	573
%		1.2	3.5	5.6	12.6	17.4	110.3	1.7	0.0	0.00	1.81	4.21	6.12	27.27	100.00	200.00	1.07	0.49	3	6	13	17	110

A4.2.3 *Feldspars*

Throughout the region K-feldspar is the dominant feldspar, which typically shows K and Na zonation from core to rim (see Table A4.5), with high K rims and high Na cores. The feldspar compositions quote in Table A4.4 are typical of K-feldspars from marbles of the central Alps (*cf.* Wenk *et al.*, 1986).

Table A4.5 Average compositions of feldspars, analysed by electron microprobe.

	HT10	Rim	HT10	Core	HT11	Rim	HT11	Core	HT14	Rim	HT14	Core
Location	Verzasca		Verzasca		Verzasca		Verzasca		Narèt		Narèt	
n	5		27		2		15		8		40	
	Mean	SD	Mean	SD	Mean	SD	Mean	SD	Mean	SD	Mean	SD
SiO_2	64.48	0.55	64.37	0.29	64.02	0.11	64.52	0.15	64.42	0.76	64.92	0.34
Al_2O_3	18.35	0.16	18.39	0.06	18.41	0.09	18.53	0.05	18.09	0.19	18.16	0.10
Fe_2O_3	0.04	0.02	0.02	0.02	0.01	0.01	0.02	0.02	0.02	0.01	0.01	0.02
CaO	0.06	0.04	0.03	0.02	0.04	0.02	0.02	0.01	0.07	0.09	0.02	0.03
Na_2O	0.89	0.07	0.98	0.12	0.66	0.16	0.89	0.06	0.70	0.40	0.86	0.18
K_2O	15.74	0.12	15.61	0.22	16.03	0.12	15.82	0.10	15.89	0.61	15.65	0.28
BaO	0.17	0.02	0.16	0.02	0.25	0.07	0.22	0.02	0.17	0.04	0.15	0.02
SrO	0.08	0.01	0.09	0.02	0.18	0.00	0.17	0.02	0.01	0.01	0.02	0.01
Total	99.80	0.72	99.64	0.31	99.59	0.21	100.19	0.20	99.36	0.81	99.80	0.39
O	32.00	0.00	32.00	0.00	32.00	0.00	32.00	0.00	32.00	0.00	32.00	0.00
Si	11.96	0.01	11.95	0.02	11.93	0.00	11.94	0.01	12.00	0.03	12.02	0.01
Al	4.01	0.01	4.02	0.02	4.04	0.01	4.04	0.01	3.97	0.03	3.96	0.01
Fe3	0.01	0.00	0.00	0.00	0.00	0.00	0.00	0.00	0.00	0.00	0.00	0.00
Ca	0.01	0.01	0.01	0.00	0.01	0.00	0.00	0.00	0.01	0.02	0.00	0.01
Na	0.32	0.02	0.35	0.04	0.24	0.06	0.32	0.02	0.25	0.14	0.31	0.06
K	3.72	0.05	3.70	0.06	3.81	0.02	3.73	0.02	3.78	0.16	3.70	0.07
Ba	0.01	0.00	0.01	0.00	0.02	0.01	0.02	0.00	0.01	0.00	0.01	0.00
Sr	0.01	0.00	0.01	0.00	0.02	0.00	0.02	0.00	0.00	0.00	0.00	0.00
Total	20.05	0.02	20.06	0.02	20.07	0.02	20.07	0.01	20.03	0.04	20.00	0.02
%An	0.30	0.20	0.17	0.08	0.17	0.07	0.11	0.04	0.34	0.44	0.09	0.14
%Alb	7.84	0.59	8.64	1.09	5.81	1.38	7.76	0.49	6.18	3.59	7.70	1.60
%Or	91.34	0.67	90.67	1.11	93.11	1.32	91.30	0.47	93.14	3.71	91.89	1.58
%Cel	0.31	0.04	0.28	0.03	0.44	0.13	0.38	0.04	0.30	0.07	0.27	0.04

Continued...

	HT15	Rim	HT15	Core	HT16	Rim	HT16	Core	HT17	Rim	HT17	Core
Location	Narèt		Narèt		Narèt		Narèt		Narèt		Narèt	
n	4		13		4		30		4		16	
	Mean	SD	Mean	SD	Mean	SD	Mean	SD	Mean	SD	Mean	SD
SiO_2	64.65	0.13	64.44	0.44	64.86	0.19	64.91	0.12	64.96	0.22	65.02	0.14
Al_2O_3	18.32	0.02	18.24	0.14	18.24	0.09	18.31	0.05	18.33	0.06	18.33	0.06
Fe_2O_3	0.02	0.01	0.01	0.01	0.01	0.01	0.01	0.01	0.02	0.02	0.01	0.01
CaO	0.10	0.10	0.06	0.04	0.08	0.04	0.03	0.02	0.06	0.05	0.03	0.01
Na_2O	0.70	0.03	0.77	0.03	0.79	0.11	0.96	0.10	0.80	0.09	1.05	0.07
K_2O	16.11	0.04	15.97	0.10	16.01	0.20	15.73	0.22	15.99	0.09	15.63	0.16
BaO	0.14	0.02	0.13	0.01	0.03	0.02	0.04	0.01	0.03	0.02	0.03	0.02
Total	100.04	0.18	99.63	0.66	100.01	0.29	99.98	0.19	100.17	0.29	100.08	0.23
O	32.00	0.00	32.00	0.00	32.00	0.00	32.00	0.00	32.00	0.00	32.00	0.00
Si	11.97	0.01	11.98	0.01	11.99	0.01	11.99	0.01	11.99	0.00	11.99	0.01
Al	4.00	0.01	3.99	0.01	3.98	0.01	3.99	0.01	3.99	0.00	3.98	0.01
Fe3	0.00	0.00	0.00	0.00	0.00	0.00	0.00	0.00	0.00	0.00	0.00	0.00
Ca	0.02	0.02	0.01	0.01	0.02	0.01	0.01	0.00	0.01	0.01	0.01	0.00
Na	0.25	0.01	0.28	0.01	0.28	0.04	0.35	0.04	0.29	0.03	0.37	0.02
K	3.81	0.01	3.79	0.02	3.78	0.05	3.71	0.05	3.76	0.03	3.68	0.04
Ba	0.01	0.00	0.01	0.00	0.00	0.00	0.00	0.00	0.00	0.00	0.00	0.00
Total	20.06	0.01	20.06	0.02	20.05	0.01	20.04	0.02	20.04	0.00	20.04	0.01
%An	0.46	0.50	0.29	0.17	0.13	0.12	0.13	0.12	0.28	0.27	0.13	0.07
%Alb	6.15	0.31	6.80	0.27	8.50	0.96	8.50	0.96	7.04	0.75	9.21	0.61
%Or	93.13	0.40	92.66	0.25	91.31	0.85	91.31	0.85	92.63	0.85	90.61	0.55
%Cel	0.24	0.04	0.24	0.02	0.06	0.02	0.06	0.02	0.04	0.04	0.05	0.03

Continued...

	HT11[a]	Rim	HT11[a]	Core	HT17[a]	Rim	HT17[a]	Core
Location	**Verzasca**		**Verzasca**					
n	**a**		**a**		**Narèt**		**Narèt**	
n	**3**		**6**		**2**		**5**	
	Mean	SD	**Mean**	SD	**Mean**	SD	**Mean**	SD
SiO_2	**57.99**	0.52	**55.60**	2.44	**63.31**	1.00	**62.65**	0.43
Al_2O_3	**25.15**	0.66	**28.05**	1.67	**22.60**	0.93	**22.91**	1.02
Fe_2O_3	**0.15**	0.11	**0.03**	0.01	**0.02**	0.02	**0.02**	0.04
CaO	**7.40**	0.39	**10.43**	2.05	**4.155**	0.775	**4.56**	0.89
Na_2O	**7.31**	0.12	**5.80**	1.10	**8.895**	0.515	**8.75**	0.43
K_2O	**0.16**	0.01	**0.12**	0.06	**0.29**	0.07	**0.32**	0.08
BaO	**0.01**	0.01	**0.01**	0.01	**0.01**	0.01	**0.01**	0.01
Total	**98.47**	1.30	**100.30**	0.25	**99.28**	0.27	**99.24**	1.33
O	**32.00**	0.00	**32.00**	0.00	**32.00**	0.00	**32.00**	0.00
Si	**10.55**	0.07	**10.00**	0.39	**11.26**	0.18	**11.18**	0.17
Al	**5.39**	0.08	**5.95**	0.38	**4.74**	0.19	**4.82**	0.17
Fe3	**0.02**	0.02	**0.00**	0.00	**0.002**	0.00	**0.00**	0.00
Ca	**1.44**	0.06	**2.01**	0.40	**0.792**	0.15	**0.87**	0.16
Na	**2.58**	0.06	**2.02**	0.37	**3.069**	0.18	**3.03**	0.18
K	**0.04**	0.00	**0.03**	0.01	**0.0645**	0.01	**0.07**	0.02
Ba	**0.00**	0.00	**0.00**	0.00	**0.0005**	0.005	**0.00**	0.00
Total	**20.05**	0.00	**20.05**	0.01	**19.9325**	0.00	**19.97**	0.022
%An	**35.26**	1.43	**49.15**	9.63	**20.18**	3.85	**21.89**	4.03
%Alb	**63.06**	1.50	**49.48**	9.36	**78.14**	4.23	**76.22**	4.40
%Or	**0.89**	0.08	**0.66**	0.33	**1.64**	0.38	**1.82**	0.42
%Cel	**0.01**	0.01	**0.01**	0.01	**0.01**	0.01	**0.01**	0.02

[a] Plagioclase analyses.

A4.2.4 *Micas*

The biotite is near end member phlogopite (Phl_{80-90}) with significant fluorine substitution (Table A4.6). There are no appreciable differences between cores and rims of grains.

The phlogopite may have formed in a dolomite / K-feldspar rich layer during prograde metamorphism (Flowers & Helgeson, 1983) by the following reaction:

$$KAlSi_3O_8 + 3CaMg(CO_3)_2 + H_2O \rightarrow KMg_3AlSi_3O_{10}(OH)_2 + 3CaCO_3 + 3CO_2$$

The phlogopite analyses indicate that the majority of the OH^- has been replaced by F^-, which reduces the amount of water required for its formation and expanding its stability (Abercrombie *et al.*, 1987), so that it probably developed in the interval 400 °C to peak temperature.

Table A4.6 Average compositions of micas, analysed by electron microprobe.

Sample	HT4		HT15		HT16		HT17		HT23		HT26	
Location	Dalpe		Narèt		Narèt		Narèt		Someo		Crevola	
n	23		20		7		44		52			
	Mean	SD	Mean	SD	Mean	SD	Mean	SD	Mean	SD	Mean	SD
SiO_2	41.82	0.97	40.59	0.32	50.76	2.33	41.03	0.55	39.80	1.71	42.61	0.64
TiO_2	0.56	0.07	0.98	0.08	0.89	0.15	0.55	0.13	0.72	0.16	0.95	0.13
Al_2O_3	15.35	0.94	16.52	0.29	25.33	2.04	16.55	0.39	15.86	0.84	15.00	0.72
Cr_2O_3	0.03	0.02	0.02	0.02	0.03	0.02	0.02	0.02	0.02	0.02	0.03	0.02
FeO	0.17	0.03	5.94	0.17	1.56	0.93	2.92	0.12	3.51	0.18	1.09	0.15
MnO	0.02	0.01	0.03	0.01	0.02	0.01	0.01	0.01	0.02	0.01	0.02	0.01
MgO	25.40	0.52	20.19	0.14	4.75	3.19	22.91	0.47	24.34	1.18	24.86	0.47
CaO	0.07	0.06	0.04	0.07	0.04	0.05	0.12	0.48	0.13	0.66	0.02	0.03
Na_2O	0.17	0.03	0.14	0.02	0.18	0.03	0.14	0.04	0.25	0.08	0.20	0.02
K_2O	10.15	0.26	10.22	0.07	10.95	0.11	10.19	0.25	9.34	1.69	9.92	0.16
BaO	0.09	0.06	0.08	0.05	0.10	0.05	0.02	0.15	0.11	0.05	0.32	0.13
F	2.34	0.24	1.42	0.13	0.37	0.25	1.48	0.06	0.55	0.12	2.01	0.14
-O=F	0.99	0.10	0.60	0.05	0.15	0.10	0.63	0.01	0.23	0.05	0.84	0.06
Cl	0.05	0.01	0.01	0.01	0.01	0.01	0.00	0.00	0.02	0.01	0.02	0.01
-O=Cl	0.01	0.00	0.00	0.00	0.00	0.00	0.04	0.05	0.00	0.00	0.00	0.01
Total	95.24	0.61	95.59	0.22	94.83	0.39	95.34	0.81	94.44	1.78	96.19	0.59
O	22.00	0.00	22.00	0.00	22.00	0.00	22.00	0.00	22.00	0.00	22.00	0.00
Si	5.88	0.11	5.90	0.04	6.86	0.23	5.89	0.04	5.70	0.18	6.06	0.08
Ti	0.06	0.01	0.11	0.01	0.09	0.02	0.06	0.01	0.08	0.02	0.10	0.01
Al	2.55	0.17	2.83	0.05	4.03	0.29	2.80	0.06	2.68	0.17	2.52	0.01
Cr	0.00	0.00	0.00	0.00	0.00	0.00	0.00	0.00	0.00	0.00	0.00	0.00
Fe2	0.02	0.00	0.72	0.02	0.18	0.12	0.35	0.01	0.42	0.03	0.13	0.02
Mn	0.00	0.00	0.00	0.00	0.00	0.00	0.00	0.00	0.00	0.00	0.00	0.00
Mg	5.32	0.09	4.37	0.04	0.97	0.71	4.90	0.08	5.20	0.28	5.27	0.09
Ca	0.01	0.01	0.01	0.01	0.01	0.01	0.02	0.08	0.02	0.11	0.00	0.00
Na	0.05	0.01	0.04	0.00	0.05	0.01	0.04	0.01	0.07	0.02	0.06	0.01
K	1.82	0.05	1.89	0.02	1.89	0.03	1.87	0.04	1.71	0.30	1.80	0.03
Ba	0.00	0.00	0.00	0.00	0.01	0.00	0.00	0.00	0.01	0.00	0.02	0.01
Total	15.72	0.10	15.88	0.03	14.08	0.39	15.94	0.04	15.89	0.11	16.87	0.08
F	1.02	0.00	0.65	0.06	0.16	0.11	0.67	0.07	0.25	0.05	0.90	0.06
Cl	0.01	0.00	0.00	0.00	0.00	0.00	0.00	0.00	0.00	0.00	0.01	0.00
ΣNa,K,Ca,Ba	1.89	0.05	1.95	0.01	1.95	0.03	1.93	0.06	1.80	0.34	1.88	0.03
Σ cations	15.72	0.11	15.88	0.03	14.08	0.39	15.94	0.04	15.89	0.11	15.96	0.08
Si + Ti + Al	8.49	0.06	8.83	0.02	10.98	0.45	8.75	0.05	8.46	0.06	8.68	0.05
Tet Al	2.06	0.12	2.00	0.04	1.05	0.23	2.05	0.04	2.22	0.19	1.84	0.08
Oct Al	0.49	0.06	0.83	0.02	2.98	0.45	0.75	0.05	0.46	0.06	0.68	0.05
Σ Oct	5.83	0.05	5.92	0.03	4.13	0.37	6.01	0.06	6.08	0.26	6.08	0.03
% Annite	0.34	0.06	12.18	0.34	4.31	1.73	5.83	0.26	6.93	0.25	2.14	0.30
% Phl	91.33	1.10	73.78	0.49	23.45	10.70	81.63	1.04	85.49	1.13	86.68	1.14
% Al EM	8.33	1.08	14.04	0.23	72.24	12.38	12.54	0.90	7.59	1.10	11.18	0.86

Continued...

Sample	HT28		HT29		HT34	
Location	Crevola		Rozzaro		Crevola	
n	12		12		36	
	Mean	SD	Mean	SD	Mean	SD
SiO_2	43.32	0.67	39.37	1.34	43.33	1.17
TiO_2	0.22	0.05	1.59	0.22	0.54	0.08
Al_2O_3	14.81	0.50	17.44	0.77	13.32	0.57
Cr_2O_3	0.02	0.01	0.06	0.03	0.02	0.02
FeO	0.14	0.02	2.06	0.17	0.82	0.07
MnO	0.02	0.01	0.02	0.01	0.02	0.01
MgO	26.81	0.29	21.29	0.73	25.47	0.44
CaO	0.07	0.08	0.47	0.64	0.22	0.44
Na_2O	1.03	0.03	0.08	0.02	0.10	0.03
K_2O	8.44	0.16	10.48	0.31	10.03	0.44
BaO	0.11	0.05	0.10	0.06	0.47	0.49
F	3.10	0.14	1.78	0.13	2.43	0.24
-O=F	1.31	0.06	0.75	0.06	1.02	0.10
Cl	0.02	0.01	0.01	0.01	0.02	0.01
-O=Cl	0.00	0.00	0.00	0.00	0.00	0.00
Total	96.80	0.56	94.00	2.02	95.75	1.67
O	22.00	0.00	22.00	0.00	22.00	0.00
Si	6.15	0.07	5.67	0.09	6.24	0.07
Ti	0.02	0.01	0.17	0.02	0.06	0.01
Al	2.48	0.01	2.96	0.10	2.26	0.08
Cr	0.00	0.00	0.01	0.00	0.00	0.00
Fe2	0.02	0.00	0.25	0.02	0.10	0.01
Mn	0.00	0.00	0.00	0.00	0.00	0.00
Mg	5.68	0.04	4.57	0.10	5.47	0.09
Ca	0.01	0.01	0.07	0.10	0.03	0.07
Na	0.28	0.01	0.02	0.01	0.03	0.01
K	1.53	0.03	1.93	0.03	1.84	0.07
Ba	0.01	0.00	0.01	0.00	0.03	0.03
Total		0.09	16.46	0.09	16.06	0.11
F	1.39	0.06	0.81	0.06	1.11	0.12
Cl	0.00	0.00	0.00	0.00	0.00	0.00
ΣNa,K,Ca,Ba	1.83	0.05	2.03	0.12	1.93	0.11
Σ cations	16.18	0.08	15.65	0.08	16.06	0.08
Si + Ti + Al	8.65	0.03	8.80	0.10	8.56	0.06
Tet Al	1.83	0.05	2.16	0.09	1.70	0.07
Oct Al	0.65	0.07	0.80	0.10	0.56	0.06
Σ Oct	6.35	0.02	5.61	0.07	6.13	0.06
% Annite	0.31	0.04	4.41	0.39	1.61	0.14
% Phl	89.45	0.47	81.38	1.47	89.27	1.04
% Al EM	10.24	0.46	14.21	1.65	9.12	1.04

A4.3 The Ion Microprobe

Ion microprobe analysis was carried out at the Ion Microprobe Facility at Edinburgh University during February and November 2000.

A4.3.1 *The Instrument*

The ion microprobe employs Secondary Ion Mass Spectrometry (SIMS) for the chemical analysis of small volumes of material. In SIMS the surface of the sample is bombarded under vacuum with a finely focused beam of primary ions (O^-). The collision cascade results in the ejection and ionisation of atoms and molecules from the surface layers of the sample. These secondary ions are accelerated into a double focusing mass spectrometer where they are separated according to their energy and mass/charge ratio before being detected. The secondary ion counts are measured in the mass spectrometer, giving results in $counts s^{-1}$, which can then be converted to ppm values. The samples were analysed using point analysis, where a focused stationary beam is used to determine the composition at a point. The spot size is normally between 1 and 25μm but is dependent on the application (in this case closer to 25 μm).

The Ion Microprobe Facility is equipped with a Cameca ims-4f (#130). This contains a duoplasmatron ion source for either positive or negative O or Ar ion generation, with additional pumping and gun isolation (IMPVAC Option). The sample voltage may be adjusted from 0 to +4500v or 0 to- 4500v, so that the analyses may be made using high offset techniques. An air lock system, which can hold eight samples, has been installed working at a vacuum of 2×10^{-8} Torr and allowing greater ease of sample exchange.

A4.3.2 *Sample Preparation*

The Cameca ims-4f sample airlock has been modified to allow eight specimens to be stored under vacuum (5×10^{-8} Torr). The holders may then be transferred into the instrument for analysis in a matter of seconds. Each specimen holder can accept a 2.54 cm diameter round sample with a maximum thickness of 1.27 cm. Samples should be flat, polished and vacuum compatible.

Epoxy resins such as Araldite (MY778 resin and HY951 hardener), Petropoxy and Epo-Thin all degas to a greater or lesser extent and will contribute to the H background in the instrument. They should therefore be used sparingly and acrylic resins should never be used. Insulating samples need to be coated with a thin layer of Au (10-30 nm). Prior to coating, samples must be ultrasonically cleaned to remove polishing compounds and chemicals to prevent the effects of surface contamination whilst undergoing analysis. Gold is used in preference to carbon due to its higher conductivity, which means only a thin layer is required which can be easily and quickly removed by the primary ion beam. Other advantages of gold coating are it is mono-isotropic, poorly ionising and of high mass; molecular complexes with gold should not therefore generate significant interferences.

A4.3.3 *Standards and Interferences*

Table A4.7 Ion microprobe standards.

Mineral	Standards
Calcite	OKA, calcite
	NCC, calcite
K-feldspar	SHF1, feldspar
	NBS, silicate glass
Phlogopite	NBS, silicate glass

Not only are ions of individual elements produced, but also ionised molecular combinations of elements present in the matrix. These molecules can travel to the mass spectrometer and cause interferences if their molecular weight is the same as the atomic weight of an element being analysed, see below for table of interferences.

Table A4.8 Isotopes measured and their interferences (all data presented in later tables are corrected for the appropriate interference).

Element	Mineral	Interference
^{23}Na	Cc, K-fsp, Phl	
^{26}Mg	Cc, K-fsp, Phl	
^{30}Si[a]	Cc, K-fsp, Phl	
^{40}Ca	K-fsp	
^{41}K	K-fsp, Phl	
^{42}Ca	Phl	
^{44}Ca[b]	Cc	
^{54}Fe	Cc, Phl	
^{56}Fe	K-fsp	Al_2, Cr
^{55}Mn	Cc, K-fsp, Phl	
^{56}Fe	K-fsp	KO, AlSi
^{85}Rb	K-fsp, Phl	FeSi
^{88}Sr	K-fsp, Phl	Ca_2, CaMgO
^{133}Cs	K-fsp, Phl	
^{138}Ba	Cc, K-fsp, Phl	La, Ce

[a] The secondary ion counts of K-feldspar and phlogopite were normalised to ^{30}Si.
[b] The secondary ion counts of calcite were normalised to ^{44}Ca.

A4.4 Ion Microprobe Data

Table A4.9 Calcite ion microprobe traverse data.

Data point	Distance	^{26}Mg	^{55}Mn	^{54}Fe	^{88}Sr	^{138}Ba
23-221	0	17113	272	3357	355	1.9
23-220	20	17415	272	3440	357	1.9
23-219	40	16802	272	3370	358	2.1
23-215	120	17145	274	3389	362	2.1
23-214	140	16973	271	3361	363	2.0
23-213	160	16843	271	3350	364	2.0
23-222	180	17747	273	3434	359	2.4
23-223	200	17742	274	3453	363	2.4
23-224	220	18829	274	3586	360	2.2

Data point	Distance	^{26}Mg	^{55}Mn	^{54}Fe	^{88}Sr	^{138}Ba
23-226	240	19470	274	3640	359	2.5
23-227	260	18639	269	3544	363	2.6
23-228	280	19187	273	3610	359	2.6
23-230	300	18912	275	3598	357	2.4
23-231	320	18597	272	3611	360	2.1
n=14	Average	17958	273	3482	360	2.2
	SD	912	2	107	3	0.2
23-184	0	19754	255	3501	360	2.2
23-183	20	19945	259	3535	362	2.2
23-182	40	20174	254	3558	357	2.2
23-181	60	20231	256	3589	357	2.2
23-180	80	18667	251	3361	359	2.2
23-178	100	17726	246	3256	360	2.2
23-177	120	19036	252	3434	360	2.2
23-175	140	18698	249	3353	362	2.3
23-174	160	19715	248	3443	364	2.3
23-171	180	15858	250	3015	348	2.7
23-186	200	19477	254	3472	354	2.5
23-187	220	19437	252	3468	356	2.4
23-188	240	19260	255	3472	356	2.2
23-190	260	18774	249	3569	357	3.3
23-191	280	18607	247	3382	361	2.4
n=15	Average	19024	252	3427	358	2.4
	SD	1072	3	141	4	0.3
15-174	0	6768	500	2401	333	1.2
15-175	42	7197	513	2463	295	0.8
15-176	67	7036	522	2446	279	0.6
15-177	88	6728	525	2385	280	0.5
15-178	113	6529	520	2318	278	0.4
15-183	160	6098	521	2254	280	0.3
15-182	210	6703	521	2400	295	0.4
15-181	285	6829	522	2412	310	0.8
15-180	395	6879	517	2438	312	0.6
Average	23	6752	518	2391	296	0.6
SD		295	7	63	18	0.2
11-250	0	2887	446	2641	828	0.8
11-251	30	2781	442	2525	820	0.6
11-252	80	2651	444	2287	814	0.5
11-253	101	2490	441	2145	804	0.5
11-254	169	2042	451	1519	702	0.5
11-255	189	1700	448		555	0.5
Average	18	2425	445	2223	754	0.6
SD		422	3	393	99	0.1

Table A4.10 Phlogopite/K-feldspar ion microprobe traverse data (from Figure 6.15).

Data Point	Distance	^{23}Na	^{26}Mg	^{40}Ca	^{41}K	^{55}Mn	^{56}Fe	^{85}Rb	^{88}Sr	^{138}Ba
17-114	0	10333.0	9.2	166.2	96809.0	64.2	149.3	224.0	93.3	370.8
17-115	20	8622.0	10.4	161.5	98984.0	65.3	154.0	230.5	93.6	417.1
17-116	40	10356.0	9.9	201.1	97512.0	63.2	145.7	227.5	92.3	406.4
17-117	60	8677.4	9.9	156.8	100580.0	64.6	143.7	232.8	91.0	389.8
17-119	80	9121.7	10.7	160.8	100230.0	65.6	147.5	232.8	98.7	404.1
17-120	100	7547.4	17.1	170.0	103240.0	65.9	146.2	240.8	105.5	425.5
17-121	120	8614.4	16.2	156.6	100770.0	66.3	155.6	228.4	107.8	390.6
17-122	140	8771.6	39.0	163.1	99780.0	64.3	156.6	224.1	119.8	333.6
	Average	9005.4	15.3	167.0	99738.1	64.9	149.8	230.1	100.2	392.2
	S D	879.5	9.4	13.5	1883.6	1.0	4.6	5.1	9.4	27.3
17-125	160	1184.8	185930.0	563.8	69816.0	188.1	3360.0	601.5	0.0	33.0
17-126	180	1202.3	187850.0	105.3	69196.0	193.2	3120.0	602.0	0.0	32.2
17-127	200	1204.0	187850.0	75.1	69727.0	192.8	3120.0	586.0	0.0	30.8
17-128	220	1266.7	188640.0	22.7	70618.0	203.9	3230.0	577.2	0.0	38.3
17-128	240	1266.7	188640.0	22.7	70618.0	203.9	3230.0	577.2	0.0	38.3
17-129	260	1250.5	189510.0	18.1	70463.0	202.9	3240.0	562.7	0.0	35.9
	Average	1229.2	188070.0	134.7	70073.0	197.5	3216.7	584.4	0.0	34.7
	S D	33.2	1110.5	194.6	532.5	6.3	81.8	14.0	0.0	2.9
17-96	0	5916.2	17598.0	292.8	102080.0	74.7		311.2	134.6	560.0
17-97	20	7721.2	25.6	216.3	102160.0	63.2	152.8	228.2	124.5	421.7
17-98	40	7015.7	105.5	779.3	106460.0	65.6	235.5	242.2	124.6	486.0
17-99	60	9072.0	191.4	1546.0	107540.0	66.4	150.7	237.1	164.0	546.0
	Average	7431.3	4480.1	708.6	104560.0	67.5	179.7	254.7	136.9	503.4
	S D	1145.0	7573.8	529.5	2469.9	4.3	39.5	33.0	16.2	54.8
17-105	100	1406.8	186650.0	325.9	72452.0	181.2	3100.0	660.2	2.3	30.7
17-104	120	1406.8	186650.0	325.9	72452.0	181.2	3110.0	660.2	2.3	30.7
17-103	140	1741.9	184150.0	452.6	73723.0	189.4	3100.0	672.9	2.4	38.0
17-102	160	1557.9	183490.0	565.2	76529.0	192.7	3110.0	667.2	2.4	41.3
17-101	180	1319.8	186510.0	298.0	69386.0	190.0	3070.0	589.3	1.6	44.0
17-100	200	1311.8	186100.0	215.1		183.9	3040.0		1.8	38.5
	Average	1457.5	185591.7	363.8	72908.4	186.4	3088.3	649.9	2.1	37.2
	S D	150.7	1280.4	113.8	2306.3	4.5	25.4	30.7	0.3	5.0
14-64	0	6712.2	6.5	164.1	103010.0	70.7	196.4	348.9	132.4	41.3
14-63	20	8387.3	5.2	119.7	100940.0	70.1	198.8	358.2	119.0	42.1
14-62	40	9006.2	5.4	85.6	102830.0	69.4	200.0	372.8	106.1	42.3
14-61	60	6958.2	5.3	101.8	103380.0	70.9	195.7	364.1	128.8	46.1
14-59	80	7866.2	5.0	122.2	101200.0	70.7	198.6	345.0	113.1	46.2
14-58	100	8918.9	5.5	162.4	99931.0	70.1	197.1	347.5	106.3	48.1
14-57	120	9700.3	10.6	189.5	99524.0	70.9	197.2	351.1	104.8	51.3
14-56	140	9826.7	4.7	147.9	98205.0	68.5	194.3	350.0	101.0	48.6
14-55	160	8981.0	6.5	167.8	98974.0	69.4	192.6	346.0	111.0	48.8
14-54	180	7441.4	6.2	130.8	101430.0	69.3	189.9	348.8	100.1	45.5
	Average	8379.8	6.1	139.2	100942.4	70.0	196.1	353.2	112.2	46.0
	S D	1040.6	1.6	31.0	1687.8	0.8	2.9	8.6	10.6	3.1
14-48	220	2097.0	22953.0	55.9	69003.0	155.5	1090.0	485.2	0.5	384.3
14-47	240	2026.6	23120.0	52.3	67893.0	149.0	1040.0	443.5	0.4	383.2
14-46	260	1924.9	23338.0	56.0	67594.0	144.5	1000.0	436.0	0.0	249.9

Data Point	Distance	^{23}Na	^{26}Mg	^{40}Ca	^{41}K	^{55}Mn	^{56}Fe	^{85}Rb	^{88}Sr	^{138}Ba
14-44	300	2021.1	23823.0	43.0	67720.0	151.0	1080.0	450.9	0.4	221.3
14-43	320	2068.8	23655.0	50.8	67952.0	152.0	1080.0	469.1	0.3	247.8
14-49	340	2036.2	23504.0	50.0	67817.0	145.5	1050.0	452.7	0.3	236.3
14-50	360	2057.9	23651.0	57.6	67542.0	144.7	1040.0	452.6	0.6	233.1
14-51	380	2063.7	23573.0	79.0	68027.0	143.8	1050.0	452.7	1.0	246.7
	Average	2037.0	23452.1	55.6	67943.5	148.3	1053.8	455.3	0.4	275.3
	S D	48.3	275.7	9.9	430.3	4.0	27.4	14.3	0.3	63.2
16-40	0	5379.8	13.8	426.4	104280.0	67.8	158.6	425.7	157.2	137.8
16-38	40	6602.9	8.0	130.8	102700.0	68.8	169.9	394.0	177.6	138.0
16-41	60	8154.3	7.6	117.2	100140.0	68.0	160.6	407.2	164.4	122.8
16-42	80	9243.7	8.1	187.2	99870.0	66.2	156.5	404.6	164.1	139.2
	Average	7345.2	9.4	215.4	101747.5	67.7	161.4	407.9	165.8	134.4
	S D	1472.5	2.6	124.6	1832.3	1.0	5.1	11.4	7.4	6.8
16-34	100	1079.6	190110.0	518.5	59379.0	133.0	4050.0	948.7	1.6	14.5
16-33	120	1541.3	168630.0	487.9	69662.0	140.8	3630.0	1102.5	1.3	14.6
16-32	140	1518.9	183770.0	363.6	72693.0	139.9	3840.0	1177.7	0.8	14.1
16-35	160	1362.0	182590.0	339.6	72188.0	134.0	3750.0	1175.0	0.8	14.2
16-36	180	1308.8	182630.0	343.8	73323.0	144.1	3780.0	1181.2	0.9	12.2
16-37	200	1069.7	182230.0	706.2	72954.0	177.8	3410.0	1194.1	1.2	22.7
	Average	1313.4	181660.0	459.9	70033.2	144.9	3743.3	1129.9	1.1	15.4
	S D	187.4	6426.1	130.5	4911.2	15.2	195.2	86.3	0.3	3.4
17-132	0	1045.0	185910.0	55.3	73541.0	229.2	3670.0	749.5	0.3	9.5
17-133	20	991.8	185120.0	70.2		227.0	3700.0	745.1	0.3	13.0
17-134	40	916.6	184630.0	53.9	72399.0	216.8	3620.0	734.3	0.3	9.7
17-135	60	799.0	184370.0	66.5	72797.0	205.1	3630.0	739.9	0.3	8.7
17-136	80	741.3	182950.0	82.2	73256.0	190.1	3590.0	729.2	0.4	10.7
17-137	100	693.0	180020.0	81.3	70937.0	192.5	3520.0	708.4	0.5	11.0
	Average	864.4	183833.3	68.2	72586.0	210.1	3621.7	734.4	0.3	10.4
	S D	129.3	1924.1	11.2	912.1	15.4	57.6	13.4	0.1	1.4
17-138	120	8998.1	59.9	205.9	98605.0	66.8	171.0	237.5	95.4	188.1
17-139	140	7998.2	9.5	194.7	101100.0	64.8	150.8	250.7	86.3	184.2
17-141	180	8034.2	11.6	156.0	103080.0	64.9	147.2	256.5	72.4	197.8
17-142	200	8504.1	10.8	178.4	99144.0	65.7	159.1	245.9	76.5	138.2
17-143	220	9303.8	8.6	143.3	98746.0	65.0	152.7	239.1	87.3	136.0
17-144	240	5534.5	165.9	115.8	96027.0	62.1	184.0	216.5	91.3	162.3
	Average	8062.2	44.4	165.7	99450.3	64.9	160.8	241.0	84.9	167.8
	S D	1225.2	57.3	30.8	2195.4	1.4	12.9	12.7	8.0	24.2
16-18	8082.15	1057.2	22620.0	61.3	63855.0	111.4	3282.7	603.1	0.3	103.9
16-23	120	1308.4	22619.0	38.7	63490.0	110.5	3500.8	602.1	0.3	110.1
16-25	180	1325.1	22382.0	41.9	64104.0	113.2	3458.3	611.1	0.3	108.7
16-26	200	1539.2	21874.0	112.8	64121.0	112.5	3560.6	596.0	0.9	115.4
	Average	1307.5	22373.8	63.7	63892.5	111.9	3450.6	603.1	0.4	109.5
	S D	170.8	304.4	29.6	255.1	1.0	103.5	5.4	0.3	4.1
16-27	0	7560.5	18.0	285.9	96889.0	73.3	184.4	497.3	184.3	232.1
16-28	20	8127.8	6.1	142.9	93555.0	71.4	180.5	500.9	138.0	217.9
16-29	40	7700.0	4.9	128.6	94913.0	70.4	181.5	497.5	140.3	211.2
16-30	60	7756.8	8.9	140.4	93848.0	68.0	166.1	481.3	144.6	208.8
16-31	80	7124.5	11.3	259.6	94922.0	68.9	173.7	478.1	160.3	205.5
	Average	7653.9	9.9	191.5	94825.4	70.4	177.2	491.0	153.5	215.1

Data Point	Distance	^{23}Na	^{26}Mg	^{40}Ca	^{41}K	^{55}Mn	^{56}Fe	^{85}Rb	^{88}Sr	^{138}Ba
	S D	324.4	4.6	67.1	1170.0	1.9	6.6	9.4	17.2	9.4

Table A4.11 Phlogopite/K-feldspar ion microprobe traverse data (from Figure 6.16).

Data Point	Distance	^{23}Na	^{26}Mg	^{40}K	^{42}Ca	^{55}Mn	^{56}Fe	^{85}Rb	^{87}Sr	^{133}Cs	^{138}Ba
15-97	0	1556.1	19832.0	62.8	61151.0	33.2	4631.9	437.5	0.9	12.7	322.5
15-98	30	1297.6	20281.0	46.4	61031.0	30.7	4619.1	426.2	0.5	13.2	274.6
15-99	60	1208.1	19945.0	48.6	61491.0	29.8	4464.3	426.9	0.6	13.7	311.6
15-100	90	1825.2	16140.0	59.0	62840.0	37.6	4795.0	406.3	3.2	9.4	327.2
15-101	115	1635.7	17749.0	54.5	62288.0	35.2	5015.9	418.6	2.0	10.7	361.6
15-102	140	2117.8	14055.0	173.1	71813.0	14.8	4383.3	456.6	75.7	12.5	521.3
	Average	1606.8	18000.3	74.1	63435.7	30.2	4651.6	428.7	13.8	12.0	353.1
	S D	307.4	2288.7	44.7	3799.9	7.4	208.9	15.6	27.7	1.5	79.4
15-103	160	6611.4	89.1	19.7	11130.0	35.3	206.6	364.3	495.6	4.3	1202.6
15-104	170	7149.9	6.7	19.2	226.1	21.2	167.9	344.4	493.2	4.2	1131.7
15-105	180	7315.5	5.6	19.0	132.2	19.3	161.0	338.2	490.7	4.2	1104.4
15-106	202	7100.2	7.0	19.0	153.4	19.1	159.9	332.3	488.3	3.9	1107.6
15-107	232	6847.3	7.9	18.9	169.9	16.6	150.8	326.9	490.6	3.4	1115.3
	Average	7004.9	23.3	19.2	2362.3	22.3	169.3	341.2	491.7	4.0	1132.3
	S D	247.5	32.9	0.3	4383.9	6.7	19.4	12.9	2.5	0.3	36.4
15-76	0	8445.1	8.2	19.9	135.4	30.6	173.2	391.1	501.8	5.4	1080.9
15-77	20	7005.6	5.3	19.4	52.3	25.6	148.6	359.8	489.9	4.8	1060.6
15-78	40	7827.0	5.4	19.0	59.3	22.4	142.0	352.1	512.4	4.9	1045.6
15-79	62	8339.0	6.0	18.8	94.8	22.7	150.1	351.2	486.8	5.1	1017.3
15-80	82	9115.8	6.8	18.6	111.9	22.5	149.6	352.6	482.2	5.4	1009.1
	Average	8146.5	6.4	19.1	90.7	24.8	152.7	361.4	494.6	5.1	1042.7
	S D	702.8	1.1	0.5	31.4	3.1	10.7	15.2	11.0	0.3	26.7
15-87	200	2005.2	16290.0	6298.6	63750.0	52.6	5157.7	402.0	17.5	9.5	256.6
15-88	225	1298.8	23148.0	40.0	58581.0	26.1	4505.7	421.5	0.2	13.5	173.7
15-89	232	1307.4	22293.0	34.2	57778.0	21.5	4545.2	411.1	0.3	14.9	298.5
15-90	252	1637.7	19446.0	37.9	60548.0	29.8	4755.9	396.4	3.8	11.9	286.2
15-91	262	1248.4	22364.0	37.2	58933.0	26.2	4683.2	405.9	0.2	13.5	237.1
15-92	277	1334.4	21023.0	33.4	60299.0	32.2	5073.2	474.3	0.2	16.3	109.0
15-93	307	1387.8	20555.0	30.2	59813.0	28.4	4762.1	465.1	0.1	15.4	91.9
15-94	327	1388.9	20763.0	43.7	59632.0	28.9	4742.4	464.8	0.1	16.1	91.0
15-95	348	1337.2	21725.0	36.9	57920.0	23.6	4306.4	421.0	0.3	16.3	254.4
	Average	1438.4	20845.2	732.5	59694.9	29.9	4725.8	429.1	2.5	14.1	199.8
	S D	226.0	1923.8	1967.9	1706.2	8.6	251.3	28.7	5.4	2.2	79.7